# Towards a Unified View of Substrate Binding in Heme Peroxidases

Thesis submitted for the degree of Doctor of Philosophy at the University of Leicester

By

Emma Joanna Murphy, MChem Biological Chemistry

Department of Chemistry
Faculty of Science
University of Leicester

October 2008

# *In Memory of My Mum*

# Acknowledgements

I would like to thank my supervisor Prof. Emma Lloyd Raven for her guidance, support and help throughout the last three years and Dr M. Dickens for helpful discussions on the progress of the project. Thanks also to Dr. P. C. E. Moody (University of Leicester, Department of Biochemistry and Henry Wellcome Laboratories for Structural Biology) for his expertise of X-ray crystallography. For financial support I am indebted to the BBSRC and the University of Leicester, also to Claire Taylor and the rest of the student welfare team whose support throughout the last three years has been amazing. I'm very grateful to Dr. C. Metcalfe, Dr. I. K. Macdonald, Dr. I. Efimov, Dr. N. Papadopoulou, Dr. S. Badyal, Dr. Z. Pipirou, Miss N. Chauhan and Miss S. Rafice for their encouragement and assistance in the lab. I would also like to acknowledge Dr. Florian Hollfelder and Dr. Linda Otten of the Biochemistry department at Cambridge University for their assistance with the creation of random mutagenesis libraries. I would like to thank Rob Cummins and his family for support throughout my time at the University of Leicester. Finally, I would like to thank my sister, Samantha, for the help and support she has given me and, of course, my mum Lesley who made all this possible.

# Towards a Unified View of Substrate Binding in Heme Peroxidases

Emma Joanna Murphy

## Abstract

Heme peroxidases catalyse the $H_2O_2$-dependent oxidation of a variety of substrates. The binding of substrates to heme peroxidases has been widely assumed to occur at the so-called δ-heme edge. Recently, however, a number of examples have appeared in which substrate binding at an alternative site, the γ-heme edge, is also possible. In this thesis substrate binding in two class I peroxidases, cytochrome *c* peroxidase (C*c*P) and ascorbate peroxidase (APX), has been examined using a variety of methods with the aim of providing a more unified view of substrate binding across the family of heme peroxidases.

It has been shown that the closely related C*c*P enzyme can duplicate the substrate binding properties of APX through the introduction of relatively modest structural changes. Hence, crystallographic data for the Y36A/N184R/W191F triple variant of C*c*P is presented showing ascorbate bound to the γ-heme edge. Functional studies have shown that a transient porphyrin π-cation radical in C*c*P, analogous to that observed in APX, is competent for ascorbate oxidation but that under steady state conditions this intermediate decays too rapidly to sustain efficient turnover of ascorbate. The first crystal structures of complexes of the tuberculosis prodrug, isoniazid, bound to APX and C*c*P are presented along with the structures of the isoniazid complexes of two active site mutants of APX. These structures provide the first unambiguous evidence for the location of the isoniazid binding site in the class I peroxidases and provide rationalization of isoniazid resistance in naturally occurring KatG mutant strains of *M. tuberculosis*. Aromatic substrate binding in C*c*P has been examined by X-ray crystallography and competitive inhibition studies and directed evolution has been used to probe aromatic substrate binding in APX. Finally, the first neutron diffraction structure of C*c*P has been solved allowing a detailed description of the resting ferric enzyme and showing that it would be a viable technique for use of studying the nature of key intermediates and gaining further insight into enzyme-substrate interactions.

Understanding the structural and chemical requirements for efficient substrate binding and oxidation by heme peroxidases will provide a more in-depth understanding of the mechanism they use and will pave the way for the production of enzymes with improved catalytic efficiency and novel functions and the development of improved therapeutic agents against diseases such as tuberculosis.

# Table of Contents

# Chapter 1: Introduction

# Chapter 2: Introduction of an Ascorbate Binding Site into Cytochrome *c* Peroxidase

# Chapter 3: Binding of Isoniazid to Peroxidases

# Chapter 4: Binding of Aromatic Substrates in Cytochrome *c* Peroxidase

# Chapter 5: Probing Aromatic Binding in APX using Directed Evolution

# Chapter 6: Neutron Diffraction Studies of Cytochrome *c* Peroxidase

# Chapter 7: Summary

# Chapter 8: Experimental

# Table of Figures

# Table of Tables



## *Appendix B*



## *Appendix C*

# Abbreviations

Amino Acids are abbreviated according to the three-letter codes recommended by the I. U. P. A.C. Joint Commission on Biochemical Nomenclature (1985).

## Enzymes

| | |
|---|---|
| APX | ascorbate peroxidase |
| rpAPX | recombinant cytosolic pea ascorbate peroxidase |
| rsAPX | recombinant cytosolic soybean ascorbate peroxidase |
| ARP | *arthromyces ramosus* peroxidase |
| C*c*P | cytochrome *c* peroxidase |
| KatG | catalase-peroxidase |
| DNase | deoxyribonuclease |
| HRP | horseradish peroxidase |
| IDO | indoleamine 2,3-dioxygenase |
| NOS | nitric oxide synthase |
| TDO | tryptophan 2,3-dioxygenase |
| LiP | Lignin peroxidase |
| MnP | manganese peroxidase |
| MAO | monoamine oxygenase |
| RNase | ribonuclease |

## Chemicals

| | |
|---|---|
| ABTS | 2,2'-azino,di(3-ethyl-benzothiazoline-6-sulfonic acid) |
| Amp | Ampicillin |
| BHA | benzhydroxamic acid |
| C | cytosine |
| dNTPs | deoxynucleotide triphosphates |

| | |
|---|---|
| EDTA | ethylenediaminetetraacetic acid |
| FA | ferulic acid |
| G | guanine |
| Hepes | N-2-hydroxyethylpiperazine-N'-2-ethanesufonic acid |
| IPTG | isopropyl-β-D thiogalactopyanoside |
| Kan | kanamycin |
| NTA | nitrilotriacetic acid |
| PEG 4000 | poly (ethylene glycol) of average molecular weight 4000 |
| SDS | sodium dodecyl sulfate |
| SHA | salicylhydroxamic acid |
| T | thymine |
| Tris | trizma base (tri[hydroxymethyl]aminomethene) |

## Techniques

| | |
|---|---|
| ENDOR | electron nuclear double resonance |
| EPR | electron paramagnetic resonance |
| EXAFS | extended X-ray absorption fine structure |
| FPLC | fast protein liquid chromatography |
| LB | Luria-Bertani broth |
| NMR | nuclear magnetic resonance |
| PAGE | polyacrylamide gel electophoresis |
| PCR | polymerase chain reaction |
| Rz | Reinheitzahl |
| StEP | staggered extension process |
| UV | ultra violet |
| Vis | visible |

## Units/Symbols

| | |
|---|---|
| A | absorption |
| ε | absorption coefficient |
| Å | Ångström (1 Å = $10^{-10}$ m) |

| | |
|---|---|
| ˚C | degrees Celsius |
| ˚ | degrees |
| g | grams |
| kDa | kilo Daltons |
| l | litres |
| m | metres |
| min | minutes |
| M | molar |
| rpm | revolutions per minute |
| s | seconds |
| V | volts |
| λ | wavelength |
| w/v | weight per volume |
| n | whole number |

## Miscellaneous

| | |
|---|---|
| DNA | deoxyribonucleic acid |
| *E. coli* | *Escherichia coli* |
| ESRF | European Synchrotron Research Facility |
| FFQ | fast flow Q Sepharose |
| I. U. P. A.C. | International Union of Pure and Applied Chemistry |
| MDL | Molecular Dimensions Ltd |
| PDB | Protein Data Bank |
| PNACL | Protein and Nucleic Acid Chemistry Laboratory |
| r.m.s. | root mean squared |
| RNA | ribonucleic acid |
| EMBL | European Molecular Biology Laboratory |
| ILL | Institut Laue-Langevin |

# Chapter 1

## *Introduction*

## 1.1 Metals in biology

Elements such as iron have been known to be essential to life since the 17th century and copper, zinc and manganese have been known to be essential since the 1930s [1]. Metals play a key role in biological systems with over 30% of proteins requiring a metal ion for structure or function. Transition metals are involved in a host of biological processes from oxygen transport to gene transcription [2] and have been implicated in diseases such as microbial infections, cancer and neurodegenerative disorders [3], they have been shown to be important in the maintenance of brain biochemistry and uncontrolled levels have been implicated in diseases of the central nervous system [4].

The chemistry of iron is central to life processes and it fulfils a vital role in virtually all living organisms [5]. The functions carried out by iron include oxygen transport, redox catalysis and electron transfer. Iron is uniquely suitable for these functions due to its relative abundance, the solubility of ferrous salts and the extreme variability of its oxidation states and the redox potentials between these states which can be finely tuned by the protein environment. Iron sites within proteins can almost cover the entire range of biologically significant redox potentials form -0.5 V to +0.6 V [6].

Despite its many attractive qualities, there are problems related to the use of iron in biological processes, for which nature has devised many sophisticated mechanisms for overcoming. The easy one-electron interconversion of $Fe^{2+}$ and $Fe^{3+}$, also makes iron toxic, by generation of oxygen-derived radicals and other damaging species [7]. Aerobic life also makes $Fe^{3+}$ the thermodynamically favored species over $Fe^{2+}$, leading to problems of solubilization. The toxicity and low solubility of free iron has been overcome by the use of transferrin [8] in mammalian systems which allows iron to be transported through the body and taken up by cells. Bacteria use an array of iron-chelating peptides and ester derivatives known as siderophores [9].

It is well known that the reactivity of a metal ion can be modulated and fine-tuned by its incorporation into a protein structure. Iron can be incorporated into a protein by co-ordination to a side chain of the protein and an inorganic non-metallic ion as in the Iron-sulphur cluster proteins [10] which include ferredoxins [11], electron transfer proteins involved in an array of biological activities and NADH

dehydrogenase [12] which catalyses the transfer of electrons from NADH to coenzyme Q in the electron transport chain. Alternatively iron can be incorporated into a protein as part of an organic compound such as the heterocyclic macromolecule porphyrin.

# 1.2 Heme Proteins

## *1.2.1 The heme prosthetic group*

Iron protoporphyrin IX or heme (Figure 1.1) is a metal complex that is used for various functions in a wide variety of proteins. The iron-containing macrocycle is made up of four pyrrole rings joined with methene bridges in a conjugated system and has an $Fe^{3+}$ in the centre of the molecule.

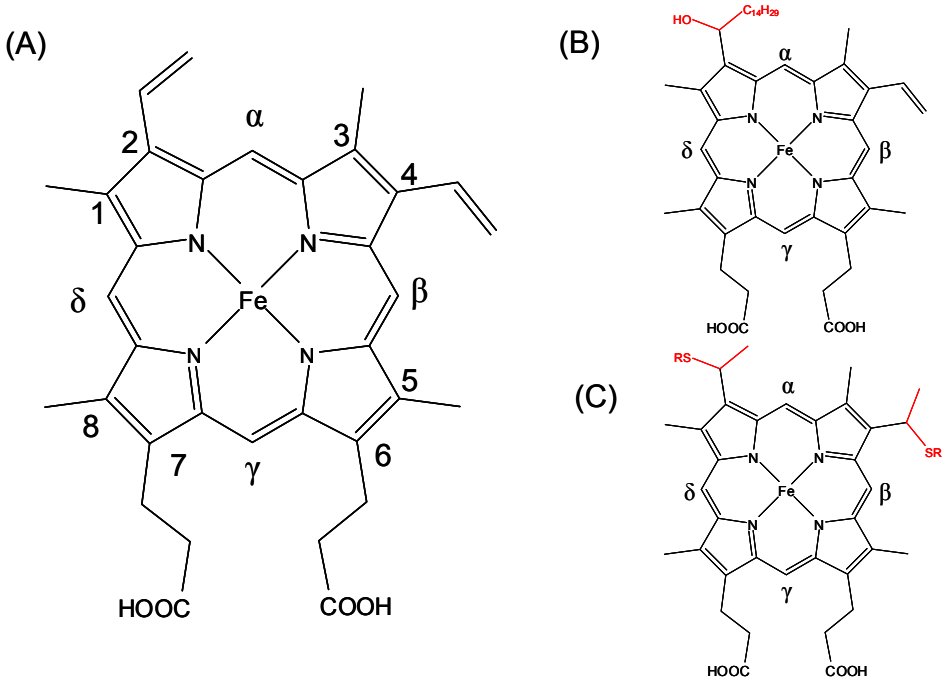


**Figure 1.1: Heme**

(A) Iron complex of protoporphyrin IX (heme). The methene bridges are designated α, β, γ and δ and the carbons are numbered with the nomenclature used in this Thesis. (B) Modified heme found in cytochromes in class *a*. (C) Modified hemes found in cytochromes *c*, where R is an aliphatic side chain. The modifications to the heme side groups are highlighted in red.

Officially, ferriprotoporphyrin IX with ferric iron is called hemin and it is only called heme when the iron is in its +2 oxidation state (ferroprotoporphyrin IX). However, due to the fact that the iron can exist in up to five oxidation states it is

clearer to call all protoporphyrin IX heme and state the oxidation state of the iron [13]. In addition to the core structure protoporphyrin IX has eight side chains, four methyl, two propionate and two vinyl groups (Figure 1.1(A)). Modifications to the heme side chains are found in some heme containing proteins and common examples of these modifications are shown in Figures 1.1(B) and (C). The net charge of the heme with a four coordinate ferric iron is +1.

### *1.2.2 Heme containing proteins*

A wide variety of proteins with biologically diverse functions incorporate the heme prosthetic group, the chemistry of which is modulated by; the protein environment of the heme active site; alterations to the side chains of the heme; or by changing the axial ligands which occupy the 5$^{th}$ (proximal) and 6$^{th}$ (distal) coordination positions of the heme (Figure 1.2).

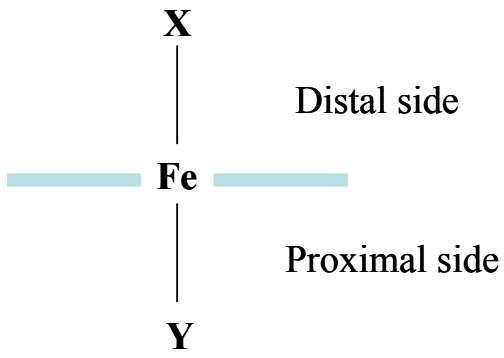


**Figure 1.2: A schematic representation of the heme group**

Y and X represent the 5$^{th}$ and 6$^{th}$ ligand respectfully. The blue bars represent the protoporphyrin ring and the two sides of the heme are labelled.

The distal and proximal ligands of the heme control the spin-state of the iron. If they are strong field ligands the heme iron will be low spin and if they are weak field ligands the heme iron will be high spin. The variety of proteins which contain the heme prosthetic group have been extensively reviewed [14-18]. The range of activity of the prosthetic group depends hugely on the environment it is in, so that the proteins which use heme as a cofactor have classically been broadly divided into three categories; oxygen transport and storage proteins, heme redox enzymes and electron transfer proteins. However, more recently the knowledge of the functional roles known to be carried out by heme proteins has increased leading to the emergence of another class of heme proteins: the heme sensor proteins.

### *1.2.2.1 Oxygen transport and storage proteins*

Oxygen binding proteins are ancient molecules and it is suggested that they have evolved from enzymes which protected species from the toxic oxygen atmosphere [19]. Although molluscs and some arthropods use hemocyanin [20], a copper containing protein that reversibly binds molecular oxygen, heme proteins (hemoglobin and myoglobin) are the principle carriers of oxygen in biological systems [21].

Hemoglobin is a tetrameric protein made up of two 141 amino acids α subunits and two 146 amino acid β subunits, which are non-covalently linked. Each subunit has a heme co-factor and can bind one molecule of oxygen (Figure 1.3(A)). The role of hemoglobin is to carry oxygen from the lungs, where oxygen concentration is high, to tissues, where the oxygen concentration is low. The release of oxygen under conditions where the partial pressure is low is facilitated by the cooperativity of the four subunits; as the partial pressure of oxygen increases the affinity of each subunit for oxygen increases.

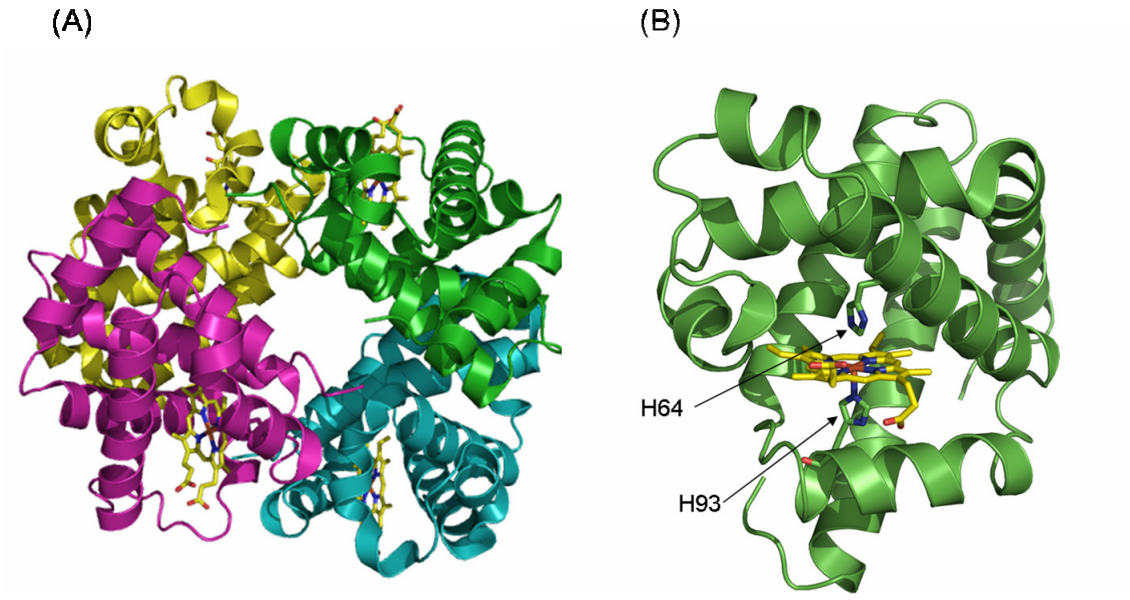


**Figure 1.3: Oxygen transport and storage proteins**
(A) Hemoglobin, each subunit it represented by a different colour. Heme groups are shown in yellow. (B) Myoglobin the heme group is shown in yellow, proximal and distal histidine residues are indicated.

Myoglobin (Figure 1.3(B)) is a related globin and, like hemoglobin, serves as an oxygen transport protein. Myoglobin is a monomeric protein, with a single heme binding just one molecule of oxygen, this structural difference from tetrameric hemoglobin accounts for the different functionality of the two proteins; myoglobin primarily transports and stores oxygen in the muscle, where the partial pressure of oxygen remains stable, hence there is no need for myoglobin to act in the cooperative way that hemoglobin does.

Both hemoglobin and myoglobin have a proximal histidine residue which co-ordinates to the heme, the sixth axial position on the distal side has water weakly bound, which is readily replaced by molecular oxygen. The iron can exist as $Fe^{2+}$ and $Fe^{3+}$ but $O_2$ binds only to ferrous iron [22]. The distal histidine which is conserved in hemoglobin and myoglobin [23, 24] is also important for oxygen binding and acts as a proton donor stabilizing the polar iron-oxygen complex.

### *1.2.2.2 Heme redox enzymes*

The oxygen transport proteins utilise the oxygen binding properties of iron in a passive way with the organic part of the heme operating as a carrier for the iron. In other heme proteins the heme can play an active role in biological processes. Redox enzymes catalyse the reduction or oxidation of a substrate and even among this subclass of heme proteins there is significant functional diversity.

The cytochrome P450s are a superfamily of heme enzymes that catalyse a range of reactions with numerous endogenous and exogenous substrates. Cytochrome P450s are monooxygenases which carry out the oxidation of a substrate by the incorporation of an atom of oxygen from molecular oxygen. The $5^{th}$ axial ligand in P450 enzymes is a cysteine residue (Figure 1.4), this thiolate coordination gives the heme iron a lower affinity for anionic ligands than that of myoglobin [25]. The cysteine ligand is a better electron donor than histidine and as a result the oxygen molecule that binds in the P450 cycle is highly activated [26].

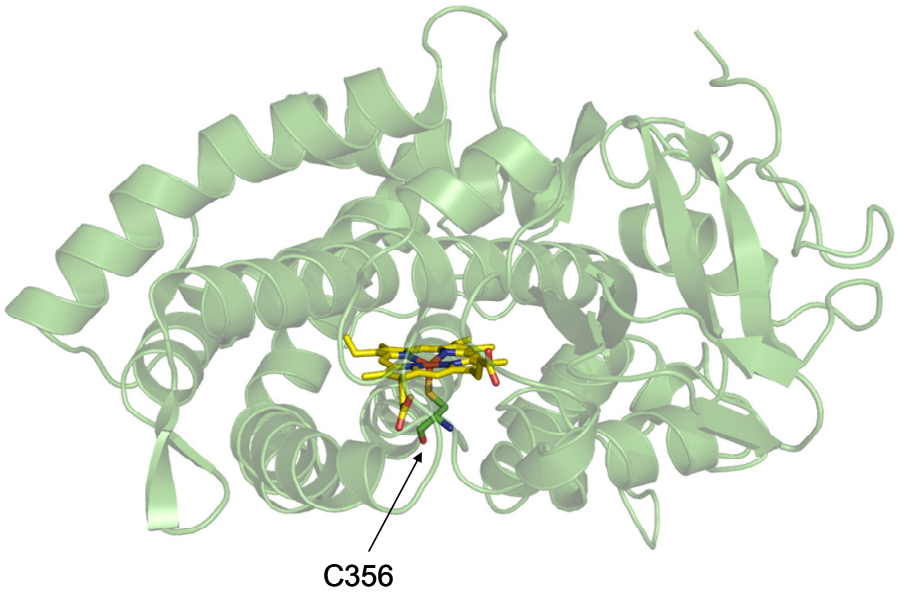


**Figure 1.4: The crystal structure of cytochrome $P450_{CAM}$**

The overall crystal structure of the monooxygenase $P450_{CAM}$ the heme is shown in yellow, the proximal cysteine ligand is also shown with the iron-thiolate coordination bond. (PDB entry 2CPP) [27].

The best understood subclass of the heme redox enzymes are those which utilise the two oxidising equivalents in $H_2O_2$ to oxidise a variety of substrates, namely peroxidases, catalases and catalase-peroxidases. The peroxidases reduce $H_2O_2$ to two molecules of water whilst oxidising a substrate and will be discussed at length throughout this Thesis. Catalases catalyse both the oxidation and reduction of $H_2O_2$ to water and molecular oxygen. The overall mechanism of catalase (Figure 1.5) is very similar to that of peroxidases (Section 1.3.2, Figure 1.9), with the main difference being that Compound I of catalase can react with a second molecule of $H_2O_2$ to release $H_2O$ and $O_2$ with the regeneration of resting ferric enzyme [28].

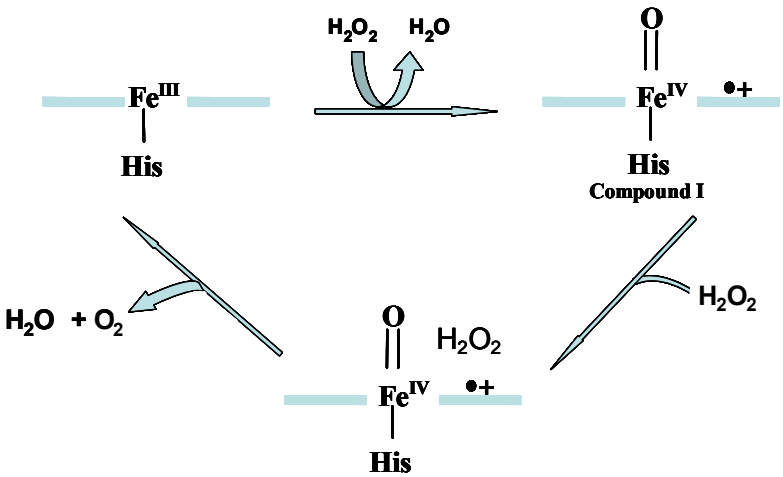


**Figure 1.5: The catalytic cycle of catalase**

In the first step $H_2O_2$ is used for Compound I formation. Compound I can then react with a second molecule of $H_2O_2$, reducing the enzyme back to the ferric state.

Classic monofunctional heme-containing catalases are homotetramers with one heme per subunit and are present in both prokaryotes and eukaryotes [29]. A well studied example of this type of catalase, beef liver catalase (BLC), is shown in Figure 1.6. In most catalases each subunit also binds an NADPH molecule, although the precise function of this cofactor remains unclear [30]. The heme environment of catalase is distinct from that of peroxidases and catalase-peroxidases with the heme being ligated to the hydroxyl group of a tyrosine instead of histidine. The distal pocket is also somewhat different with a conserved asparagine residue replacing the conserved arginine found in peroxidases.

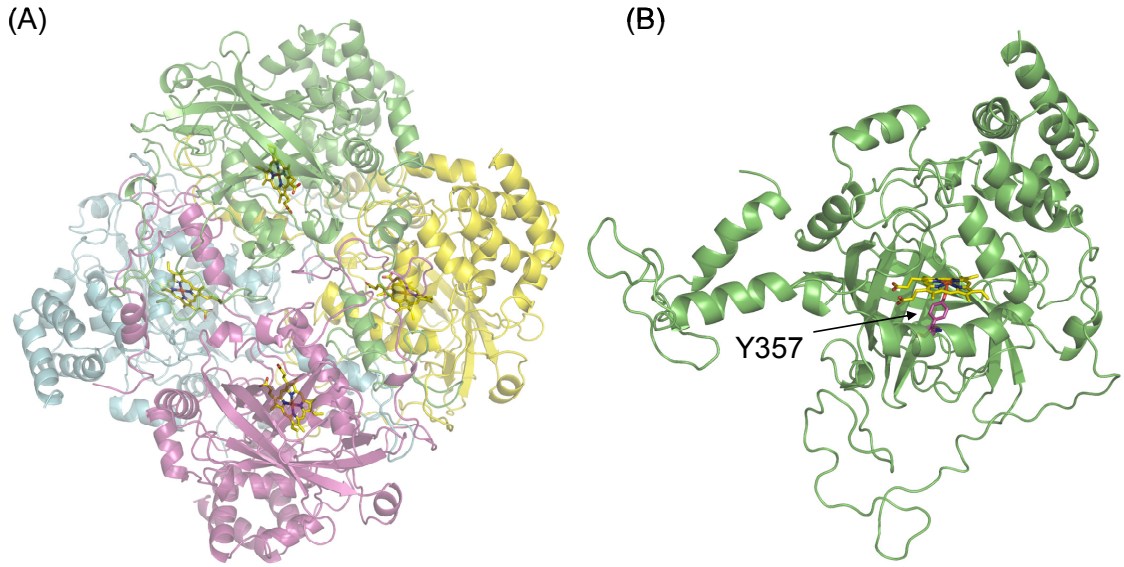


**Figure 1.6: The crystal structure of beef liver catalase**

(A) Beef liver catalase (PDB entry 4BLC) the four subunits are shown in different colours for clarity with the heme being shown in yellow. (B) A single subunit of beef liver catalase, the heme is shown in yellow with the proximal tyrosine shown in pink.

As the name suggests, catalase-peroxidases are able to carry out both catalase and peroxidase reactions. Bacterial catalase-peroxidases (KatGs) are classified as class I peroxidases (see Section 1.3.1), they are homomultimeric proteins with monomers approximately twice the size of those of other class I peroxidases. They comprise of an N-terminal heme binding domain and a C-terminal domain (the C-terminal domain is thought to have arisen from a gene replication event since it shares

sequence homology with the N-terminal domain but contains mutations which mean it is no longer capable of binding heme [31]). KatGs have attracted significant interest over the past ten years or so due to their ability to activate the prodrug isoniazid, a key chemotherapeutic agent against the disease tuberculosis and are discussed further in Chapter 3.

Other types of heme proteins in the class of heme redox enzymes include the dioxygenases indoleamine 2,3-dioxygenase and tryptophan 2,3-dioxygenase. These enzymes catalyse the oxidative cleavage of tryptophan by insertion of both atoms of molecular oxygen to form N-formylkynurenine [32-34] (see Section 1.7.3). Another important heme redox enzyme is nitric oxide synthase (NOS), which catalyses the oxidation of one L-arginine guanidinium nitrogen atom to form NO, this then serves as a second messenger by activation of guanylyl cyclase [35] (see Section 1.7.2).

### *1.2.2.3 Electron transfer proteins*

Heme containing electron transfer proteins are commonly termed cytochromes (although this term is often used in reference to other types of heme proteins) and several different types exist. Cytochromes can be classified according to the nature of the heme group they contain (see Figure 1.1, Section 1.2.1); if the heme is unmodified the cytochromes are referred to as *b*-type and if the heme is covalently attached to cysteine thiol groups the cytochrome is referred to as *c*-type. Other types of cytochromes have heme molecules with modifications to their porphyrin ring, including *a*-, *d*- and *o*-types [36]. Cytochromes undergo reversible oxidation and reduction, formally this redox change involves a single-electron, reversible equilibrium between Fe(II) and Fe(III). The cytochromes are important in photosynthesis and respiration.

### *1.2.2.4 Heme sensor proteins*

Heme sensor proteins are important regulatory proteins and can be divided into two groups: heme-responsive heme sensor proteins, where the binding of heme to the protein triggers activation of a catalytic or DNA binding domains; and gas-responsive heme sensor proteins, where binding of a gas such as CO or NO to the heme leads to the activation of a functional part of the protein.

Heme-responsive heme sensor proteins include the transcription factor Hap1 in yeast [37], which forms large aggregates with other proteins in the absence of heme decreasing its affinity for DNA. Upon heme binding, Hap1-associated proteins are released and DNA affinity is subsequently increased. The eIF2α kinase (HRI) system regulates protein synthesis, providing a balance between globin proteins and the levels of heme in red blood cells. In normal conditions HRI has heme bound to the kinase active site rendering it inactive, this means that eIF2α, an initiation factor for translation which regulates the translation of genes required for globin synthesis is non-phosphorylated and able to activate translation. Under conditions of low heme, heme dissociates from HRI allowing access to the kinase active site, this leads to phosphorylation of eIF2α preventing it binding to RNA and hence preventing translation. All of the heme-responsive heme sensor proteins examined to date have a cysteine residue as an axial ligand [38], thiolate coordination to the heme may be important in the heme-responsive heme sensor proteins for rapid dissociation of the heme [39].

Gas-responsive heme sensor proteins include the soluble guanylate cyclases [40] which catalyse the cyclisation of guanosine 5'-triphosphate (GTP) to guanosine 3',5'-cyclic monophosphate (cGMP), a second-messenger important in vasodilation. The transcription factor CooA is probably the most well studied of the gas-responsive heme sensor enzymes. CooA is a homodimeric transcription factor that belongs to the catabolite activator protein (CAP) family [41]. CooA is responsible for regulating CO metabolism in bacteria by controlling the genes necessary for the production of CO oxidising enzymes [42]. CooA is a dimer with each subunit containing a heme group, in the inactive form of CooA each heme is coordinated by a histidine residue and the N-terminal proline from the opposite subunit, when CO is present CO binds to the 6$^{th}$ axial position causing dissociation of the N-terminal proline, this leads to large conformational changes which enable CooA to bind DNA and activate transcription.

## 1.3 Heme peroxidases

### *1.3.1 Function and classification of peroxidases*

Heme containing peroxidase enzymes are widely distributed throughout the plant and animal kingdom and have also been isolated from various micro-organisms

[43]. They are distinct from a second group of peroxidases that contain no heme and instead use elements such as vanadium and selenium [44]. Heme peroxidases catalyse the $H_2O_2$-dependent oxidation of a variety of substrates and carry out a vast array of biological functions.

Heme peroxidases can be divided into two superfamilies; the mammalian peroxidases and the plant peroxidases. The mammalian peroxidase superfamily include myeloperoxidase (MPO), eosinophil peroxidase (EPO), lactoperoxidase (LPO) and thyroid peroxidase (TPO). An alternative and highly important pathway utilised by mammalian peroxidases, along with the classic peroxidase pathway shown in Section 1.3.2, Figure 1.9, is the halogenation cycle [13]. Depending on substrate availability, in the presence of $H_2O_2$ and a halide, MPO can catalyse a halogenation reaction that plays an important role in the antibacterial activity of leukocytes [45]. Mammalian peroxidases are highly important and are implicated in many different diseases including asthma [46], Alzheimer's disease (AD) [47] and inflammatory vascular disease [48].

The plant peroxidase superfamily contains enzymes of plant, bacterial and fungal origin [49] and are found in virtually all green plants, many fungi and aerobic bacteria. Plant peroxidases carry out a diverse range of physiological functions, but their main role is to serve as antioxidants protecting the organism from the harmful effects of toxic peroxides produced *in vivo* by oxidase activity [50]. The plant peroxidases were further classified into three classes based on sequence homology, by Welinder [49]:

1. Class I: intracellular peroxidases and peroxidases of prokaryotic origin
2. Class II: secreted peroxidases of fungal origin.
3. Class III: classical secretory plant peroxidases.

Peroxidases from all three classes contain ~ 10 α helices in similar positions and 13 conserved regions (Figure 1.7) [44].

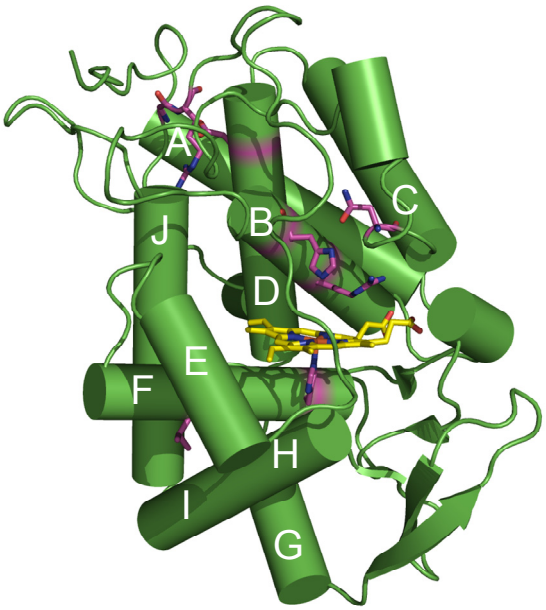


**Figure 1.7: Helical structure of peroxidases**

Crystal structure of C*c*P (PDB entry 2CYP) showing the 10 α helices (A-J) (*NB.* in C*c*P there is no region of amino acids in between helices H and I ). The residues conserved in all plant peroxidases are indicated in purple with the heme in yellow.

All plant peroxidases from classes I-III have a histidine residue as their proximal ligand and a conserved histidine and arginine (His52 and Arg48 in C*c*P) on the distal side of the heme, along with a conserved asparagine (Asn82 in C*c*P). On the proximal side of the heme a valine, a histidine, two aspartates, a glycine and an arginine (Val169, His175, Asp235, Asp106, Gly129 and Arg130 in C*c*P) are all conserved.

There are two plant peroxidases which don't fit into the Welinder classification. Chloroperoxidase [51] which has a cysteine as the proximal ligand and catalyses the halogenation of aliphatic substrates, and *Pseudomonas aeruginosa* cytochrome *c* peroxidase [52] which contains two covalently attached *c*-type heme groups with the active resting form having one ferrous heme and one ferric heme.

Important examples of class I heme peroxidases include ascorbate peroxidase (APX) and cytochrome *c* peroxidase (C*c*P) which will be discussed at length throughout this Thesis. Class I also contains the bacterial catalase-peroxidases; KatGs. Class I peroxidases have no disulphide bridges, no carbohydrate components and no signal peptide for secretion.

Class II plant peroxidases include lignin peroxidase (LiP) from *Phanerochaete chysosporium* [53], which plays an essential role in the degradation of the plant cell wall component, lignin. A structurally related class II peroxidase, manganese peroxidase [54] also from *Phanerochaete chysosporium,* oxidises Mn(II) to Mn(III), Mn(III) then forms a complex with a dicarboxylic acid that is capable of oxidising various substrates [55]. *Arthromyces ramosus* peroxidase (ARP), also known as ink cap mushroom peroxidase [56] also falls into the class II peroxidases. ARP is structurally very similar to LiP and MnP, however the substrate specificity of ARP is more like that of the class III peroxidases with small aromatic molecules being the preferred substrate. Class II heme peroxidases all contain two calcium ion binding sites [57], one proximal and one distal to the heme, and four conserved disulphide bridges. Class II peroxidases are invariably glycosylated and all contain an N-terminal signal peptide for secretion.

The class III peroxidases contain perhaps the most well-studied of all the peroxidases, horseradish peroxidase (HRP), which has been extensively reviewed in the literature [58, 59]. Like class II peroxidases, class III peroxidases contain two calcium binding sites, four disulphide bridges, an N-terminal peptide signal for secretion and ~ 22% carbohydrates [29]. Unlike class I and II peroxidases, class III peroxidases contain a long insertion (34 residues in the C isoenzyme of HRP [60]) between helices F and G which forms two extra helices F' and F'' (Figure 1.8). This region is highly variably even amongst the class III peroxidases and defines the substrate access site. Other class III peroxidases include peanut [61] and barley [62] peroxidases.

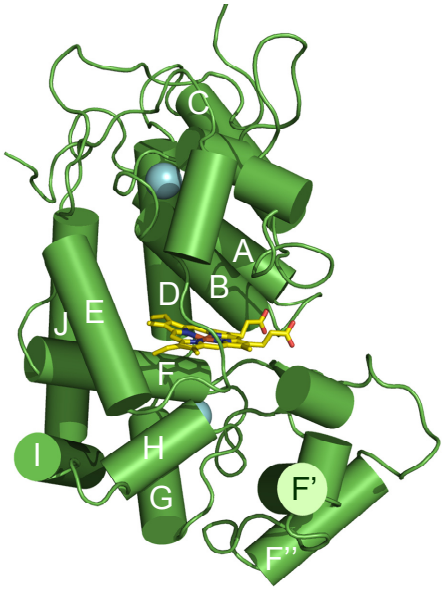


**Figure 1.8: Representation of the overall structure of class III peroxidases**

Crystal structure of HRP (PDB entry 1ATJ) showing the extra α helices present in class III peroxidases F' and F''. The heme is shown in yellow and calcium ions are represented by cyan spheres.

### *1.3.2 The catalytic mechanism of heme peroxidases*

All heme peroxidases utilise a catalytic cycle that involves the formation of a two-equivalent oxidized intermediate known as Compound I, followed by oxidation of substrate producing a second reactive intermediate Compound II. Compound II then reacts with a second molecule of substrate to regenerate the resting ferric enzyme (Figure 1.9).

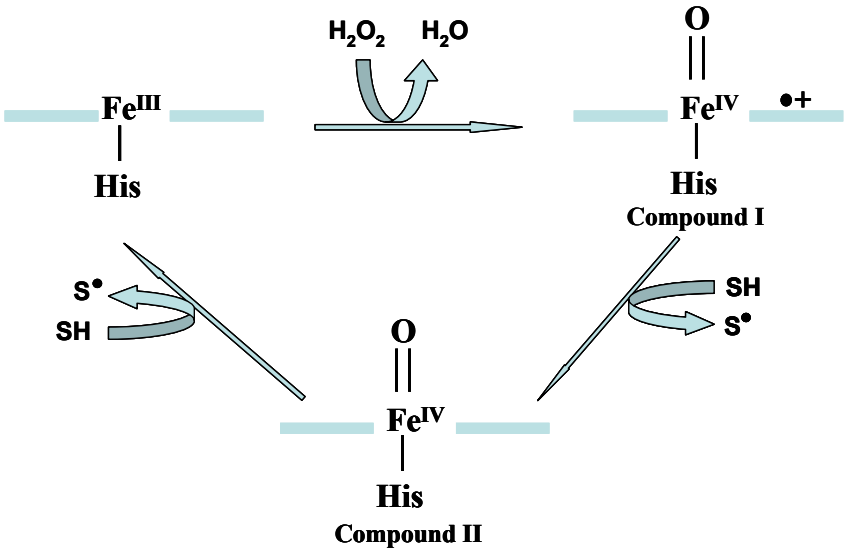


**Figure 1.9:A schematic of the catalytic peroxidase cycle**

SH represents the reduced substrate and S$^{\bullet}$ represents oxidised substrate.

Peroxidases are distinguished from other heme proteins due to their ability to rapidly react with $H_2O_2$. The mechanism for this reaction, resulting in Compound I formation, has been well studied [63-65]. In 1980 it was proposed by Poulos and Kraut [66] that the distal histidine, conserved throughout the peroxidases, acts as a general acid-base catalyst, and it has since been shown that the distal histidine is critical for the rapid reaction of peroxidases with $H_2O_2$ [67-69]. The exact nature of Compound I has still not been unambiguously assigned, despite the availability of crystal structures of the intermediate. EXAFS work [70, 71] on C*c*P estimated Fe-O bond lengths to be in the region of 1.6 Å indicating a [Fe(IV) = O] species, whereas the high resolution crystal structure obtained by Poulos [72] showed an Fe-O bond length of 1.87 Å which they characterised as a ferryl bound hydroxyl species [Fe(IV) - OH].

Compound I is two-oxidising equivalents above the resting ferric heme with the iron being in the ferryl state and a radical either on the porphyrin ring or on an

amino acid residue [73]. Compound I is reduced by substrate to generate Compound II which is one-oxidising equivalent above the resting ferric heme, lacking the cation radical. Compound II is an oxyferryl species with a similar structure to Compound I. The Fe-O bond length is longer than that seen for Compound I and the oxygen is thought to be protonated facilitating the formation of the second water molecule from the overall reaction [74]. Compound II oxidises a second molecule of substrate with the bound oxygen being released as a water molecule and the heme returning to its ferric resting state, the reduction of Compound II is usually the rate-limiting step in the catalytic cycle.

## 1.4 Ascorbate peroxidase

Ascorbate-dependent peroxidase activity was first reported in 1979 [75]. Defining a heme peroxidase as an ascorbate peroxidase (APX) can be quite difficult as they are often indiscriminate in their choice of redox partner and many utilise small organic substrates, typical of those for class III peroxidases, at a rate comparable to that at which they oxidise ascorbate. Peroxidases are usually classified as an APX when their specific activity for ascorbate is higher than that of other substrates [76].

Ascorbate peroxidases are widespread plant enzymes that rid plant cells of potentially harmful $H_2O_2$, this is especially important in legume root nodules due to their potential for creating activated oxygen species. APXs are class I peroxidases which have now been isolated and purified from a number of sources. Sequence analysis of APX genes identified so far result in 7 types of APX; two are chloroplastic and five are cytosolic, three of which are membrane bound [77]. Cytosolic enzymes have been purified from many sources including pea (pAPX) [75], soybean (sAPX) [78], wheat [79], potato tubers [80], maize [81] and tea [82].

The chloroplastic and cytosolic isoenzymes are very similar with the main difference being the sensitivity of chloroplastic peroxidases to conditions where ascorbate is low, when they tend to degrade rapidly [83]. The cytosolic APXs are the most extensively characterized and bacterial expression systems have been reported for many of them, including soybean APX allowing heterologous expression of rsAPX [84].

APXs are homodimeric heme proteins with a subunit mass of between 27,000 and 30,000 Da, they utilise ascorbate as the substrate, oxidising it in a $H_2O_2$-

dependent manner to produce the radical monodehydroascsorbate which, under physiological conditions, is reduced back to ascorbate by monodehydroascorbate reductase [85]. In the absence of monodehydroascorbate reductase, two of the radicals can disproportionate to form one molecule of dehydroascorbate and reform one molecule of ascorbate [13] (Figure 1.10).

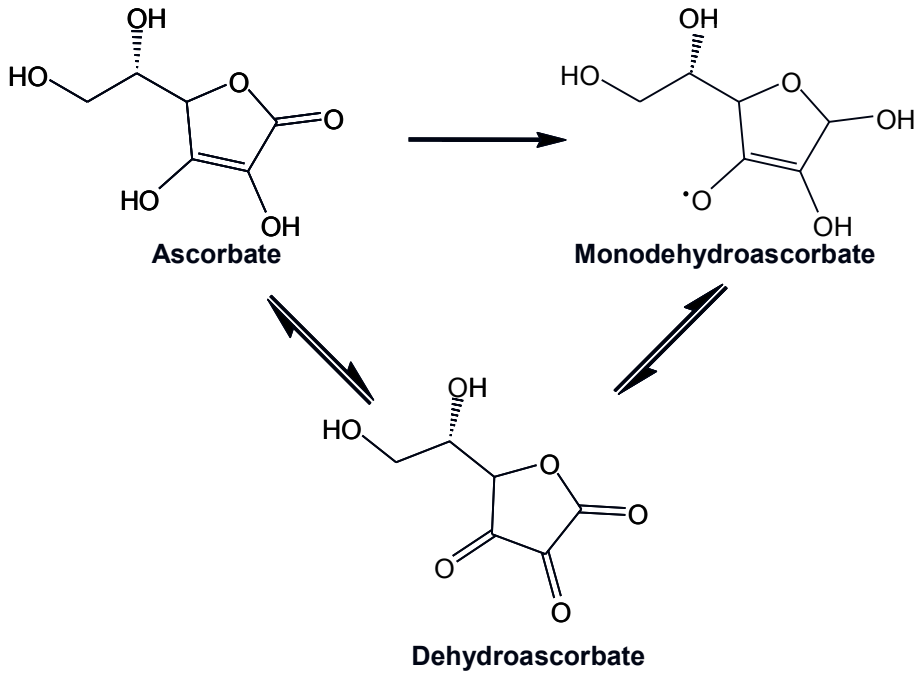


**Figure 1.10: Oxidation of ascorbate**

Ascorbate is oxidised to monodehydroascorbate by APX, in the absence of monodehydroascorbate reductase this spontaneously disproportionates to ascorbate and dehydroascorbate.

The crystal structure of recombinant soy ascorbate peroxidase (rsAPX, which will be referred to as APX throughout the rest of this Thesis) was solved by Sharp et al in 2003 [86] and was shown to be virtually identical to the structure of recombinant pea ascorbate peroxidase (rpAPX) (r.m.s. deviation between Cα positions 0.443 Å) [87], with which it shares 91% sequence homology. The structure is also very similar to another well characterized class I peroxidase, C*c*P (see Chapter 2 for a detailed comparison). The overall crystal structure of APX is shown in Figure 1.11 along with the active site.

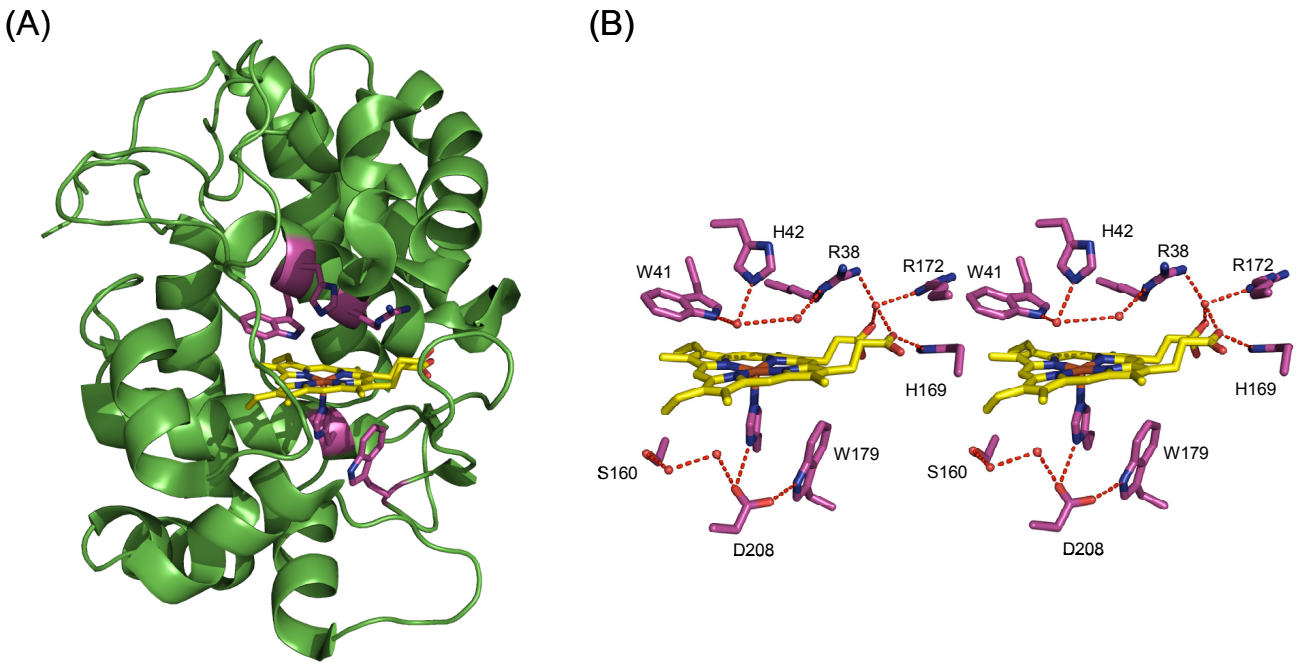


**Figure 1.11: The crystal structure of ascorbate peroxidase**

(A) The overall crystal structure of APX, heme is shown in yellow and active site residues are highlighted in purple (PDB entry 1OAG). (B) Stereo representation of the active site of APX. Side chains for important residues are shown, potential hydrogen bonds are indicated by red dashes and water molecules are represented by red spheres.

The heme in APX is bound by a coordinate bond to His163 and a hydrogen bond between the heme 7-propionate and His169. The distal pocket contains the key active site residues, Trp41, His42 and Arg38. The catalytic His-Asp-Trp triad is found on the proximal side (His163-Asp208-Trp179) which is a feature present in C*c*P. The pea APX structure shows a $K^+$ ion bound in a position close to the heme which is proposed to destabilize formation of a Trp179 radical in Compound I [88], however, this metal site is not seen in soybean APX and it is proposed that the oxidation of ascorbate by Compound I proceeds directly through the heme (as discussed in Chapter 2).

C*c*P has been *the* model for the study of peroxidases due to its early expression [89] and crystal structure [90] which have allowed extensive structure-function studies. However, the fact that it utilises a protein radical in Compound I and its substrate is a large protein, as discussed in Chapter 2, means that it is not ideal as a general model of peroxidases. The high sequence homology of C*c*P with APX, along

with the use of a more typical substrate and porphyrin π-cation by APX, places APX at an important interface in terms of our overall understanding of peroxidase activity.

## 1.5 Cytochrome *c* peroxidase

Cytochrome *c* peroxidase (C*c*P) is the most thoroughly investigated class I peroxidase. C*c*P was discovered in brewers yeast in the 1940s [91] and is found in the mitochondria of aerobically grown yeast cells. The primary biological function of C*c*P is to protect yeast cells during oxidative stress by removal of harmful $H_2O_2$ [92]. C*c*P catalyses the $H_2O_2$-dependent oxidation of the mobile electron carrier cytochrome *c*, from ferrocytochrome *c* to ferricytochrome *c*.

In the 1960s a simple isolation procedure for C*c*P was developed [93], the gene was cloned into *E. coli* in 1982 [94] and the first mutagenesis studies on C*c*P were carried out when it was expressed in yeast in 1986 [95]. By 1987 C*c*P was overexpressed in *E. coli* [89], the availability of the enzyme made it a valuable system for the study of peroxidases and when the crystal structure was solved [96], providing the first structure of a heme enzyme, extensive structure-function studies became possible which defined many aspects of peroxidase catalysis for the first time. C*c*P is an ~ 34,000 Da protein with 293 amino acids and a single, non-covalently bound, *b*-type heme. The overall crystal structure is shown in Figure 1.12, along with the active site.

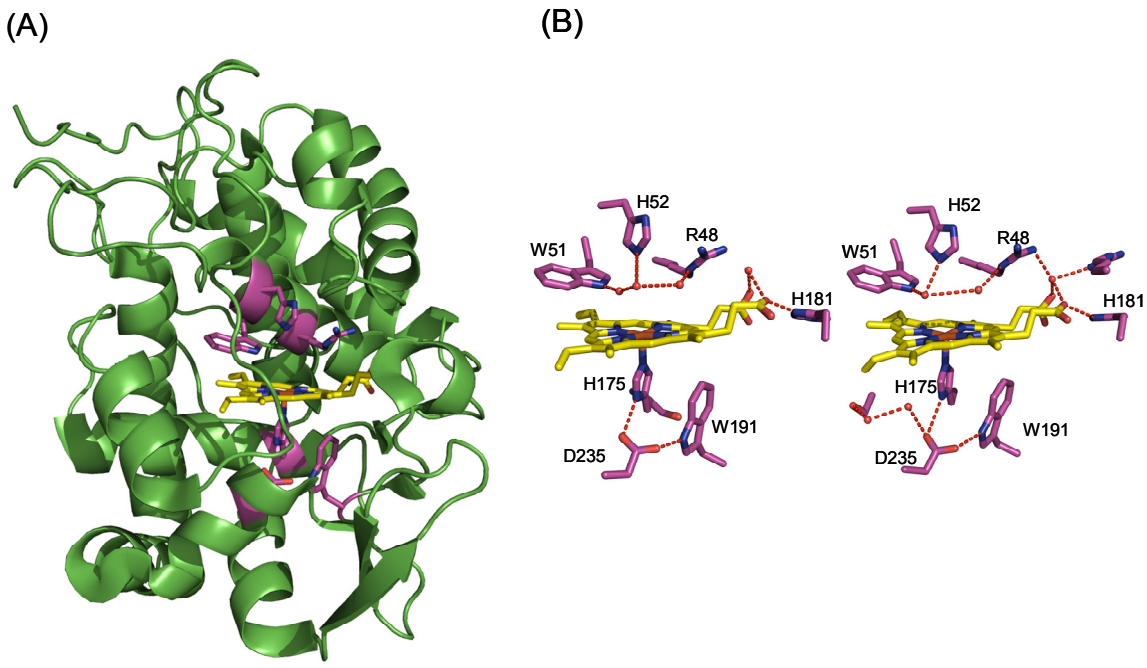


**Figure 1.12: The crystal structure of cytochrome *c* peroxidase**

(A) Overall structure of C*c*P, the heme is shown in yellow and important catalytic residues are highlighted in purple. (B) The active site of C*c*P, side chains of important residues are shown, hydrogen bonds are indicated by red dashes and water molecules are represented by red spheres (PDB entry 2CYP).

C*c*P shares the same overall structure as other class I peroxidases. Like in APX, the heme is bound to the protein through a coordinate bond with the proximal histidine, His175, and through a hydrogen bond between the heme 7-propionate and His181. The distal side of the heme has Arg48, Trp51 and His52, analogous to the distal pocket of APX and the proximal side has the catalytic triad His175-Asp235-Trp191, again analogous to APX. C*c*P does not contain the potassium binding site seen in pea APX and the introduction of a metal binding site has been shown to destabilise the protein radical formed on Trp191 in Compound I [97].

## 1.6 Substrate binding in heme proteins

Due to the huge diversity of substrates for heme proteins there is necessarily diversity in the binding of substrates and details of substrate binding for many heme proteins are still not fully understood. The protein tertiary structure provides conduits for substrate access to and from the heme active site, which can be modulated by

conformational changes resulting in 'gated' substrate access. Substrate binding sites are designed to place the substrate in a specific orientation and at a specific distance from the heme active site to facilitate rapid and stereo-specific chemistry.

### *1.6.1 Substrate binding in cytochrome P450s*

The cytochrome P450 superfamily contains members with many different functions and the number of different substrates for cytochrome P450s is estimated to be in the 1000s [98]. The diverse reactions catalyzed by these enzymes include: hydroxylation, *N*-oxidation, sulfoxidation, epoxidation, oxidative ester and amide cleavage, peroxidation, deamination, and dehalogenation, to name just a few [99]. Substrates for P450s include fatty acids, steroids, amino acids and multitude of organic compounds with specific binding interactions varying from one P450 to another and, in some instances, between the diverse chemical substrates for the same P450.

One of the most extensively studied P450 enzymes is cytochrome $P450_{CAM}$ from *Pseudomonas putida*, which catalyses the stereoselective hydroxylation of camphor to 5-exo-hydroxycamphor (Figure 1.13(A)) [100], the crystal structure of $P450_{CAM}$ in complex with camphor is shown in Figure 1.13(B).

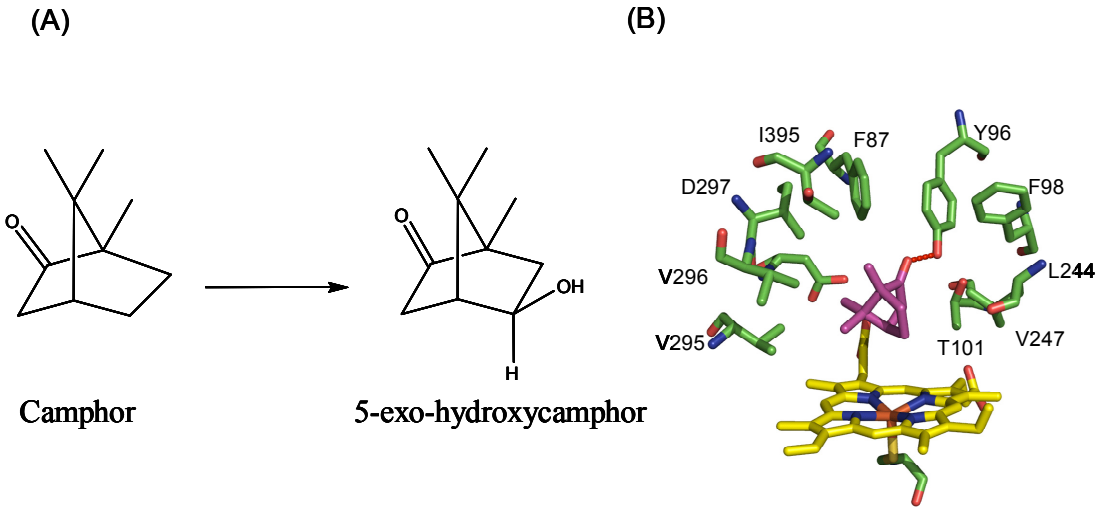


**Figure 1.13: Substrate binding in cytochrome $P450_{CAM}$**

(A) The selective hydroxylation of camphor catalysed by $P450_{CAM}$. (B) The crystal structure of the distal heme pocket of $P450_{CAM}$, showing the heme (yellow) and camphor bound (purple). The residues which define the pocket are labeled and hydrogen bonding interactions are represented by red dashes.

Camphor binds in the distal heme pocket forming numerous van der Waals interactions between the camphor methyl groups and the protein, a hydrogen bond is formed between the camphor carbonyl group and the hydroxyl group of Tyr96. Cytochrome $P450_{eryF}$ hydroxylates 6-deoxyerythronolide B (6-DEB) (Figure 1.14(A)) to erythronolide B at the C-6 atom as one step in erythromycin A production in *Saccaropolyspora ertherea* [101]. The crystal structure of $P450_{eryF}$ [102] has also been solved in the substrate bound form (Figure 1.14(B)), the substrate for $P450_{eryF}$ is much larger than camphor and comparison with the structure of $P450_{CAM}$-camphor complex shows the B' helix, which provides key substrate-protein contact points in $P450_{CAM}$, adopts a totally different conformation in $P450_{eryF}$ resulting in the formation of a much larger active site necessary to accommodate 6-DEB (Figure 1.14(C)).

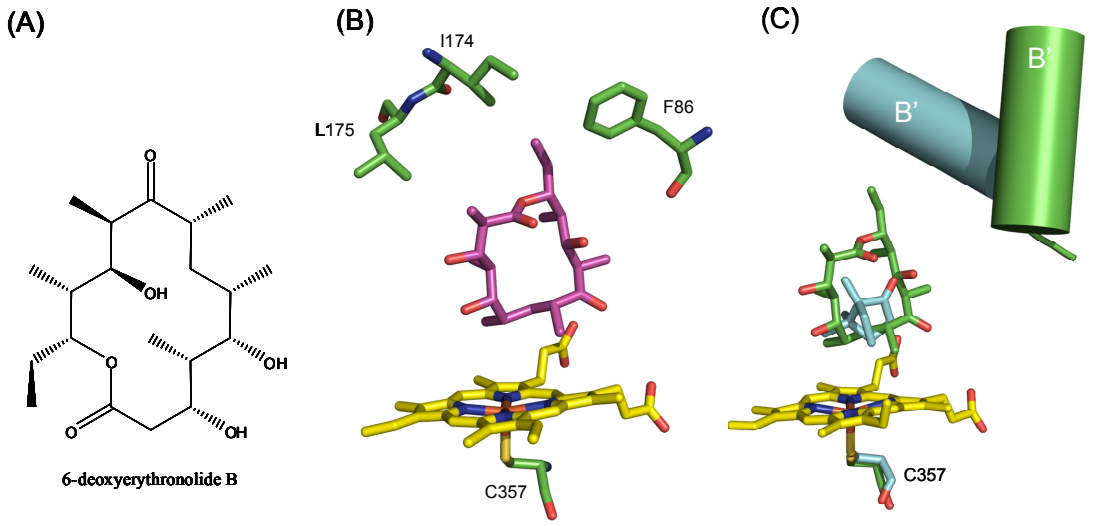


**Figure 1.14: Substrate binding in cytochrome $P450_{eryF}$**

(A) The physiological substrate of $P450_{eryF}$; 6-DEB. (B) The distal heme pocket of $P450_{eryF}$, the heme is shown in yellow and 6-DEB in purple. (C) A comparison of the distal heme pockets of $P450_{eryF}$ and $P450_{CAM}$ showing the difference in the position of the B' helix allowing for the difference in the substrate size of each enzyme.

The structures of $P450_{CAM}$ and $P450_{eryF}$ do not show a channel by which substrates can access the heme and it is postulated that a conformational change must occur in order to allow substrate binding in the distal pocket [103]. Cytochrome $P450_{BM-3}$ is a bacterial fatty acid hydroxylase from *Bacillus megaterium* [104] in which the P450 heme protein is fused to an FAD/FMN reductase this means that the enzyme is catalytically self sufficient and does not require additional proteins to transfer electrons from NAD(P)H to the heme iron. Substrates for $P450_{BM-3}$ can be

between 12 and 18 carbons long [105] the crystal structure of the $P450_{BM-3}$ heme domain has been solved with the substrate palmitic acid bound [103] (Figure 1.15(A)).

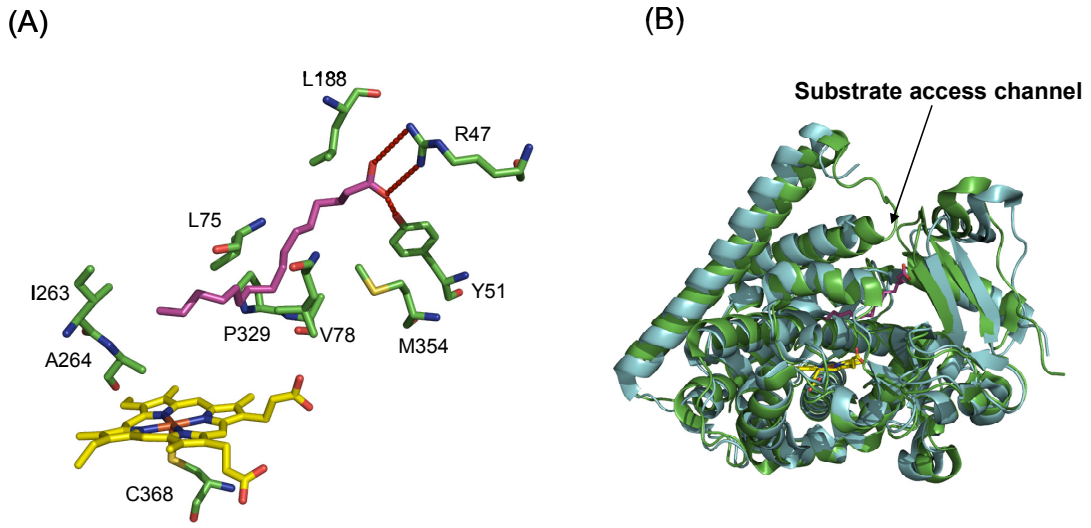


**Figure 1.15: Substrate binding in cytochrome $P450_{BM-3}$**

(A) The active site of $P450_{BM-3}$ showing palmitic acid bound (PDB entry 2UWH) residues defining the distal heme pocket are shown, hydrogen bonds are indicated by red dashes. (B) An overlay of the $P450_{BM-3}$-palmitic acid complex (green) and the substrate free form (Cyan) (PDB entry 2IJ2) showing the conformational change which allows the substrate to access the heme.

Like $P450_{CAM}$ and $P450_{eryF}$, palmitic acid binds in the distal heme pocket of $P450_{BM-3}$, although the atom which is hydroxylated is 7.5 Å from the heme iron (4.2 and 4.8 Å from the heme iron in $P450_{CAM}$ and $P450_{eryF}$ respectively). The substrate carboxylate forms hydrogen bonds with Tyr51 and Arg47 and the alkyl tail is held in place by Leu75 and Val78. The structure of the substrate-free form of $P450_{BM-3}$ has also been solved and comparison of the two shows that the substrate free form has a channel which allows substrate access to the heme, in the bound form a conformational change takes place reducing the size of this channel (Figure 1.15(B)).

### *1.6.2 Substrate binding in nitric oxide synthase*

Nitric oxide synthases (NOSs) are a family of enzymes that catalyse the oxidation of L-arginine to L-citrulline and NO (Figure 1.16) [106, 107].

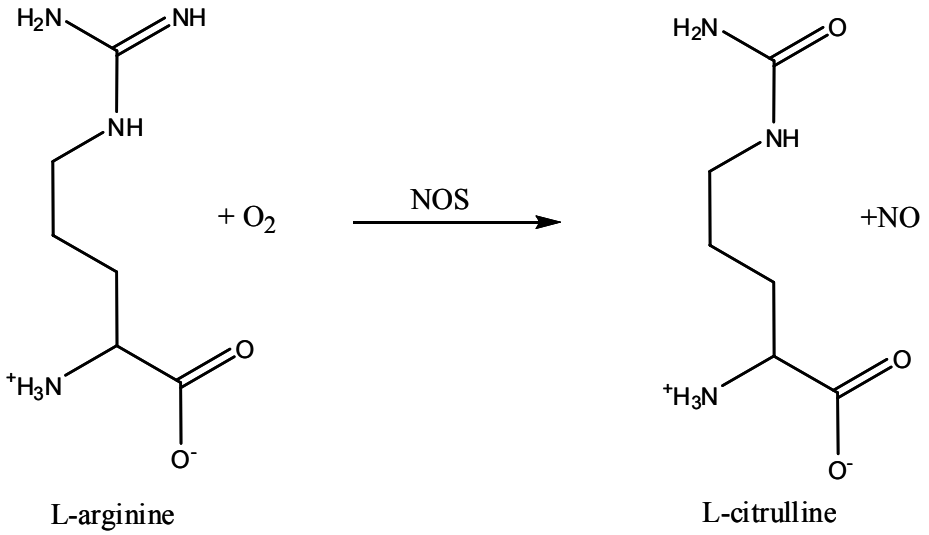


**Figure 1.16: The production of L-citrulline and NO by NOS**

NOSs are catalytically self-sufficient with two major functional domains: a C-terminal reductase domain which binds FMN, FAD and NADPH and an N-terminal catalytic domain which binds heme and the redox cofactor tetrahydrobiopterin ($BH_4$). The architecture of the FAD/FMN domain is similar to that of the FAD/FMN domain of cytochrome $P450_{BM-3}$ [104]. The heme is bound to the protein via a coordinate bond to a cysteine residue and unsurprisingly the mechanism of NOS is similar to that of cytochrome P450 enzymes, which are also heme-thiolate enzymes. NOS is only active in its dimeric form, crystal structures of all NOS enzymes solved to date show a tightly associated homodimer with $BH_4$ found at the dimer interface. Reducing equivalents from NADPH are taken through FAD then FMN and finally to the heme. A feature unique to NOS is the presence of the redox active cofactor $BH_4$: this reduces the ferric heme-superoxy intermediate that forms during the activation of bound dioxygen. Electron transfer from the bound cofactor to the heme allows formation of the heme-oxy species that reacts with L-arginine. The binding of $BH_4$ occurs at the γ-heme edge and the cofactor remains permanently bound to NOS [108], cycling between the fully reduced and one electron oxidised forms [35]. Figure 1.17 shows $BH_4$ bound to NOS.

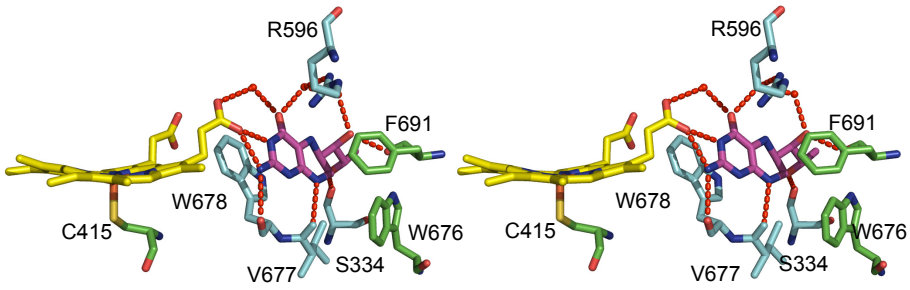


**Figure 1.17: The crystal structure of the NOS-$BH_4$ complex**

Stereo representation of the crystal structure of $BH_4$ bound at the γ-heme edge in NOS (PDB entry 1OM4). The heme is shown in yellow with important residues indicated in cyan (for residues that come from the subunit to which the heme and $BH_4$ are bound) and green (for residues which come from a second subunit of NOS). The hydrogen bonding network is shown as red dashes and water molecules are represented by red spheres.

$BH_4$ is held in place by π-stacking interactions between the substrate and a tryptophan residue of one subunit (Trp678) and a phenylalanine residue of the other subunit (Phe691). There are hydrogen bonding interactions between most of the heteroatoms of $BH_4$ and the protein side chains and backbone. Potentially the most important interaction between $BH_4$ and NOS is the interaction with the heme 7-propionate, a hydrogen bond is formed between this propionate and N3 of $BH_4$ proposed to be the route through which electron transfer from $BH_4$ to the heme occurs [109]. The one electron oxidised $BH_4$ is then converted back to the fully reduced form via a "through-heme" mechanism by the flavoprotein domain [110]. Like in cytochrome P450s and heme dioxygenases, the substrate for NOS, L-arginine, binds in the distal heme pocket, however the substrates for cytochromes P450s are universally hydrophobic while the physiological substrate for NOS is hydrophilic. Figure 1.18 shows the distal heme binding pocket of the NOS-L-arginine complex.

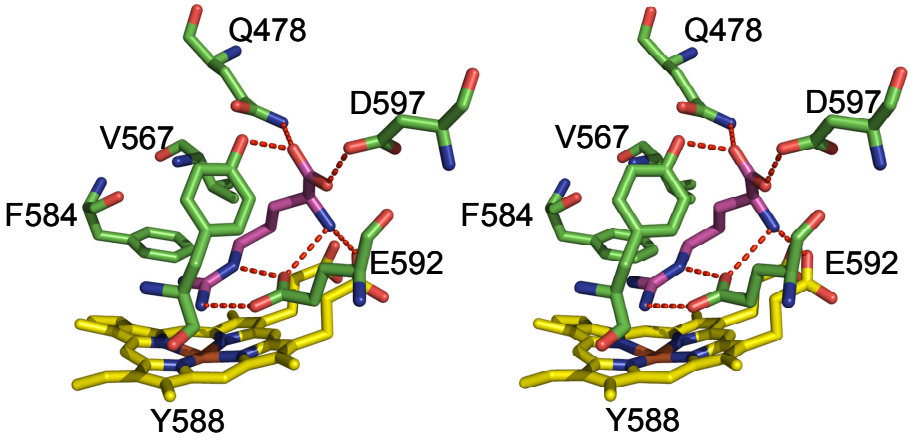


**Figure 1.18: The crystal structure of the NOS-L-arginine complex**

Stereo representation of the crystal structure of the distal heme pocket of NOS with L-arginine bound (purple). The heme is shown in yellow and the hydrogen bonding network is represented by red dashes. (PDB entry 1OM4).

L-arginine is held in place by a number of hydrogen bonds and all of the protein residues that make direct contact with L-arginine are conserved among the NOSs. In contrast to cytochrome P450s, the distal heme pocket is considerably more hydrophilic with three of the residues which form important interactions with the substrate being glutamine, aspartate and glutamate.

## *1.6.3 Substrate binding in heme dioxygenases*

Tryptophan 2,3-dioxygenase (TDO) and indoleamine 2,3-dioxygenase (IDO) are important, yet relatively poorly understood, heme enzymes. The L-kynurenine pathway leads to the formation of NAD and is the major catabolic route of L-tryptophan. The initial cleavage of L-tryptophan to N-formylkynurenine (Figure1.19) is catalysed by IDO and TDO.

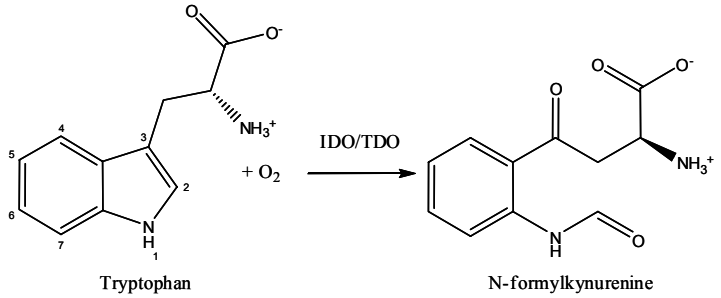


**Figure 1.19: The formation of N-formylkynurenine catalysed by IDO and TDO**

TDO is a homotetrameric enzyme with high specificity for L-tryptophan as the substrate. In comparison, IDO is monomeric, and shows activity towards a more diverse range of substrates. IDO was first isolated in 1967 [111], however, until recently very little was known about the enzyme. The catalytic mechanism involves the reduction of the ferric heme, binding of $O_2$ to the ferrous heme and binding of L-Trp, although the order in which they bind is still unknown [33].

In 2006 the crystal structure of IDO was solved [112], although the structure of the substrate bound form has still not been solved, the environment of the heme distal pocket and analysis of site directed mutants show that substrate recognition is likely to involve complementarities between the indole ring of the substrate and protein groups and that the correct geometry between the substrate and the iron-bound dioxygen are necessary for the reaction. The structure of the closely related TDO in complex with L-Trp has been solved [113] (Figure 1.20), providing further insight into substrate binding in the heme dioxygenases.

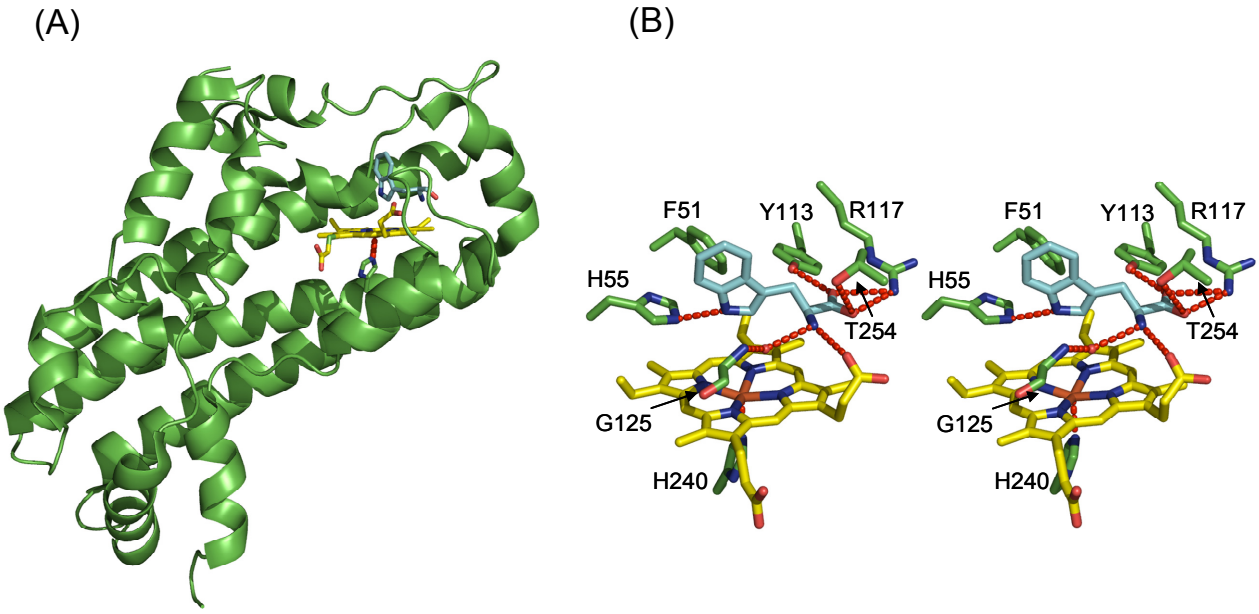


**Figure 1.20: Substrate binding in tryptophan 2,3-dioxygenase**

(A) The overall crystal structure of the TDO-L-Trp complex (PDB entry 2NW8), the heme is shown in yellow and the coordinate bond between the proximal His240 is shown as red dashes. (B) Stereo representation of L-Trp (cyan) bound in the distal heme pocket of TDO, the side chains of residues important for substrate binding are shown. Contacts between the protein and substrate are shown as red dashes and water molecules are represented by red spheres.

L-Trp is located in the distal heme pocket, with an ion-pair interaction between the carboxylate of L-Trp and Arg117, which is also hydrogen bonded to the hydroxyl of Tyr113 and the main chain amide of Thr254. The ammonium ion of L-Trp is recognized by the heme 7-propionate and is hydrogen bonded to Thr254. The indole ring is perpendicular to the heme and held in place via van der Waals interactions with Phe51. The N1 nitrogen of the indole ring is hydrogen bonded to the side chain of His55.

The structural information suggests that TDO is an induced-fit enzyme with the active site pocket being well defined in the substrate bound structure but disordered in the free enzyme, with Arg117 adopting a different conformation in the absence of substrate. The structure of the TDO in complex with L-Trp allows further insight into substrate binding in IDO. The key active-site residues are similar in TDO and IDO and it is likely that L-Trp has the same binding mode to the active site of IDO, as residues important for recognizing the L-Trp ammonium ion and carboxylate group are conserved in IDO (Arg 231 and the heme 7-propionate), explaining why L-Trp is a much better substrate than D-Trp for IDO. The tyrosine proposed to hydrogen bond to the substrate carboxylate in TDO is replaced by a phenylalanine in IDO, similarly the threonine thought to hydrogen bond to the ammonium group is missing in IDO and the equivalent residue to His55 is Ser167 in IDO. It has been proposed [32, 113] that these differences account for the lower specificity of IDO towards L-Trp.

## 1.7 Substrate binding in plant peroxidases

Since the structure of substrates for heme peroxidases is so diverse, it would be expected that the binding sites for substrates would be equally diverse. Classically, with the exception of the C*c*P-cytochrome *c* complex (which has an unusual substrate) and the manganese peroxidase-$Mn^{2+}$ complex (which utilises the γ-heme edge [114]) it was thought that the δ-heme edge was *the* substrate binding location in peroxidases. With the emergence of novel crystal structures and the application of site-directed mutagenesis techniques this consensus has evolved. The evolution of this consensus and the development of a more unified view of substrate binding in peroxidases will be discussed in this Thesis.

## *1.7.1 Substrate binding in class I peroxidases*

### *1.7.1.1 Substrate binding in APX*

APX is capable of oxidising two types of substrate: its physiological substrate, ascorbate, and aromatic substrates, more typical of the class III peroxidases [115]. Figure 1.21 shows some of the typical aromatic substrates used by heme peroxidases. The binding of these two different types of substrate has been shown to occur at different locations. Ascorbate binding occurs close to the γ-heme edge with important interactions to the heme 6-propionate [86] and is discussed further in Chapter 2; aromatic substrate binding occurs close to the δ-heme edge [116] and is discussed in Chapters 3, 4 and 5.

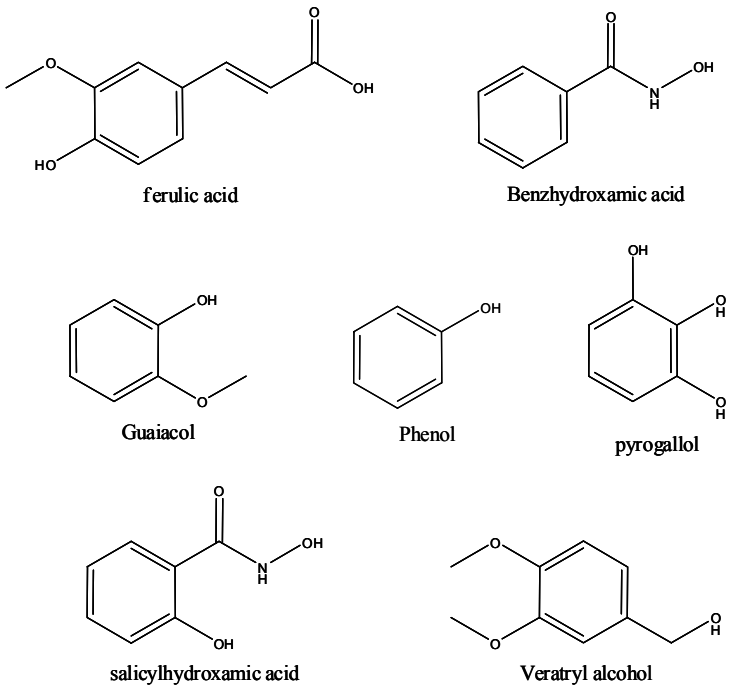


**Figure 1.20: The structures of typical aromatic substrates used by peroxidases**

### *1.7.1.2 Substrate binding in CcP*

The physiological substrate for C*c*P is anomalous to usual peroxidase substrates in that it is a protein, cytochrome *c*. The nature of the C*c*P-cytochrome *c* interaction has been of interest for many years and is still under active investigation with the number of binding sites, their location and their affinity for cytochrome *c* still unknown [117]. In 1992 Pelletier and Kraut solved the crystal structure of the

C*c*P-cytochrome *c* complex [118] and proposed a single specific binding site for cytochrome *c* (Figure 1.22).

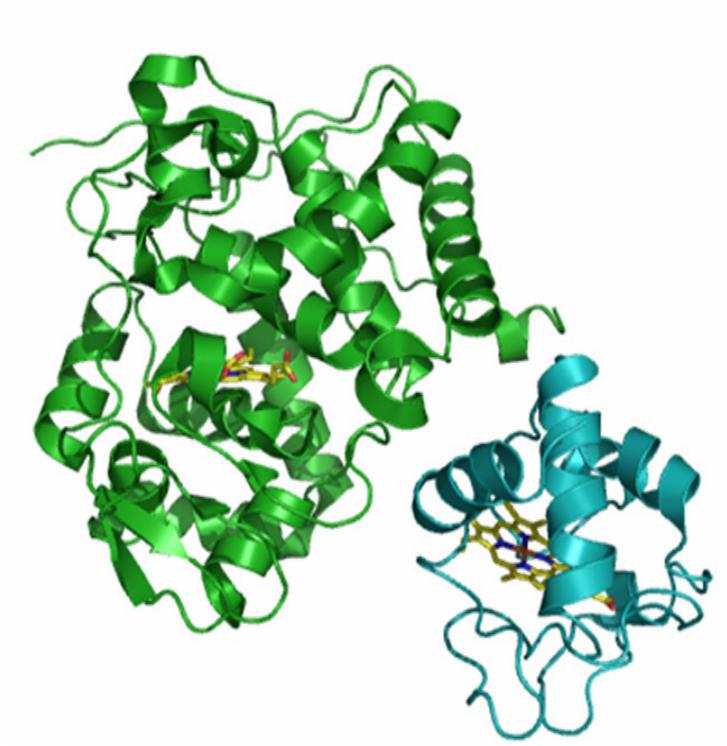

**Figure 1.21: The crystal structure of the C*c*P-cytochrome *c* complex**

The overall crystal structure of the 1:1 complex of cytochrome *c* (cyan) bound to C*c*P (green). Heme groups are shown in yellow (PDB entry 2PCB).

Four residues are reported to form important interactions between the anionic surface of C*c*P and the cationic surface of cytochrome *c*, Asp34, Ala193, Ala194 and Glu290. The C*c*P residue, Asp34 is within 4.2 Å of the cytochrome *c* surface residue Lys87 and is proposed to form a salt bridge with slight movements of the side chains [118]. Similarly Glu290 of C*c*P has the potential to form a salt bridge with Lys73 on the surface of cytochrome *c*. Possibly one of the most important interactions between the C*c*P and cytochrome *c* is the contact between Ala193 and Ala194 of C*c*P and the cytochrome *c* heme C3 methyl group, which is proposed to be the point of electron transfer between the two proteins [118] (Figure 1.23).

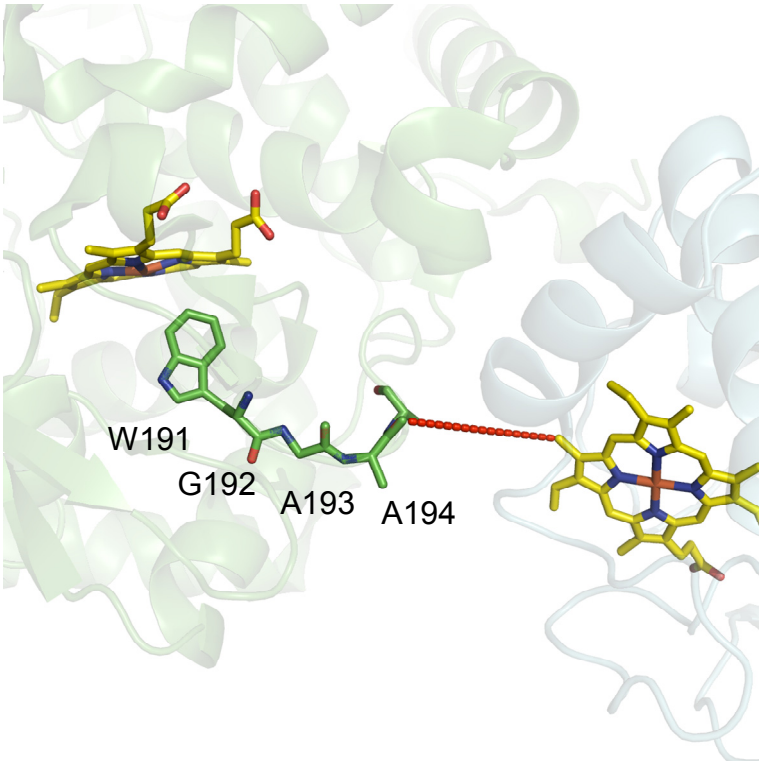


**Figure 1.22: The proposed electron transfer pathway in C*c*P**

The crystal structure of the 1:1 C*c*P-cytochrome *c* complex, the heme groups are indicated in yellow along with the residues proposed to be part of the wire through which electron transfer occurs; Ala194, Ala193, Gly192 and Trp191.

In addition to the possible salt bridges formed between C*c*P and cytochrome *c,* van der Waals interactions involving Arg31, Tyr39, Val197 and Gln120 of C*c*P exist; the interaction between the two proteins appears to be dominated by their overall electrostatic potentials [119]. The utilization of a single cytochrome *c* binding site by C*c*P to form a specific 1:1 C*c*P-cytochrome *c* complex has often been questioned and there is evidence that both a 1:1 complex and a 2:1 complex can exist under various experimental conditions [120, 121]. The site seen in the crystal structure is proposed to have a high-affinity for cytochrome *c* binding but it is thought that a second cytochrome *c* binding site exists which has a much lower affinity. The location of the second C*c*P binding site, proposed to allow formation of the 2:1 complex, is still unknown although experimental evidence using isothermal titration calorimetry (ITC) indicate that the weak-binding site includes the C*c*P residues 146-150 [122].

More recently a covalently cross-linked complex between C*c*P and cytochrome *c* was engineered by the introduction of specific cysteine residues to both proteins, allowing the formation of an intermolecular disulfide bond [123]. This complex closely resembles the structure of the non-covalently linked complex and

kinetic experiments carried out on the engineered complex support the view that C*c*P binds cytochrome *c* as proposed by Pelletier and Kraut [118] and that binding of cytochrome *c* at the second low-affinity site does not support reduction of Compound I.

It has long been known that in addition to its physiological substrate C*c*P is also capable of oxidising small aromatic substrates albeit at a much reduced rate [93], and that binding of these substrates occurs at a site other than that utilised by cytochrome *c* [124]. The location of this site has not to date been unambiguously assigned and is discussed further in Chapters 3 and 4.

### *1.7.1.3 Substrate binding in KatG*

As noted previously the catalase-peroxidases (KatGs) have attracted significant interest due to their ability to activate the prodrug isoniazid (INH), a key chemotherapeutic agent against the disease tuberculosis (TB). The binding mode of INH to KatGs is therefore of great interest and it is hoped that determination of the binding mode and mechanism of activation will lead to the development of novel therapeutic agents against TB. So far the crystal structure of KatG in complex with INH has not been determined and identification of this site is essential in order to understand the key structural elements in INH activation.

The structure of the active site of KatG is very similar to that of C*c*P and APX (see Chapter 3) and early computational studies suggested INH binding near the δ-heme edge [125]. Due to the similarities between KatG and other class I and III peroxidases, models for INH binding in these enzymes provide valuable insights into the mode of INH binding and activation in KatGs. NMR studies and molecular docking of INH to HRP, C*c*P and APX have been used to describe potential enzyme-drug interactions [126]. As discussed in Chapter 3, the first structures of INH bound to activating peroxidases have been determined which provide unambiguous evidence that INH binding occurs at the δ-heme edge and also rationalize INH resistance seen in naturally occurring KatG mutant strains of *M. tuberculosis*.

## *1.7.2 Substrate binding in class II peroxidases*

Lignin peroxidase (LiP) degrades lignin indirectly with its substrate, veratryl alcohol, acting as a redox mediator. There is no indication that LiP is able to form

complexes with small aromatic substrates [44] and the mechanism by which it oxidises veratryl alcohol is thought to be slightly different to that of other heme peroxidases. It has been proposed that an LiP-veratryl cation radical complex forms and is able to react to with a second molecule of veratryl alcohol [127]. In addition to this unusual feature, the substrate channel to the δ-heme edge is relatively inaccessible in LiP [128] and smaller than that in C*c*P (Figure 1.24). This has been used to explain why heme in LiP is not modified by hydrazines [129], whereas it is in C*c*P, and why veratryl alcohol does not bind at the δ-heme edge. Instead a site close to Trp171 has been proposed to form a novel, non-heme edge, electron transfer site [130].

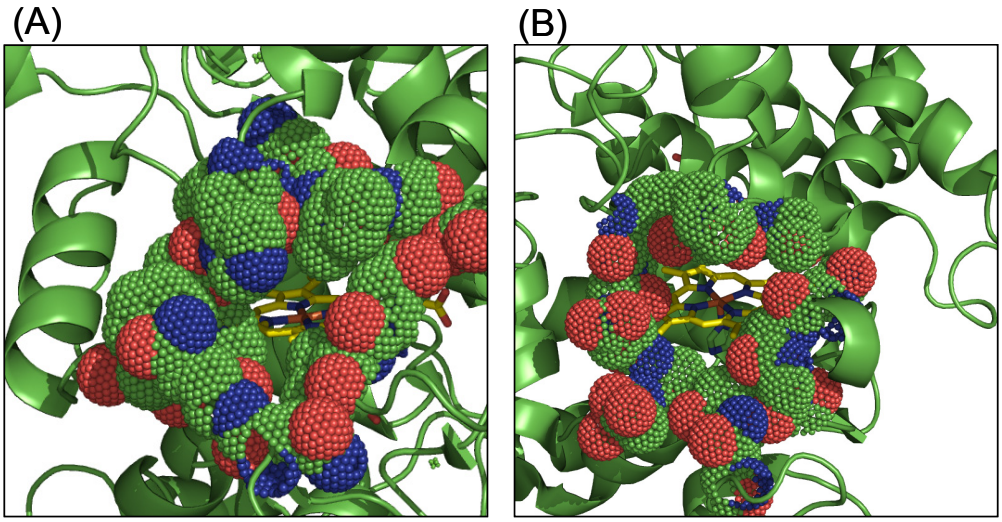


**Figure 1.23: The substrate access channels in LiP and C*c*P**

The δ-heme edge access channel in LiP (A) and C*c*P (B), heme is shown in yellow and the van der Waals radii of residues defining the access channel are represented by dots.

Manganese peroxidase oxidises the metal ion Mn(II) which acts as a redox mediator. Mn(II) binds to the heme 6-propionate and is coordinated to five other ligands with octahedral geometry [131, 132] (Figure 1.25).

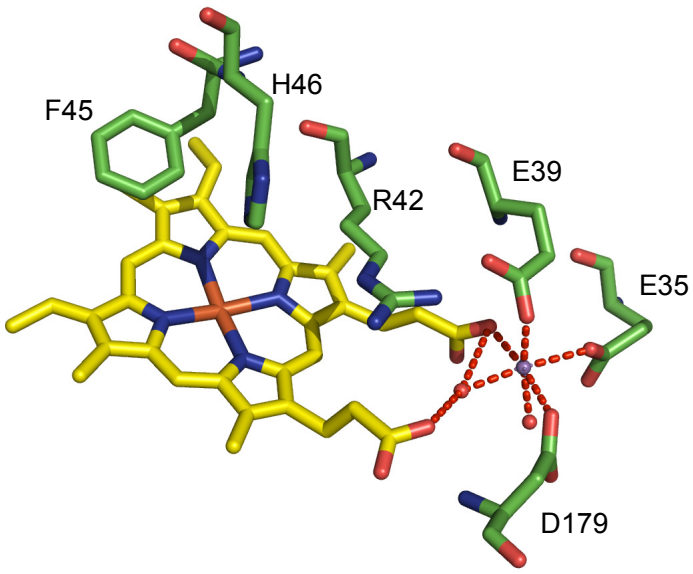


**Figure 1.24: Substrate binding in Manganese peroxidase**

The crystal structure of the MnP-Mn(II) complex, the heme is shown in yellow with Mn(II) represented as a purple sphere. Hydrogen bonds between the propionate groups and a bridging water molecule and the 6 octahedral coordinate bonds to Mn(II) are shown by red dashes, water molecules are represented by red spheres (PDB entry 1YYD).

Three of the Mn(II) ligands are acidic amino acid side chains, Glu35, Glu39, and Asp179, two are oxygen atoms of water molecules and one is the heme 6-propionate. The site is at the surface of the protein and is accessible to the solvent. MnP was one of the first heme peroxidases shown to be able to utilise the γ-heme edge for substrate binding. The direct interaction of Mn(II) with the heme 6-propionate means that rapid electron transfer from the Mn(II) can take place. As discussed further in Chapter 2, the crystal structure of the MnP-Mn(II) complex provided the first crystallographic evidence that the heme propionates, once thought of solely as anchoring points to hold the heme in place, could be active players in the redox chemistry of heme enzymes.

As noted previously, the substrate specificity of A*rthromyces ramosus* peroxidase (ARP) [56] is similar to that of the class III peroxidases with small aromatic molecules being the preferred substrate. In 1997 the crystal structure of ARP in complex with benzhydroxamic acid (BHA) was solved (Figure 1.26), this provided the first structural evidence that small aromatic substrates were bound and oxidised at the δ-heme edge (see Chapter 4) [133].

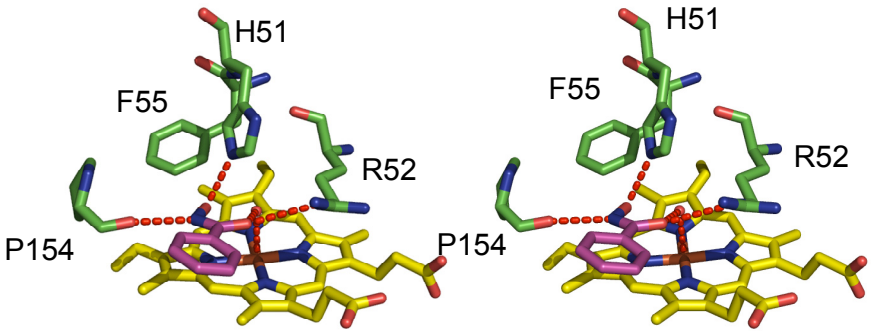


**Figure 1.25: The crystal structure of the ARP-benzhydroxamic acid complex**

Stereo representation of the crystal structure of the ARP-BHA complex (PDB entry 1HSR). The heme is shown in yellow with the bound BHA shown in purple, interactions between the protein and substrate are indicated by red dashes and water molecules are represented by red spheres.

The 1.6 Å structure of the ARP-BHA complex shows BHA bound in a distal location with its aromatic ring almost parallel to the heme. A number of productive hydrogen bonds are made between BHA and ARP namely between Pro154, the distal histidine (His56) and Arg52. An indirect interaction between the BHA hydroxyl group and the heme iron is made via an active site water molecule. The crystal structure of salicylhydroxamic acid (SHA) in complex with ARP has also been solved [134] showing SHA binding to take place at the δ-heme edge.

In addition to small aromatic molecules, ARP also oxidises iodide by a mechanism thought to involve a single two-electron reduction of Compound I [135, 136]. The binding site is between the two peptide segments, Phe90-Pro91-Ala92 and Ser151-Leu152-Ile153, which form the upper part of the substrate access channel. The iodide is bound 12.8 Å from the heme iron and electron transfer is proposed to occur through a long-range mechanism as seen in the C*c*P-cytochrome *c* complex [135].

### *1.7.3 Substrate binding in class III peroxidases*

Horseradish peroxidase (HRP) is one of the most extensively studied heme peroxidases and plays important roles in many biotechnological fields, including diagnostics, biosensors and biocatalysis. HRP catalyses the $H_2O_2$-dependent oxidation of a variety of aromatic substrates and, like APX and C*c*P, HRP is thought to utilise

the δ-heme edge for substrate binding as shown by heme modification and NMR experiments [137, 138]. Crystal structures of HRP in complex with BHA [139], and ferulic acid [140] gave structural evidence for substrate binding at the δ-heme edge. The crystal structure of the HRP-ferulic acid complex is shown in Figure 1.27.

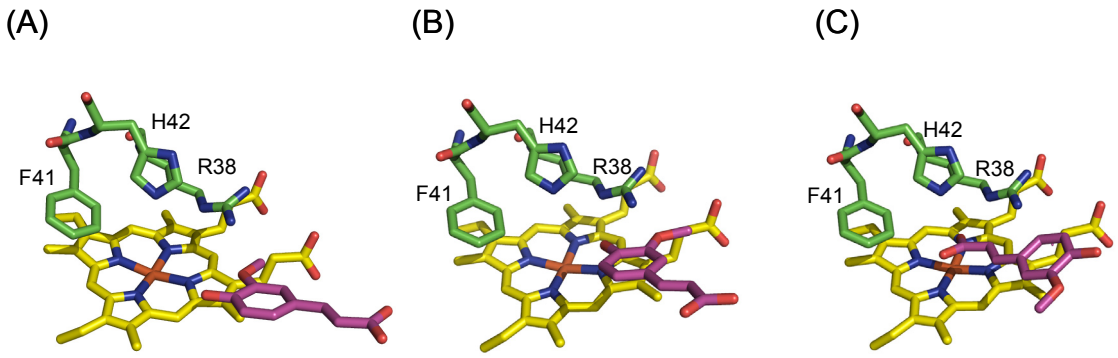


**Figure 1.26: The crystal structure of the HRP-ferulic acid complex**

The crystal structure of the HRP-ferulic acid complex, ferulic acid (purple) is bound in the distal heme pocket at the δ-heme edge. Three orientations for ferulic acid were seen in the crystal structure (A-C). Heme is shown in yellow (PDB entry 6ATJ).

The crystal structure revealed three possible binding orientations of ferulic acid, the binding orientation shown in Figure 1.27(C), with the carboxylate group facing inwards, is unlikely to occur *in vivo*, due to ferulic acid being esterified to the hydroxyl groups of polysaccharides *in vivo*. Benzhydroxamic acid is a substrate for HRP although no physiological role has been established, the crystal structure of the HRP-BHA complex is shown in Figure 1.28.

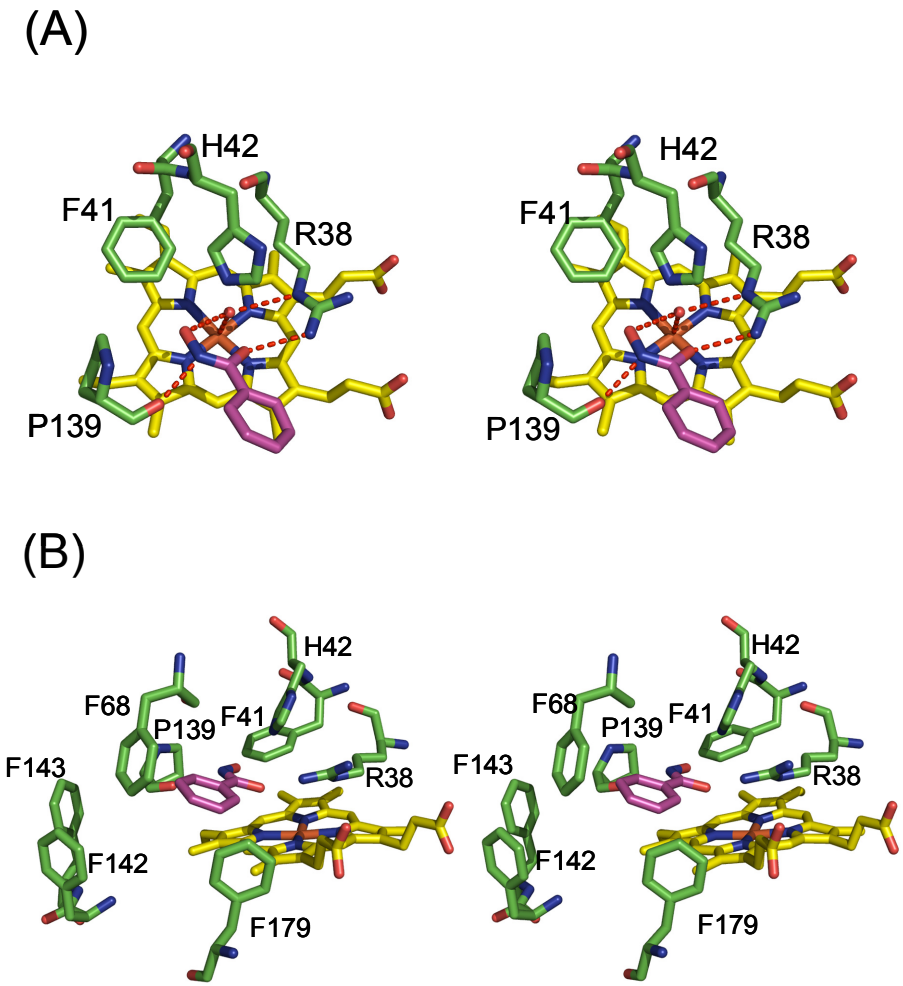


**Figure 1.27: The crystal structure of the HRP-BHA complex**

(A) Stereo representation of the crystal structure of the HRP-BHA complex in the region of the distal heme pocket. The substrate, BHA (purple), is shown bound at the δ-heme edge. (B) Stereo representation of the crystal structure of the HRP-BHA complex showing the hydrophobic residues important in binding. Heme is shown in yellow, hydrogen bonds are shown as red dashes and water molecules are represented by red spheres (PDB entry 2ATJ).

As in the HRP-ferulic acid complex, BHA is shown bound in the distal heme pocket at the δ-heme edge. The hydrophilic part of BHA forms hydrogen bonds with the side chain of the distal arginine (Arg38) and with the backbone carbonyl of Pro139, a hydrogen bond between the hydroxyl group and a water molecule links BHA indirectly to the heme iron (Figure 1.28(A). The hydrophobic aromatic ring is held in place by interactions with Phe68, Phe142, Phe142 and Phe179 (Figure 1.28(B)).

## 1.8 Aims

As discussed above, there is an increasing awareness that binding of substrates to heme peroxidases does not, necessarily, have to occur at the δ-heme edge. The detailed structural and functional knowledge of the two class I heme peroxidases; cytochrome *c* peroxidase and ascorbate peroxidase, make them ideal models for detailed studies on substrate binding in heme enzymes. The overall aim of this thesis was to utilise different techniques in order to study substrate binding and its importance in the catalytic functioning of the enzyme. Protein engineering has been used to probe the different substrate properties of C*c*P and APX, and to determine whether substrate binding is sufficient to confer the functionality of the enzyme (Chapter 2). Aromatic binding has been investigated using X-ray crystallography, steady state and transient kinetics, competitive inhibition studies and directed evolution with the aims of providing further support to the evidence that aromatic substrate binding does indeed occur at the δ-heme edge and to ascertain whether other sites can be employed for aromatic substrate binding. The work in this Thesis has shown that different binding sites for different types of substrates exist, some of which are non-specific and that substrate binding sites can be introduced. At the end of the Thesis, this is discussed in the context of what is known across the heme family of proteins in order to provide a more unified view of substrate binding in the heme peroxidases.

## 1.9 References


1. Williams, D.R., *Historical Outline of the Biological Importance of Trace-Metals.* J. Inherit. Metab. Dis., 1983. **6**: 1-4.
2. Zhang, L. and Hach, A., *Molecular mechanism of heme signalling in yeast: the transcriptional activator HAP1 serves as the key mediator.* Cell. Mol. Life. Sci., 1999. **56**(5-6): 415-426.
3. Editorial, *Metals in chemical biology.* Nat. Chem. Biol., 2008. **4**(3): 143-143.
4. Madsen, E. and Gitlin, J.D., *Copper and Iron Disorders of the Brain.* Annu. Rev. Neurosci., 2007. **30**(1): 317-337.
5. Crichton, R.R. and Ward, R.J., *Iron homeostasis and iron toxicity.* J. Inorg. Biochem., 2001. **86**(1): 36-36.
6. Pierre, J.L., Fontecave, M., and Crichton, R.R., *Chemistry for an essential biological process: the reduction of ferric iron.* Biometals, 2002. **15**(4): 341-346.
7. Baker, H.M., Anderson, B.F., and Baker, E.N., *Dealing with iron: Common structural principles in proteins that transport iron and heme.* P. Natl. Acad. Sci. USA, 2003. **100**(7): 3579-3583.
8. Jordan, I. and Kaplan, J., *The Mammalian Transferrin-Independent Iron Transport-System May Involve a Surface Ferrireductase Activity.* Biochem. J., 1994. **302**: 875-879.
9. Neilands, J.B. and Nakamura, K., *Regulation of Iron Assimilation in Microorganisms.* Nutr. Rev., 1985. **43**(7): 193-197.
10. Beinert, H., Holm, R.H., and Munck, E., *Iron-sulfur clusters: Nature's modular, multipurpose structures.* Science, 1997. **277**(5326): 653-659.
11. Dolla, A., Guerlesquin, F., and Bruschi, M., *Characterization of the cytochrome-$C_3$-ferredoxin electron-transfer domain through cross-linking studies.* J. Protein Chem., 1988. **7**(3): 217-219.
12. Ohnishi, T., Blum, H., Galante, Y.M., and Hatefi, Y., *Iron-sulfur N-1 clusters studied in NADH-ubiquinone oxidoreductase and in soluble NADH dehydrogenase.* J. Biol. Chem., 1981. **256**(17): 9216-9220.
13. Dunford, H.B., *Heme Peroxidases*. 1999, New York: Wiley-VCH.
14. Ator, M.A. and De Montellano P. R. O, *Protein control of prosthetic heme reactivity. Reaction of substrates with the heme edge of horseradish peroxidase.* J. Biol. Chem., 1987. **262**: 1542-1551.
15. Gray, H.B. and Winkler, J.R., *Electron transfer in proteins.* Annu. Rev. Biochem., 1996. **65**: 537-561.
16. Dawson, J.H., *Probing structure-function relations in heme-containing oxygenases and peroxidases* Science, 1988. **240**: 433-439.
17. De Montellano, P.R.O., *Control of the catalytic activity of prosthetic heme by the structure of hemoproteins.* Acc. Chem. Res., 1987. **20**: 289-294.
18. English, A.M. and Tsaprailis, *Catalytic and structure-function relationships in heme proteins.* Adv. Inorg. Chem, 1995. **43**: 79.
19. Terwilliger, N.B., *Functional adaptations of oxygen-transport proteins.* J. Exp. Biol., 1998. **201**(8): 1085-1098.
20. Karlin, K.D., Cruse, R.W., Gultneh, Y., Farooq, A., Hayes, J.C., and Zubieta, J., *Dioxygen copper reactivity - reversible binding of $O_2$ and CO to a phenoxo-bridged dicopper(I) complex.* J. Am. Chem. Soc., 1987. **109**(9): 2668-2679.

21. Antonini, M., and Brunori, E. , *Hemogloblin and Myoglobin and their Reactions with Ligands*. North-Holland Research Monographs Frontiers of Biology, ed. A. Neuberger and E.L. Tatum. Vol. 21. 1971, Amsterdam, London.: North Holland Publishing company.
22. Linberg, R., Conover, C.D., Shum, K.L., and Shorr, R.G.L., *Hemoglobin based oxygen carriers: How much methemoglobin is too much?* Artif. Cell. Blood. Sub., 1998. **26**(2): 133-148.
23. Quillin, M.L., Arduini, R.M., Olson, J.S., and Phillips, G.N., *High-Resolution Crystal-Structures of Distal Histidine Mutants of Sperm Whale Myoglobin.* J. Mol. Biol., 1993. **234**(1): 140-155.
24. Springer, B.A., Sligar, S.G., Olson, J.S., and Phillips, G.N., *Mechanisms of ligand recognition in myoglobin.* Chem. Rev., 1994. **94**(3): 699-714.
25. Lu, Y., Berry, S.M., and Pfister, T.D., *Engineering novel metalloproteins: Design of metal-binding sites into native protein scaffolds.* Chem. Rev., 2001. **101**(10): 3047-3080.
26. Sono, M., Roach, M.P., Coulter, E.D., and Dawson, J.H., *Heme-containing oxygenases.* Chem. Rev., 1996. **96**(7): 2841-2887.
27. Poulos, T.L., Finzel, B.C., and Howard, A.J., *High-resolution crystal-structure of cytochrome-P450$_{CAM}$.* J. Mol. Biol., 1987. **195**(3): 687-700.
28. Regelsberger, G., Jakopitsch, C., Furtmuller, P.G., Rueker, F., Switala, J., Loewen, P.C., and Obinger, C., *The role of distal tryptophan in the bifunctional activity of catalase-peroxidases.* Biochem. Soc. Trans., 2001. **29**: 99-105.
29. Bhaskar, B., Lad, L., and Poulos, T., *Iron: heme proteins, peroxidases, catalases and catalase-peroxidases.* Encyclopedia of Inorganic Chemistry, 2006.
30. Deluca, D.C., Dennis, R., and Smith, W.G., *Inactivation of an Animal and a Fungal Catalase by Hydrogen-Peroxide.* Arch. Biochem. Biophys., 1995. **320**(1): 129-134.
31. Wilming, M. and Johnsson, K., *Inter- and intramolecular domain interactions of the catalase-peroxidase KatG from M tuberculosis.* Febs Letters, 2001. **509**(2): 272-276.
32. Chauhan, N., Basran, J., Efimov, I., Svistunenko, D.A., Seward, H.E., Moody, P.C.E., and Raven, E.L., *The role of serine 167 in human indoleamine 2,3-dioxygenase: A comparison with tryptophan 2,3-dioxygenase.* Biochemistry, 2008. **47**(16): 4761-4769.
33. Papadopoulou, N.D., Mewies, M., Mclean, K.J., Seward, H.E., Svistunenko, D.A., Munro, A.W., and Raven, E.L., *Redox and spectroscopic properties of human indoleamine 2,3-dioxygenase and a His303Ala variant: Implications for catalysis.* Biochemistry, 2005. **44**(43): 14318-14328.
34. Basran, J., Rafice, S.A., Chauhan, N., Efimov, I., Cheesman, M.R., Ghamsari, L., and Raven, E.L., *A kinetic, spectroscopic, and redox study of human tryptophan 2,3-dioxygenase.* Biochemistry, 2008. **47**(16): 4752-4760.
35. Li, H.Y. and Poulos, T.L., *Structure-function studies on nitric oxide synthases.* J. Inorg. Biochem., 2005. **99**(1): 293-305.
36. Ferguson, S.J., *Keilin's cytochromes: How bacteria use them, vary them and make them.* Biochem. Soc. Trans., 2001. **29**: 629-640.
37. Zhang, L., Hach, A., and Wang, C., *Molecular mechanism governing heme signaling in yeast: a higher-order complex mediates heme regulation of the transcriptional activator HAP1.* Mol. Cell. Biol., 1998. **18**(7): 3819-3828.

38. Igarashi, J., Kitanishi, K., Martinkova, M., Murase, M., Iizuka, A., and Shimizu, T., *The roles of thiolate-heme proteins, other than the P450 cytochromes, in the regulation of heme-sensor proteins.* Acta Chi. Slov., 2008. **55**(1): 67-74.
39. Miksanova, M., Igarashi, J., Minami, M., Sagami, I., Yamauchi, S., Kurokawa, H., and Shimizu, T., *Characterization of heme-regulated eIF2 alpha kinase: Roles of the N-terminal domain in the oligomeric state, heme binding, catalysis, and inhibition.* Biochemistry, 2006. **45**(32): 9894-9905.
40. Condorelli, P. and George, S.C., *In vivo control of soluble guanylate cyclase activation by nitric oxide: A kinetic analysis.* Biophys. J., 2001. **80**(5): 2110-2119.
41. Lanzilotta, W.N., Schuller, D.J., Thorsteinsson, M.V., Kerby, R.L., Roberts, G.P., and Poulos, T.L., *Structure of the CO sensing transcription activator CooA.* Nat. Struct. Biol., 2000. **7**(10): 876-880.
42. Shelver, D., Kerby, R.L., He, Y.P., and Roberts, G.P., *Carbon monoxide-induced activation of gene-expression in rhodospirillum-rubrum requires the product of CooA, a member of the cyclic-amp receptor protein family of transcriptional regulators.* J. Bacteriol., 1995. **177**(8): 2157-2163.
43. Isaac, I.S. and Dawson, J.H., *Heme-containing peroxidases.* Essays in Biochemistry, 1999. **34**(4): 51-69.
44. Smith, A.T. and Veitch, N.C., *Substrate binding and catalysis in heme peroxidases.* Curr. Opin. Chem. Biol., 1998. **2**(2): 269-278.
45. Furtmuller, P.G., Zederbauer, M., Jantschko, W., Helm, J., Bogner, M., Jakopitsch, C., and Obinger, C., *Active site structure and catalytic mechanisms of human peroxidases.* Arch. Biochem. Biophys., 2006. **445**(2): 199-213.
46. Sanz, M.L., Parra, A., Prieto, I., Dieguez, I., and Oehling, A.K., *Serum eosinophil peroxidase (EPO) levels in asthmatic patients.* Allergy, 1997. **52**(4): 417-422.
47. Reynolds, W.F., Hiltunen, M., Pirskanen, M., Mannermaa, A., Helisalmi, S., Lehtovirta, M., Alafuzoff, I., and Soininen, H., *MPO and APOE epsilon 4 polymorphisms interact to increase risk for AD in Finnish males.* Neurology, 2000. **55**(9): 1284-1290.
48. Lau, D. and Baldus, S., *Myeloperoxidase and its contributory role in inflammatory vascular disease.* Phramacol. Therapeut., 2006. **111**(1): 16-26.
49. Welinder, K.G., *Superfamily of plant, fungal and bacterial peroxidases.* Curr. Opin. Struct. Biol., 1992. **2**: 388-393.
50. Isaac, I.S. and Dawson, J.H., *Haem iron-containing peroxidases.* Essays Biochem., 1999. **34**: 51-69.
51. Griffin, B.W., *Chloroperoxidase: a review.* Peroxidases in Chemistry and Biology, ed. J. Everse, Everse, K.E. and Grisham, M.B., Eds. Vol. vol. II,pp. 85-137. 1991, Boca Raton: CRC Press,.
52. Fulop, V., Ridout, C.J., Greenwood, C., and Hajdu, J., *Crystal-Structure of the Di-Heme Cytochrome-C Peroxidase from Pseudomonas-Aeruginosa.* Structure, 1995. **3**(11): 1225-1233.
53. Piontek, K., Smith, A.T., and Blodig, W., *Lignin peroxidase structure and function.* Biochem. Soc. Trans., 2001. **29**: 111-116.
54. Sundaramoorthy, M., Kishi, K., Gold, M.H., and Poulos, T.L., *The crystal-structure of manganese peroxidase from Phanerochaete-Chrysosporium at 2.06 angstrom resolution.* J. Biol. Chem., 1994. **269**(52): 32759-32767.

55. Tuor, U., Wariishi, H., Schoemaker, H.E., and Gold, M.H., *Oxidation of phenolic arylglycerol beta-aryl ether lignin model compounds by manganese peroxidase from Phanerochaete-Chrysosporium - oxidative cleavage of an alpha-carbonyl model-compound.* Biochemistry, 1992. **31**(21): 4986-4995.
56. Petersen, J.F.W., Tams, J.W., Vind, J., Svensson, A., Dalboge, H., Welinder, K.G., and Larsen, S., *Crystallization and X-Ray diffraction analysis of recombinant Coprinus-Cinereus peroxidase.* J. Mol. Biol., 1993. **232**(3): 989-991.
57. Howes, B.D., Feis, A., Raimondi, L., Indiani, C., and Smulevich, G., *New insight into the roles of the structural $Ca^{2+}$ ions of horseradish peroxidase.* J. Inorg. Biochem., 2001. **86**(1): 271-271.
58. Dunford, H.B., *Horseradish peroxidase: structure and kinetic properties.* In Peroxidases in Chemistry and Biology, ed. J. Everse, et al. Vol. 2. 1991, Boca Raton, FL: CRC Press.
59. Gajhede, M., *Horseradish peroxidase*. in Handbook of metalloproteins, ed. A. Messerschmidt, et al. Vol. 1, 2 p.195. 2001, Chichester: John Wiley and Sons.
60. Gajhede, M., Schuller, D.J., Henriksen, A., Smith, A.T., and Poulos, T.L., *Crystal structure of horseradish peroxidase C at 2.15 angstrom resolution.* Nat. Struct. Biol., 1997. **4**(12): 1032-1038.
61. Schuller, D.J., Ban, N., Vanhuystee, R.B., Mcpherson, A., and Poulos, T.L., *The crystal structure of peanut peroxidase.* Structure, 1996. **4**(3): 311-321.
62. Henriksen, A., Welinder, K.G., and Gajhede, M., *Structure of barley grain peroxidase refined at 1.9-angstrom resolution - A plant peroxidase reversibly inactivated at neutral pH.* J. Biol. Chem., 1998. **273**(4): 2241-2248.
63. Jones, P. and Dunford, H.B., *Mechanism of Compound-I Formation from Peroxidases and Catalases.* J. Theor. Biol., 1977. **69**(3): 457-470.
64. Jones, P. and Dunford, H.B., *The mechanism of Compound I formation revisited.* J. Inorg. Biochem., 2005. **99**(12): 2292-2298.
65. Hiner, A.N.P., Raven, E.L., Thorneley, R.N.F., Garcia-Canovas, F., and Rodriguez-Lopez, J.N., *Mechanisms of compound I formation in heme peroxidases.* J. Inorg. Biochem., 2002. **91**(1): 27-34.
66. Poulos, T.L. and Kraut, J., *The stereochemistry of peroxidase catalysis.* J. Biol. Chem., 1980. **255**(17): 8199-8205.
67. Erman, J.E., Vitello, L.B., Miller, M.A., and Kraut, J., *Active-site mutations in cytochrome c peroxidase - a critical role for histidine-52 in the rate of formation of Compound I.* J. Am. Chem. Soc., 1992. **114**(16): 6592-6593.
68. Lad, L., Mewies, M., Basran, J., Scrutton, N.S., and Raven, E.L., *Role of histidine 42 in ascorbate peroxidase - Kinetic analysis of the H42A and H42E variants.* Eur. J. Biochem., 2002. **269**(13): 3182-3192.
69. Newmyer, S.L. and De Montellano, P.R.O., *Horseradish peroxidase His-42-Ala, His-42-Val, and Phe-41-Ala mutants: Histidine catalysis and control of substrate access to the heme iron.* J. Biol. Chem., 1995. **270**(33): 19430-19438.
70. Chance, B., Powers, L., Ching, Y., Poulos, T., Schonbaum, G.R., Yamazaki, I., and Paul, K.G., *X-Ray Absorption Studies of Intermediates in Peroxidase-Activity.* Arch. Biochem. Biophys., 1984. **235**(2): 596-611.
71. Penner-Hahn, J.E., Mcmurry, T.J., Renner, M., Latosgrazynsky, L., Eble, K.S., Davis, I.M., Balch, A.L., Groves, J.T., Dawson, J.H., and Hodgson, K.O., *X-Ray Absorption Spectroscopic Studies of High Valent Iron Porphyrins -*

*Horseradish-Peroxidase Compound I and Compound II and Synthetic Models.* J. Biol. Chem., 1983. **258**(21): 2761-2764.

72. Bonagura, C.A., Bhaskar, B., Shimizu, H., Li, H.Y., Sundaramoorthy, M., Mcree, D.E., Goodin, D.B., and Poulos, T.L., *High-resolution crystal structures and spectroscopy of native and Compound I cytochrome c peroxidase.* Biochemistry, 2003. **42**(19): 5600-5608.
73. Miller, M.A., Vitello, L., and Erman, J.E., *Regulation of interprotein electron-transfer by Trp191 of cytochrome c peroxidase.* Biochemistry, 1995. **34**(37): 12048-12058.
74. Berglund, G.I., Carlsson, G.H., Smith, A.T., Szoke, H., Henriksen, A., and Hajdu, J., *The catalytic pathway of horseradish peroxidase at high resolution.* Nature, 2002. **417**(6887): 463-468.
75. Kelly, G.J. and Latzko, E., *Soluble ascorbate peroxidase - detection in plants and use in vitamin-C estimation.* Naturwissenschaften, 1979. **66**(12): 617-618.
76. Raven, E.L., *Understanding functional diversity and substrate specificity in haem peroxidases: what can we learn from ascorbate peroxidase?* Nat. Prod. Rep., 2003. **20**(4): 367-381.
77. Jespersen, H.M., Kjaersgard, I.V.H., Ostergaard, L., and Welinder, K.G., *From sequence analysis of three novel ascorbate peroxidases from Arabidopsis thaliana to structure, function and evolution of seven types of ascorbate peroxidase.* Biochem. J., 1997. **326**: 305-310.
78. Dalton, D.A., Hanus, F.J., Russell, S.A., and Evans, H.J., *Purification, Properties, and Distribution of Ascorbate Peroxidase in Legume Root-Nodules.* Plant Physiol., 1987. **83**(4): 789-794.
79. Degara, L., Depinto, M.C., and Arrigoni, O., *Ascorbate synthesis and ascorbate peroxidase activity during the early stage of wheat germination.* Plant Physiol., 1997. **100**(4): 894-900.
80. Elia, M.R., Borraccino, G., and Dipierro, S., *Soluble Ascorbate Peroxidase from Potato-Tubers.* Plant Sci., 1992. **85**(1): 17-21.
81. Koshiba, T., *Cytosolic Ascorbate Peroxidase in Seedlings and Leaves of Maize (Zea-Mays).* Plant Cell Physiol., 1993. **34**(5): 713-721.
82. Kvaratskhelia, M., Winkel, C., and Thorneley, R.N.F., *Purification and characterization of a novel class III peroxidase isoenzyme from tea leaves.* Plant Physiol., 1997. **114**(4): 1237-1245.
83. Chen, G.X. and Asada, K., *Ascorbate Peroxidase in Tea Leaves - Occurrence of 2 Isozymes and the Differences in Their Enzymatic and Molecular-Properties.* Plant Cell Physiol., 1989. **30**(7): 987-998.
84. Dalton, D.A., Delcastillo, L.D., Kahn, M.L., Joyner, S.L., and Chatfield, J.M., *Heterologous expression and characterization of soybean cytosolic ascorbate peroxidase.* Arch. Biochem.and Biophys., 1996. **328**(1): 1-8.
85. Murthy, S.S. and Zilinskas, B.A., *Molecular-cloning and characterization of a cDNA-encoding pea monodehydroascorbate reductase.* J. Biol. Chem., 1994. **269**(49): 31129-31133.
86. Sharp, K.H., Mewies, M., Moody, P.C.E., and Raven, E.L., *Crystal structure of the ascorbate peroxidase-ascorbate complex.* Nat. Struct. Biol., 2003. **10**(4): 303-307.
87. Patterson, W.R. and Poulos, T.L., *Crystal-structure of recombinant pea cytosolic ascorbate peroxidase.* Biochemistry, 1995. **34**(13): 4331-4341.

88. Patterson, W.R., Poulos, T.L., and Goodin, D.B., *Identification of a porphyrin Pi-cation-radical in ascorbate peroxidase Compound I.* Biochemistry, 1995. **34**(13): 4342-4345.
89. Fishel, L.A., Villafranca, J.E., Mauro, J.M., and Kraut, J., *Yeast cytochrome c peroxidase: Mutagenesis and expression in E. coli Show Trp51 is not the radical site in Compound I.* Biochemistry, 1987. **26**(2): 351-360.
90. Poulos, T.L., Freer, S.T., Alden, R.A., Edwards, S.L., Skogland, U., Takio, K., Eriksson, B., Xuong, N.H., Yonetani, T., and Kraut, J., *Crystal-Structure of Cytochrome-C Peroxidase.* Journal of Biological Chemistry, 1980. **255**(2): 575-580.
91. Altschul, A.M., Abrams, R., and Hogness, T.R., *Cytochrome c Peroxidase.* J. Biol. Chem., 1940. **136**: 777-794.
92. Kwon, M., Chong, S., Han, S., and Kim, K., *Oxidative stresses elevate the expression of cytochrome c peroxidase in Saccharomyces cerevisiae.* B.B.A. Gen. Subjects, 2003. **1623**(1): 1-5.
93. Yonetani, T., and Ray, G. S, *Studies on cytochrome c peroxidase: purification and some properties.* J. Biol. Chem., 1965. **240**: 4503-4514.
94. Goltz, S., Kaput, J., and Blobel, G., *Isolation of the yeast nuclear gene encoding the mitochondrail protein, cytochrome c peroxidase.* J. Biol. Chem., 1982. **257**: 11160-11190.
95. Goodin, D.B., Mauk, A.G., and Smith, M., *Studies of the radical species of compound ES of cytochrome c peroxidase altererd by site-directed mutagenesis.* Proc. Natl. Acad. Sci. USA., 1986. **83**: 1295-1299.
96. Poulos, T.L., Freer, S.T., Alden, R.A., Edwards, S.L., Skogland, U., Takio, K., Eriksson, B., Xuong, N.H., Yonetani, T., and Kraut, J., *Crystal structure of cytochrome c peroxidase.* J. Biol. Chem., 1980. **255**(2): 575-580.
97. Bonagura, C.A., Sundaramoorthy, M., Pappa, H.S., Patterson, W.R., and Poulos, T.L., *An engineered cation site in cytochrome c peroxidase alters the reactivity of the redox active tryptophan.* Biochemistry, 1996. **35**(19): 6107-6115.
98. Coon, M.J., *Enzyme ingenuity in biological oxidations: A trail leading to cytochrome P450.* J. Biol. Chem., 2002. **277**(32): 28351-28363.
99. Guengerich, F.P., *Uncommon P450-catalyzed reactions.* Curr. Drug. Metab., 2001. **2**(2): 93-115.
100. Raag, R., Li, H.Y., Jones, B.C., and Poulos, T.L., *Inhibitor-induced conformational change in cytochrome $P450_{CAM}$.* Biochemistry, 1993. **32**(17): 4571-4578.
101. Andersen, J.F., Tatsuta, K., Gunji, H., Ishiyama, T., and Hutchinson, C.R., *Substrate specificity of 6-Deoxyerythronolide-B hydroxylase, a bacterial cytochrome P450 of erythromycin-a biosynthesis.* Biochemistry, 1993. **32**(8): 1905-1913.
102. Cupp-Vickery, J.R., Garcia, C., Hofacre, A., and Mcgee-Estrada, K., *Ketoconazole-induced conformational changes in the active site of cytochrome $P450_{eryF}$.* J. Mol. Biol., 2001. **311**(1): 101-110.
103. Li, H.Y. and Poulos, T.L., *The structure of the cytochrome $P450_{BM-3}$ heme domain complexed with the fatty acid substrate, palmitic acid.* Nat. Struct. Biol., 1997. **4**(2): 140-146.
104. Narhi, L.O. and Fulco, A.J., *Characterization of a catalytically self-sufficient 119,000 Da cytochrome P450 monooxygenase induced by barbiturates in Bacillus-Megaterium.* J. Biol. Chem., 1986. **261**(16): 7160-7169.

105. Miura, Y. and Fulco, A.J., *Omega-1, omega-2 and omega-3 hydroxylation of long chain fatty acids, amides and alcohols by a soluble enzyme-system from Bacillus-Megaterium.* BIiochim. Biophys. Acta, 1975. **388**(3): 305-317.
106. Griffith, O.W. and Stuehr, D.J., *Nitric oxides synthases - properties and catalytic mechanism.* Ann. Rev. Physiol., 1995. **57**: 707-736.
107. Marletta, M.A., *Nitric-oxide synthase structure and mechanism.* J. Biol. Chem., 1993. **268**(17): 12231-12234.
108. Giovanelli, J., Campos, K.L., and Kaufman, S., *Tetrahydrobiopterin, a cofactor for rat cerebellar nitric oxide synthase, does not function as a reactant in the oxygenation of arginine.* Proc. Natl. Acad. Sci. USA., 1991. **88**(16): 7091-7095.
109. Crane, B.R., Arvai, A.S., Ghosh, S., Getzoff, E.D., Stuehr, D.J., and Tainer, J.A., *Structures of the N-omega-hydroxy-L-arginine complex of inducible nitric oxide synthase oxygenase dimer with active and inactive pterins.* Biochemistry, 2000. **39**(16): 4608-4621.
110. Wei, C.C., Wang, Z.Q., Tejero, J., Yang, Y.P., Hemann, C., Hille, R., and Stuehr, D.J., *Catalytic reduction of a tetrahydrobiopterin radical within nitric-oxide synthase.* J. Biol. Chem., 2008. **283**(17): 11734-11742.
111. Yamamoto, S. and Hayaishi, O., *Tryptophan pyrrolase of rabbit intestine.* J. Biol. Chem., 1967. **242**: 5260-5266.
112. Sugimoto, H., Oda, S.I., Otsuki, T., Hino, T., Yoshida, T., and Shiro, Y., *Crystal structure of human indoleamine 2,3-dioxygenase: Catalytic mechanism of $O_2$ incorporation by a heme-containing dioxygenase.* Proc. Natl. Acad. Sci. USA., 2006. **103**(8): 2611-2616.
113. Forouhar, F., Anderson, J.L.R., Mowat, C.G., Vorobiev, S.M., Hussain, A., Abashidze, M., Bruckmann, C., Thackray, S.J., Seetharaman, J., Tucker, T., Xiao, R., Ma, L.C., Zhao, L., Acton, T.B., Montelione, G.T., Chapman, S.K., and Tong, L., *Molecular insights into substrate recognition and catalysis by tryptophan 2,3-dioxygenase.* Proc. Natl. Acad. Sci. USA., 2007. **104**(2): 473-478.
114. Sundaramoorthy, M., Kishi, K., Gold, M.H., and Poulos, T.L., *The crystal structure of manganase peroxidase from Phanerochaete crysosporium at 2.06 angstrom resolution.* J. Biol. Chem., 1994. **269**: 32759-32767.
115. Dalton, D.A., *Peroxidases in Chemistry and Biology (pp 139-154)*, ed. Everse J, Everse K. E, and M.B. Grisham. 1991, Boca Raton: CRC Press.
116. Sharp, K.H., Moody, P.C.E., Brown, K.A., and Raven, E.L., *Crystal structure of the ascorbate peroxidase-salicylhydroxamic acid complex.* Biochemistry, 2004. **43**(27): 8644-8651.
117. Pearl, N.M., Jacobson, T., Arisa, M., Vitello, L.B., and Erman, J.E., *Effect of single-site charge-reversal mutations on the catalytic properties of yeast cytochrome c peroxidase: Mutations near the high-affinity cytochrome c binding site.* Biochemistry, 2007. **46**(28): 8263-8272.
118. Pelletier, H. and Kraut, J., *Crystal-structure of a complex between electron-transfer partners, cytochrome c peroxidase and cytochrome c.* Science, 1992. **258**(5089): 1748-1755.
119. Erman, J.E. and Vitello, L.B., *Yeast cytochrome c peroxidase: mechanistic studies via protein engineering.* Biochim. Biophys. Acta, Protein Struct. Mol. Enzymol., 2002. **1597**(2): 193-220.
120. Stemp, E.D.A. and Hoffman, B.M., *Cytochrome c peroxidase binds 2 molecules of cytochrome c: Evidence for a low-affinity, electron-transfer-*

*active site on cytochrome c peroxidase.* Biochemistry, 1993. **32**(40): 10848-10865.
121. Zhou, J.S. and Hoffman, B.M., *Stern-Volmer in reverse - 2;1 stoichiometry of the cytochrome c-cytochrome c peroxidase electron transfer complex.* Science, 1994. **265**(5179): 1693-1696.
122. Leesch, V.W., Bujons, J., Mauk, A.G., and Hoffman, B.M., *Cytochrome c peroxidase cytochrome c complex: Locating the second binding domain on cytochrome c peroxidase with site-directed mutagenesis.* Biochemistry, 2000. **39**(33): 10132-10139.
123. Guo, M.L., Bhaskar, B., Li, H.Y., Barrows, T.P., and Poulos, T.L., *Crystal structure and characterization of a cytochrome c peroxidase-cytochrome c site-specific cross-link.* Proc. Natl. Acad. Sci. USA., 2004. **101**(16): 5940-5945.
124. Depillis, G.D., Sishta, B.P., Mauk, A.G., and De Montellano, P.R.O., *Small substrates and cytochrome c are oxidized at different sites of cytochrome c peroxidase.* J. Biol. Chem., 1991. **266**(29): 19334-19341.
125. Bertrand, T., Eady, N.A.J., Jones, J.N., Nagy, J.M., Jamart-Gregoire, B., Raven, E.L., and Brown, K.A., *Crystal structure of Mycobacterium tuberculosis catalase-peroxidase.* J. Biol. Chem., 2004. **279**(37): 38991-38999.
126. Pierattelli, R., Banci, L., Eady, N.A.J., Bodiguel, J., Jones, J.N., Moody, P.C.E., Raven, E.L., Jamart-Gregoire, B., and Brown, K.A., *Enzyme-catalyzed mechanism of isoniazid activation in class I and class III peroxidases.* J. Biol. Chem., 2004. **279**(37): 39000-39009.
127. Khindaria, A., Yamazaki, I., and Aust, S.D., *Veratryl alcohol cation-radical - an EPR and visible absorption study.* Abstr. Pap. Am. Chem. S., 1995. **210**: 259-PHYS.
128. Poulos, T.L., Edwards, S.L., Wariishi, H., and Gold, M.H., *Crystallographic refinement of lignin peroxidase at 2 angstrom.* J. Biol. Chem., 1993. **268**(6): 4429-4440.
129. Depillis, G.D., Wariishi, H., Gold, M.H., and Demontellano, P.R.O., *Inactivation of lignin peroxidase by phenylhydrazine and sodium-azide.* Arch. Biochem.and Biophys., 1990. **280**(1): 217-223.
130. Blodig, W., Smith, A.T., Doyle, W.A., and Piontek, K., *Crystal structures of pristine and oxidatively processed lignin peroxidase expressed in Escherichia coli and of the W171F variant that eliminates the redox active tryptophan 171. Implications for the reaction mechanism.* J. Mol. Biol., 2001. **305**(4): 851-861.
131. Sundaramoorthy, M., Kishi, K., Gold, M.H., and Poulos, T.L., *Preliminary crystallographic analysis of manganese peroxidase from Phanerochaete-Chrysosporium.* J. Mol. Biol., 1994. **238**(5): 845-848.
132. Sundaramoorthy, M., Youngs, H.L., Gold, M.H., and Poulos, T.L., *High-resolution crystal structure of manganese peroxidase: Substrate and inhibitor complexes.* Biochemistry, 2005. **44**(17): 6463-6470.
133. Itakura, H., Oda, Y., and Fukuyama, K., *Binding mode of benzhydroxamic acid to Arthromyces ramosus peroxidase shows by X-ray crystallographic analysis of the complex at 1.6 angstrom resolution.* FEBS Lett., 1997. **412**(1): 107-110.
134. Tsukamoto, K., Itakura, H., Sato, K., Fukuyama, K., Miura, S., Takahashi, S., Ikezawa, H., and Hosoya, T., *Binding of salicylhydroxamic acid and several aromatic donor molecules to Arthromyces ramosus peroxidase, investigated*

*by X-ray crystallography, optical difference spectroscopy, NMR relaxation, molecular dynamics, and kinetics.* Biochemistry, 1999. **38**(39): 12558-12568.

135. Fukuyama, K., Sato, K., Itakura, H., Takahashi, S., and Hosoya, T., *Binding of iodide to Arthromyces ramosus peroxidase investigated with X-ray crystallographic analysis, H-1 and I-127 NMR spectroscopy, and steady-state kinetics.* J. Biol. Chem., 1997. **272**(9): 5752-5756.
136. Ohtaki, S., Nakagawa, H., Kimura, S., and Yamazaki, I., *Analyses of catalytic intermediates of hog thyroid peroxidase during its iodinating reaction.* J. Biol. Chem., 1981. **256**(2): 805-810.
137. Ator, M.A., David, S.K., and De Montellano, P.R.O., *Structure and catalytic mechanism of horseradish peroxidase: Regiospecific meso-alkylation of the prosthetic heme group by alkylhydrazines.* J. Biol. Chem., 1987. **262**(31): 14954-14960.
138. Adak, S., Mazumder, A., and Banerjee, R.K., *Probing the active site residues in aromatic donor oxidation in horseradish peroxidase: Involvement of an arginine and a tyrosine residue in aromatic donor binding.* Biochem. J., 1996. **314**: 985-991.
139. Henriksen, A., Schuller, D.J., Meno, K., Welinder, K.G., Smith, A.T., and Gajhede, M., *Structural interactions between horseradish peroxidase C and the substrate benzhydroxamic acid determined by X-ray crystallography.* Biochemistry, 1998. **37**(22): 8054-8060.
140. Henriksen, A., Smith, A.T., and Gajhede, M., *The structures of the horseradish peroxidase C-ferulic acid complex and the ternary complex with cyanide suggest how peroxidases oxidize small phenolic substrates.* J. Biol. Chem., 1999. **274**(49): 35005-35011.

# Chapter 2

## *Introduction of an Ascorbate Binding Site in Cytochrome c Peroxidase*

# 2.1 Introduction

The two most notable and extensively characterized class I peroxidases are cytochrome *c* peroxidase (C*c*P) and ascorbate peroxidase (APX). C*c*P was the first peroxidase to have its crystal structure solved [1] and the first to be overexpressed in *E. coli* [2]. This meant that extensive structure-function studies were possible and thus C*c*P became *the* benchmark against which all other peroxidases were compared. However, C*c*P has two anomalous features. First it uses a protein radical at Trp191 [3] rather than the more usual porphyrin π-cation radical utilized by other peroxidases such as HRP. Second its physiological substrate is the heme enzyme cytochrome *c*, whereas peroxidase substrates are typically small and usually organic molecules. APX uses the more common porphyrin π-cation radical and its physiological substrate is ascorbate, a small organic molecule much more typical of other peroxidases especially class III peroxidases such as HRP.


**Figure 2.1: Sequence alignment of APX and C*c*P**

The numbering is as for the pea cytosolic APX enzyme [9] (adapted from Veitch and Smith [10]). The rpAPX sequence is identical to rsAPX except at positions 10 (Pro in rpAPX), 16 (Ile), 21 (Arg), 31 (Lys), 36 (Ile), 49 (Ser), 50 (Lys), 63 (Gln), 69 (Gly), 84 (Ile), 86 (Glu), 87 (Gln), 91 (Val), 107 (Ile), 152 (Ser), 196 (Thr), 200 (Asp), 213 (Thr), 215 (Ser), 222 (Glu), 230 (Val), 240 (Leu) and 249 (Glu). Active site residues, (●), the residues involved in binding of the potassium site in rpAPX (▼), the residues involved in binding of ascorbate in APX (■) and the residues involved in binding of cytochrome *c* in C*c*P (▲) are indicated. The additional loops in C*c*P and the C-terminal truncation in APX can be seen.

The high sequence homology of C*c*P with APX and the fact that APX has, but does not use [4-6], a tryptophan at residue 179 (equivalent to Trp191 in C*c*P) places APX at an important interface in terms of our overall understanding of peroxidase activity. C*c*P has 37% sequence homology with APX, Figure 2.1 and an almost identical 3D structure, Figure 2.2 [7]. Despite the similarity of the two proteins the ability of C*c*P to oxidize ascorbate is ~ 100-fold lower than that of APX which has a $k_{cat}$ 80 ± 6 $s^{-1}$ [8] compared to 0.8 ± 0.1 $s^{-1}$ for C*c*P.

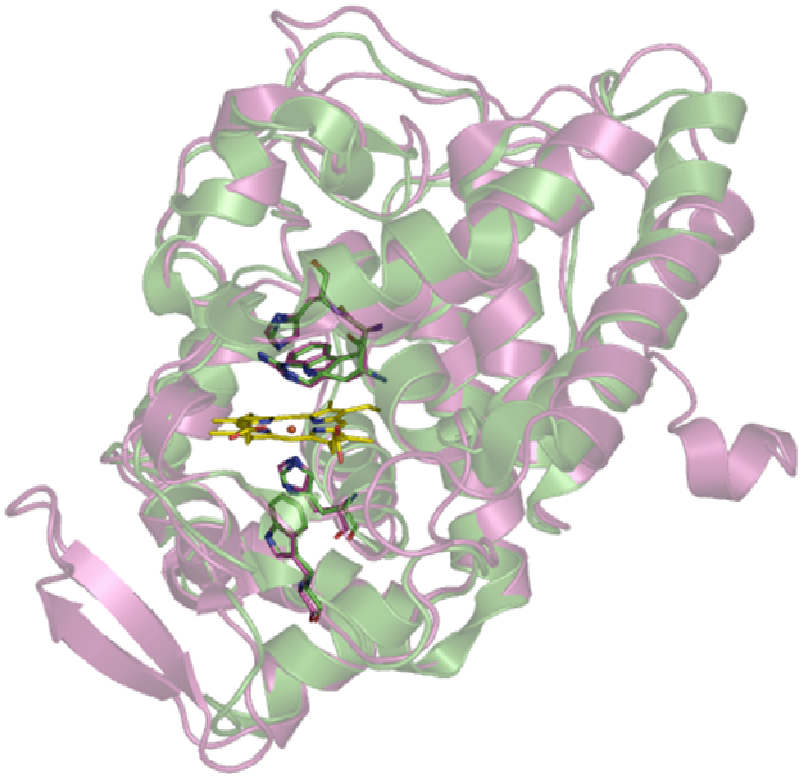

**Figure 2.2: Structural comparison of APX and C*c*P**

Overlay of C*c*P (PDB accession code 2CYP) (purple) and APX (PDB accession code 1OAG) (green). This figure shows their almost identical 3-dimensional structure and superposition of the important active site residues. The three major structural differences can also be seen: (i) the APX C-terminal truncation, (ii) the additional β-sheet structure in C*c*P (residues 210-224) and (iii) the loop containing residues 34-41 in C*c*P, missing in APX.

The first crystal structure of the APX-ascorbate complex [11] had wide implications for our detailed comparative understanding of substrate binding in the class I peroxidases and this has led to a focus on how substrate binding is linked to function in other peroxidases. The question that has arisen is that if C*c*P and APX are so similar then why is their ability to oxidise ascorbate so different? Sharp et al [11]

have shown that the structural architecture of APX and C*c*P is subtly different. The features required for anionic ascorbate binding in APX (Arg172 and Lys30) are replaced by Asn184 and Asp33 in C*c*P. C*c*P has an extra region (loop containing residues 34-41) which includes three anionic residues Asp34, Glu35 and Asp37 necessary for binding of cationic cytochrome *c* [12, 13] not present in APX. In addition APX lacks Glu290 due to a C-terminal truncation. The additional loop and the side chain of Tyr36 prevent ascorbate binding in C*c*P, Figure 2.3, allowing rationalization of the low activity of C*c*P towards ascorbate [14]. The low activity of APX towards cytochrome *c* [15] can also be rationalized by the absence of the loop.

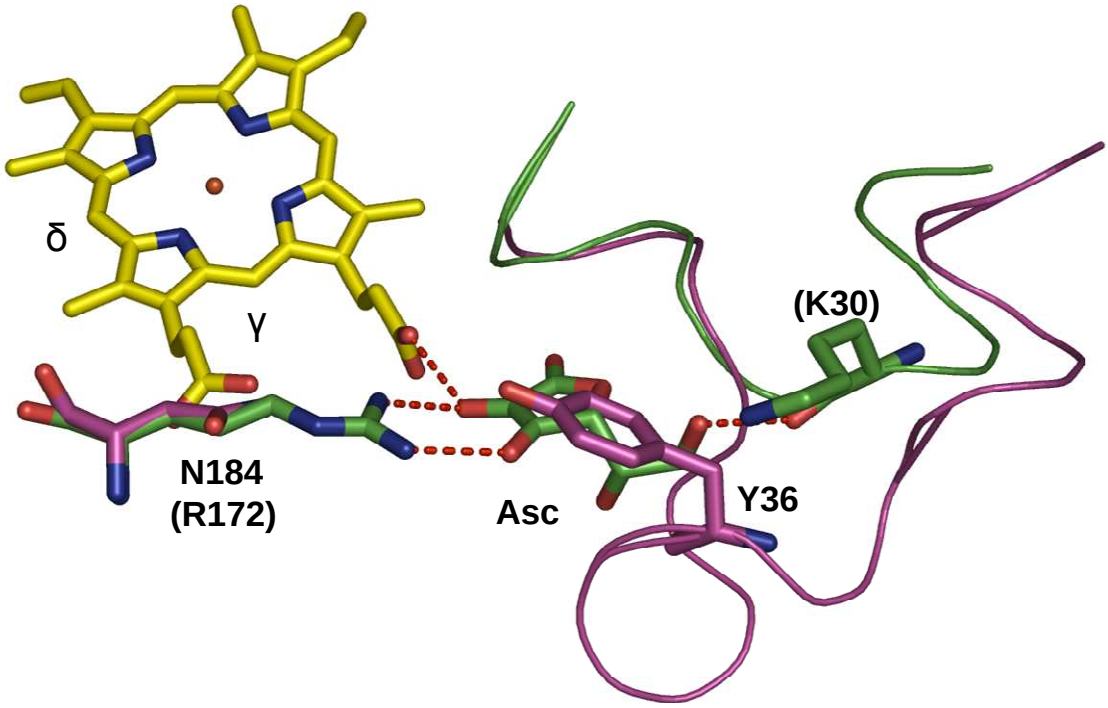


**Figure 2.3: Comparison of APX/ascorbate complex with C*c*P**

The structure of the APX-ascorbate complex (PDB accession code 1OAF) [11] (green) overlaid with that of C*c*P (purple). The three important interactions between APX and ascorbate are shown in red. The loop regions (APX residues 26-36 and C*c*P residues 28-45) are shown along with the side chain of Tyr36 which blocks the equivalent ascorbate binding site in APX. The δ- and γ-heme edges are indicated.

The structures also allow an explanation as to why APX uses a porphyrin π-cation despite having an oxidisable tryptophan at a position analogous to Trp191 in C*c*P. Ascorbate has a direct interaction with the heme 6-propionate at the γ-heme edge

allowing reduction of Compound I to occur directly through the heme bypassing Trp179. In contrast the C*c*P-cytochrome *c* interaction [16] has cytochrome *c* bound in an orientation that involves Trp191 as part of an electron transfer pathway to the heme in Compound I.

In 2006 Macdonald et al [8] carried out a detailed study on the interactions of ascorbate with APX. The individual and collective contributions of the hydrogen bonding interactions were dissected using site-directed mutagenesis, steady state and pre-steady state kinetics. It was revealed that Lys30 only played a minor role in ascorbate binding and that the hydrogen bonds to Arg172 and the heme 6-propionate play a major part in stabilization of bound ascorbate. A comparative analysis of both C*c*P and APX provides a unique insight into the features that control substrate binding and in this Chapter this approach has been used to develop a more unified view of substrate binding and catalysis across the family of heme peroxidases.

Three approaches to enhance ascorbate binding and oxidation in C*c*P weree taken. First, steric bulk was removed: the side chain Y36A directly blocks the equivalent ascorbate binding site in C*c*P and so was replaced with a less bulky alanine residue. Second, the residue equivalent to Arg172 in APX is Asn184, Asn overlays directly with Arg172 and is orientated in the same direction (*i.e.* towards the ascorbate): hence the N184R mutant was prepared in order to introduce potential hydrogen bonding interactions. Third, to establish whether C*c*P can support electron transfer directly through the heme via the γ-heme edge (bypassing the need for Trp191) the tryptophan was replaced by a phenylalanine residue.

## 2.2 Results

### *2.2.1 Expression and purification of CcP*

Samples of C*c*P were prepared from *Escherichia Coli* BL21-DE3 Gold cells using a *p*T7CCP expression vector (a kind gift from Prof. Mauk) which confers ampicillin resistance. The yeast C*c*P gene used in this work is modified in order to improve overexpression in *E. coli* and is termed C*c*P(MKT) [2]. C*c*P(MKT) is identical to that of cytochrome c peroxidase obtained from commercial yeast except for the three N-terminal residues, which have been changed from Thr-Thr-Pro to Met-Lys-Thr. The original C*c*P(MKT) construct also contained two additional mutations,

Ile53 and Gly152, the crystal structure of bakers yeast C*c*P shows these residues to be Thr and Asp respectively. The C*c*P used throughout this Thesis contains Thr53 and Asp152, hence, it is identical to the bakers yeast protein, as seen in the crystal structure, except for the first three residues and will be referred to as wild type C*c*P throughout this Thesis. C*c*P was purified as previously described [2] by ion exchange and gel filtration chromatography. Further purification was achieved by recrystallisation into water. All variants containing the Y36A mutation failed to recrystallise against water as per the published procedure and so further purification after gel filtration chromatography was carried out by Fast Protein Liquid Chromatography (FPLC) (Superdex 75 gel filtration column), after which crystallisation occurred. The purity of C*c*P was determined by measuring Reinheitzal ($R_z$) values and polyacrylamide gel electrophoresis (SDS-PAGE). Protein was stored at -80 ºC as a crystalline suspension in water.

### *2.2.2 Mutagenesis*

Site-directed mutagenesis of the C*c*P gene was performed according to the Quikchange$^{TM}$ protocol (Stratagene Ltd, Cambridge, UK). Mutations were confirmed by DNA sequencing as reported previously [17]. In total seven mutant forms of C*c*P were prepared with different combinations of mutations at: Y36, N184 and W191: these were Y36A, N184R, Y36A/N184R, Y36A/W191F, N184R/W191F and Y36A/N184R/W191F.

### *2.2.3 Crystallisation*

Crystals of C*c*P were prepared by microdialysis of a 10-30 mg/ml solution of C*c*P in 500 mM potassium phosphate, pH 6.0 against 50 mM potassium phosphate, pH 6.0 containing 30% 2-methyl-2,4-pentanediol by volume. After approximately 2 days (mutant dependent) at 4 ºC large bright red crystals were seen, Figure 2.4. The triple mutant needed up to 2 weeks to crystallise at 4 ºC and crystals were much smaller.

**Figure 2.4: Crystal of C*c*P mounted in cryostream (magnified)**

## *2.2.4 Data collection and refinement*

Diffraction data were collected for all mutants of C*c*P in house using a Rigaku RU2HB X-ray generator with copper anode and Xenocs multilayer optics and an R-Axis IV detector. All data were collected at 100 K. Data were indexed, integrated and scaled using MOSFLM [18] and SCALA [19]. Data collection statistics are shown in Table 2.1. The structures were refined from the 1.70 Å wild type C*c*P structure [20] (Protein data bank entry 2CYP). All refinement used REFMAC5 [21] from the CCP4 suite [19]. COOT [22] was used throughout for manual adjustment, ligand fitting and interpretation of the water structure.

**Table 2.1:** Data collection and refinement statistics for the ascorbate binding C*c*P variants and for the Y36A/N184R/W191F-ascorbate complex

| Protein | W191F | N184R/ W191F | Y36A | Y36A/ W191F | Y36A/ N184R | N184R | Y36A/N184R/ W191F | Y36A/N184R/W191F-ascorbate complex |
|---|---|---|---|---|---|---|---|---|
| **Data Collection** | | | | | | | | |
| Space group | $P2_12_12_1$ | $P2_12_12_1$ | $P2_12_12_1$ | $P2_12_12_1$ | $P2_12_12_1$ | $P2_12_12_1$ | $P2_12_12_1$ | $P2_12_12_1$ |
| Unit Cell (Å) | | | | | | | | |
| A | 51.1 | 51.0 | 51.1 | 51.0 | 51.1 | 51.0 | 51.0 | 51.0 |
| B | 75.3 | 74.6 | 75.8 | 75.0 | 75.1 | 74.5 | 74.5 | 74.4 |
| C | 106.3 | 106.7 | 107.1 | 106.4- | 107.3 | 106.3 | 106.5 | 106.6 |
| Resolution (Å) | 27.16-1.80 (1.90-1.80) | 27.17 - 1.80 (1.90-1.80) | 46.13-2.01 (2.12-2.01 | 45.93-2.10 (2.21-2.10) | 30.28-2.01 (2.11-2.01) | 61.78-1.40 (1.48-1.40) | 39.13 - 1.86 (1.96-1.86) | 42.03- 2.01 (2.12-2.01) |
| Total observations | 74923 (6085) | 87578 (8923) | 58833 (8129) | 196453 (27085) | 38648 (4669) | 411140 (31869) | 120110 (16654) | 15047 (2103) |
| Unique reflections | 29668 (3257) | 34080 (4620) | 26868 (3737) | 24405 (3514) | 18732 (2625) | 80702 (11309) | 31259 (4618) | 12304 (1668) |
| $I/\sigma I$ | 22.9 (4.0) | 18.7 (5.3) | 15.2 (6.6) | 9.1 (4.3) | 15.1 (3.0) | 15.6 (4.4) | 18.0 (3.4) | 17.3 (5.2) |
| $R_{merge}$ | 0.039 (0.218) | 0.044 (0.125) | 0.047 (0.112) | 0.076 (0.298) | 0.055 (0.389) | 0.082 (0.275) | 0.063 (0.271) | 0.033 (0.104) |
| Completeness (%) | 76.8 (59.4) | 88.8 (77.5) | 95.0 (92.1) | 99.7 (99.5) | 65.8 (64.6) | 98.9 (95.9) | 90.4 (92.3) | 45.9 (42.5)* |
| **Refinement statistics** | | | | | | | | |
| $R_{work}$ | 0.174 | 0.186 | 0.161 | 0.168 | 0.165 | 0.172 | 0.169 | 0.187 |
| $R_{free}$ | 0.214 | 0.216 | 0.203 | 0.210 | 0.201 | 0.193 | 0.205 | 0.246 |
| R.M.S.D | | | | | | | | |
| Bonds (Å) | 0.012 | 0.013 | 0.015 | 0.015 | 0.014 | 0.007 | 0.013 | 0.013 |
| Angles (°) | 1.41 | 1.37 | 1.37 | 1.34 | 1.39 | 1.12 | 1.25 | 1.44 |

## *2.2.5 Crystal structures*

### *2.2.5.1 Crystal structures of the CcP mutants*

Crystal structures were obtained for all of the mutants presented in this Chapter. The structures of the seven mutants in the region of the heme are shown in Figure 2.5. In

all cases, the structures were as expected and did not show major perturbations of the structure as compared to the wild type protein.

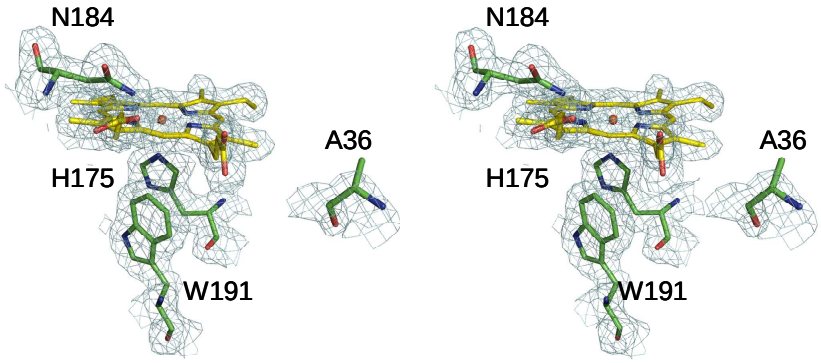


(A) Y36A

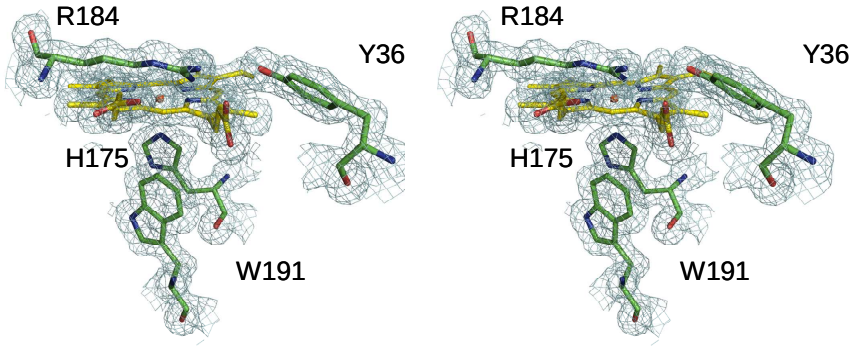


(B) N184R

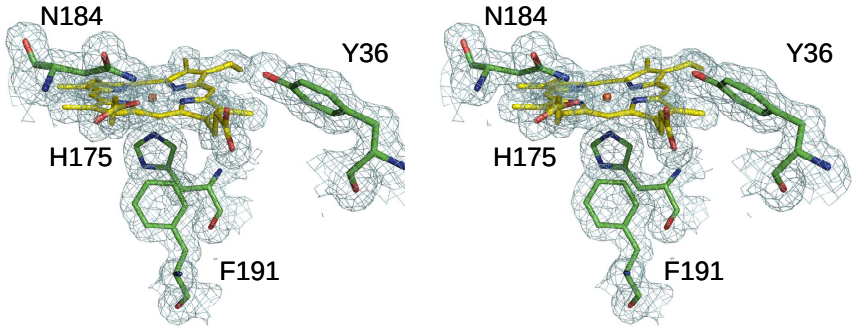


(C) W191F

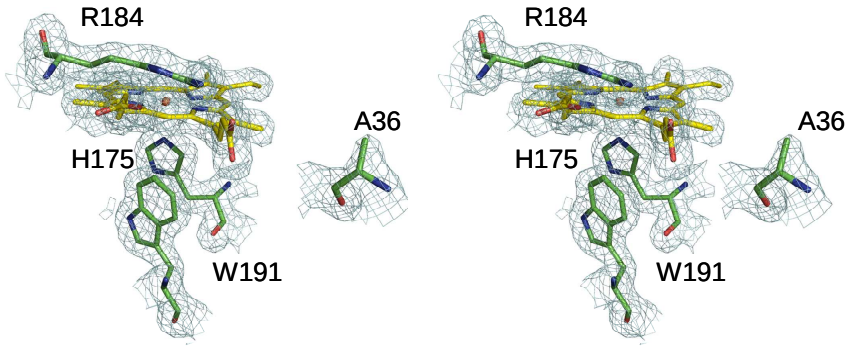


(D) Y36A/N184R

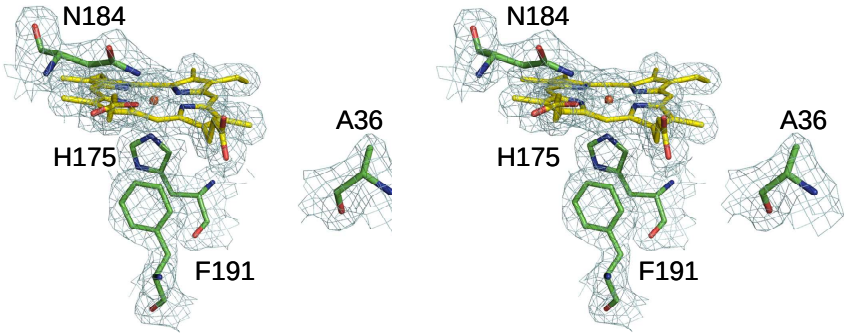


(E) Y36A/W191F

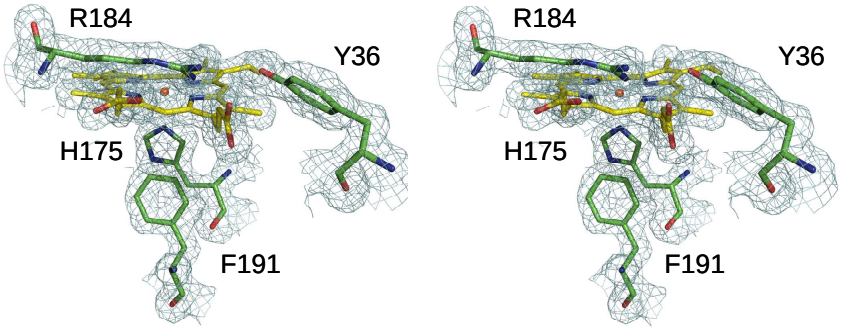


(F) N184R/W191F

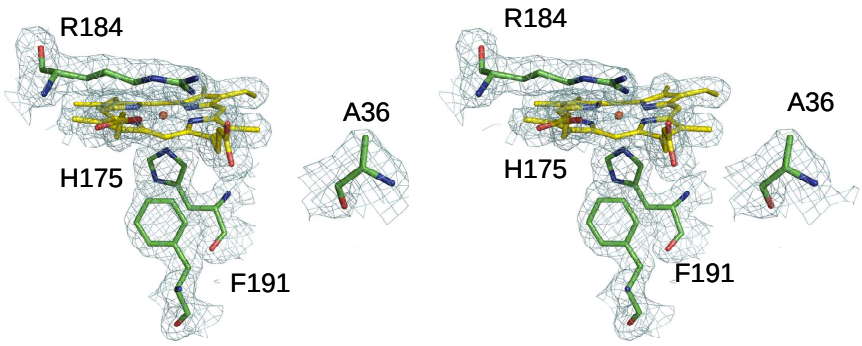


(G) Y36A/N184R/W191F

**Figure 2.5: Stereo representations of structures of mutants examined in this chapter**

Refined electron density is shown in aquamarine. (A) Y36A, (B) N184R, (C) W191F, (D) Y36A/N184R, (E) Y36A/W191F, (F) N184R/W191F, and (G) Y36A/N184R/W191F .

The structure of the triple Y36A/N184R/W191F mutant close to the expected ascorbate binding site is shown in Figure 2.6(A). The mutant contains a cavity which was previously occupied by the side chain of Tyr36 and a single water molecule, Figure 2.6(B). Examination of the electron density in the new cavity reveals two well-ordered water molecules which form hydrogen bonds to the engineered Arg184 residue and the heme 6-propionate. The first water molecule (labelled 1 in Figure 2.6(A)) is 2.70 Å from the O1 of the heme 6-propionate and 2.82 Å from the NH1 group of Arg184; the second is 2.82 Å from the NH2 of Arg184. Comparison of this structure with that of APX in the absence of ascorbate, Figure 2.6(C), shows that these water molecules in the triple mutant are in analogous positions to two (also labeled 1 and 2 in Figure 2.6(C)) of the five seen in the ascorbate binding site of APX.

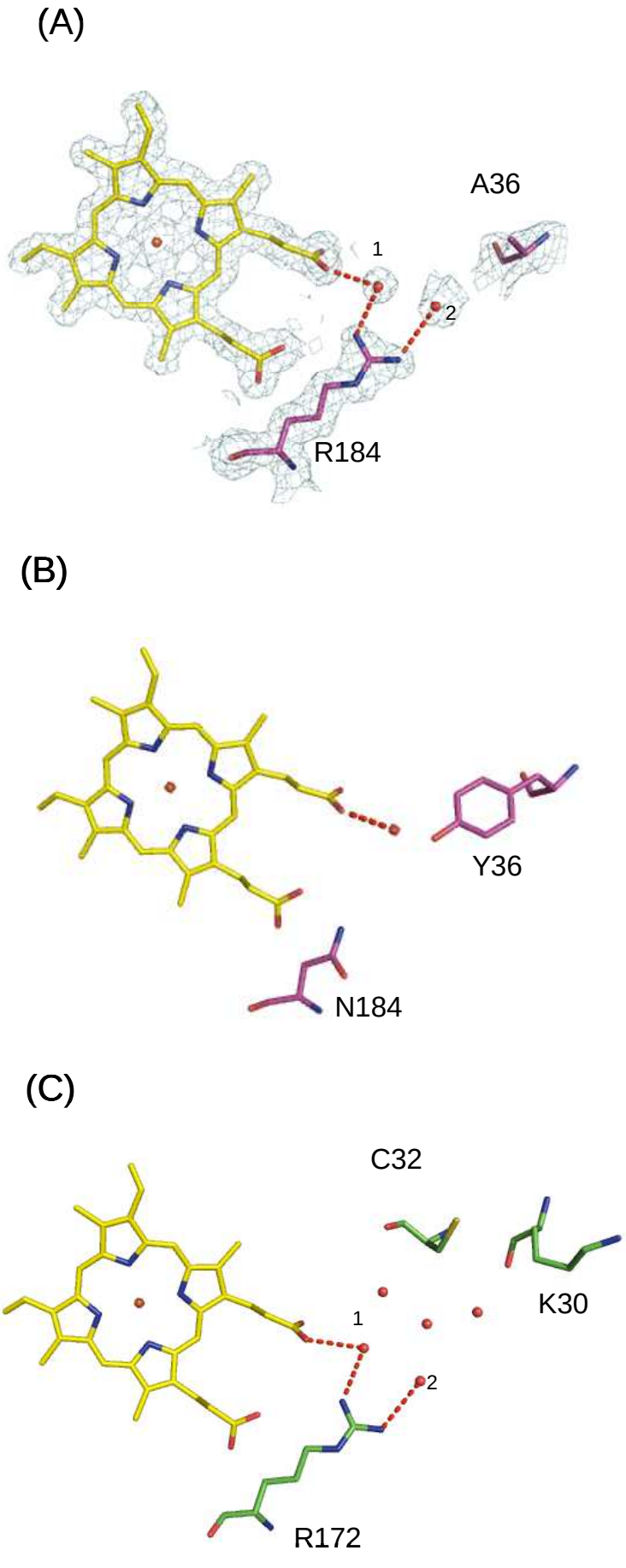


**Figure 2.6: Comparison of Y36A/N184R/W191F with APX**

(A) Structure of Y36A/N184R/W191F in the region of the ascorbate binding site. The F191 residue in the Y36A/N184R/W191F variant lies directly underneath the heme and is not shown in this Figure. In comparison to wild type C*c*P (B) two well ordered water molecules (labelled 1 and 2) occupy the new cavity created in Y36A/N184R/W191F in similar positions to two of the water molecules (also labelled 1 and 2) seen in the ascorbate binding cavity of APX (C). Water molecules are shown as red spheres.

### *2.2.5.2 Crystal structure of the CcP ascorbate complex*

For the ascorbate-bound structure of Y36A/N184R/W191F, crystals were soaked in mother liquor containing 100 mM ascorbate for 5 minutes before rapid cooling to 100 K. Soaks at higher concentrations of ascorbate and for longer times caused the crystals to crack and many variations of the soak (including variations in length of soak and ascorbate concentration) were attempted before the ascorbate bound structure was obtained.

The structure of the Y36A/N184R/W191F triple mutant in complex with ascorbate is shown in Figure 2.7. Comparison with the ascorbate-free structure shows that binding of ascorbate leads to no major structural rearrangements of the enzyme (r.m.s deviation in Cα positions of 0.288 Å).

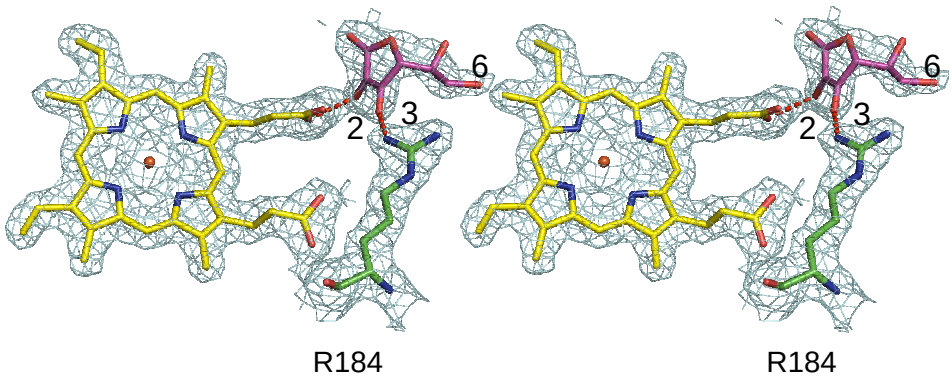


**Figure 2.7: Stereo representation of ascorbate bound to C*c*P.**

The refined electron density (aquamarine) for ascorbate (magenta) bound to the new cavity in Y36A/N184R/W191F. Hydrogen bonds are indicated in red. Hydroxyl groups on ascorbate are numbered.

Soaking of crystals was very difficult due to the crystals cracking, when the crystal structure presented in this paper was obtained an error occurred during data collection. Consequently only 45.9 % of data was collected for the ascorbate bound structure. The credibility of the ascorbate-bound structure can be verified by comparing the unsoaked crystal data with the bound structure.

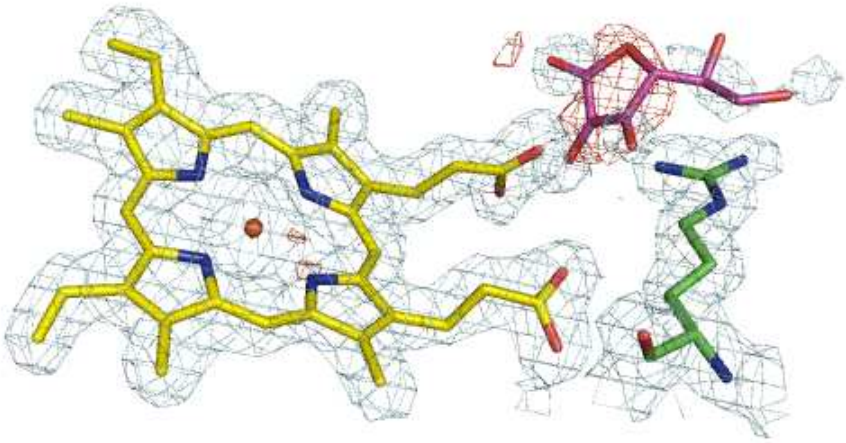

**Figure 2.8: Validation of ascorbate binding**

Diffraction data from the unsoaked Y36A/N184R/W191F crystal ($F_o$) was used with the co-ordinates of the ascorbate-bound structure ($F_c$ and phases) to calculate these maps. The $2F_o$-$F_c$ density is shown in aquamarine and the $F_o$-$F_c$ is map is shown in green (positive density) and red (negative density). Experimental difficulties with both the soaking and data collection resulted in only 45.9% of the unique data from the complex being recorded: hence, this calculation was undertaken to cross-validate the presence of bound ascorbate. As only the reflections observed and their equivalents are used in this calculation, there will be no bias from the missing reflections. No electron density corresponding to ascorbate was found with data from all other variants discussed in this Chapter.

The diffraction data for the unbound structure was refined for 1 cycle using the ascorbate bound structure as the model. Figure 2.8 shows the calculated omit map using diffraction data from an unsoaked crystal with the model of the bound structure, clear negative electron density is seen in the site that is occupied by ascorbate in the ascorbate soaked crystal. The results of this calculation show that the unsoaked ascorbate structure does not have electron density in the region where ascorbate is bound in the soaked structure, verifying the presence of extra electron density attributable to ascorbate in the bound ascorbate structure.

Ascorbate binds at the new cavity created at the γ-heme edge in an analogous position to that observed for ascorbate bound to APX in place of the two water molecules seen in the unbound structure [11]. The refined atomic positions, Figure 2.7 show hydrogen bonds between the 2-OH (p$K_a$ 4.0 [23]) of the substrate and the

heme 6-propionate (2.56 Å) and from the 3-OH (p$K_a$ 11.3 [23]) of the substrate and the NH1 of Arg184 (2.43 Å). There are no clear interactions for the 6-OH which is hydrogen bonded to Lys30 in APX although this interaction is not thought to be essential for ascorbate activity in APX [8]. There is no evidence of ascorbate binding to any other site in the protein. By comparing the Y36A/N184R/W191F-ascorbate complex with APX-ascorbate, Figure 2.9, it is possible to see that the ascorbate is orientated slightly differently, this prevents H-bonding between the 2-OH of the substrate and the NH1 of Arg184 in C*c*P which is seen in APX. The 3-OH of the substrate interacts with the NH2 of Arg172 in APX this interaction is also prevented in the C*c*P-ascorbate structure due to the slight difference in orientation of the substrate.

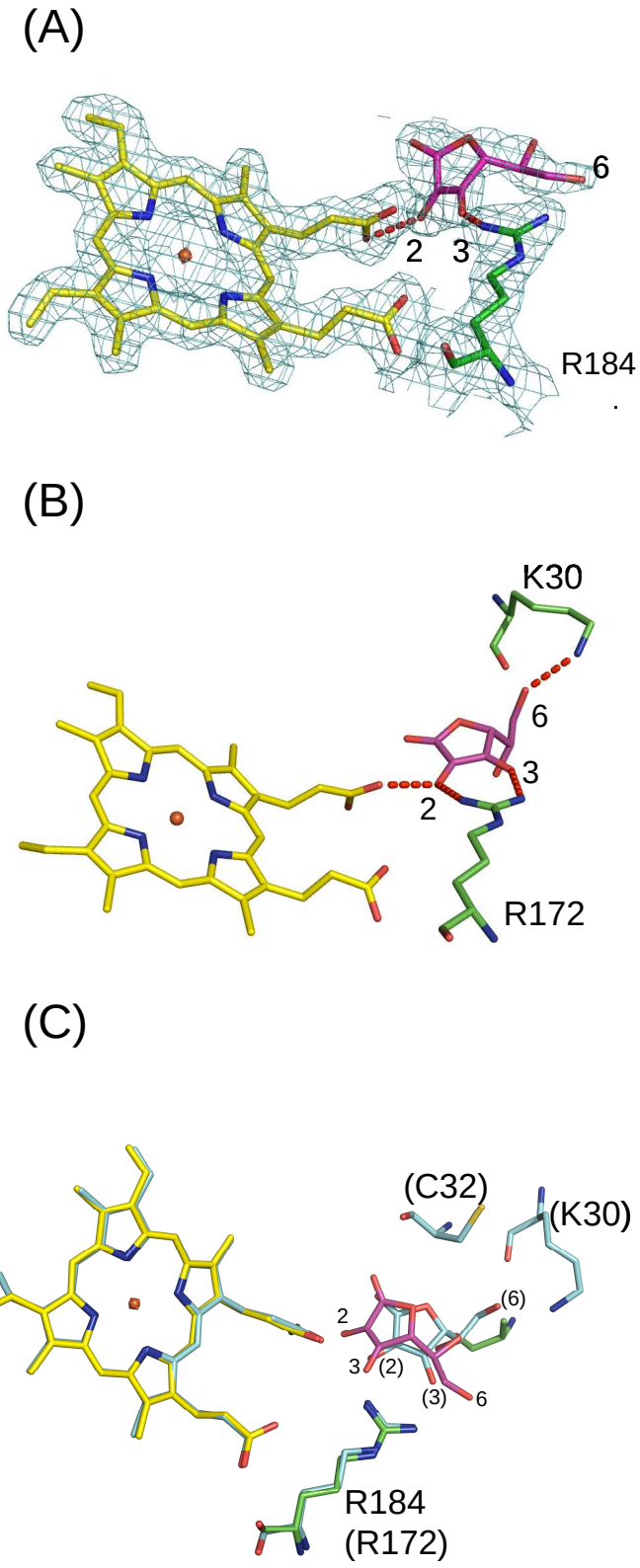


**Figure 2.9: Comparison of ascorbate binding in APX and C*c*P**

(A) Ascorbate bound to the new cavity in Y36A/N184R/W191F. (B) Ascorbate bound to APX, residues in C*c*P are labelled. (C) Comparison of the mode of ascorbate binding in the APX-ascorbate complex (cyan) and Y36A/N184R/W191F (magenta). Residues in C*c*P are labelled, with those for the equivalent residues in APX in parentheses. The difference in the binding orientation is clearly visible. Hydroxyl groups on ascorbate are labelled with those for the ascorbate-APX complex in parentheses. Hydrogen bonds are indicated by red dashes.

## *2.2.6 Electronic absorption spectra*

Wavelength maxima for the ferric derivatives of all mutants are indicated in Table 2.2.

**Table 2.2:** Electronic absorption spectra

Wavelength maxima (nm) for ferric derivatives of wild type C*c*P and mutants examined in this chapter. Absorption coefficients for the ferric derivatives ($mM^{-1}cm^{-1}$) are shown in parentheses. sh = shoulder.

| ***Mutant*** | ***Wavelength maximum (nm)*** | | | | |
|---|---|---|---|---|---|
| | **Soret** | **CT1** | **β** | **α** | **CT2** |
| **Wild type C*c*P** | 408 (102) | 506 | 544 (sh) | 589 (sh) | 647 |
| **Y36A** | 408 (104) | 502 | 538 (sh) | 585 (sh) | 630 |
| **N184R** | 408 (102) | 507 | 544 (sh) | 589 (sh) | 644 |
| **W191F** | 408 (109) | 504 | 544 (sh) | 589 (sh) | 645 |
| **N184R/W191F** | 412 (99) | - | 536 | 563 (sh) | 645 (sh) |
| **Y36A/W191F** | 414 (98) | 485 (sh) | 533 | 566 | 632 (sh) |
| **Y36A/N184R/W191F** | 414 (100) | 489 (sh) | 536 | 567 | 620 (sh) |
| **Y36A/N184R** | 414 (96) | 489 (sh) | 534 | 568 | 620 (sh) |

The electronic absorption spectra of the seven C*c*P mutants and wild type C*c*P can be split into three main categories, Figure 2.10. The first contains wild type C*c*P and all three single mutants. Ferric heme proteins typically have four absorption bands in the visible region of the spectrum, the α and β bands which occur at ~570 nm and ~540 nm respectively and two charge transfer bands CT1 (~500 nm) and CT2 (~630 nm) [24, 25]. Wild type C*c*P and the single mutants have spectra which have maxima at the charge transfer bands with weak shoulders at the α and β positions, this is consistent with predominantly high spin heme species, either pentacoordinate or hexacoordinate with a water at the $6^{th}$ axial position. The N184R/W191F mutant has a slightly (4 nm) red shifted Soret and a β band at 536 nm, the lack of a CT1 band and the weak shoulder at CT2 is consistent with a mixed-spin species with water or possible a hydroxyl at the $6^{th}$ axial position. The Y36A/W191F, Y36A/N184R and Y36A/N184R/W191F mutants have similar spectra which are distinct from that of wild type C*c*P. These are predominantly low-spin species with weak shoulders at the charge transfer bands and prominent α and β bands characteristic of the alkaline form of C*c*P [26]. The positions of the α and β bands (~ 567 nm and 533 nm respectively)

along with the shoulder seen at ~380 nm for these three mutants is characteristic of imidazole coordination to the 6$^{th}$ axial position [27, 28] and it is thought that the distal histidine in C*c*P can coordinate to the heme in alkaline conditions [27, 29]. However the crystal structures show no evidence for bis-histidine ligation to the heme, and the low-spin mutants are thought to be hydroxyl-ligated heme, with the hydroxyl hydrogen bonded to Trp51, Figure 2.11, and possibly the distal histidine (as proposed previously [30]) allowing the hydroxyl group to become a stronger field ligand and cause the characteristic low-spin spectra.

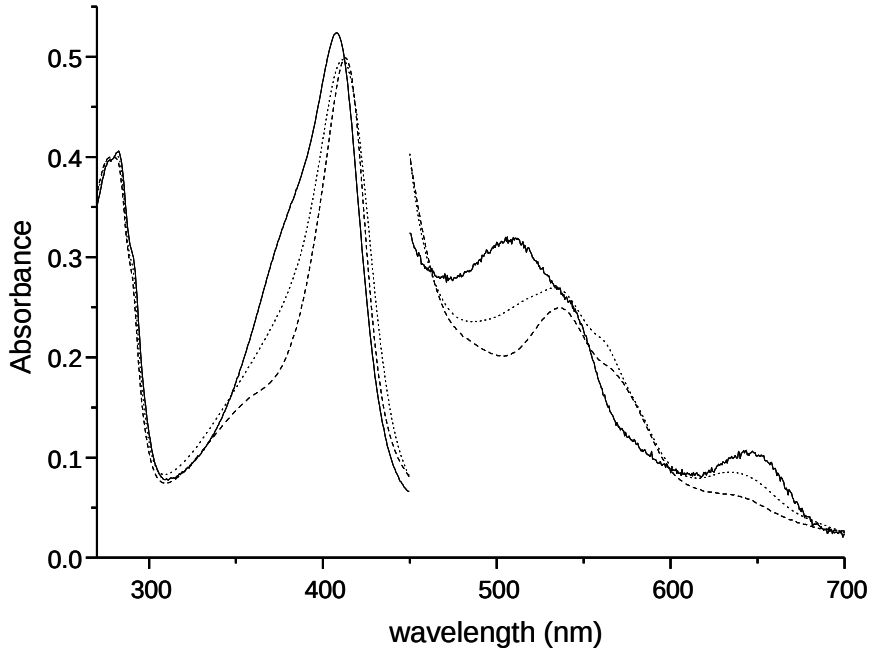


**Figure 2.10: Electronic absorption spectra of C*c*P mutants examined in this Chapter**

The spectra of wild type C*c*P (solid line), N184R/W191F (dotted line) and Y36A/N184R/W191F (dashed line). Spectra were recorded at pH 6.0 in 100 mM KPi buffer at 25 ºC. Each of the three single mutants (Y36A, W191F and N184R) have similar spectra to the wild type with charge transfer bands at ~505 nm and ~647 nm characteristic of a high spin species. The spectrum of N184R/W191F has weaker charge transfer bands and α and β bands showing a mixed spin species. The spectra of Y36A/N184R, Y36A/W191F and Y36A/N184R/W191F all have spectra characteristic of a low spin species with a heme ligated by a relatively strong field ligand.

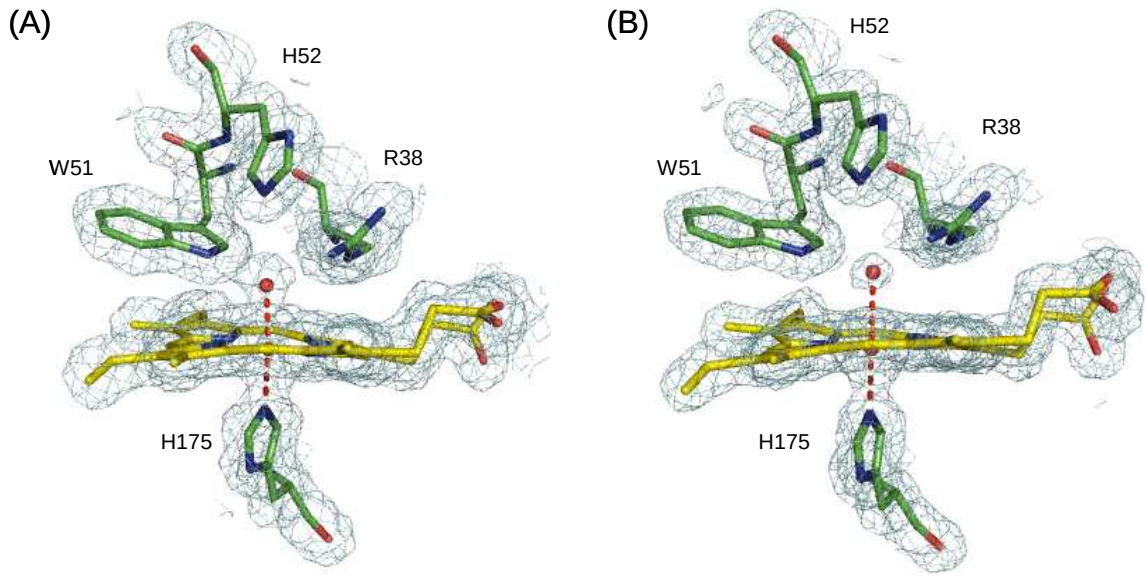


**Figure 2.11: The sixth axial ligand of the heme**

(A) The heme environment of Y36A/N184R/W191F (mutations not shown). The hydroxyl is bound to the iron at a distance of 2.19 Å; the proximal histidine is 2.07 Å from the heme and the distal histidine 3.25 Å from the hydroxyl group. $N^{\varepsilon 1}$ of the distal tryptophan is 2.56 Å from the hydroxyl and there is clear electron density between the two. (B) The heme environment of wild type C*c*P. The $6^{th}$ axial position is occupied by a water molecule which is 2.52 Å from the heme, the proximal histidine is 2.15 Å from the heme and the distal histidine 3.04 Å from the water.

There was no simple and direct correlation between the Fe-O distance and the spin state of the heme, this is due in part to the resolution of the crystal structures which does not allow an accurate assessment of this distance.

## *2.2.7 Transient state kinetics: reaction with $H_2O_2$*

The presence of any intermediates that accumulate during the reaction of C*c*P and its mutants with $H_2O_2$ was examined by multiple wavelength stopped-flow spectroscopy with the aid of Dr. Jaswir Basran. For the wild type protein, addition of a stoichiometric amount of $H_2O_2$ leads to a red shift of the Soret band (from 410 nm to 421 nm) and the formation of two new bands at 533 nm and 562 nm, Figure 2.12. This is consistent with Compound I formation in C*c*P [31] where a protein radical is seen. The time dependent spectral changes (Figure 2.13) can be fitted to a one step A→B model, in these experiments the observed rate constant for Compound I formation ($k_1$,obs) for wild type C*c*P was 62 $s^{-1}$.

The time dependent spectral changes for all mutants, except W191F, N184R/W191F and Y36A/W191F were also fitted to a one step (A→B) model, Figure 2.12(A). The spectral changes occurring upon reaction of W191F and N184R/W191F mutants with $H_2O_2$ were best fitted to a two step model (A→B→C); Figure 2.12(C) and 2.12(D)). In both mutants, Species B has maxima at 412 nm 543 nm and 656 nm and species C has maxima at 423 nm 535 nm and 565 nm. The W191F mutant has been shown to react with $H_2O_2$ to form an oxy-ferryl centre and a transient porphyrin π-cation radical [32] which rapidly decays back to a species with a similar spectra to Compound I where a protein radical is present. Spectral changes for the W191F mutant upon reaction with $H_2O_2$ are shown in Figure 2.12(C) where species B is predicted to be the transient porphyrin π-cation radical and species C an oxy-ferryl species with an undetermined protein radical. The rates of formation of species B and C were similar in both enzymes, ca. 75 $s^{-1}$ and 20 $s^{-1}$ respectively.

Two of the mutants, Y36A/N184R and Y36A/W191F, displayed very minor spectral changes when reacted with $H_2O_2$, Figure 2.12(F) and 2.12(G), respectively. For Y36A/W191F, the rate of Compound I formation could not be determined due to the small spectral change and that for Y36A/N184R was shown to be slow at 13 $s^{-1}$. This has been seen previously in other mutants of C*c*P [13, 27] and it is suggested that these mutants do not react stoichiometrically with $H_2O_2$ and that only a fraction of the enzyme is $H_2O_2$-reactive For Y36A/N184R and Y36A/W191F there were no further spectral changes even upon addition of a 10-fold excess of $H_2O_2$. The mutants that show this behaviour with $H_2O_2$ are also the mutants which have a ferric form with a higher proportion of 6-coordinate low spin character. The Y36A/N184R/W191F mutant, upon reaction with $H_2O_2$, does show weak spectral changes with maxima at 418 nm, 535 nm and 562 nm. The rate of Compound I formation in this mutant is 10-fold lower than that of wild type C*c*P ($k_{1,\,obs}$ = 6 $s^{-1}$).

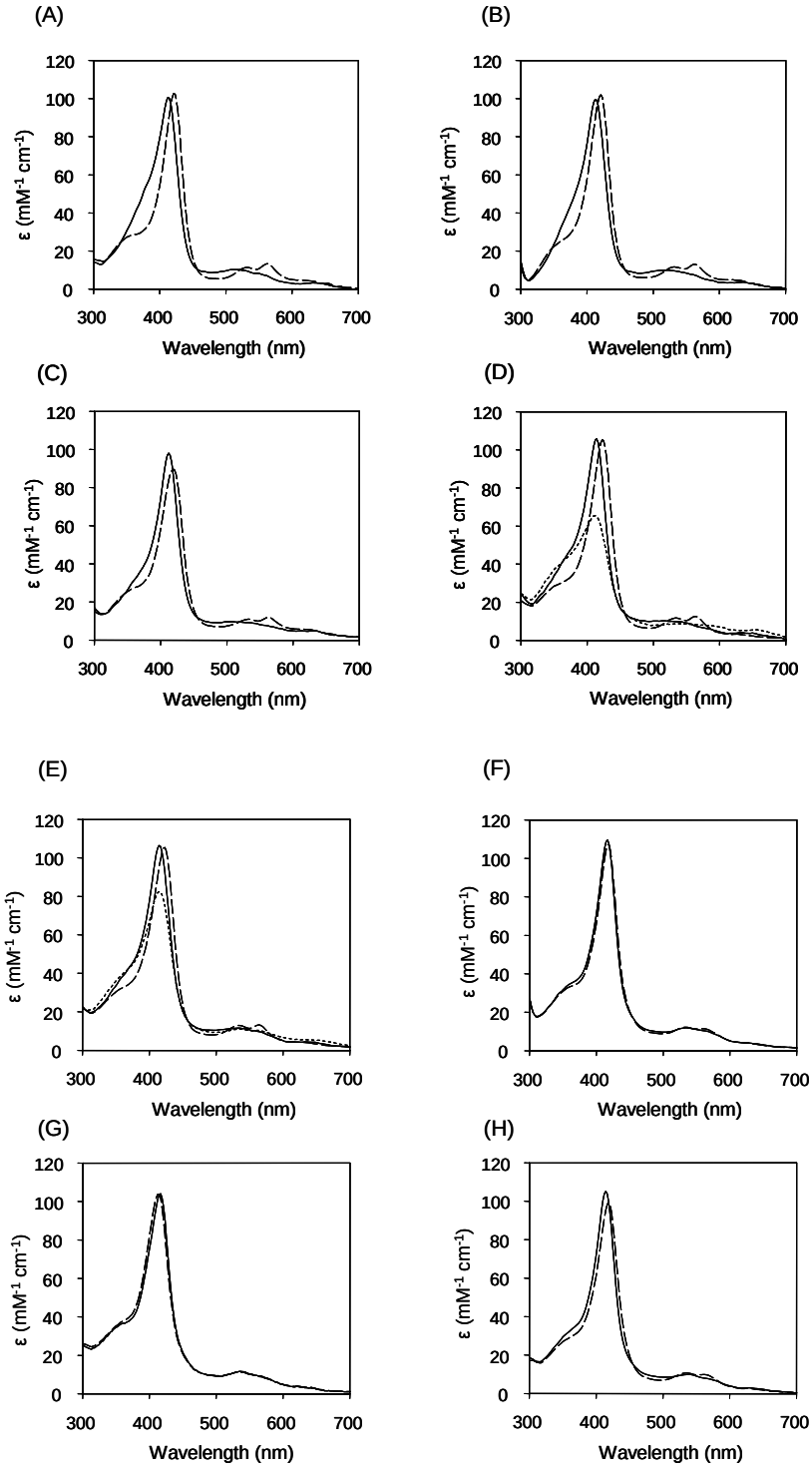


**Figure 2.12: Photodiode array spectra of the reaction of C*c*P with $H_2O_2$**

PDA spectra before addition of $H_2O_2$ (solid line) and after addition of $H_2O_2$ (dashed line). Time-dependent changes were fitted either to an A→B model or an A→B→C model, if intermediates were seen these are indicated by the dotted line. (A) Wild type C*c*P, (B) N184R, (C) Y36A, (D) W191F, (E) N184R/W191F, (F) Y36A/N184R, (G) Y36A/W191F, and (H) Y36A/N184R/W191F.

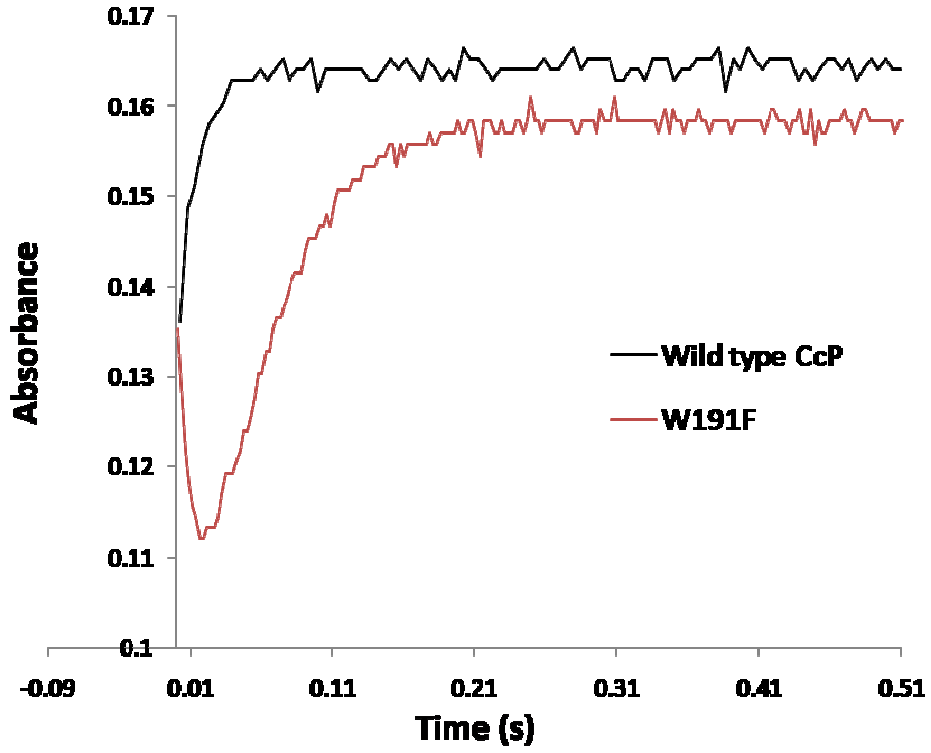


**Figure 2.13: Time dependent stopped flow traces for the reactions of C*c*P with $H_2O_2$**

The reaction of C*c*P with $H_2O_2$ was followed at 421 nm. For wild type C*c*P the reaction is best fitted to a one step (A→B) model. For the W191F and N184R/W191F variants the absorbance shows a rapid decrease as the porphyrin radical (A→B) is formed, followed by an increase as the radical is reduced by an internal electron donor (B→C).

## *2.2.8 Steady-state kinetics*

In order to assess the effects of the mutation on the function of C*c*P steady-state kinetics were carried out for three substrates: The physiological substrate cytochrome *c*; a small aromatic substrate thought to bind at the δ-heme edge, guaiacol; and the substrate that the mutants were engineered to oxidise, ascorbate. Table 2.3 shows data for the steady-state oxidation of these three substrates. For each case v/[E] was plotted against substrate concentration and the plot fitted to the Michaelis-Menten equation (Eq. 2.1) where [S] is a fixed substrate concentration, $v$ is the initial rate at a given substrate concentration, $V_{max}$ is the maximum velocity where enzyme is saturated with substrate and $K_M$ is the Michaelis constant which is the substrate concentration at which the enzyme reaches half of its maximum velocity.

$$\frac{v}{V_{max}} = \frac{[S]}{K_M + [S]} \qquad 2.1$$

**Table 2.3:** Steady-state kinetic parameters

Kinetic parameters for the oxidation of guaiacol ascorbate and cytochrome *c*, all assays were carried out in 0.1 M KPi buffer at pH 6.0 and 25 ºC.

| *Mutant* | *Guaiacol* | | *Ascorbate* | | *Cytochrome c* | |
|---|---|---|---|---|---|---|
| | $k_{cat}$ ($s^{-1}$) | $K_M$ (mM) | $k_{cat}$ ($s^{-1}$) | $K_M$ (mM) | $k_{cat}$ ($s^{-1}$) | $K_M$ (μM) |
| **Wild type C*c*P** | 4.1 ± 0.3 | 53 ± 6.0 | 0.83 ± 0.14 | 0.71 ± 0.22 | 1510 ± 259 | 93 ± 31 |
| **W191F** | 14 ± 0.6 | 57 ± 4.6 | 0.25 ± 0.01 | 0.45 ± 0.004 | 1.7 ± 0.13 | 100 ± 16 |
| **N184R** | 3.0 ± 0.1 | 27 ± 1.6 | 1.5 ± 0.10 | 1.7 ± 0.21 | 570 ± 40 | 140 ± 18 |
| **N184R/W191F** | 4.9 ± 0.2 | 34 ± 2.2 | 0.27 ± 0.01 | 0.31 ± 0.004 | 0.08 ± 0.01 | 670 ± 110 |
| **Y36A** | 5.4 ± 0.2 | 36 ± 3.1 | 1.3 ± 0.08 | 1.7 ± 0.19 | 580 ± 35 | 230 ± 28 |
| **Y36A/W191F** | 3.2 ± 0.2 | 45 ± 2.5 | 0.45 ± 0.06 | 0.50 ± 0.13 | 0.06 ± 0.01 | 160 ± 17 |
| **Y36A/N184R** | 0.9 ± 0.01 | 16 ± 0.7 | 0.66 ± 0.03 | 0.48 ± 0.06 | 600 ± 27 | 110 ± 10 |
| **Y36A/N184R/W191F** | 1.5 ± 0.1 | 14 ± 1.2 | 2.6 ± 0.35 | 1.3 ± 0.22 | 1.6 ± 0.13 | 300 ± 27 |

As expected and shown previously [32, 33], mutants that contained the W191F mutation had a markedly decreased ability to oxidise cytochrome *c*, Figure 2.14. This is due to disruption of the electron transfer pathway between the heme and cytochrome *c*. Mutants which did not contain the W191F mutation did not show a substantial difference in their ability to oxidise cytochrome *c*.

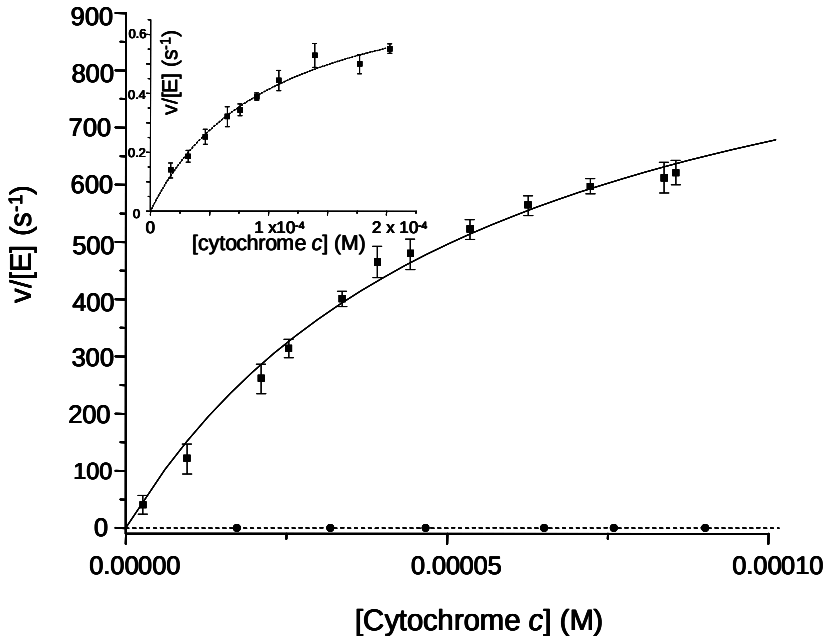


**Figure 2.14: Steady-state oxidation of cytochrome *c***

Wild type C*c*P (solid line) and W191F (dashed line). Reactions conditions were 0.1 M KPi, pH 6.0, 25 ºC, data were fitted to the Michaelis-Menten equation. The inset shows an expanded view of the steady-state oxidation of cytochrome *c* by W191F. Average values of three independent measurements are shown for each point; error bars represent the standard deviation.

Guaiacol oxidation was not significantly affected by any of the mutations, with relatively small differences seen in the derived steady state parameters. This is consistent with guaiacol binding at a separate site close to the δ-heme edge. Note that oxidation of guaiacol by W191F is also unaffected, also consistent with the availability a different electron transfer pathway for the oxidation of these types of aromatic substrate.

Ascorbate oxidation is measurable but slow for wild type C*c*P. A $k_{cat} = 0.83 \pm 0.14$ $s^{-1}$ was measured, Figure 2.15. Yonetani et al have reported a $k_{cat}$ of 3 $s^{-1}$ [14] however C*c*P oxidises two moles of substrate per mole of enzyme and so this value should be divided by two which would give a $k_{cat}$ of 1.5 $s^{-1}$, the measured $k_{cat}$ is therefore in reasonable agreement with the reported value. Oxidation of ascorbate was observed for all of the mutants; on the whole, however, the rates of oxidation are not markedly increased from those of wild type C*c*P, with the highest value of $k_{cat}$ observed for the Y36A/N184R/W191F mutant Figure 2.15, ($k_{cat} = 2.63 \pm 0.35$ $s^{-1}$). Despite the increase being very small, this variant does not have the preferred electron transfer pathway utilized during cytochrome *c* oxidation and so would be expected to have a lower $k_{cat}$ than wild type C*c*P if Trp191 was the only conduit for electron transfer. The fact that it has not shows that an electron transfer pathway potentially more like that utilized by APX has come into play.

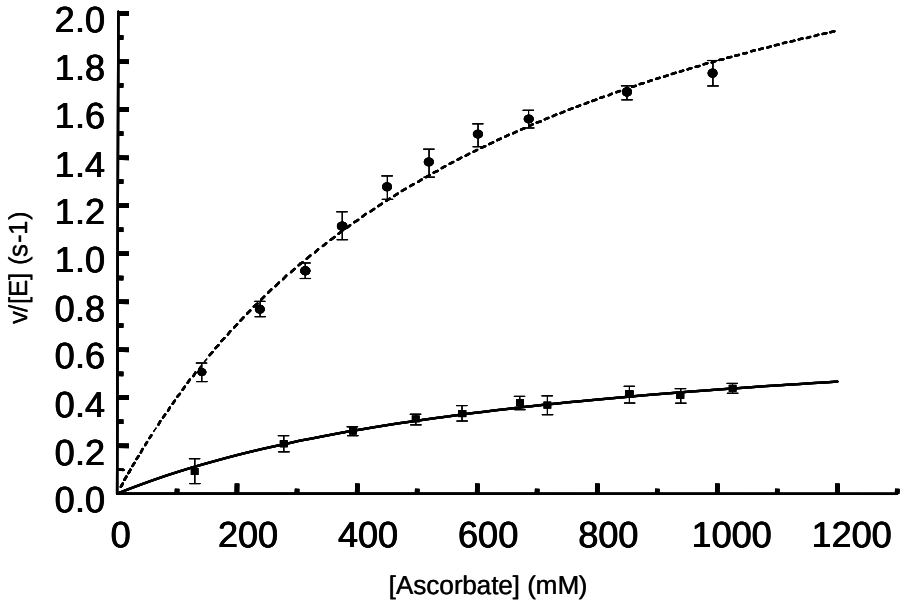


**Figure 2.15: Steady-state oxidation of L-ascorbate**

Wild type C*c*P (solid line) and Y36A/N184R/W191F (dashed line) (0.1 M KPi, pH 6.0, 25 ºC, data were fitted to the Michaelis-menten equation). Average values of three independent measurements are shown for each point; error bars represent the standard deviation.

## *2.2.9 Reactivity of the porphyrin π-cation intermediate with ascorbate*

The rates of ascorbate oxidation are similar for all of the mutants studied in this chapter despite the fact that mutants containing W191F are clearly capable of forming a porphyrin π-cation, this raises the question as to whether the reactive porphyrin π-cation intermediate might be competent for ascorbate oxidation under different conditions where its rapid decay was not observed (*i.e.* in the pre-steady state). In double mixing experiments with W191F and N184R/W191F, the initial formation of the transient porphyrin π-cation intermediate was observed on reaction of the ferric enzymes with $H_2O_2$. On addition of ascorbate in a second mixing event, conversion to the final product (*i.e.* B → C) occurred much faster than in the absence of ascorbate ($k_{2,\ obs}$ = 75 $s^{-1}$ even at low ascorbate compared to ~20 $s^{-1}$ in the absence of ascorbate), Figure 2.16(A). Oxidation of L-ascorbate by the W191F and N184R/W191F mutants of C*c*P was measured using the sequential mixing mode of the stopped-flow apparatus: C*c*P was mixed with $H_2O_2$ and formation of the porphyrin π-cation radical intermediate was allowed to proceed by aging the solution for 20 ms before mixing with ascorbate. In order to obtain a second-order rate constant for the conversion of the porphyrin π-cation radical intermediate form of Compound I to

Compound II ($k_2$), oxidation of ascorbate was monitored at 423 nm at a range of substrate concentrations. A linear dependence of $k_{2,\ obs}$ on L-ascorbate concentration was observed for both mutants between 100 and 1000 μM, Figure 2.16(B). The bimolecular rate constants ($k_2$) for oxidation of ascorbate are 1.1 x $10^5$ $M^{-1}$ $s^{-1}$ (W191F) and 1.0 x $10^5$ $M^{-1}$ $s^{-1}$ (N184R/W191F).

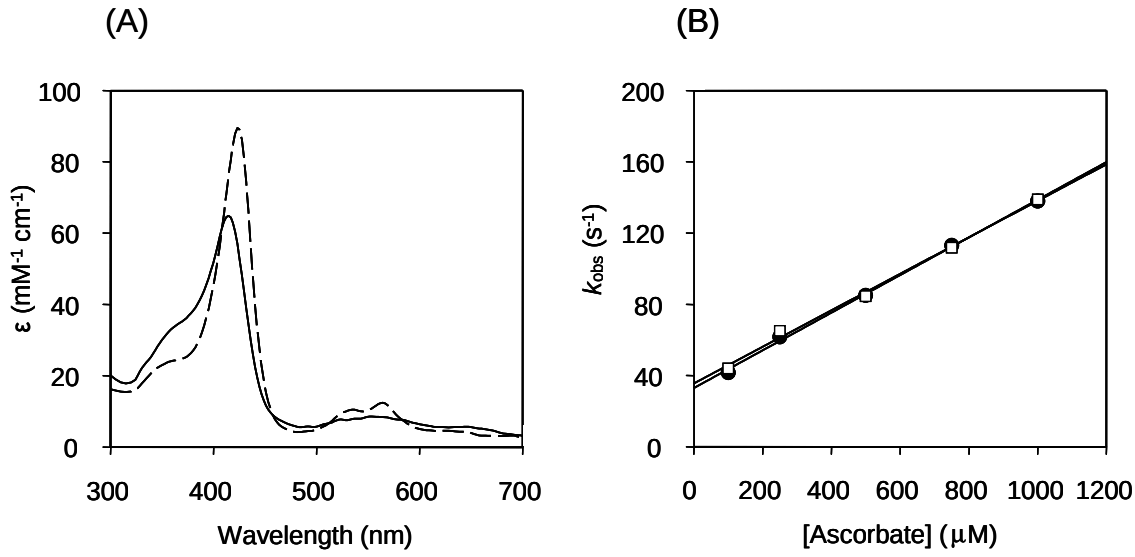


**Figure 2.16: Oxidation of ascorbate by the transient porphyrin π-cation intermediate**.

(A) Deconvoluted spectra for the reaction of the porphyrin π-cation intermediate with ascorbate. W191F 20 ms after reaction with $H_2O_2$ (solid line), after addition of ascorbate (dashed line). Data were fitted to a one step model (A → B). Conditions: 4 μM W191F C*c*P, 6 μM $H_2O_2$ (both cell concentrations) 100 mM KPi, pH 6.0 and premixed before reaction with ascorbate (500 μM). (B) Concentration dependence of the observed rate constant ($k_{2,\ obs}$) measured at 423 nm for ascorbate oxidation for W191F C*c*P (filled circles) and N184R/W191F C*c*P (open squares). All reactions performed at 10 °C.

These data indicate that in cases where a porphyrin π-cation intermediate forms it is indeed capable of ascorbate oxidation but that its decay under steady state conditions occurs much too rapidly for efficient turnover. An alternative mechanism for ascorbate oxidation must operate under steady state conditions, and this is the main route through which ascorbate oxidation occurs explaining why the $k_{cat}$ values for ascorbate oxidation are broadly similar for all mutants studied in this Chapter.

## 2.3 Discussion

Substrate binding across the family of heme peroxidases was initially thought to occur at the δ-heme edge [34-38]. This consensus was heavily influenced by early experiments using alkylhydrazines [39] and NMR [40, 41] and early crystal structures in which binding of aromatic substrates was observed close to the δ-heme edge. With the exception of the C*c*P-cytochrome *c* complex, which has an unusual substrate, and the MnP-$Mn^{2+}$ structure, which utilises the γ-heme edge [42], it was thought until recently that the δ-heme edge was *the* substrate binding location in peroxidases. It was only later, when other structures appeared (*e.g.* for the APX-ascorbate [11] and nitric oxide synthase-tetrahydrobiopterin (Chapter 1, Section 1.6.2) [43, 44] complexes appeared that also involved binding at the γ-heme edge, that it became clear that substrate oxidation at *both* the δ- and the γ-sites was possible. This allows the use of more than one electron transfer pathway and so oxidation of different *types* of substrate can be accommodated within the same structural framework, for example in APX where aromatic substrates and ascorbate binding occurs at different sites [11, 34]

C*c*P has an anomalous Compound I intermediate that is designed for rapid oxidation of its anomalously large substrate. Although it was known [14, 45] from very early on that C*c*P was also capable of oxidising aromatic substrates, the location of this binding site was not established crystallographically. It has been shown recently [46] that C*c*P binds the aromatic substrate isoniazid at the δ-heme edge (see Chapters 3 and 4); APX also binds isoniazid at this site, although the precise mode of binding varies slightly. This means that C*c*P is clearly capable of utilising a different substrate binding site in turn showing that a separate conduit for electron transfer, independent of that used for oxidation of cytochrome *c*, must be available. Although the details are not known, the fact that guaiacol and ascorbate oxidation are not affected by the mutation W191F, which drastically reduces cytochrome *c* oxidation rates, lends more credibility to the possibility of different electron transfer paths for different substrates.

In this Chapter a further binding mode has been shown for C*c*P at the γ-heme edge. With minimal structural changes at Tyr36 and Asn184 ascorbate has been shown to bind to C*c*P in precisely the same site as that observed for APX. The kinetic experiments carried out show that the triple mutant of C*c*P is functionally competent

for oxidation of the substrate at this site. From the crystallographic and kinetic data presented in this Chapter it is possible to conclude that C*c*P has a latent activity for ascorbate and since wild type C*c*P is known to be capable of ascorbate oxidation there must be a latent binding site for ascorbate.

A comparison of the kinetic parameters for ascorbate oxidation by the engineered C*c*P mutant (Y36A/N184R/W191F) and APX shows the mutant to be ~130 times less efficient in $k_{cat}/K_M$. This is a result of a combination of a ~30-fold lower $k_{cat}$ and a ~5-fold larger $K_M$ and so the necessary structural features of ascorbate binding as determined by the study of the APX-ascorbate structure are not sufficient to confer the function of the enzyme.

The nature of the radical in Compound I appears to be one of the most important factors in ascorbate oxidation by APX, the fact that APX utilises a porphyrin π-cation meaning that rapid electron transfer directly from ascorbate to the heme is possible is likely to be the reason for such a high $k_{cat}$ compared to that of C*c*P. Although W191F and N184R/W191F (and, presumably Y36A/N184R/W191F, although not under the conditions of our experiments) clearly form a porphyrin π-cation radical, as for APX, upon reaction with $H_2O_2$ the formation of this intermediate does not translate into high ascorbate activity in the steady state. Hence, the decay of the porphyrin π-cation species is much too rapid ($k_1 \approx 20$ $s^{-1}$ compared to $\approx 0.03$ $s^{-1}$ for APX) to support oxidation of the substrate ($k_{cat} \approx 1$ $s^{-1}$ compared to $\approx 80$ $s^{-1}$ for APX) in the steady state. Although the porphyrin π-cation intermediate is capable of ascorbate oxidation as seen by transient state kinetics the rapid decay of this radical competes with ascorbate oxidation meaning that steady state oxidation does not utilise the porphyrin π-cation radical. Hence, turnover of ascorbate cannot be sustained in the engineered triple mutant because decay of the transient porphyrin π-cation radical is much faster than the steady state rate of ascorbate oxidation. This is in contrast to the situation in APX, where decay of Compound I is much slower and is not competitive with steady state turnover.

It is the combination of efficient substrate binding, together with the formation of a suitably stable porphyrin π-cation radical, that seems to be the key to rapid substrate oxidation at the γ-heme edge. The importance of efficient electron transfer from Compound I has been indicated, however, $V_{max}$ and $K_M$ are also influenced by the second electron transfer from Compound II and in this case may be influenced by

hydrogen transfer to the ascorbate radical. Further transient state kinetic studies need to be carried out in order to determine the rate constants of all the steps in the reaction mechanism.

## 2.4 References


1. Poulos, T.L., Freer, S.T., Alden, R.A., Edwards, S.L., Skogland, U., Takio, K., Eriksson, B., Xuong, N.H., Yonetani, T., and Kraut, J., *Crystal structure of cytochrome c peroxidase.* J. Biol. Chem., 1980. **255**(2): 575-580.
2. Fishel, L.A., Villafranca, J.E., Mauro, J.M., and Kraut, J., *Yeast cytochrome c peroxidase: Mutagenesis and expression in E. coli Show Trp51 is not the radical site in Compound I.* Biochemistry, 1987. **26**(2): 351-360.
3. Sivaraja, M., Goodin, D.B., Smith, M., and Hoffman, B.M., *Identification by endor of Trp191 as the free-radical site in cytochrome c peroxidase compound ES.* Science, 1989. **245**(4919): 738-740.
4. Patterson, W.R., Poulos, T.L., and Goodin, D.B., *Identification of a porphyrin pi-cation-radical in ascorbate peroxidase Compound I.* Biochemistry, 1995. **34**(13): 4342-4345.
5. Lad, L., Mewies, M., Basran, J., Scrutton, N.S., and Raven, E.L., *Role of histidine 42 in ascorbate peroxidase - Kinetic analysis of the H42A and H42E variants.* Eur. J. Biochem., 2002. **269**(13): 3182-3192.
6. Lad, L., Mewies, M., and Raven, E.L., *Substrate binding and catalytic mechanism in ascorbate peroxidase: Evidence for two ascorbate binding sites.* Biochemistry, 2002. **41**(46): 13774-13781.
7. Patterson, W.R. and Poulos, T.L., *Crystal-structure of recombinant pea cytosolic ascorbate peroxidase.* Biochemistry, 1995. **34**(13): 4331-4341.
8. Macdonald, I.K., Badyal, S.K., Ghamsari, L., Moody, P.C.E., and Raven, E.L., *Interaction of ascorbate peroxidase with substrates: A mechanistic and structural analysis.* Biochemistry, 2006. **45**(25): 7808-7817.
9. Mittler, R. and Zilinskas, B.A., *Molecular-cloning and nucleotide-sequence analysis of a cDNA-encoding pea cytosolic ascorbate peroxidase.* FEBS Lett., 1991. **289**(2): 257-259.
10. Veitch, N.C. and Smith, A.T., *Horseradish peroxidase.* ADv. Inorg. Chem., 2001. **51**: 107-162.
11. Sharp, K.H., Mewies, M., Moody, P.C.E., and Raven, E.L., *Crystal structure of the ascorbate peroxidase-ascorbate complex.* Nat. Struct. Biol., 2003. **10**(4): 303-307.
12. Pearl, N.M., Vitello, L.B., and Erman, J.E., *Effect of charge-reversal mutations on the catalytic activity of cytochrome c peroxidase.* FASEB J., 2007. **21**(5): A272-A272.
13. Pearl, N.M., Jacobson, T., Arisa, M., Vitello, L.B., and Erman, J.E., *Effect of single-site charge-reversal mutations on the catalytic properties of yeast cytochrome c peroxidase: Mutations near the high-affinity cytochrome c binding site.* Biochemistry, 2007. **46**(28): 8263-8272.
14. Yonetani, T., and Ray, G. S, *Studies on cytochrome c peroxidase: purification and some properties.* J. Biol. Chem., 1965. **240**: 4503-4514.
15. Dalton, D.A., *Peroxidases in Chemistry and Biology (pp 139-154)*, ed. Everse J, Everse K. E, and M.B. Grisham. 1991, Boca Raton: CRC Press.
16. Pelletier, H. and Kraut, J., *Crystal-structure of a complex between electron-transfer partners, cytochrome c peroxidase and cytochrome c.* Science, 1992. **258**(5089): 1748-1755.

17. Metcalfe, C.L., Ott, M., Patel, N., Singh, K., Mistry, S.C., Goff, H.M., and Raven, E.L., *Autocatalytic formation of green heme: Evidence for $H_2O_2$-dependent formation of a covalent methionine-heme linkage in ascorbate peroxidase.* J. Am. Chem. Soc., 2004. **126**(49): 16242-16248.
18. Leslie, A.G.W., *Joint CCP4 + ESF-EAMCB Newsletter on Protein Crystallography.* 1992. **No. 26**.
19. Bailey, S., *The CCP4 Suite - Programs for protein crystallography.* Acta Crystallogr., Sect. D. Biol. Crystallogr., 1994. **50**: 760-763.
20. Finzel, B.C., Poulos, T.L., and Kraut, J., *Crystal structure of yeast cytochrome c peroxidase refined at 1.7 angstrom resolution.* J. Biol. Chem., 1984. **259**(21): 3027-3036.
21. Murshudov, G.N., Vagin, A.A., and Dodson, E.J., *Refinement of macromolecular structures by the maximum-likelihood method.* Acta Crystallogr., Sect. D. Biol. Crystallogr., 1997. **53**: 240-255.
22. Emsley, P. and Cowtan, K., *COOT: model-building tools for molecular graphics.* Acta Crystallogr., Sect. D. Biol. Crystallogr., 2004. **60**: 2126-2132.
23. Bryan, D.M., Pell, S.D., Kumar, R., Clarke, M.J., Rodriguez, V., Sherban, M., and Charkoudian, J., *Stable pentaammineruthenium(Iii) complexes of reductic acids - synthesis, linkage isomers, and autoxidation kinetics.* J. Am. Chem. Soc., 1988. **110**(5): 1498-1506.
24. Iizuka, T. and Yonetani, T., *Spin changes in hemoproteins.* Adv. Biophys., 1970. **1**: 157-182.
25. Smith, D.W. and Williams, R.J.P., *Analysis of the visible spectra of some sperm-whale ferrimyoglobin derivatives.* Biochem. J., 1968. **110**: 297-301.
26. Pond, A.E., Sono, M., Elenkova, E.A., Goodin, D.B., English, A.M., and Dawson, J.H., *Influence of protein environment on magnetic circular dichroism spectral properties of ferric and ferrous ligand complexes of yeast cytochrome c peroxidase.* Biospectroscopy, 1999. **5**(5): S42-S52.
27. Vitello, L.B., Erman, J.E., Miller, M.A., Mauro, J.M., and Kraut, J., *Effect of Asp-235-Asn Substitution on the Absorption-Spectrum and Hydrogen-Peroxide Reactivity of Cytochrome-C Peroxidase.* Biochemistry, 1992. **31**(46): 11524-11535.
28. Sievers, G., Gadsby, P.M.A., Peterson, J., and Thomson, A.J., *Assignment of the axial ligands of the heme in milk lactoperoxidase using magnetic circular-dichroism spectroscopy.* Biochim. Biophys. Acta, 1983. **742**(3): 659-668.
29. Smulevich, G., Miller, M.A., Kraut, J., and Spiro, T.G., *Conformational change and histidine control of heme chemistry in cytochrome c peroxidase - resonance Raman evidence from Leu52 and Gly181 mutants of cytochrome c peroxidase.* Biochemistry, 1991. **30**(39): 9546-9558.
30. Kobayashi, N., Nozawa, T., and Hatano, M., *Magnetic circular-dichroism studies on acid and alkaline forms of horseradish-peroxidase.* Biochim. Biophys. Acta, 1977. **493**(2): 340-351.
31. Coulson, A.F.W., Erman, J.E., and Yonetani, T., *Studies on cytochrome c peroxidase No.17: Stoichiometry and mechanism of reaction of compound ES with donors.* J. Biol. Chem., 1971. **246**(4): 917-&.
32. Miller, M.A., Vitello, L., and Erman, J.E., *Regulation of interprotein electron-transfer by Trp191 of cytochrome c peroxidase.* Biochemistry, 1995. **34**(37): 12048-12058.
33. Mauro, J.M., Fishel, L.A., Hazzard, J.T., Meyer, T.E., Tollin, G., Cusanovich, M.A., and Kraut, J., *Tryptophan-191-Phenylalanine, a Proximal-Side*

*Mutation in Yeast Cytochrome-C Peroxidase That Strongly Affects the Kinetics of Ferrocytochrome-C Oxidation.* Biochemistry, 1988. **27**(17): 6243-6256.

34. Sharp, K.H., Moody, P.C.E., Brown, K.A., and Raven, E.L., *Crystal structure of the ascorbate peroxidase-salicylhydroxamic acid complex.* Biochemistry, 2004. **43**(27): 8644-8651.
35. Henriksen, A., Schuller, D.J., Meno, K., Welinder, K.G., Smith, A.T., and Gajhede, M., *Structural interactions between horseradish peroxidase C and the substrate benzhydroxamic acid determined by X-ray crystallography.* Biochemistry, 1998. **37**(22): 8054-8060.
36. Henriksen, A., Smith, A.T., and Gajhede, M., *The Structures of the Horseradish Peroxidase C-Ferulic Acid Complex and the Ternary Complex with Cyanide Suggest How Peroxidases Oxidize Small Phenolic Substrates.* J. Biol. Chem., 1999. **274**(49): 35005-35011.
37. Itakura, H., Oda, Y., and Fukuyama, K., *Binding mode of benzhydroxamic acid to Arthromyces ramosus peroxidase shows by X-ray crystallographic analysis of the complex at 1.6 angstrom resolution.* FEBS Lett., 1997. **412**(1): 107-110.
38. Tsukamoto, K., Itakura, H., Sato, K., Fukuyama, K., Miura, S., Takahashi, S., Ikezawa, H., and Hosoya, T., *Binding of salicylhydroxamic acid and several aromatic donor molecules to Arthromyces ramosus peroxidase, investigated by X-ray crystallography, optical difference spectroscopy, NMR relaxation, molecular dynamics, and kinetics.* Biochemistry, 1999. **38**(39): 12558-12568.
39. Ator, M.A., David, S.K., and De Montellano, P.R.O., *Structure and catalytic mechanism of horseradish peroxidase: Regiospecific meso-alkylation of the prosthetic heme group by alkylhydrazines.* J. Biol. Chem., 1987. **262**(31): 14954-14960.
40. Hill, A.P., Modi, S., Sutcliffe, M.J., Turner, D.D., Gilfoyle, D.J., Smith, A.T., Tam, B.M., and Lloyd, E., *Chemical, spectroscopic and structural investigation of the substrate-binding site in ascorbate peroxidase.* Eur. J. Biochem., 1997. **248**(2): 347-354.
41. Mandelman, D., Jamal, J., and Poulos, T.L., *Identification of two electron-transfer sites in ascorbate peroxidase using chemical modification, enzyme kinetics, and crystallography.* Biochemistry, 1998. **37**(50): 17610-17617.
42. Sundaramoorthy, M., Kishi, K., Gold, M.H., and Poulos, T.L., *The crystal-structure of manganese peroxidase from Phanerochaete-Chrysosporium at 2.06 angstrom resolution.* J. Biol. Chem., 1994. **269**(52): 32759-32767.
43. Poulos, T.L., Li, H.Y., Raman, C.S., and Schuller, D.J., *Structures of gas-generating heme enzymes: Nitric oxide synthase and heme oxygenase.* ADv. Inorg. Chem., 2001. **51**: 243-293.
44. Wei, C.C., Crane, B.R., and Stuehr, D.J., *Tetrahydrobiopterin radical enzymology.* Chem. Rev., 2003. **103**(6): 2365-2383.
45. Chance, B., *Enzymes and enzyme systems* ed. J. Edsall, T. 1951, Cambridge, MA: Harvard University Press.
46. Metcalfe, C., Macdonald, I.K., Murphy, E.J., Brown, K.A., Raven, E.L., and Moody, P.C.E., *The tuberculosis prodrug isoniazid bound to activating peroxidases.* J. Biol. Chem., 2008. **283**(10): 6193-6200.

# Chapter 3

## *Isoniazid Binding in Peroxidases*

# 3.1 Introduction

As seen in Chapter 1, KatG is a catalase-peroxidase from *Mycobacterium tuberculosis* (*M. tuberculosis*) consisting of an N-terminal heme-binding domain and a C-terminal domain. *M. tuberculosis* KatG (*Mtb*KatG; KatG) has been the subject of intense research due to its ability to activate the prodrug, isonicotinic acid hydrazide (isoniazid; INH) which has been extensively used as a frontline chemotherapeutic to treat tuberculosis for many years [1]. The activation of INH by KatG involves removal of hydrazine from INH [2] to form the isonicotinoyl radical, which is then thought to react with the liberated hydrazine to form isonicotinamide (Figure 3.1). Isonicotinamide then reacts nonenzymatically with oxidized $NAD^+$ to generate isonicotinoyl-NAD [3], the active form of the drug. Isonicotinoyl-NAD interferes with the synthesis of mycolic acid, and in turn with bacterial cell wall synthesis, by binding to InhA, an enoyl-acyl carrier protein reductase, and blocking its NADH binding site [4].

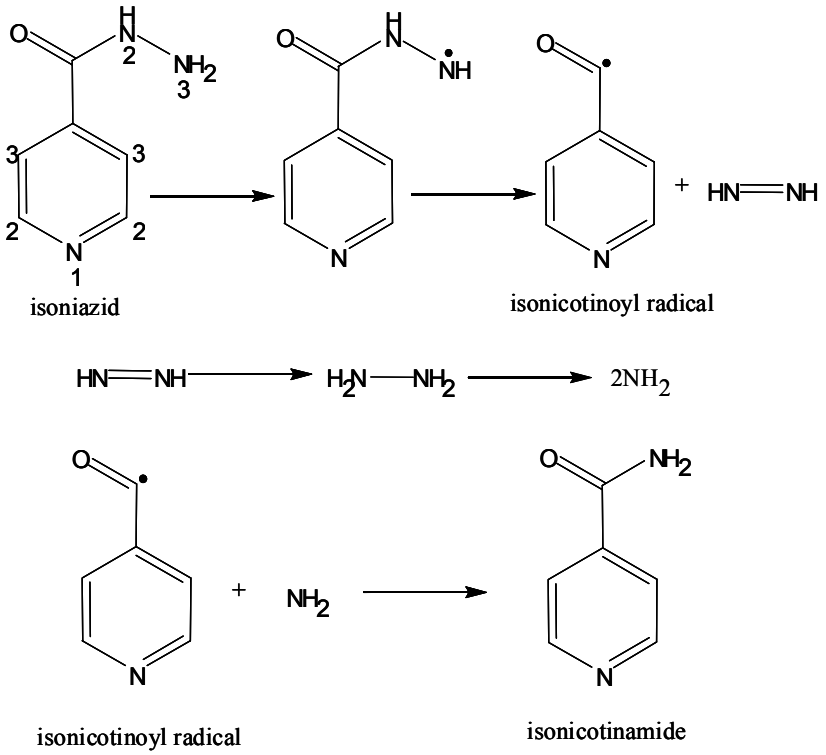


**Figure 3.1: The proposed catalytic mechanism of INH oxidation**

The oxidation of INH as carried out by class I peroxidases, the first stage is the formation of the isonicotinoyl radical which then goes on to react with the liberated hydrazine to form isonicotinamide.

The proposed mechanism requires the conversion of diazene to hydrazine, it is proposed that the diazene reaction intermediate may be stabilized in the active site of the enzyme by interactions with Trp-107 and Asp-137. Transformation of diazene to hydrazine and ammonia may involve deprotonation of the His-108 and Asp-137 side chains, however, chemically this reaction would be difficult to achieve and the mechanism proposed represents a "best guess" to date, further studies with KatG and other class I peroxidases is needed in order to fully elucidate the mode of INH activation.

More than eight million people are diagnosed with tuberculosis each year, with one quarter of cases being fatal [5]. The central role of KatG in INH activation is evident in the significant fraction of INH-resistant cases of tuberculosis attributable to mutations in KatG [6]. Despite the worldwide success of INH to treat tuberculosis very little is understood about INH activation by KatG or the effects of the drug when activated. The emergence of INH and multidrug-resistant strains of tuberculosis has highlighted the need for this fundamental lack of knowledge to be addressed.

As discussed previously (Chapter 1, Section 1.8.1.3), very little is known about the binding site of INH in KatG and the best evidence to date comes from an NMR model of INH bound to HRP [1]. In this Chapter the first crystal structures of INH bound to class I peroxidases, C*c*P and APX, are presented; both peroxidases are known to be activators of INH [1]. In addition, the crystal structures of INH bound to mutant forms of APX are presented which provide rationalization of isoniazid resistance in naturally occurring KatG mutant strains of *M. tuberculosis*. This work has been published in the Journal of Biological Chemistry [7].

# 3.2 Results

## *3.2.1 Expression and purification of CcP and APX*

C*c*P was expressed and purified as detailed in Chapter 2, Section 2.2.1. The C*c*P used in this Chapter is optimized for crystallisation and contains two mutations: Y39A and N184R. Samples of APX were prepared from *E. coli* SG 1300 supercompetent cells (containing the pREP4 vector) incorporating a pQE30-APX construct as described by Dalton et al [8]. APX enzyme was purified from the cells by

means of affinity chromatography using a $Ni^{2+}$-nitrilotriacetic acid (NTA) agarose column which retained the enzyme by means of six histidine residues on the C-terminal end of the protein (His-tag). The protein was eluted from the column by dropping the pH from pH 6.0 to pH 4.2 therefore weakening the ionic interactions between the enzyme and the column. Further purification was carried out by Fast Protein Liquid Chromatography (FPLC) (Superdex 75 gel filtration column). The purity of APX was determined by measuring Reinheitzal ($R_z$) values and polyacrylamide gel electrophoresis (SDS-PAGE), samples with an $R_z$ value of greater than two were considered pure. Protein was snap frozen using dry ice and ethanol and stored at -80 ºC.

### *3.2.2 Mutagenesis of APX*

Site-directed mutagenesis of the APX gene was performed according to the Quikchange™ protocol (Stratagene Ltd, Cambridge, UK). Mutations were confirmed by DNA sequencing as reported previously [9]. Two mutant forms of APX were prepared: W41A and H42A.

### *3.2.3 Crystallisation*

Crystals of C*c*P were prepared as detailed in Chapter 2, Section 2.2.3. Crystals of APX were prepared in 24-well plates using the sitting drop method at 19 ºC. Once grown, crystals of C*c*P were soaked in mother liquor saturated with INH for 5 minutes prior to rapid cooling to 100 K. APX crystals were soaked in mother liquor containing INH (100 mM) overnight before freezing in liquid nitrogen.

### *3.2.4 Data collection and refinement*

Data collection for the C*c*P-INH complex was collected in house as described for C*c*P crystals in Chapter 2, Section 2.2.4. Data for the APX-INH complexes including those using wild type, H42A and W41A mutants were collected at the European Radiation Synchrotron Facility (ESRF) (Grenoble, France) (Figure 3.2) using an ADSC Q4R detector on stations ID14-3 and ID14-1. All data were collected at 100 K.

Data were indexed, integrated and scaled using MOSFLM [10] and SCALA [11]. Data collection statistics are shown in Table 3.1. The structures were refined

from the 1.70 Å wild type C*c*P structure [12] (Protein data bank entry 2CYP); the 1.45 Å structure of APX-ascorbate complex (PDB entry 1OAF); or the 1.35 Å structure of the W41A mutant of APX [13] (PDB entry 2GGN). All refinement used REFMAC [14] from the CCP4 suite [11] and INH was incorporated into the last cycle of refinement. COOT [15] was used throughout for manual adjustment, ligand fitting and interpretation of the water structure.

**Table 3.1:** Data collection and refinement statistics for C*c*P-INH, APX-INH, W41A-INH, H42A and the H42A-INH complex

| Protein | C*c*P-INH | APX-INH | W41A-INH | H42A | H42A-INH Complex |
|---|---|---|---|---|---|
| **Data Collection** | | | | | |
| Space group | $P2_12_12_1$ | $P4_22_12$ | $P4_22_12$ | $P4_22_12$ | $P4_22_12$ |
| Unit Cell (Å) | | | | | |
| A | 51.15 | 82.24 | 82.13 | 82.074 | 81.74 |
| B | 75.13 | 82.24 | 82.13 | 82.074 | 81.74 |
| C | 106.86 | 74.97 | 75.16 | 75.224 | 74.94 |
| Resolution (Å) | 30.28-1.68 (1.77-1.68) | 27.11-1.80 (1.90-1.80) | 37.58-1.20 (1.26-1.20) | 27.72-1.70 (1.79-1.70) | 57.45 -2.00 (2.11-2.00) |
| Total observations | 129214 (1652) | 170464 (24801) | 732420 (82637) | 120973 (4889) | 177758 (24715) |
| Unique reflections | 38990 (1367) | 24461 (3497) | 78730 (11128) | 25015 (2264) | 17571 (2519) |
| $I/\sigma I$ | 27.4 (5.8) | 17.4 (4.7) | 17.2 (2.5) | 31.8 (3.7) | 19.4 (6.9) |
| $R_{merge}$ | 0.031 (0.133) | 0.091 (0.378) | 0.063 (0.687) | 0.038 (0.190) | 0.105 (0.394) |
| Completeness (%) | 81.9 (20.3) | 100 (100) | 97.9 (96) | 87.0 (54.9) | 100 (100) |
| **Refinement statistics** | | | | | |
| $R_{work}$ | 0.15601 | 0.15413 | 0.19422 | 0.16015 | 0.14508 |
| $R_{free}$ | 0.18034 | 0.18848 | 0.20917 | 0.21940 | 0.19058 |
| R.M.S.D | | | | | |
| Bonds (Å) | 0.010 | 0.012 | 0.007 | 0.011 | 0.014 |
| Angles (°) | 1.157 | 1.234 | 1.151 | 1.235 | 1.354 |

**Figure 3.2: The European Synchrotron Radiation Facility, Grenoble, France**

All work on the W41A APX mutant including protein preparation, data collection and refinement was carried out by Dr. Sandip Badyal and Dr. Clive Metcalfe. Data collection and refinement of the wild type C*c*P-INH complex and the wild type APX-INH complex were carried out by Dr. Clive Metcalfe.

### *3.2.5 Crystal structures of INH bound to peroxidases; CcP and APX*

The δ-heme edge has been shown to be the binding site of aromatic substrates in class I peroxidases by a variety of experimental methods as discussed in Chapter 4. The class I peroxidases share many structural features and the hydrophobic distal heme pocket is shown to be almost identical across the class. Figure 3.3 compares the architecture of this site for APX, C*c*P and KatG.

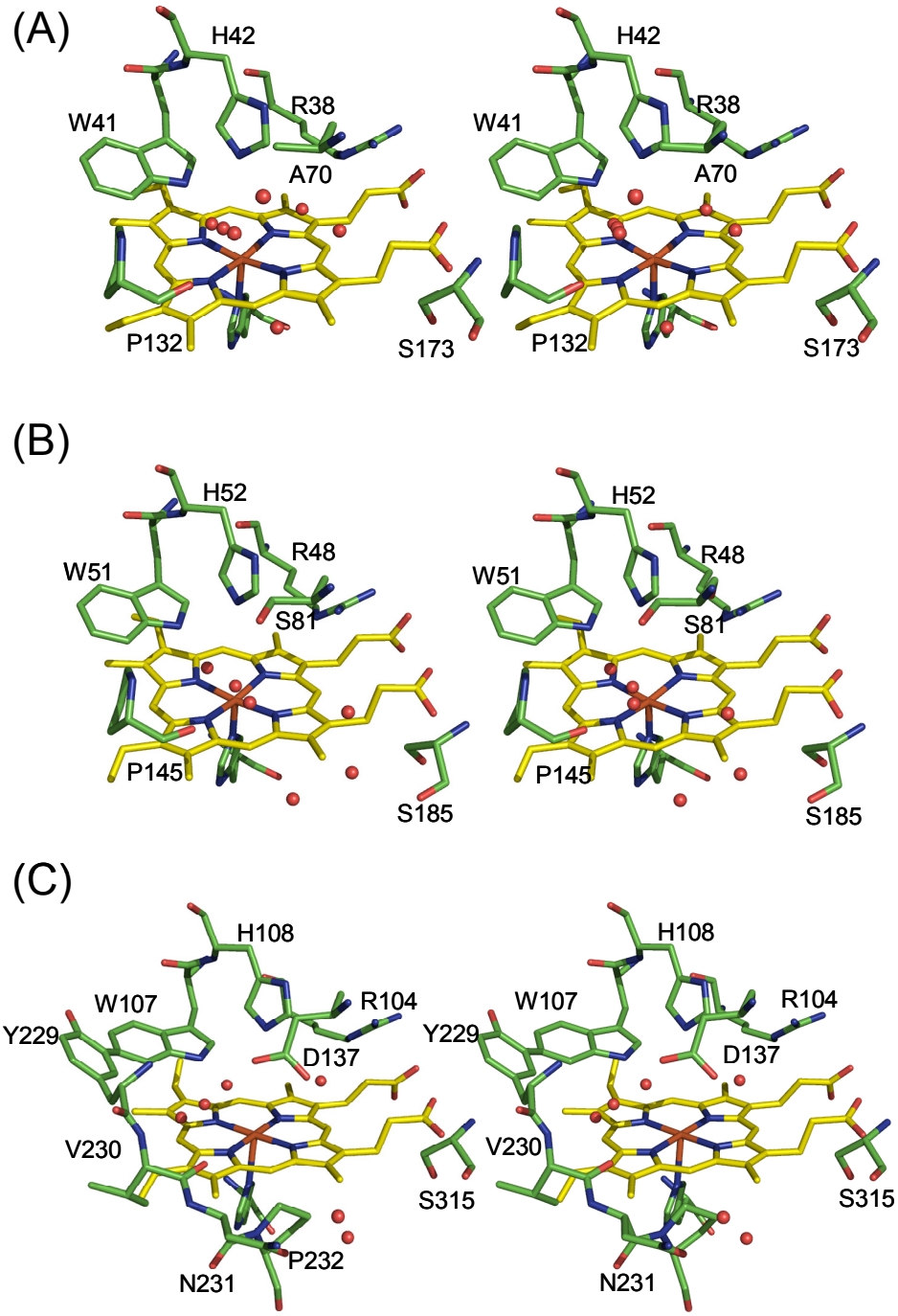


**Figure 3.3: Stereo representations of the δ-heme edge of class I peroxidases**

Stereo representations of the crystal structures of APX, C*c*P and KatG; (A) The heme region of APX; (B) the heme region of C*c*P and; (C) the heme region of KatG. The heme is shown in yellow and water molecules are represented by red spheres.

The structure of the distal heme pocket in APX (Figure 3.3(A)) is defined by residues Pro132, Ser173, Arg38, Trp41 and His42, with the "bottom" of the pocket being defined by the pyrrole ring IV of the heme group. The δ-heme edge is open to

the solvent forming a channel which allows substrate access to the binding site. The distal heme pocket of C*c*P (Figure 3.3(B) is almost identical to that of APX, with the defining residues being Pro145, Ser185, Arg48, Trp51 and His52.

The hydrophobic binding pocket of KatG (Figure 3.3(C)) is very similar to that of APX and C*c*P, with Arg104, Trp107, His108 and Ser315 defining the upper part of the pocket. However, unlike in APX and C*c*P, KatG contains a Trp-Tyr-Met covalent cross-link adduct in the vicinity of the distal heme pocket. The role of this adduct remains unclear, although it is thought to provide protection against oxidative damage [16].

The structures of the distal pocket in APX, C*c*P and KatG reveal the presence of ordered water molecules, hydrogen bonded within the pocket and leading out into the bulk solvent. The similarity of the sites suggests that the binding mode of INH and the mechanism of its activation will likewise be similar for all three enzymes.

### *3.2.5.1 The crystal structure of the CcP-INH complex*

The crystal structure of the C*c*P-INH complex shows INH bound at the δ-heme edge, in place of the four water molecules seen within the hydrophobic binding pocket of C*c*P (Figure 3.4). The orientation of INH allows a hydrogen bond between N2 of the substrate and the backbone carbonyl of Pro145 (2.84 Å). The carbonyl oxygen of the substrate is 2.93 Å from the side chain of Arg48 and forms a hydrogen bond with the $NH_2$ group. The INH pyridinyl nitrogen hydrogen bonds to a water molecule, which is in turn hydrogen bonded to Ser185 and another water molecule leading out to bulk solvent. The guanidinium group of Arg48 swings out to accommodate the substrate (Cζ moves by 2 Å) and displaces a further water molecule. The position of INH is similar to the NMR derived model [1], however the crystal structure is inconsistent with a hydrogen bond predicted between the conserved distal tryptophan (Trp51) and N3 of INH.

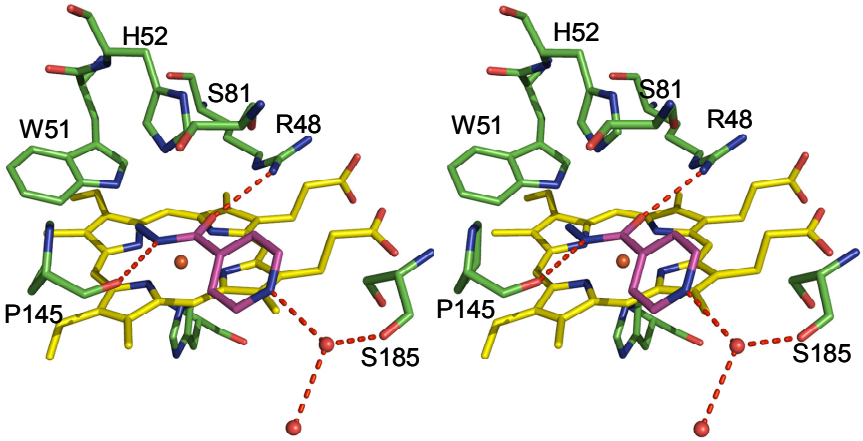


**Figure 3.4: Crystal structure of the C*c*P-INH complex**

Stereo representation of the δ-heme edge hydrophobic binding pocket of the C*c*P-INH complex. The heme group is shown in yellow with residues forming interactions with bound INH (purple) indicated. Hydrogen bonding interactions are shown as red dashes and water molecules are represented by red spheres (PDB entry 2V2E).

### *3.2.5.2 The crystal structure of the APX-INH complex*

Like the structure of the C*c*P-INH complex, the structure of the APX-INH complex shows INH bound in the hydrophobic pocket at the δ-heme edge, Figure 3.5.

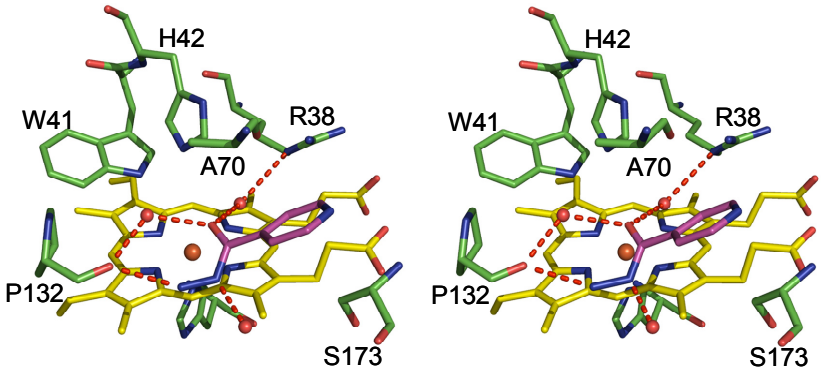


**Figure 3.5: Crystal structure of the APX-INH complex**

Stereo representation of the δ-heme edge hydrophobic binding pocket of the APX-INH complex. The heme group is shown in yellow with residues forming interactions with bound INH (purple) indicated. Hydrogen bonding interactions are shown as red dashes and water molecules are represented by red spheres (PDB entry 2VCF).

In the APX-INH complex, the INH is rotated through approximately 90° compared to the orientation in C*c*P and the predicted APX-INH model [1]. The

pyridine ring of INH is positioned directly over Ser173 and the substrate is held in position *via* three hydrogen bonds, two of which are to the same residues that are used to bind INH in C*c*P. The main chain carbonyl of Pro132 hydrogen bonds to N3 of the INH, the carbonyl oxygen of INH hydrogen bonds *via* a water molecule to the $N_{\varepsilon}$ group of Arg48 and the N2 of INH is hydrogen bonded to a water molecule.

The electron density maps of INH soaked APX also show density consistent with a second INH molecule bound within the ascorbate binding pocket at the γ-heme edge, which has previously been identified as the primary site of catalysis within the enzyme [17] (Figure 3.6).

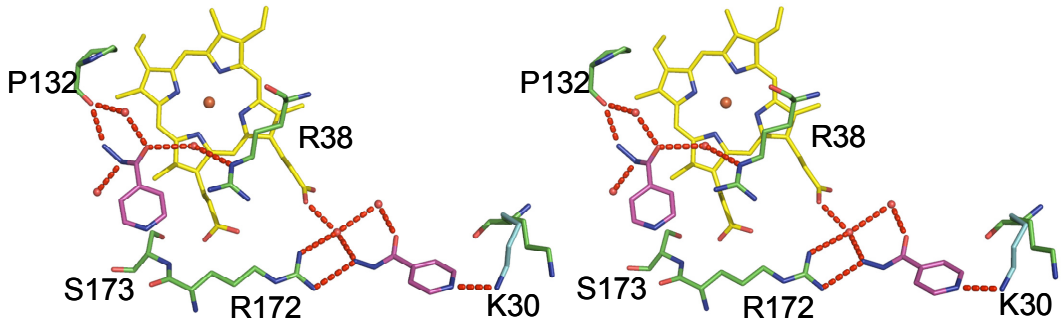


**Figure 3.6: Crystal structure of INH bound at the γ-heme edge**

Stereo representation of the crystal structure of the APX-INH complex, the second binding site for INH at the γ-heme edge is shown. The heme is shown in yellow with hydrogen bonds indicated by red dashes. Water molecules are represented by red spheres. Protein residues are shown in green, the movement of the side chain of Lys30 is shown with its position in the APX-INH complex in cyan. (PDB entry 2VCF).

The INH molecule binds in place of five well ordered water molecules which occupy the pocket in the absence of ascorbate (see Chapter 2). The $NH_2$ group of INH forms two hydrogen bonds, one to the side chain of Arg172 and one *via* a water molecule to the heme 6-propionate. The flexible Lys30 also partially swings in from solvent to form a hydrogen bond to N1 of INH. Movement of Lys30 on binding of ascorbate has also been observed [17]. As previously discussed (Chapters 1 and 2) the role of the heme propionates has, traditionally, been believed to be in stabilising the

heme prosthetic group within the protein structure. The data presented in this Chapter add to the growing evidence that the propionates may also play an active role and, for the first time, that the γ-heme edge might also be capable of binding aromatic substrates.

### *3.2.6 The role of point mutations in INH resistance*

A major problem in treating tuberculosis is resistance to the clinically effective drugs Rifampicin and INH. Various point mutations of KatG have been identified in INH-resistant strains [18] with one of the mutation hotspots being Ser315 (mutated to asparagine, isoleucine, arginine, glycine but most commonly threonine [19-21]. Ser315 is conserved in both C*c*P and APX as Ser185 and Ser173 respectively. In the C*c*P-INH structure the Cα of Ser185 is approximately 4.0 Å from the aromatic ring of INH and in sAPX the Cβ of Ser173 is approximately 3.8 Å away and located directly below it. All of these mutations would introduce considerably more steric bulk than serine thereby placing the side chain of the mutated residue at position 315 closer than allowed van der Waal's contact distances, blocking the binding of the INH molecule. These observations are consistent with predictions that these mutations produce a steric interference to INH binding [22].

Active site residues His108 and Ala110 are also frequently mutated in KatG sequenced from isolates demonstrating resistance to INH [23, 24]. Mutation of active site residues of peroxidases have been shown [13] to introduce conformational mobility into the distal cavity possibly promoting alternative inhibitive INH binding orientations. In order to probe this, the structures of INH bound to two active site mutations of APX (W41A and H42A) were determined.

#### *3.2.5.3 The crystal structure of the H42A-INH complex*

As for the wild type APX-INH structure, INH binds at δ-heme edge of the H42A mutant of APX, however the structure of the H42A-INH complex reveals a different binding orientation of INH within the distal cavity (Figure 3.7).

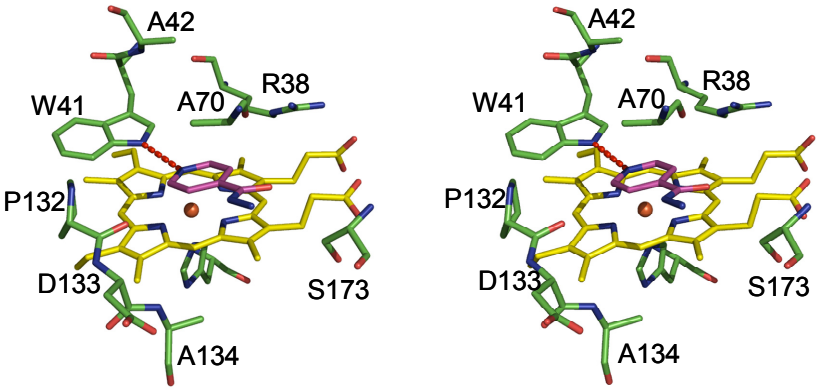


**Figure 3.7: Crystal structure of the H42A-INH complex**

Stereo representation of the crystal structure of INH (purple) bound at the δ-heme edge of the H42A mutant of APX. The heme group is shown in yellow with hydrogen bonds indicated as red dashes. (PDB entry 2VCS).

In the H42A-INH complex INH is rotated 90° anticlockwise compared to the orientation of INH in wild type APX. The removal of His42 creates enough space for the aromatic ring of INH to sit directly above the iron and hydrogen bond through N1 to the indole NH of Trp41. This provides evidence that Trp41 influences coordination to the heme iron, and although the cavity in APX-H42A can contain the INH molecule, the steric clash with Trp41 prevents coordination. Kinetic studies show no INH turnover by the H42A mutant of APX; however it has been previously shown that peroxidase activity in this mutant [25] is severely reduced. A reduction in INH activation is consistent with the observation of INH resistance in H108X mutations of KatG.

### *3.2.5.4 The crystal structure of the W41A-INH complex*

Removal of the distal tryptophan in the W41A mutant of APX opens up the distal cavity and imparts a degree of conformational mobility within the distal cavity [13]. The crystal structure of the W41A-INH complex shows a molecule of INH occupying the hydrophobic pocket in an identical position to that found in the wild type APX-INH complex. A second INH molecule is also seen coordinated directly to

the heme iron through the $NH_2$ of the acyl hydrazide, with the aromatic ring occupying the pocket created by removal of the indole of Trp41 (Figure 3.8).

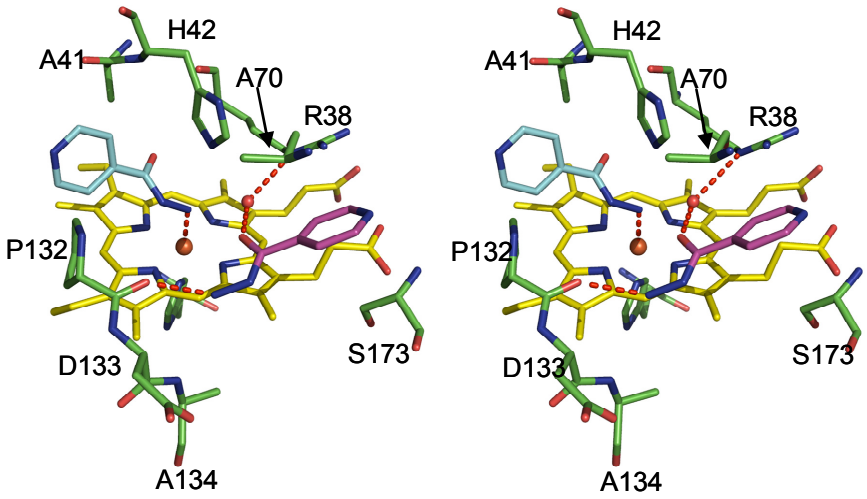


**Figure 3.8: Crystal structure of the W41A-INH complex**

Stereo representation of the crystal structure of the W41A-INH complex showing the distal heme binding pocket. Two molecules of INH are seen bound (one cyan, one purple), the heme is shown in yellow with hydrogen bonds indicated by red dashes and red spheres representing water molecules. (PDB entry 2VCN).

The mode of binding of the second molecule of INH (shown in cyan in Figure 3.8) has been seen previously [26] in APX for aromatic acids such as salicylhydroxamic acid (SHA), which is an inhibitor of APX peroxidase activity. However, coordination of INH to the iron is only possible when an additional pocket is created in the W41A mutant, whereas coordination of SHA is possible with W41 *in situ* [26]. This is because SHA forms a hydrogen bond between its iron coordinating O and the NH of Trp41. However INH has an $NH_2$ group coordinated to the iron which is unable to hydrogen bond to the NH of Trp41, furthermore its bulk would also result in a steric clash (Figure 3.9). The removal of Trp41 allows the INH to move around through 90° to coordinate to the iron without this steric conflict.

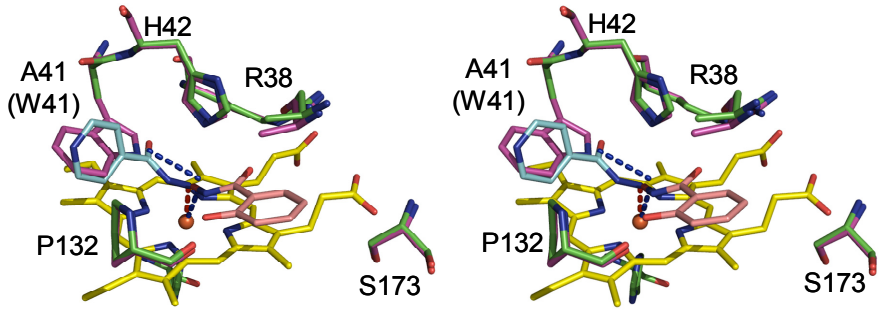


**Figure 3.9: Comparison of INH and SHA binding in the W41A mutant of APX**

Stereo representaion of an overlay of the crystal structures of the APX-SHA complex (PDB entry 1V0H) (purple) and W41A-INH complex (green), INH is shown in cyan with SHA shown in salmon pink. Residues are labeled, with those for wild type APX in parenthesis. Red dashes indicate interactions between INH and APX and blue dashes indicate interactions between SHA and APX.

Kinetic studies show that INH becomes an inhibitor of W41A peroxidase activity, determined by competition with guaiacol ($k_{cat}$ for guaiacol oxidation is 98.3 ± 12 $s^{-1}$ in the absence of INH compared to 5.0 ± 0.04 $s^{-1}$ in the presence of 50 mM INH (data not shown)). These observations are consistent with the structure of W41A-INH which shows INH bound directly to the heme iron, thus in solution the reaction of the enzyme with $H_2O_2$ is blocked by preventing the formation of the Compound I intermediate (by a mechanism similar to that proposed for SHA [26]).

## 3.3 Discussion

The structures presented in this Chapter provide unambiguous structural evidence for the location of INH binding in the class I peroxidases C*c*P and APX, supporting earlier evidence that aromatic binding in class I peroxidases occurs at the δ-heme edge, as discussed further in Chapter 4. The similarity of the structures of C*c*P and APX with KatG allow expansion of the previous predictions of prodrug activation in KatG [1].

Previous mechanistic studies have proposed a KatG-catalyzed activation mechanism which involves splitting of the C-N bond of the hydrazide moiety of INH yielding a diazene which is stabilized by Asp137 (Figure 3.10) [1, 27].

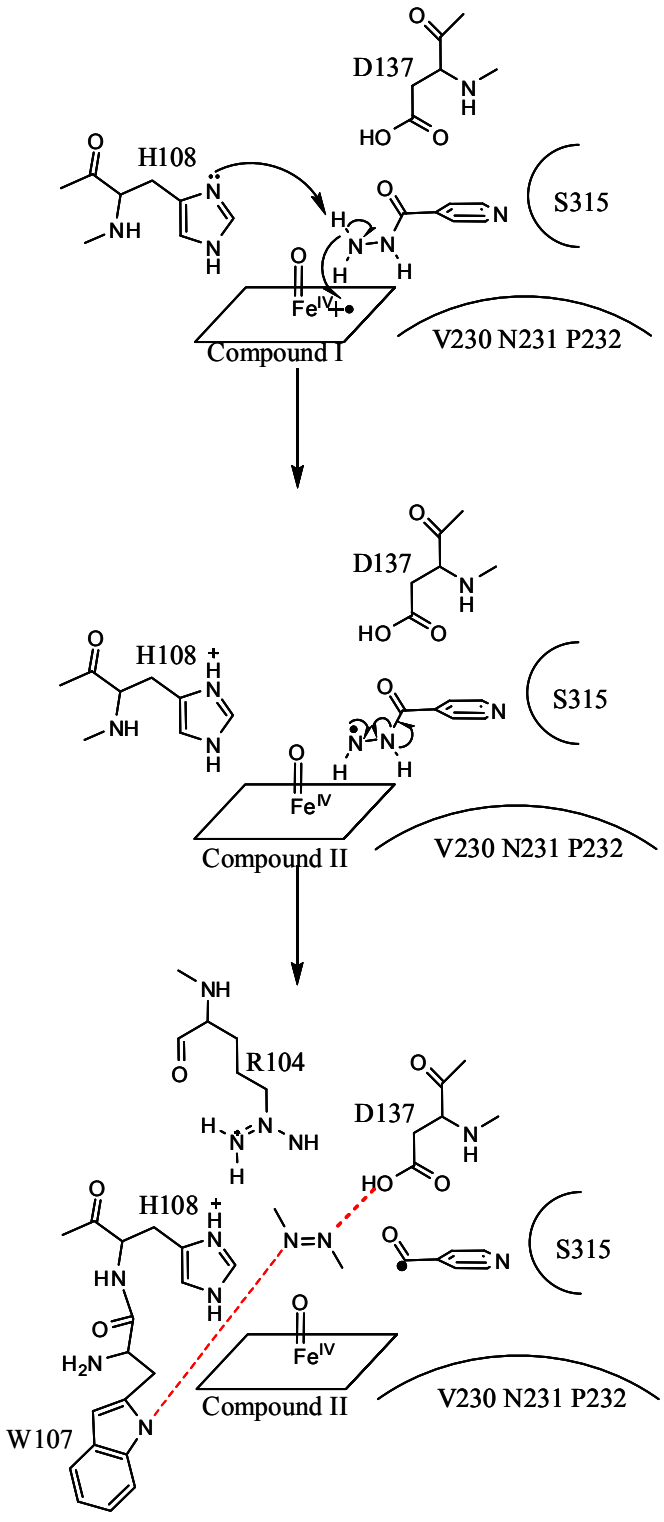


**Figure 3.10: A proposed catalytic mechanism of INH activation by KatG**

The active site residues of KatG which are proposed to be involved in the catalytic mechanism of INH oxidation [7]. Possible stabilising interactions are indicated by red dashed lines and the heme is represented as a rhombus. The equivalent residues in C*c*P and APX are as follows: R104 ≡ R48, R38; W107 ≡ W51, W41; H108 ≡ H52, H42; D137 ≡ S81, A70. D137 of KatG is thought to play a major role in stabilising the catalytic intermediate of INH oxidation.

In *M. tuberculosis* KatG the acid group of Asp137 is predicted to be located directly above the carbonyl of INH and is ideally orientated to provide a stabilizing acid/base interaction with the reacting INH. However, in C*c*P and APX, Asp137 is replaced with Ser81 and Ala70, respectively; Ser81 could still offer some rudimentary stabilization for the activated INH whereas this is unlikely with Ala70. This hypothesis is supported by the relative reaction rates of INH oxidation, KatG>>C*c*P>APX [1].

The binding modes of INH seen in the APX mutants in this Chapter are subtly different for those found in the wild type class I peroxidases, comparison of the way INH binds at the δ-heme edge in these mutants has lead to the identification of three separate modes of drug resistance in naturally occurring INH resistant strains of *Mycobacterium tuberculosis*. These being: steric hindrance of the δ-heme edge INH binding site; direct binding to the heme iron (and consequent inhibition of Compound I formation); and the loss of peroxidatic activity due to the mutation of essential catalytic residues.

The work presented in this Chapter has lead to a broader understanding of aromatic substrate binding and activation in the heme peroxidases and has added to the wealth of evidence that aromatic substrates bind and are oxidised at the δ-heme edge. Single point mutations can dramatically alter substrate binding and oxidation, indicating that the sites may be more promiscuous than previously thought. In addition the crystal structure of an aromatic substrate binding at the γ-heme edge has been presented, this strengthens the idea that that substrate oxidation can occur at *both* the δ- and γ-heme edges, which, as discussed in Chapter 2, allows the use of more than one electron transfer pathway.

## 3.4 References


1. Pierattelli, R., Banci, L., Eady, N.A.J., Bodiguel, J., Jones, J.N., Moody, P.C.E., Raven, E.L., Jamart-Gregoire, B., and Brown, K.A., *Enzyme-catalyzed mechanism of isoniazid activation in class I and class III peroxidases.* J. Biol. Chem., 2004. **279**(37): 39000-39009.
2. Zhang, Y., Heym, B., Allen, B., Young, D., and Cole, S., *The Catalase peroxidase gene and isoniazid resistance of Mycobacterium tuberculosis.* Nature, 1992. **358**(6387): 591-593.
3. Johnsson, K., King, D.S., and Schultz, P.G., *Studies on the mechanism of action of isoniazid and ethionamide in the chemotherapy of tuberculosis.* J. Am. Chem. Soc., 1995. **117**(17): 5009-5010.
4. Rozwarski, D.A., Grant, G.A., Barton, D.H.R., Jacobs, W.R., and Sacchettini, J.C., *Modification of the NADH of the isoniazid target (InhA) from Mycobacterium tuberculosis.* Science, 1998. **279**(5347): 98-102.
5. Vallanjohn, M. in *World Health Organisation, Reports on Infectious Diseases*. 2002. Geneva.
6. Johnsson, K. and Schultz, P.G., *Mechanistic studies of the oxidation of isoniazid by the catalase peroxidase from Mycobacterium tuberculosis.* J. Am. Chem. Soc., 1994. **116**(16): 7425-7426.
7. Metcalfe, C., Macdonald, I.K., Murphy, E.J., Brown, K.A., Raven, E.L., and Moody, P.C.E., *The tuberculosis prodrug isoniazid bound to activating peroxidases.* J. Biol. Chem., 2008. **283**(10): 6193-6200.
8. Dalton, D.A., *Peroxidases in Chemistry and Biology (pp 139-154)*, ed. Everse J, Everse K. E, and M.B. Grisham. 1991, Boca Raton: CRC Press.
9. Metcalfe, C.L., Ott, M., Patel, N., Singh, K., Mistry, S.C., Goff, H.M., and Raven, E.L., *Autocatalytic formation of green heme: Evidence for $H_2O_2$-dependent formation of a covalent methionine-heme linkage in ascorbate peroxidase.* J. Am. Chem. Soc., 2004. **126**(49): 16242-16248.
10. Leslie, A.G.W., *Joint CCP4 + ESF-EAMCB Newsletter on Protein Crystallography.* 1992. **No. 26**.
11. Bailey, S., *The CCP4 Suite - Programs for protein crystallography.* Acta Crystallogr., Sect. D. Biol. Crystallogr., 1994. **50**: 760-763.
12. Finzel, B.C., Poulos, T.L., and Kraut, J., *Crystal structure of yeast cytochrome c peroxidase refined at 1.7 angstrom resolution.* J. Biol. Chem., 1984. **259**(21): 3027-3036.
13. Badyal, S.K., Joyce, M.G., Sharp, K.H., Seward, H.E., Mewies, M., Basran, J., Macdonald, I.K., Moody, P.C.E., and Raven, E.L., *Conformational mobility in the active site of a heme peroxidase.* J. Biol. Chem., 2006. **281**(34): 24512-24520.
14. Murshudov, G.N., Vagin, A.A., and Dodson, E.J., *Refinement of macromolecular structures by the maximum-likelihood method.* Acta Crystallogr., Sect. D. Biol. Crystallogr., 1997. **53**: 240-255.
15. Emsley, P. and Cowtan, K., *COOT: model-building tools for molecular graphics.* Acta Crystallogr., Sect. D. Biol. Crystallogr., 2004. **60**: 2126-2132.
16. Bhaskar, B., Lad, L., and Poulos, T., *Iron: heme proteins, peroxidases, catalases and catalase-peroxidases.* Encyclopedia of Inorganic Chemistry, 2006.

17. Sharp, K.H., Mewies, M., Moody, P.C.E., and Raven, E.L., *Crystal structure of the ascorbate peroxidase-ascorbate complex.* Nat. Struct. Biol., 2003. **10**(4): 303-307.
18. Heym, B., Alzari, P.M., Honore, N., and Cole, S.T., *Missense mutations in the catalase-peroxidase gene, KatG, are associated with isoniazid resistance in Mycobacterium tuberculosis.* Mol. Microbiol., 1995. **15**(2): 235-245.
19. Marttila, H.J., Soini, H., Eerola, E., Vyshnevskaya, E., Vyshnevskiy, B.I., Otten, T.F., Vasilyef, A.V., and Viljanen, M.K., *A Ser315Thr substitution in KatG is predominant in genetically heterogeneous multidrug-resistant Mycobacterium tuberculosis isolates originating from the St. Petersburg area in Russia.* Antimicrob. Agents Chemother., 1998. **42**(9): 2443-2445.
20. Haas, W.H., Schilke, K., Brand, J., Amthor, B., Weyer, K., Fourie, P.B., Bretzel, G., Stichtgroh, V., and Bremer, H.J., *Molecular analysis of katG gene mutations in strains of Mycobacterium tuberculosis complex from Africa.* Antimicrob. Agents Chemother., 1997. **41**(7): 1601-1603.
21. Kohner, P., Uhl, J., Kolbert, C., Persing, D., and Cockerill, F., *Comparison of susceptibility testing methods with mecA gene analysis for determining oxacillin (methicillin) resistance in clinical isolates of Staphylococcus aureus and coagulase-negative Staphylococcus spp.* J. Clin. Microbiol., 1999. **37**(9): 2952-2961.
22. Kapetanaki, S., Chouchane, S., Girotto, S., Yu, S.W., Magliozzo, R.S., and Schelvis, J.P.M., *Conformational differences in Mycobacterium tuberculosis catalase-peroxidase KatG and its S315T mutant revealed by resonance Raman spectroscopy.* Biochemistry, 2003. **42**(13): 3835-3845.
23. Rouse, D.A., Li, Z.M., Bai, G.H., and Morris, S.L., *Characterization of the KatG and InhA Genes of isoniazid-resistant clinical isolates of Mycobacterium tuberculosis.* Antimicrob. Agents Chemother., 1995. **39**(11): 2472-2477.
24. Musser, J.M., Kapur, V., Williams, D.L., Kreiswirth, B.N., Vansoolingen, D., and Vanembden, J.D.A., *Characterization of the catalase-peroxidase gene (KatG) and InhA locus in isoniazid-resistant and -susceptible strains of Mycobacterium tuberculosis by automated DNA sequencing: Restricted array of mutations associated with drug resistance.* J. Infect. Dis., 1996. **173**(1): 196-202.
25. Lad, L., Mewies, M., Basran, J., Scrutton, N.S., and Raven, E.L., *Role of histidine 42 in ascorbate peroxidase - Kinetic analysis of the H42A and H42E variants.* Eur. J. Biochem., 2002. **269**(13): 3182-3192.
26. Sharp, K.H., Moody, P.C.E., Brown, K.A., and Raven, E.L., *Crystal structure of the ascorbate peroxidase-salicylhydroxamic acid complex.* Biochemistry, 2004. **43**(27): 8644-8651.
27. Tsukamoto, K., Itakura, H., Sato, K., Fukuyama, K., Miura, S., Takahashi, S., Ikezawa, H., and Hosoya, T., *Binding of salicylhydroxamic acid and several aromatic donor molecules to Arthromyces ramosus peroxidase, investigated by X-ray crystallography, optical difference spectroscopy, NMR relaxation, molecular dynamics, and kinetics.* Biochemistry, 1999. **38**(39): 12558-12568.

# Chapter 4

## *Binding of Aromatic Substrates in Cytochrome c Peroxidase*

# 4.1 Introduction

Many class I peroxidases, as well as oxidizing their physiological substrates, are capable of oxidizing a variety of aromatic substrates that are more typical of class II and III peroxidases. In addition to cytochrome *c,* C*c*P is able to oxidize substrates such as guaiacol and phenol, albeit at a much reduced rate. It is the general consensus in the literature that small aromatic substrates, such as those shown in Figure 4.1, are oxidised by binding at the δ-heme edge.

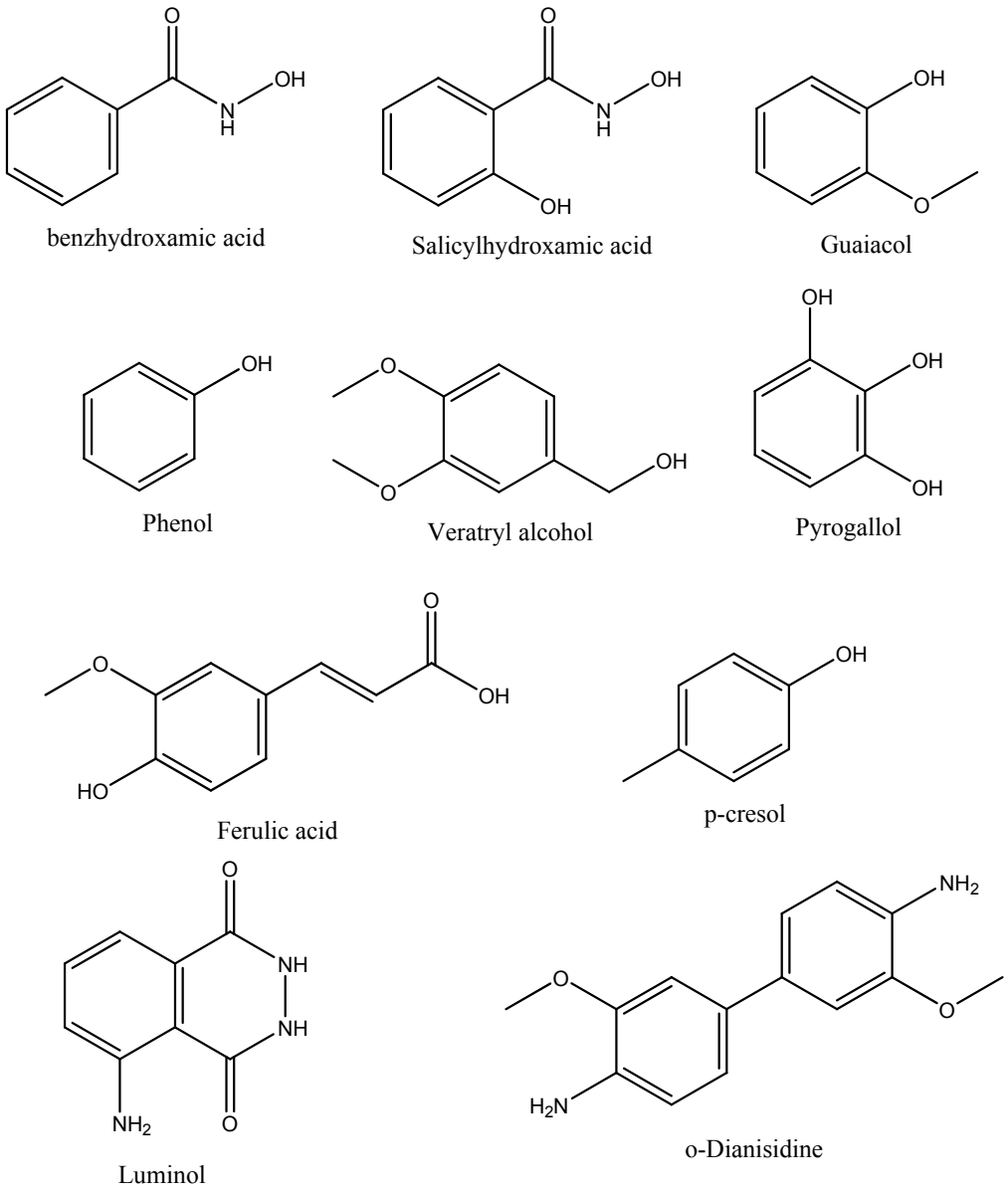


**Figure 4.1: Examples of small aromatic substrates oxidised by peroxidases**

Early experiments on HRP [1] used alkylhydrazines to inactivate aromatic oxidation. The regiospecificity of alkyl radical attack at the δ-meso carbon, to produce a δ-meso-alkylheme, implicated the δ-heme edge in substrate interactions. HRP reconstituted with δ-meso-ethylheme reacts with $H_2O_2$ to form a ferryl species, but was shown to be catalytically inactive towards aromatic substrates, whereas HRP reconstituted with δ-meso-methylheme retained some catalytic activity. This demonstrated that the meso substituent did not alter the conformation or the redox properties of the heme and that catalytic activity was affected by a steric mechanism. NMR studies have also been carried out on HRP which show substrate binding in the vicinity of the heme 8-methyl group [2]. Similar inactivation with phenylhydrazine and NMR studies have been carried out on APX [3, 4], which also led to the conclusion that small aromatic molecules are oxidized at the δ-heme edge.

The first structural evidence that aromatic substrate binding occurred at the δ-heme edge came in 1997, when a crystal structure of an enzyme from the plant peroxidase family, complexed to an aromatic donor molecule, was solved [5]. A 1.6 Å structure showed benzhydroxamic acid (BHA) bound to *Arthromyces Ramosus* peroxidase (ARP) in a distal location with its aromatic ring almost parallel to the heme. A number of productive hydrogen bonds are made between BHA and ARP namely between Pro154, the distal histidine (His56) and Arg52. An indirect interaction between the BHA hydroxyl group and the heme iron is made via an active site water molecule (see Chapter 1, Section 1.8.2, Figure 1.32). Other structures have since emerged showing HRP complexed with BHA (see Chapter 1, Section 1.8.3, Figure 1.34) [6], ARP complexed with SHA [7] and APX complexed with salicylhydroxamic acid (SHA) (see Chapter 5, Section 5.2.1.1, Figure 5.4) [8]. In all cases the binding location of the substrate is similar and close to the δ-heme edge. This evidence led to the general consensus in the literature that substrate binding and oxidation in peroxidases occurred at the δ-heme edge, with the exception of the cytochrome *c* peroxidase/cytochrome *c* complex which has a large protein substrate and the manganese peroxidase/Mn(II) complex, which showed Mn(II) bound close to the γ-heme edge [9]. As discussed in Chapter 2, this general consensus has evolved and it has since been shown that other binding sites exist in peroxidases for example APX-ascorbate complex [10] and the nitric oxide synthase/tetrahydrobiopterin complex [11, 12], which both show substrate binding at the γ-heme edge. It has

become clear that substrate binding at the δ-heme edge was not the only means by which the enzyme and substrate might productively associate with one another.

C*c*P is known to bind aromatic substrates at a different location to its physiological substrate, cytochrome *c* [13], and the δ-heme edge as been implicated by reconstitution with δ-meso-ethylheme, which interferes with small substrate oxidation but not with formation of the ferryl/protein radical complex or oxidation of cytochrome *c* [14]. This is supported by site directed mutagenesis, since the introduction of methionine and tyrosine at Ala147 was shown to block access to the δ-heme edge, a subsequent reduction in aromatic oxidation was observed where there was no corresponding effect on cytochrome *c* oxidation [15]. The key aromatic substrate hydrogen bonding residues in APX (Arg38, Trp41 and Pro132) are conserved in C*c*P (Arg48, Trp51 and Pro145) meaning that C*c*P contains a similar binding pocket to that identified in other class I peroxidases, and so it is possible to assume that aromatic binding will occur in the same manner. More recently a structure of C*c*P complexed with INH has been published [16], showing INH bound at the δ-heme edge (see Chapter 3). To date there is just one example in the literature of phenol bound to C*c*P and binding occurs away from the δ-heme edge, in an artificial cavity created by the mutation of Trp191 to glycine [17].

Guaiacol is an almost universal substrate for peroxidases and offers an easy colorimetric assay for peroxidase activity, because of this guaiacol has been used as *the* substrate to probe aromatic binding and oxidation in peroxidases. Despite its extensive use in the literature, however, so far the site of guaiacol binding and oxidation has not been determined unambiguously, this is largely due to the low solubility of guaiacol compared to other aromatic molecules such as SHA and BHA, meaning that obtaining crystal structures of complexes with guaiacol has so far not been achieved.

This Chapter presents the crystal structures of phenol and guaiacol bound to C*c*P along with kinetic analysis of the catalytic activity of the binding sites, adding to the general development of the understanding of substrate binding across the family of heme peroxidases.

# 4.2 Results

## *4.2.1 Expression of CcP and mutants*

Wild type C*c*P and all mutants were expressed, purified and crystallised as detailed in Chapter 2 (Section 2.2.1-2.2.4).

## *4.2.2 Crystal structures of CcP in complex with aromatic substrates*

### *4.2.2.1 Aromatic soaks, data collection and refinement*

Crystals of C*c*P were either soaked for 10 minutes in guaiacol solution (150 mM) which had been previously solubilised in 20% methanol or in phenol solution (100 mM). Diffraction data were collected in house using a Rigaku RU2HB X-ray generator with copper anode and Xenocs multilayer optics and an R-Axis IV detector, all data were collected at 100 K. Data was collected to 1.61 Å for the C*c*P-guaiacol structure and 2.20 Å for the C*c*P-phenol structure. Data were collected over 90º rotation in 0.5 º images. Data collection statistics are shown in Table 4.1, and 5% of the data were flagged for the calculation of $R_{free}$ and excluded from subsequent refinement. The structures were refined from the 1.70 Å wild type C*c*P structure [18] (Protein data bank entry 2CYP). All refinement used REFMAC [19] from the CCP4 suite [20] .Calculation of difference Fourier maps showed clear and unambiguous electron density for bound guaiacol and phenol molecules in all of the structures. Guaiacol and phenol were incorporated into the last cycles of refinement. COOT [21] was used throughout for manual adjustment, ligand fitting and interpretation of the water structure.

**Table 4.1:** Data Collection and refinement statistics for aromatic binding C*c*P variants

| Protein | C*c*P-Guaiacol | C*c*P-Phenol | M119W-Guaiacol | S81W |
|---|---|---|---|---|
| **Data collection** | | | | |
| Space group | $P2_22_12_1$ | $P2_22_12_1$ | $P2_22_12_1$ | $P2_22_12_1$ |
| Unit Cell (Å) | | | | |
| a | 51.1058 | 51.116 | 51.1020 | 51.000 |
| b | 74.9896 | 75.117 | 74.5612 | 74.4900 |
| c | 106.9031 | 107.192 | 106.6782 | 106.47000 |
| Resolution (Å) | 27.24-1.61 (1.69-1.61) | 27.20-2..20 (2.32-2.20) | 45.98-2.01 (2.12-2.01) | 33.08-1.71 (1.80-1.71) |
| Total observations | 192254 (2692) | 68320 (9587) | 62544 (7656) | 105421 (15609) |
| Unique reflections | 46241 (1991) | 21669 (3096) | 24226 (3082) | 43966 (6177) |
| $I/\sigma I$ | 30.8 (5.6) | 37.7 (31.5) | 19.6 (3.5) | 14.4(4.7) |
| $R_{merge}$ | 0.031 (0.135) | 0.025 (0.031 | 0.051 (0.296) | 0.068 (0.235) |
| Completeness (%) | 85.1 (25.9) | 99.9 (99.9) | 86.7 (77.2) | 97.9 (96.2) |
| **Refinement statistics** | | | | |
| $R_{work}$ | 0.17908 | 0.16078 | 0.17298 | 0.17848 |
| $R_{free}$ | 0.20991 | 0.18740 | 0.23148 | 0.21111 |
| R.M.S.D | | | | |
| Bonds (Å) | 0.009 | 0.009 | 0.019 | 0.012 |
| Angles (°) | 1.128 | 1.101 | 1.658 | 1.239 |

### *4.2.2.2 The CcP guaiacol structure*

The overall structure of wild type C*c*P in complex with guaiacol is shown in Figure 4.2(A). Guaiacol binding leads to no major structural rearrangements of the protein as shown by comparison with the structure of guaiacol-free wild type C*c*P [18] (data not shown). Two molecules of guaiacol are bound to C*c*P in sites not previously identified as aromatic binding sites.

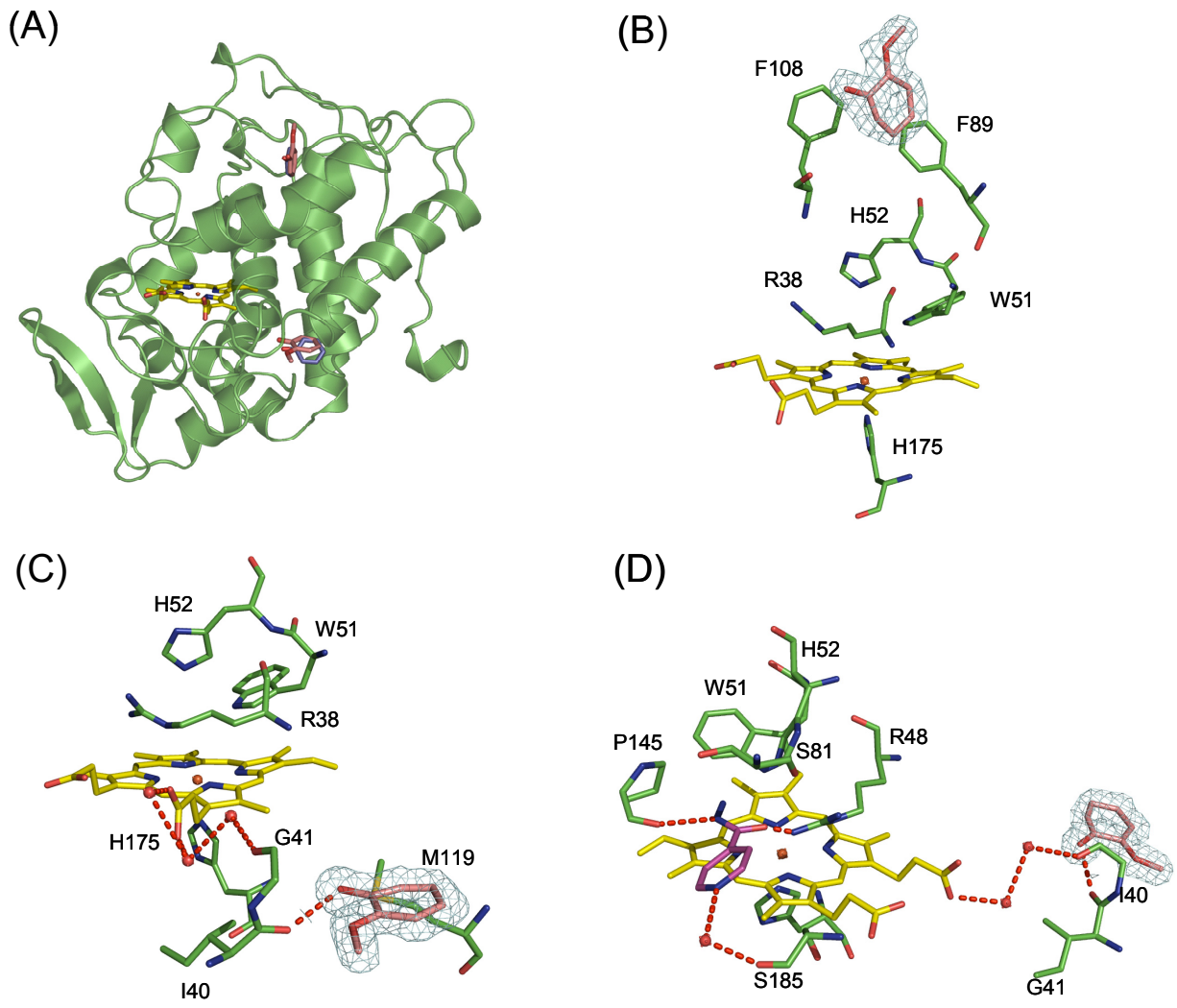


**Figure 4.2: The two novel binding sites in C*c*P**

(A) The overall crystal structures of the C*c*P-guaiacol complex and the C*c*P-phenol complex, guaiacol (purple) and phenol (blue) are bound in two novel phenolic binding sites. (B) A close up of the guaiacol binding site 22 Å from the heme, unlikely to have catalytic potential. (C) A close up of the site that may have catalytic potential showing the possible hydrogen bonding network between guaiacol and the heme 6-propionate. (D) An overlay of the C*c*P-INH structure and the C*c*P-guaiacol structure showing INH bound at the δ-heme edge. Guaiacol is in salmon pink, INH in purple. Electron density maps are shown in aquamarine. (Figure created using PyMOL [22])

The first site is a hydrophobic pocket defined by Phe89 and Phe108. The methoxy group has access to the solvent and is located approximately 23 Å from the heme iron (Figure 4.2(B)), due to the distance from the heme, this site is not thought to be catalytically relevant. The second site is 15.50 Å from the heme iron. The structure of the wild type C*c*P-guaiacol complex in the heme region is shown in

Figure 4.2(C). The guaiacol hydroxyl group is able to hydrogen bond to the backbone carbonyl of Ile40 (2.74 Å), a hydrogen bonding network links the guaiacol to the 6-propionate of the heme via Gly41 and two water molecules. For comparison, the structure of the heme region of the wild type C*c*P-INH complex [16] overlaid with the C*c*P-guaiacol structure, is shown in Figure 4.2(D). INH is bound at the δ-heme edge as described in Chapter 3 Section 3.5.2.1. INH occupies the site proposed to be the aromatic binding site in peroxidases which is a similar position to INH in the APX-INH complex [16] and a similar position to small aromatic molecules in other peroxidase-aromatic complexes such as APX-SHA [8], ARP-SHA and ARP-BHA [5].

### *4.2.2.3 Crystal structure of CcP-Phenol complex*

In order to confirm the two sites seen for guaiacol binding as general aromatic binding sites, C*c*P crystals were also soaked in phenol. The C*c*P-phenol structure (Figure 4.3) also shows binding of the substrate in two sites and is as described for the C*c*P-guaiacol structure.

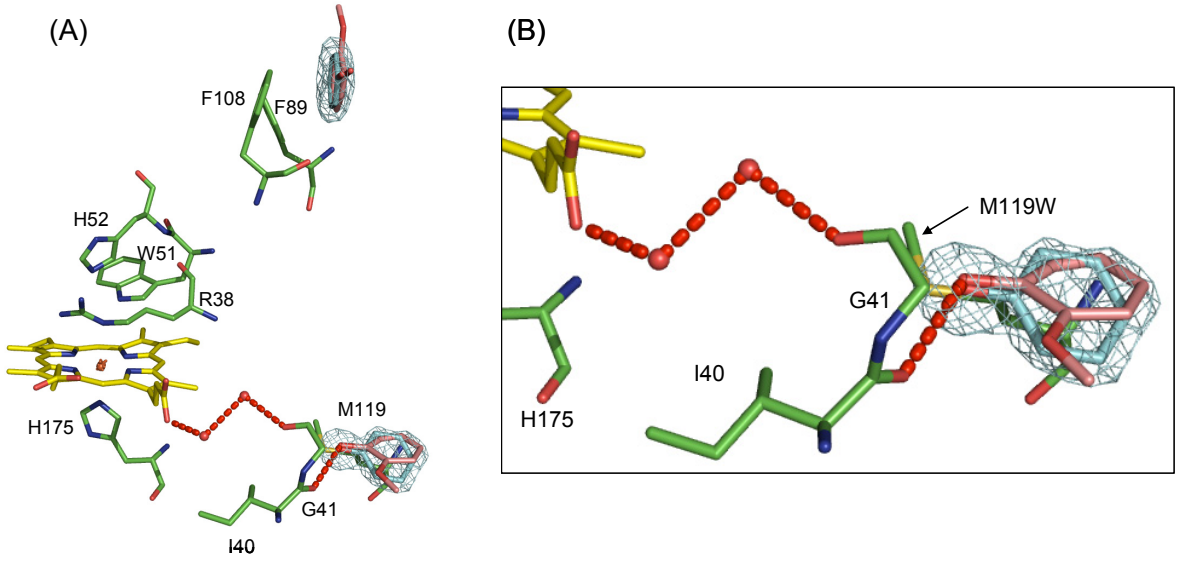


**Figure 4.3: Crystal structure of the C*c*P-phenol complex**

(A) The structure of the C*c*P-phenol complex showing phenol (cyan) bound at the same sites as in the C*c*P-guaiacol crystal structure, the electron density for phenol is shown in aquamarine. (B) A close up of phenol binding at the second guaiacol binding site showing the interaction between the hydroxyl group of phenol and Gly41. Hydrogen bonds are indicated by red dashes and water molecules are represented by red spheres. Guaiacol is shown in salmon pink.

### *4.2.3 Catalytic activity of novel guaiacol binding sites*

It was not clear from the data above whether or not the sites identified crystallographically were catalytically relevant, out of the two guaiacol binding sites seen in the structure of the C*c*P-guaiacol complex the site close to the heme may be utilised by C*c*P for the oxidation of small aromatic molecules. The catalytic activity of this site was probed by competitive inhibition studies using INH (known to bind at the δ-heme edge), since guaiacol oxidation would be expected to be unaffected by INH if there are two distinct sites for guaiacol and INH as seen structurally. Site directed mutagenesis was also used to investigate the catalytic relevance of the two sites.

### *4.2.4 Steady state kinetics*

Steady state kinetics of guaiacol oxidation were carried out as reported previously [23-25] and as seen in Chapter 2 (Section 2.2.8), data were fitted to the Michaelis-Menten equation. The rate of guaiacol oxidation by C*c*P is slow compared to that of cytochrome *c* oxidation ($k_{cat}$ 4.10 ± 0.30 $s^{-1}$ and 1500 ± 250 $s^{-1}$ respectively).

#### *4.2.4.1 INH inhibition of aromatic oxidation*

Any substance that reduces the rate of an enzyme-catalysed reaction is an inhibitor of that enzyme. There are many different forms of inhibition and inhibition studies can lead to information about the nature of the active site and the catalytic mechanism of the enzyme. There are three simple inhibition systems; competitive inhibition, noncompetitive inhibition and uncompetitive inhibition. In the former case a competitive inhibitor combines with the free enzyme in a way that prevents substrate binding. The substrate and the inhibitor act in a mutually exclusive way, usually competing to bind at the same site, the maximum velocity of the enzyme can still be reached although the concentration of substrate required to reach it is increased, this in turn means that the $K_M$ of the enzyme is increased. A noncompetitive inhibitor has no effect on substrate binding and substrate and inhibitor bind independently at two different sites. In the case of noncompetitive inhibition when the inhibitor is bound to the enzyme it renders the enzyme inactive. Since at any concentration of inhibitor there will always be some inactive form of the enzyme the maximum velocity that the enzyme can reach is reduced, so in this case $K_M$ will remain the same for any concentration of inhibitor but $V_{max}$ will decrease as inhibitor

concentration increases. In uncompetitive inhibition the inhibitor binds to the enzyme-substrate complex. In the presence of an uncompetitive inhibitor some of the enzyme will always be in the inactive form and so $V_{max}$ will be reduced, however, unlike in noncompetitive inhibition, $K_M$ will also decrease since some of the enzyme-substrate complex will be inactivated changing the equilibrium of the reaction between enzyme and substrate.

If guaiacol and INH bind independently at different sites then unless INH affects the overall catalytic activity of C*c*P guaiacol oxidation would be expected to be unaffected by the presence of INH. Steady-state assays for guaiacol oxidation were carried out in the presence of various concentrations of INH ranging from 1-10 mM. Figure 4.4 shows the initial rates of guaiacol oxidation by C*c*P plotted against guaiacol concentration for various concentrations of INH, they have been fitted to the Michaelis-Menten equation as described previously [25].

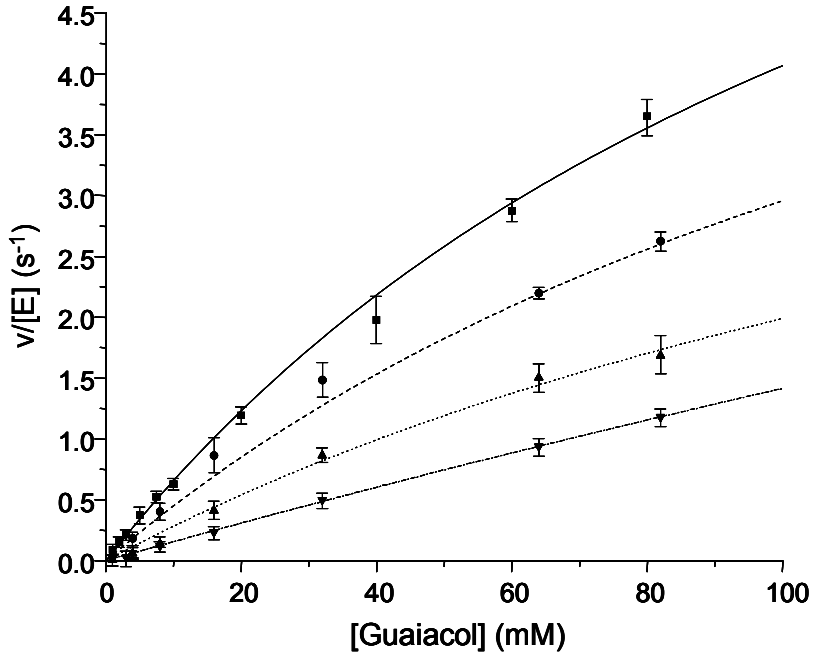


**Figure 4.4: Oxidation of guaiacol by wild type C*c*P in the presence of INH**

Michaelis-Menten plots for the oxidation of guaiacol by wild type C*c*P in the presence of various concentrations of INH. No INH (■, Solid line), 1 mM INH (●, dashed line), 5 mM INH (▲, dot-dashed line) and 10mM INH (▼, dot-dash-dot line). All reactions were carried out in 100 mM KPi, pH 6.0, 25 ºC. Average values of three independent measurements are shown for each point; error bars represent the standard deviation.

$V_{max}$ values remain unchanged at each INH concentration (Table 4.2). However, as the concentration of INH is increased the apparent $K_m$ value also increases, this is consistent with competitive inhibition by INH, indicating that INH and guaiacol compete for the same binding site.

**Table 4.2:** Kinetic data for steady state guaiacol oxidation in the presence of INH

Variation of steady state kinetics in the presence of INH. Assays were carried out at pH 6.0, 100 mM KPi, 25 ºC. *NB*: The apparent increase in $k_{cat}$ for wild type C*c*P as INH concentration is increased and the increasing error in $K_M$ is due to the inability to produce accurate Michaelis-Menten plots in the presence of INH, as the concentrations of guaiacol needed to reach $V_{max}$ at high INH concentrations are not accessible.

| | ***Wild type CcP*** | | ***M119W*** | | ***S81W*** | |
|---|---|---|---|---|---|---|
| | **$k_{cat}$ ($s^{-1}$)** | **$K_m$ (mM)** | **$k_{cat}$ ($s^{-1}$)** | **$K_m$ (mM)** | **$k_{cat}$ ($s^{-1}$)** | **$K_m$ (mM)** |
| **No INH** | 4.14 ± 0.13 | 52.95 ± 6.24 | 5.84 ± 0.17 | 27.84 ± 1.90 | 1.24 ± 0.03 | 19.47 ± 1.14 |
| **1 mM INH** | 7.48 ± 0.35 | 151. 81 ± 11.15 | 5.80 ± 0.27 | 45.38 ± 4.05 | 1.36 ± 0.05 | 42.73 ± 1.18 |
| **5 mM INH** | 10.89 ± 3.17 | 441.87 ± 155.80 | 5.20 ± 0.42 | 47.60 ± 7.04 | 1.10 ± 0.05 | 114.71 ± 8.62 |
| **10 mM INH** | 12.17 ± 6.52 | 1058.7 ± 618.09 | 5.28 ± 0.54 | 104.08 ± 15.18 | 1.06 ± 0.11 | 169.21 ± 21.74 |

Figure 4.5 shows Lineweaver-Burk plots for the oxidation of guaiacol by wild type C*c*P in the presence of INH, the plots are consistent with competitive inhibition of guaiacol oxidation [26]. A replot of the slope of the reciprocal plots versus [INH] is linear (Figure 4.5 inset), also consistent with competitive inhibition, and can be used to obtain the dissociation constant for the binding of INH to C*c*P, $K_i$. Using the x-axis intercept of this plot the apparent $K_i$ for INH was found to be 2.90 mM.

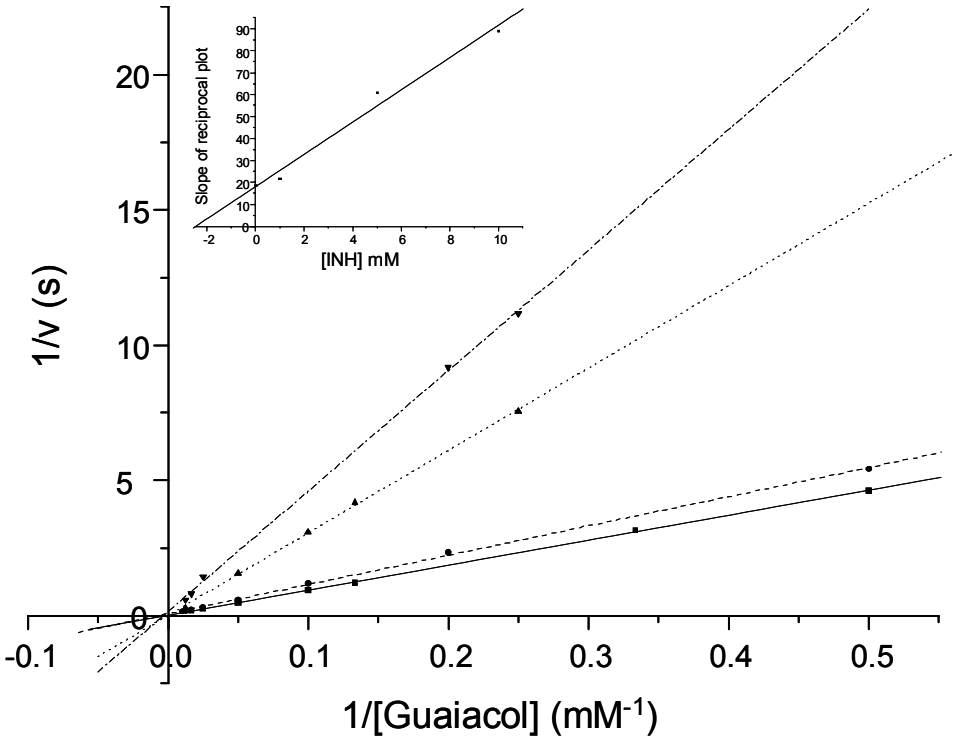


**Figure 4.5: Lineweaver-Burk plots for guaiacol oxidation by wild type C*c*P**

Lineweaver-Burk plots for guaiacol oxidation in the absence of INH (solid line), with 1 mM INH (dashed line), with 5 mM INH (dotted line) and 10 mM INH (dashed-dotted line). The increase in slope while the y-axis intercept remains the same is consistent with competitive inhibition of guaiacol oxidation by INH. The inset shows a replot of the slope of the reciprocal plots versus [INH].

### *4.2.4.2 INH inhibition of cytochrome c oxidation*

From the INH inhibition of guaiacol oxidation by C*c*P, it can be concluded that INH either affects the mechanism of oxidation by C*c*P in a way that shows competitive inhibition, or that INH competes with guaiacol for the same binding site. In order to examine the mechanism of INH inhibition the effect of the presence of INH on cytochrome *c* oxidation was investigated. Figure 4.6 shows the Michaelis-Menten plots for cytochrome *c* oxidation in the presence of various concentrations of INH, INH has no effect on either $k_{cat}$ or $K_m$ for cytochrome *c* oxidation.

Lineweaver-Burk plots for cytochrome *c* oxidation in the presence of INH are shown in Figure 4.7. There is no change in the slope or the y-axis intercept indicating that cytochrome *c* oxidation is not inhibited by the presence of INH. This shows that INH does not affect the formation of the ferryl/protein radical (Compound I) or cytochrome *c* binding.

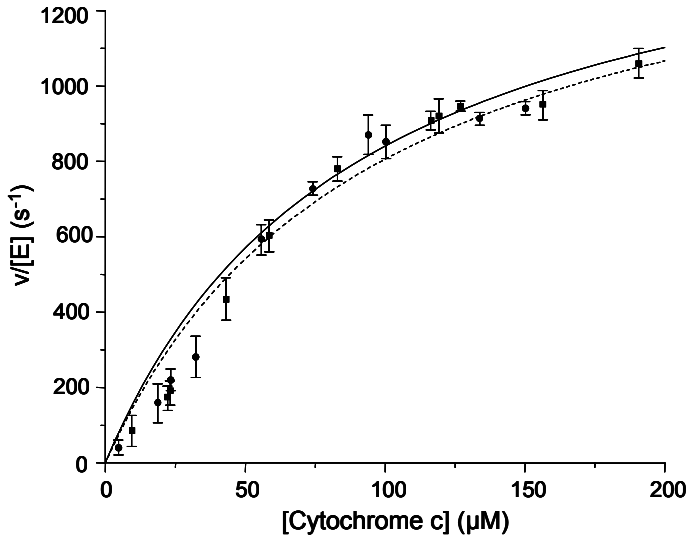


**Figure 4.6: Steady state oxidation of cytochrome *c* in the presence of INH**

Cytochrome *c* oxidation in the absence of INH (■, solid line) and in the presence of 10 mM INH (●, dashed line). All reactions were carried out in 100 mM KPi buffer, pH 6.0, 25 ºC. Average values of three independent measurements are shown for each point; error bars represent standard deviations.

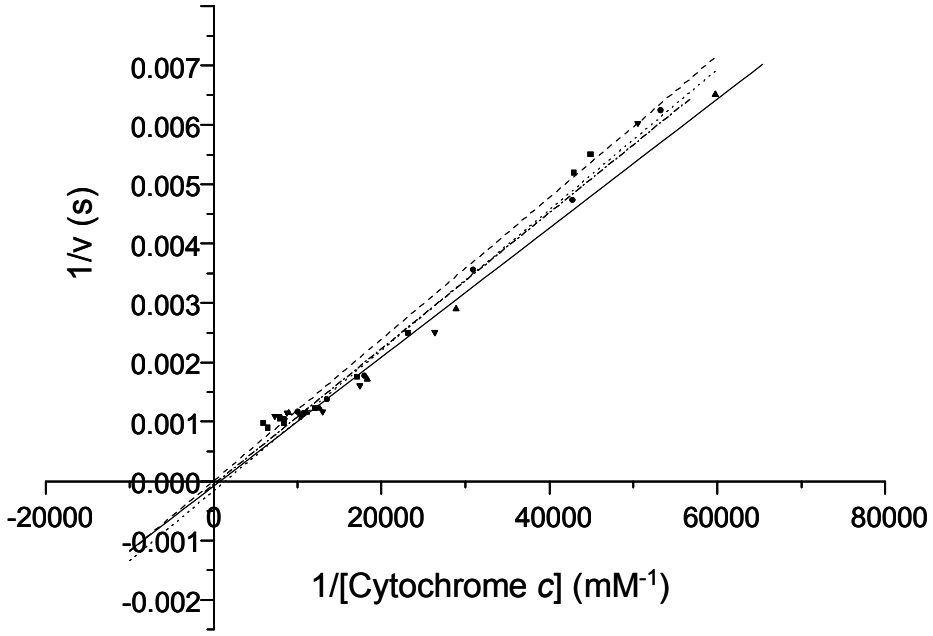


**Figure 4.7: Lineweaver-Burk plots for cytochrome *c* oxidation by wild type C*c*P**

Lineweaver-Burk plots for cytochrome *c* oxidation by wild type C*c*P in the absence of INH (solid line), with 1 mM INH (dashed line), with 5 mM INH (dotted line) and 10 mM INH (dashed-dotted line). Plots are unaffected by INH even at high [INH] consistent with no inhibition.

## *4.2.5 Mutagenesis*

The inhibition studies suggest that INH and guaiacol compete for the same binding site conflicting with the structural data which shows the molecules bound at two distinct sites. In order to probe this data further Met119 was replaced with a tryptophan residue (see Figure 4.2 (C)). This mutation was proposed to sterically block the second guaiacol binding site allowing determination of whether this site is important catalytically.

### *4.2.5.1 Crystal structure of M119W Guaiacol complex*

The crystal structure of the M119W-guaiacol complex is shown in Figure 4.8. Only one molecule of guaiacol is bound in this structure and is positioned at the distant site, 23 Å from the heme iron, seen in the wild type C*c*P-guaiacol complex. The introduction of tryptophan at position 119 has efficiently blocked the second guaiacol binding site. In addition there is a slight structural change where the loop comprised of Ala193-Phe198 has moved, this slight structural rearrangement accommodates the bulkier tryptophan side chain, but binding of guaiacol is sterically hindered (Figure 4.9), as in the wild type C*c*P-guaiacol structure, guaiacol is not seen bound at the δ-heme edge.

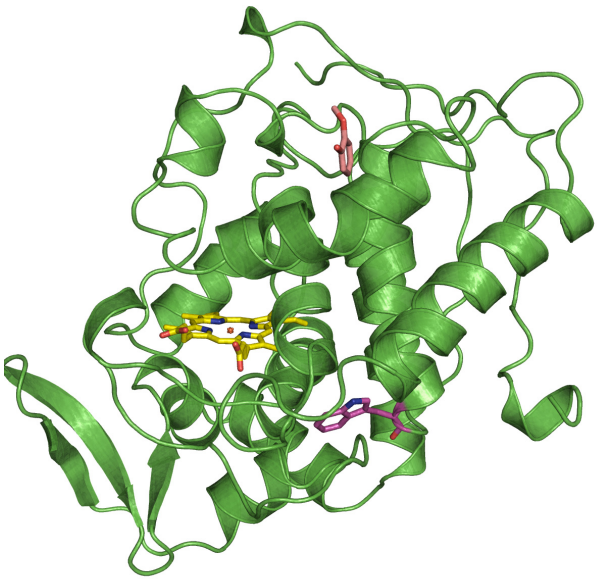

**Figure 4.8: C*c*P M119W-guaiacol complex**

M119W C*c*P-guaiacol complex, only the distant phenolic site is occupied. Guaiacol (salmon pink) is prevented from binding at the site close to the heme by the added tryptophan residue at 119 (purple).

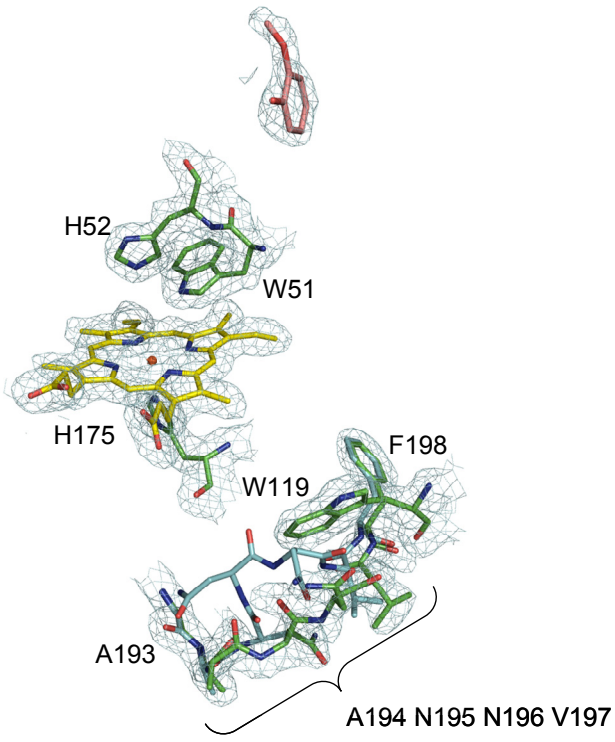


**Figure 4.9: Close up of the heme region of M119W C*c*P**

A close up of the mutation (M119W in green and wild type C*c*P in cyan) showing the slight movement of the loop comprising Ala193 to Phe198. Guaiacol is seen bound at the distant site (salmon pink) (Figure created using PyMOL [22]).

### *4.2.5.2 Steady state kinetics of guaiacol oxidation by M119W*

If the second binding site is the catalytically active site for C*c*P, the M119W mutant would be expected to show a decreased ability to oxidise guaiacol. However, steady state kinetics show that the catalytic activity of this mutant is unaffected with a comparable $k_{cat}$ and $K_M$ to wild type C*c*P with respect to guaiacol oxidation, Table 4.3.

**Table 4.3: kinetic data for steady state guaiacol oxidation**

Steady state kinetic data for guaiacol oxidation by C*c*P. Assays were carried out at pH 6.0, 100 mM KPi, 25 ºC.

| Mutant C*c*P | $k_{cat}$ ($s^{-1}$) | $K_M$ (mM) | $k_{cat}/K_M$ ($mM^{-1}$ $s^{-1}$) |
|---|---|---|---|
| **Wild type C*c*P** | 4.14 ± 0.13 | 52.95 ± 6.24 | 0.078 |
| **S81W** | 1.24 ± 0.03 | 19.47 ± 1.14 | 0.064 |
| **M119W** | 5.94 ± 0.16 | 27.84 ± 1.90 | 0.226 |

In the M119W mutant guaiacol oxidation and binding can no longer take place at the second guaiacol site seen in the C*c*P-guaiacol structure. Inhibition studies using the M119W mutant were carried out to test whether guaiacol was still binding to the same site as INH in this mutant and, as for wild type C*c*P, INH competitively inhibits

guaiacol oxidation (Figure 4.10) with a $K_i$ of 3.20 mM (inset), indicating guaiacol and INH are binding at the same site in this mutant.

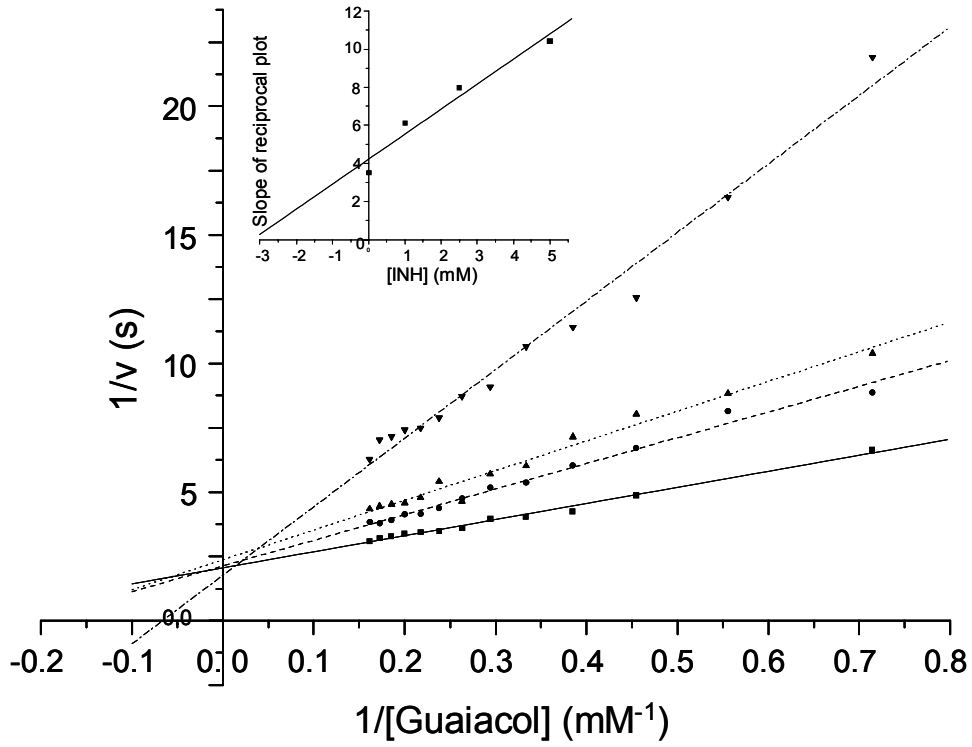


**Figure 4.10: Lineweaver-Burk plots of guaiacol oxidation by M119W C*c*P**

Lineweaver-Burk plots in the absence of INH (solid line), with 1 mM INH (dashed line), with 5 mM INH (dotted line) and 10 mM INH (dashed-dotted line). The increase in slope while the y-axis intercept remains the same is consistent with competitive inhibition of guaiacol oxidation by INH. The inset shows the slope of the reciprocal plot versus [INH], the linear fit is consistent with competitive inhibition.

### *4.2.5.3 Crystal structure of S81W*

Further mutagenesis with the aim of blocking aromatic binding at the δ-heme edge was carried out. Serine 81 was replaced by tryptophan which was proposed to occupy the site of INH binding. However, steady state guaiacol oxidation of this mutant shows little change compared to wild type C*c*P Table 4.3 (a slight reduction in $k_{cat}$ is seen from 4.14 ± 0.32 $s^{-1}$ for wild type C*c*P to 1.24 ± 0.03 $s^{-1}$ for S81W, probably due to a slight increase in steric hindrance in the binding site). Figure 4.11 reveals that the architecture of the distal binding pocket has not been altered by the introduction of a tryptophan residue at position 81 and so as seen by the INH modelled in the same position it is found in the wild type C*c*P-INH complex, aromatic binding can still occur at the δ-heme edge. This is due to the side chain of the

tryptophan swinging outwards to form a hydrogen bond with Asp146 instead of the occupying the site occupied by INH as predicted.

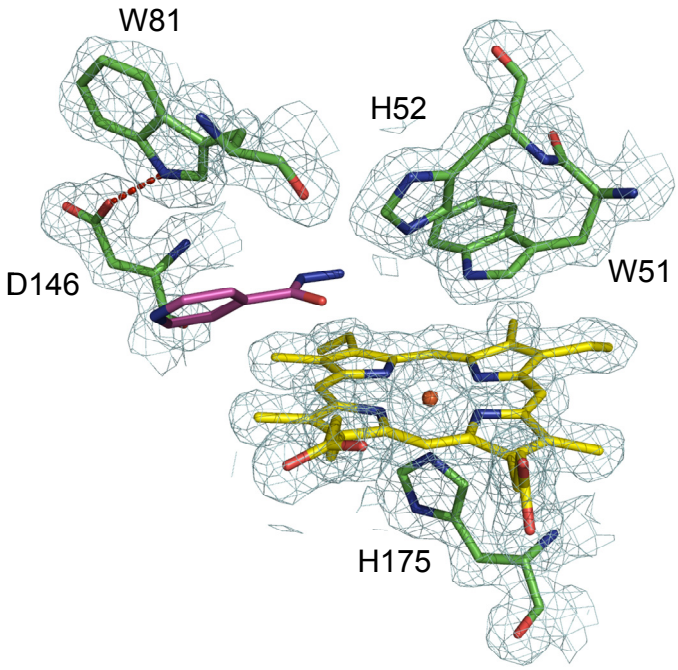


**Figure 4.11: The δ-heme edge region of S81W**

The introduced tryptophan is able to form a hydrogen bond with the acid group of Asp146. This interaction means that instead of occupying the INH site, as predicted, it is orientated away from the hydrophobic pocket. The position of INH (magenta), modelled in using the wild type C*c*P-INH structure, shows that the δ-heme edge is still accessible to aromatic molecules**.**

Inhibition studies using S81W (Figure 4.12) support the fact that both guaiacol and INH are still able to bind in this mutant, and that binding is likely to occur at the same site, as competitive inhibition of guaiacol oxidation by INH is seen.

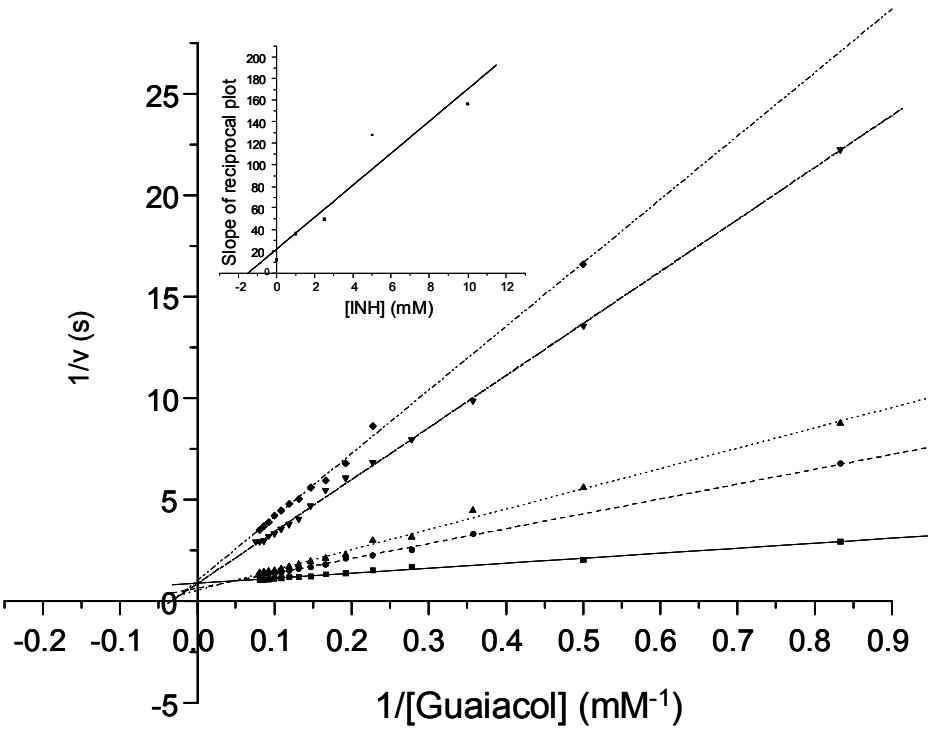


**Figure 4.12: Lineweaver-Burk plots for guaiacol oxidation by S81W C*c*P**

Lineweaver-Burk plots in the absence of INH and in the presence of 1 mM INH (dashed line), 2.5 mM INH (dotted line), 5 mM INH (dashed-dotted line) and 10 mM INH (short dashed-dotted line). The plots are consistent with competitive inhibition. The inset shows the slope of the reciprocal plot versus [INH], the linear fit is again consistent with competitive inhibition.

## 4.3 Discussion

Guaiacol is a universal substrate for peroxidases, utilized by the all known peroxidases, even if it is not the physiological substrate. It has been used as a standard assay for the measure of peroxidase activity since the early 1950s [27] and is still used today. Despite its role in the study of peroxidases, its exact binding location, although predicted by chemical based studies and comparison with structures of similar substrate binding, has not been defined. Although guaiacol is not seen bound at the δ-heme edge in the crystal structure, the inhibition data and mutagenesis carried out in this work strongly suggest that the catalytic binding site for guaiacol is the δ-heme edge. The approximate value of $K_i$ for INH is 2.70 mM, this gives an indication of the strength of INH binding and why it is possible to see it bound in the crystal structure, the $K_M$ for guaiacol is 20-fold greater than this, which may offer an explanation as to

why guaiacol is not seen bound in the crystal structure as much higher guaiacol concentrations are needed to saturate the enzyme. Although these studies show that there is competitive competition between guaiacol and INH and the two sites described by the crystal structures have not been shown to have catalytic potential, it does not necessarily mean that they play no role in guaiacol oxidation by C*c*P, it is possible that guaiacol may bind at these sites prior to migrating to the δ-heme edge, which would facilitate faster oxidation by ensuring substrate and enzyme were colocalised.

The C*c*P-guaiacol crystal structure shows guaiacol bound at two sites distinct from the cytochrome *c* binding site and the δ-heme edge. The solution studies show that guaiacol and INH bind at the same site, as competitive inhibition of guaiacol oxidation by INH is seen. Since it is known that INH binds at the δ-heme edge [16] it can be concluded that guaiacol also binds and is oxidised at the δ-heme edge. This compliments the phenylhydrazine modifications that have been carried out on C*c*P [14] which show that guaiacol oxidation by C*c*P is completely lost when δ-meso-phenylheme is present.

Further support for guaiacol binding at the δ-heme edge is given by the fact that the aromatic binding pocket at the δ-heme edge is well preserved amongst the peroxidases and the key hydrogen bonding residues for SHA binding in APX (Arg38, Trp41 and Pro132) [8] are conserved in C*c*P (Arg48, Trp51 and Pro145). Directed evolution experiments carried out to enhance the oxidation of guaiacol show that there is a 300-fold increase in the activity of C*c*P towards guaiacol when the distal arginine, Arg48, is mutated to a glutamine [28]. This mutation leads to an increase in the accessibility of the δ-heme edge lending further support to the hypothesis that this is the site of guaiacol oxidation.

Comparison of the distant site seen for guaiacol binding, defined by Phe89 and Phe108 in the C*c*P-guaiacol crystal structure, with APX and HRP (Figure 4.13) reveals that the site is not conserved amongst peroxidases.

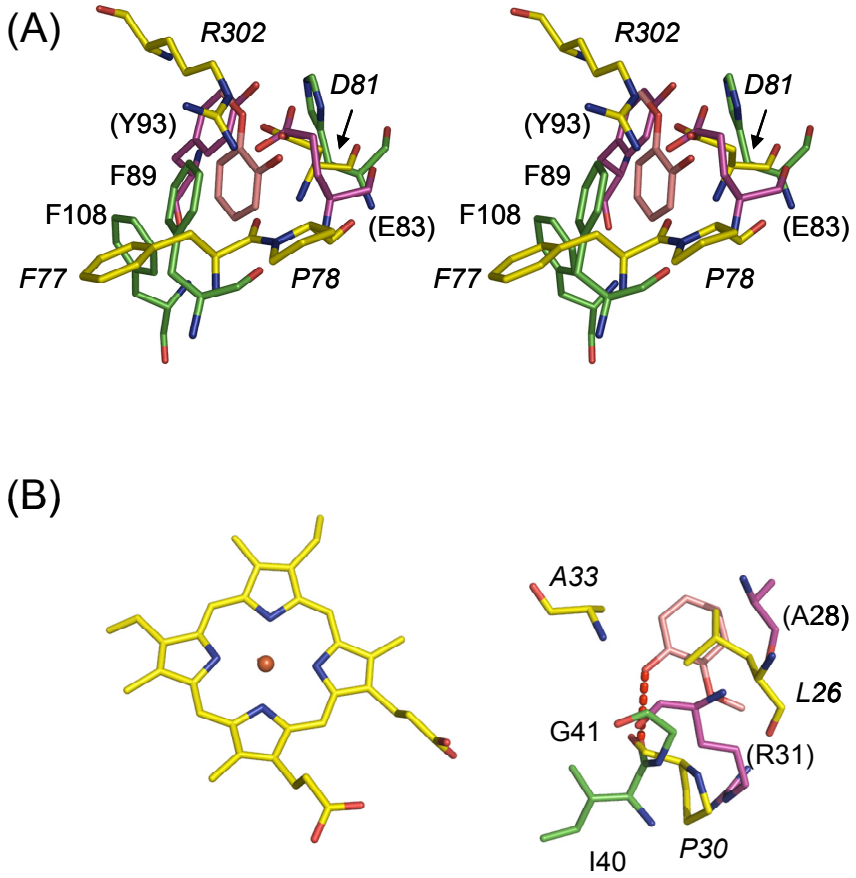


**Figure 4.13: Comparison of the guaiacol binding sites in C*c*P with APX and HRP.**

Neither APX nor HRP would be able to support guaiacol binding at the sites seen in C*c*P. In the first site (A) steric hindrance by Asp81, Phe77, Pro78 and Arg302 in HRP and by Tyr93 and Glu82 in APX would prevent binding of guaiacol. (B) The second binding site in C*c*P, closer to the heme, in this case steric hindrance is seen by Pro30, Leu26 and Ala33 in HRP and by Ala28 and Arg31 in APX. C*c*P is shown in green, APX in purple and HRP in yellow. Residues are labelled for C*c*P with those for APX in parenthesis and those for HRP in italics. Guaiacol is shown in salmon pink.

Access to the distant site is sterically hindered by Asp81, Phe77, Pro78 and Arg302 in HRP and by Tyr93 and Glu82 in APX (Figure 4.13(A)) meaning that this site is unlikely to be used by other peroxidases and is unique to C*c*P. Similarly the second guaiacol site, closer to the heme, is a cavity which is also seen in APX and HRP. However, the residues defining the cavity vary between the three proteins and again steric hindrance is seen by Pro30, Leu26 and Ala33 in HRP and by Ala28 and Arg31 in APX (Figure 4.13(B)). It is therefore possible to conclude that this binding site is also unique to C*c*P.

## 4.4 References


1. Ator, M.A., David, S.K., and De Montellano, P.R.O., *Structure and catalytic mechanism of horseradish peroxidase: Regiospecific meso-alkylation of the prosthetic heme group by alkylhydrazines.* J. Biol. Chem., 1987. **262**(31): p. 14954-14960.
2. Sakurada, J., Takahashi, S., and Hosoya, T., *NMR studies on the spatial relationship of aromatic donor molecules to the heme iron of horseradish peroxidase.* J. Biol. Chem., 1986. **261**(21): p. 9657-9662.
3. Hill, A.P., Modi, S., Sutcliffe, M.J., Turner, D.D., Gilfoyle, D.J., Smith, A.T., Tam, B.M., and Lloyd, E., *Chemical, spectroscopic and structural investigation of the substrate-binding site in ascorbate peroxidase.* Eur. J. Biochem., 1997. **248**(2): p. 347-354.
4. Mandelman, D., Jamal, J., and Poulos, T.L., *Identification of two electron-transfer sites in ascorbate peroxidase using chemical modification, enzyme kinetics, and crystallography.* Biochemistry, 1998. **37**(50): p. 17610-17617.
5. Itakura, H., Oda, Y., and Fukuyama, K., *Binding mode of benzhydroxamic acid to Arthromyces ramosus peroxidase shows by X-ray crystallographic analysis of the complex at 1.6 angstrom resolution.* Febs Letters, 1997. **412**(1): p. 107-110.
6. Henriksen, A., Schuller, D.J., Meno, K., Welinder, K.G., Smith, A.T., and Gajhede, M., *Structural interactions between horseradish peroxidase C and the substrate benzhydroxamic acid determined by X-ray crystallography.* Biochemistry, 1998. **37**(22): p. 8054-8060.
7. Tsukamoto, K., Itakura, H., Sato, K., Fukuyama, K., Miura, S., Takahashi, S., Ikezawa, H., and Hosoya, T., *Binding of salicylhydroxamic acid and several aromatic donor molecules to Arthromyces ramosus peroxidase, investigated by X-ray crystallography, optical difference spectroscopy, NMR relaxation, molecular dynamics, and kinetics.* Biochemistry, 1999. **38**(39): p. 12558-12568.
8. Sharp, K.H., Moody, P.C.E., Brown, K.A., and Raven, E.L., *Crystal structure of the ascorbate peroxidase-salicylhydroxamic acid complex.* Biochemistry, 2004. **43**(27): p. 8644-8651.
9. Sundaramoorthy, M., Kishi, K., Gold, M.H., and Poulos, T.L., *The crystal structure of manganase peroxidase from Phanerochaete crysosporium at 2.06 angstrom resolution.* J. Biol. Chem., 1994. **269**: p. 32759-32767.
10. Sharp, K.H., Mewies, M., Moody, P.C.E., and Raven, E.L., *Crystal structure of the ascorbate peroxidase-ascorbate complex.* Nat. Struct. Biol., 2003. **10**(4): p. 303-307.
11. Wei, C.C., Crane, B.R., and Stuehr, D.J., *Tetrahydrobiopterin radical enzymology.* Chem. Rev., 2003. **103**(6): p. 2365-2383.
12. Poulos, T.L., Li, H.Y., Raman, C.S., and Schuller, D.J., *Structures of gas-generating heme enzymes: Nitric oxide synthase and heme oxygenase.* ADv. Inorg. Chem., 2001. **51**: p. 243-293.
13. Yonetani, T., and Ray, G. S, *Studies on Cytochrome c Peroxidase: Purification and some properties.* J. Biol. Chem., 1965. **240**: p. 4503-4514.

14. Depillis, G.D., Sishta, B.P., Mauk, A.G., and De Montellano, P.R.O., *Small substrates and cytochrome c are oxidized at different sites of cytochrome c peroxidase.* J. Biol. Chem., 1991. **266**(29): p. 19334-19341.
15. Wilcox, S.K., Jensen, G.M., Fitzgerald, M.M., Mcree, D.E., and Goodin, D.B., *Altering substrate specificity at the heme edge of cytochrome c peroxidase.* Biochemistry, 1996. **35**(15): p. 4858-4866.
16. Metcalfe, C., Macdonald, I.K., Murphy, E.J., Brown, K.A., Raven, E.L., and Moody, P.C.E., *The tuberculosis prodrug isoniazid bound to activating peroxidases.* J. Biol. Chem., 2008. **283**(10): p. 6193-6200.
17. Brenk, R., Vetter, S.W., Boyce, S.E., Goodin, D.B., and Shoichet, B.K., *Probing molecular docking in a charged model binding site.* J. Mol. Biol., 2006. **357**(5): p. 1449-1470.
18. Finzel, B.C., Poulos, T.L., and Kraut, J., *Crystal structure of yeast cytochrome c peroxidase refined at 1.7 angstrom resolution.* J. Biol. Chem., 1984. **259**(21): p. 3027-3036.
19. Murshudov, G.N., Vagin, A.A., and Dodson, E.J., *Refinement of macromolecular structures by the maximum-likelihood method.* Acta Crystallogr., Sect. D. Biol. Crystallogr., 1997. **53**: p. 240-255.
20. Bailey, S., *The CCP4 Suite - Programs for protein crystallography.* Acta Crystallogr., Sect. D. Biol. Crystallogr., 1994. **50**: p. 760-763.
21. Emsley, P. and Cowtan, K., *COOT: model-building tools for molecular graphics.* Acta Crystallogr., Sect. D. Biol. Crystallogr., 2004. **60**: p. 2126-2132.
22. Delano, W.L., *The PyMOL Molecular Graphics System*. 2002, DeLano Scientific: San Carlos, CA.
23. Kang, D.S. and Erman, J.E., *The cytochrome c peroxidase catalyzed oxidation of ferrocytochrome c by hydrogen peroxide: Steady-state kinetic mechanism.* J. Biol. Chem., 1982. **257**(21): p. 2775-2779.
24. Lad, L., Mewies, M., Basran, J., Scrutton, N.S., and Raven, E.L., *Role of histidine 42 in ascorbate peroxidase - Kinetic analysis of the H42A and H42E variants.* Eur. J Biochem., 2002. **269**(13): p. 3182-3192.
25. Lad, L., Mewies, M., and Raven, E.L., *Substrate binding and catalytic mechanism in ascorbate peroxidase: Evidence for two ascorbate binding sites.* Biochemistry, 2002. **41**(46): p. 13774-13781.
26. Segel, I.H., *Enzyme Kinetics Behaviour and Analysis of Rapid Equilibrium and Steady-State Enzyme Systems*. Wiley Classics Library Edition ed. 1993: Wiley. 955.
27. Maehly, A.C. and Chance, B., *The assay of catalases and peroxidases.* Methods Biochem. Anal., 1954. **1**: p. 357-424.
28. Wilming, M., Iffland, A., Tafelmeyer, P., Arrivoli, C., Saudan, C., and Johnsson, K., *Examining reactivity and specificity of cytochrome c peroxidase by using combinatorial mutagenesis.* Chembiochem, 2002. **3**(11): p. 1097-1104.

# Chapter 5

## *Probing Aromatic Binding in APX using Directed Evolution*

# 5.1 Directed molecular evolution

"In nature evolution and creation of new functionalities is achieved by mutagenesis, recombination and survival of the fittest" [1]. Darwin showed that if a particular characteristic had benefit to the individual, then this individual was more likely to survive and pass this characteristic on to its offspring [2]. Directed evolution mimics the process of natural evolution and is a process of iterative cycles of producing mutants and finding the mutant with the desired properties reducing the timescale of natural evolution from millions of years to months or weeks. Directed evolution is broadly used in two major applications [1]:

1. Industrial biocatalysis: enzymes are engineered to produce suitable biocatalysts with high catalytic activity and stability.
2. Research: directed evolution has become a new tool for understanding the molecular basis of protein function, structure and the natural evolutionary process.

## *5.1.1 Biocatalysis*

Enzymes (biocatalysts) are molecular machines that have the ability to accelerate even the most complex chemical reactions by many orders of magnitude with unsurpassed selectivity and specificity. Features of biocatalysts, such as high stereo-, chemo- and regioselectivity at ambient temperatures, pHs, pressures and often under mostly aqueous conditions, makes them far superior to most chemical catalysts. With applications ranging from commercial synthesis to biomedical research there is great demand for enzymes with improved activity and novel catalytic function [1, 3-5]. Biocatalysts are already used in many synthetic applications, currently more than 500 commercial products use enzymes in their synthesis including the sweetener aspartame and the antibiotic amoxicillin [4]. The demands of modern synthesis and their commercial applications were obviously not targeted during the natural evolution of enzymes and the activities of natural molecules are often reduced when they are used for technological or medical purposes [6]. Two technologies have the potential to alter enzyme function so that they are more efficient and better suited to a particular purpose:

1. Rational design: this technique is very information-intensive requiring the availability of structure of the enzyme and a knowledge of how the structure is related to the function. Rational design requires the identification of specific sites that can be manipulated in order to enhance particular properties of the enzyme such as substrate specificity or thermostability. The information intensive requirement of rational design can be some what overcome by the use of large public structure data bases and molecular modelling to predict how to increase selectivity, activity and stability of enzymes even with a lack of structural data by using enzymes with high homology as models, however the effect of the change, even if the structure and catalytic cycle are well known is often difficult to predict. Another major drawback is that changing one or two amino acids in hundreds often has little effect when planning total catalytic redesign [3, 4, 7, 8].

2. Directed evolution: this technique is highly attractive because it has simple principles which don't require an extensive knowledge of structure, function or mechanism. Many of the mutations identified in directed evolution experiments have been found far from the active site and in many cases the mutated residue does not come into contact with the substrate [9], this leads to examples of improved enzyme variants with mutations that would have not have been considered in the rational design process.

### *5.1.2 General strategy for directed evolution experiments*

There are two fundamental components of any directed evolution experiment: (1) the creation of a library of mutant proteins, (2) selection of proteins with the desired phenotype from a large pool of related phenotypes [10] (Figure 5.1).

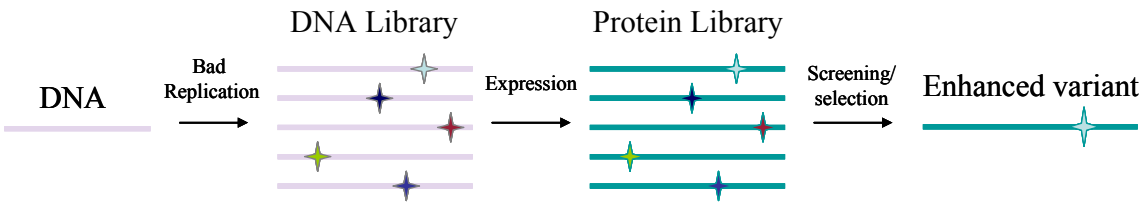


**Figure 5.1: Representation of a standard directed evolution experiment**

Mutations are represented by stars, for clarity only five mutants are shown, in reality there would be thousands.

The first step in any directed evolution experiment is the creation of diversity. The most straightforward approach to create a library of proteins is to introduce random mutations into the gene encoding the protein. It is essential to maintain the link between the gene and the protein but this gives the advantage that mutations created can be easily identified by DNA sequencing.

Although the production of an extensive and unbiased library is very important, the success of a directed evolution experiment depends on the method that is used to find the best mutant enzyme *i.e.* the screen or the selection process [11].

#### *5.1.2.1 Creation of diversity*

Methods for the creation of protein-encoding DNA libraries may be broadly divided into 3 categories [10].

1. Random methods which introduce changes at positions throughout a gene sequence.
2. Focused methods which group together methods used to cause randomization at specific positions in a gene sequence.
3. Recombination methods which bring existing diversity together in new combinations.

No consensus about which method of creating diversity has emerged and it remains unclear whether it is more efficient to mutate the whole enzyme randomly or just its active site. Experimental evolutionists generally base the choice of method on intuition rather than a systematic understanding of adaptive protein evolution [12].

#### *5.1.2.2 Random mutagenesis*

Introduction of point mutations into random positions within the entire gene sequence can be achieved either *in vitro* or *in vivo*. *In vivo* methods exploit the lack of DNA repair capability in mutator strains of *E. coli* such as XL1-Red strain (Stratagene). This is a very simple way of mutating DNA but the mutagenesis is indiscriminate and so host genome DNA is also affected meaning that cells are very slow growing and constructing a library containing 1-2 nucleotide changes per gene can require several passages of the DNA through the mutator strain [10]. One successful example of this approach was the mutation of an esterase from

*Pseudomonas fluorescens* to produce an enzyme with altered substrate specificity [13].

The *in vitro* approach exploits the error prone nature of the Polymerase Chain Reaction (PCR). Although the level of mutation produced in a normal PCR is not high enough for the creation of a library for directed evolution there are two ways to increase the level of mutations: the use of $Mn^{2+}$ and biased levels of dNTPs to increase the error rate of Taq polymerase and the use of Mutazyme®, a highly error prone DNA polymerase from Stratagenes GeneMorph® kit [10].

Taq polymerase has an error rate of 0.001% to 0.02% per nucleotide per pass of the polymerase depending on the reaction conditions [14]. The presence of $Mn^{2+}$ along with the over representation of dGTP and dTTP leads to error rates of ~ 1 nt/kb, the level of mutagenesis can be controlled by the number of amplification cycles and the final concentration of $Mn^{2+}$ in the reaction. The level of mutagenesis when using Mutazyme® can be controlled by the concentration of template DNA used and the number of amplification cycles [10].

An ideal library is one in which all possible mutants are equally represented [10] but error prone PCR has a source of bias, specific types of error are more common than others for example conversion of one nucleotide to another occurs much more often than single nucleotide insertions or deletions. This is desirable for library construction as insertions and deletions lead to frameshifts which often lead to non-functional proteins.

#### *5.1.2.3 Focused mutagenesis*

Focused mutagenesis introduces random mutations at specific points in the gene sequence known to be important via structural studies or PCR. A thorough study of the role of an important residue requires substitution with all 19 other amino acids: saturated site mutagenesis. This method uses high fidelity PCR but instead of using two primers it uses a mixture of primers which between them contain the codon for all 20 amino acids at the chosen position. The codon of interest is completely randomized at the first two positions and has G or C at the third position meaning that only one stop codon is possible. Saturated mutagenesis can be used to change between one and five amino acids in a single PCR experiment but if more residues are changed more screening is required in order to observe every possible combination of mutations. For

example mutation of one residue gives 20 different PCR products and 200 colonies need to be screened to observe each product. If two residues are mutated 2000 possible PCR products are produced meaning that 20,000 colonies need to be screened [12, 15, 16].

### *5.1.2.4 Recombinatorial mutagenesis*

The methods described so far introduce diversity into the gene sequence. Natural evolution also incorporates recombination, bringing together advantageous mutations in novel ways and separating out deleterious ones [10]. DNA shuffling (Figure 5.2) refers to the *in vitro* homologous recombination of a library of genes and was first introduced by Stemmer in 1994 [17]. The method of DNA shuffling involves digesting copies of the genes in the library with DNase I giving a pool of different sized DNA fragments, fragments from different genes are brought together by PCR reassembly to create a new gene library containing novel sequences [6, 17, 18].

A variation on this, StEP (staggered extension process) (Figure 5.2) is also widely used in directed evolution experiments. StEP is similar to DNA shuffling in that it requires repeated cycles of PCR to build full length genes. In StEP, a PCR experiment using the original gene pool as template DNA is carried out; by keeping the extension time short only partial elongation is possible. The growing strand is melted from the template and may anneal to a different template in the next cycle creating a crossover [6, 10, 18].

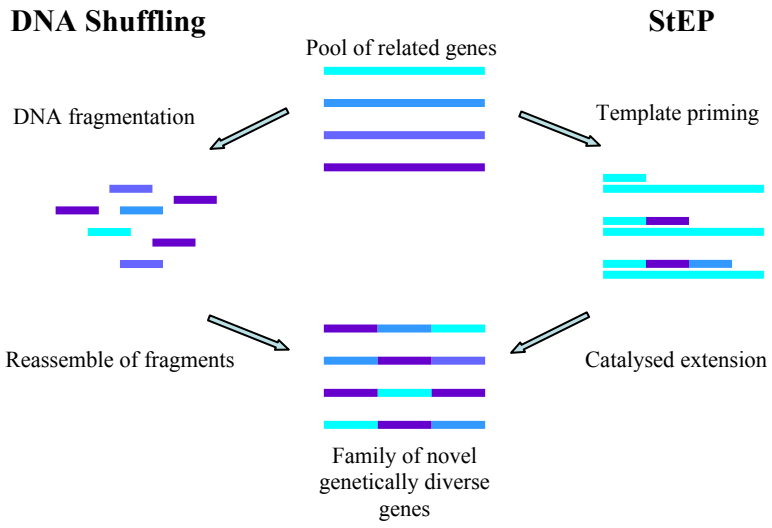


**Figure 5.2: Representation of DNA shuffling and StEP**

Various other recombination techniques are also available such as RACHITT [19] (random chimeragenesis on transient templates), which is conceptually similar to StEP but allows many more crossovers, and ITCHY [20] (iterative truncation for the creation of hybrid enzymes). Using ITCHY it is possible to recombine gene sequences with as little as 50 % homology which is useful since genes which encode functionally very similar proteins do not always have high levels of sequence homology.

#### *5.1.2.5 Selection and screening*

Choosing the mutated proteins with the desired property is often the most challenging part of a directed evolution experiment and can be achieved either through selection or screening. The basis of all screening and selection methodologies is a linkage between the gene, the enzyme it encodes and the product of the activity of the enzyme [21].

Screening and selection methods should meet a number of requirements; they should directly detect the property of interest "you get what you select for" is the first rule of directed evolution [22]. The first rounds of selection/screening require high isolation so that all mutants, even variants with very small improvements will be selected. Further rounds of screening need to be more stringent so that only the best mutants are isolated [21].

Selection mimics the natural survival of the fittest strategy and is the most efficient method of finding the best mutant since only mutants with the desired phenotype will survive the process. For example, in order to evolve temperature resistant mutants the library can be grown at high temperatures and only those with mutations that confer temperature resistance will grow. It is not always possible to use selection to distinguish between different enzymes in a library as it requires the activity of interest to be essential to the bacterium, however, it is possible to couple the activity of interest to an essential process of the bacterium allowing selection to be used but this is often very challenging. The advantage of selection is that much larger libraries of mutants can be examined; the number of colonies that can be subjected to selection are generally five orders of magnitude above those that can be sorted using advanced screening.

Screening requires the activity of interest to be directly observable using physical or biochemical analysis. Mutants need to be spatially separated either by spreading them on an agar plate or by the use of 96-well microtiter plates in order to analyse individual colonies. Screens need to be simple and efficient so that as many colonies as possible can be examined. Commonly used assays for enzymatic activity are based on visual detection for example the formation of coloured or fluorescent products or halos around a colony on a plate [1, 6, 21]. However "screenings on the basis of colour or halo formation are at best semi-quantitative and rather insensitive to tiny changes in enzymatic activity" [6]. Colorimetric assays are still widely used, for example, the formation of a blue product, 5-bromo-4-chloro-3indolyl β-galactoside (X-Gal), can be used to assay β-galactosidase activity.

#### *5.1.2.6 Directed molecular evolution of heme proteins*

Heme enzymes are prime targets for biocatalyst engineering and although few directed evolution experiments have been performed on heme enzymes due to difficulties with heterologous expression and screening, there are still examples of successful experiments in the literature.

Redox enzymes such as peroxidases catalyse valuable reactions on a vast spectrum of substrates and although they have synthetic potential, due to their relative complexity and sometimes low catalytic activity this potential is often unrealised. Directed evolution of these enzymes can be used to improve existing functions which may not be biologically relevant. Such evolutionary design experiments will provide new insights into structure function relationships as they also work to develop useful catalysts [6, 18].

Heme enzymes are a rich source of potential industrial biocatalysts and an excellent testing ground for directed evolution experiments. Many experiments have already generated heme enzymes with novel abilities and the same approaches should allow further exploration of the interconversion of function between different heme enzymes and hopefully to allow us a better understanding of how protein structure modulates heme chemistry [6].

Examples of directed evolution of heme enzymes include the increase in intrinsic peroxidase activity of Catalase I from 2 % to 58 % by Matsuura *et al* [23], the alteration of the substrate specificity of $P450_{BM-3}$ to allow it to hydroxylate indole

by Li *et al* [24] and a 25-fold increase in the intrinsic peroxidase activity of horse heart myoglobin by Wan *et al* [25].

#### *5.1.2.7 Directed evolution of heme peroxidases*

Peroxidases oxidise a wide variety of substrates and are ideally suited to directed evolution experiments. Striking examples for the functional diversity of heme-containing peroxidases can be found within the super family of bacterial, plant and fungal peroxidases whose members not only oxidise a wide variety of different substrate, but also possess different locations of their substrate binding sites [18].

One of the most important questions in heme peroxidase chemistry is how the protein scaffold controls the reactivity of the heme cofactor. In order to probe this question Iffland *et al* [26] used directed evolution to create C*c*P mutants with novel substrate specificities. The aim of their work was to generate mutants with increased activity against the classical peroxidase substrate guaiacol. After three rounds of DNA shuffling and screening mutants were isolated with a 300-fold increase in guaiacol activity and a 1000-fold increase in specificity for guaiacol over the natural substrate cytochrome *c* all selected mutants contained the mutation Arg48His, thought to reduce the steric constraints for guaiacol access to the binding site whilst still providing enough charge to maintain activity.

Cherry and co workers [27] evolved a fungal peroxidase (ARP) to resist high temperatures, high pH and high hydrogen peroxide concentrations. The best mutant showed a 174-fold increase in thermal stability and a 100-fold increase in oxidative stability. Morawski et al [28] increased the activity of horseradish peroxidase (HRP) by a total of 40-fold compared to the wild type with a 5.4-fold increase in activity towards ABTS and a 2.3-fold increase in activity towards guaiacol.

## 5.2 Directed evolution of APX

As stated previously in this Thesis and elsewhere, it has been shown by mutational studies that APX contains two distinct binding sites, one for ascorbate and one for aromatic substrates, and although the location of this site was proposed to be at the δ-heme edge it was not until the resolution of the APX-salicylhydroxamic acid (SHA) crystal structure [29] that structural evidence was obtained.

The overall aim of this work was to enhance the rate of aromatic oxidation by APX by directed evolution hopefully leading to information of how guaiacol binds at the δ-heme edge. The oxidation of aromatic compounds is an important step in many synthetic reactions; a quick and mild way to carry out this reaction could prove useful to both industry and academia.

A colorimetric screen for the oxidation of aromatic substrates by APX has been designed by Sharp [30] which involves the oxidation of colourless guaiacol to the red product tetraguaiacol. The main aim of the directed evolution project was therefore to create diversity in the APX gene by random and saturated site mutagenesis and to assess the kinetic parameters of the mutants selected by the screen.

A total of seven protein libraries were created, four using saturated mutagenesis on residues thought to be involved in aromatic binding and three using random mutagenesis throughout the gene sequence in an attempt to discover novel residues that may be important in aromatic oxidation. The libraries created were screened using a colorimetric screen based on the production of red tetraguaiacol from the oxidation of colourless tetraguaiacol; two variations on the screen were used. A selection of mutants chosen from the screen were expressed, purified and the efficiency of the screen was assessed by determining guaiacol activity either by using the standard guaiacol assay or by using a stopped-flow based assay and comparing their activity to the activity of the wild type.

## *5.2.1 Creation of diversity*

### *5.2.1.1 Site saturated mutagenesis*

The residues targeted for saturated mutagenesis were originally chosen by Sharp based on a model of guaiacol bound into the aromatic binding site (Figure 5.3(A)) which was produced using the APX-salicylhydroxamic acid crystal structure as a starting point [29].

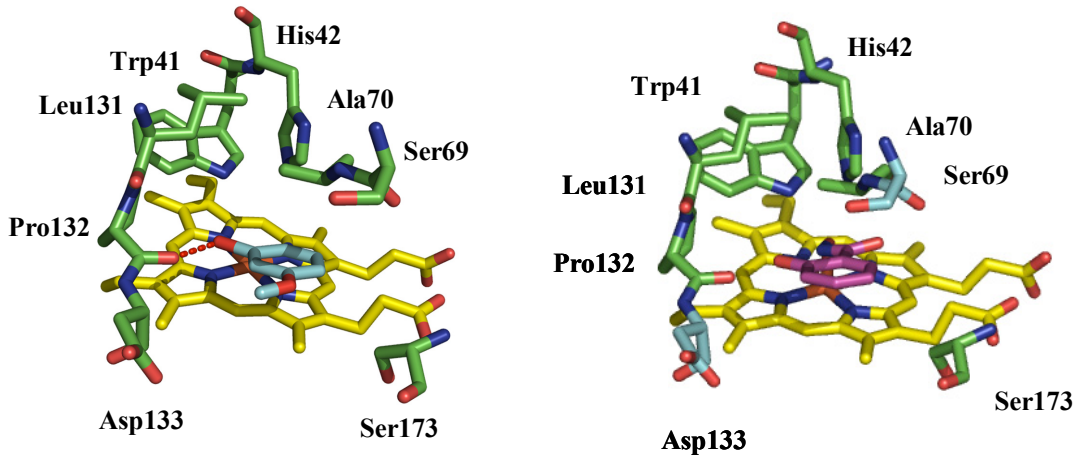


**Figure 5.3: Model of guaiacol binding to APX based on the APX-SHA complex structure**

The heme is shown in yellow with residues thought to be important in substrate binding indicated. (Left panel) The modelled guaiacol is shown (cyan) and proposed hydrogen bonds are indicated by red dashes. The model is based on (Right panel) APX-SHA complex (PDB entry 1V0H), and was created using PyMOL [31]. The heme is shown in yellow, the bound SHA is shown in violet and residues chosen for saturated mutagenesis are shown in cyan.

Residues that may affect guaiacol binding are Ser69, Ala70, Leu131, Asp133 and Ser173. Ala70 forms a hydrophobic pocket and is likely to be a key residue in guaiacol binding so mutations here may reduce guaiacol binding. Leu131 is orientated away from the guaiacol molecule and so is unlikely to play a key role in guaiacol binding. Ser173 is equivalent to Phe179 in HRP which is thought to be a key residue in the formation of hydrophobic interactions for guaiacol binding in HRP [32], although in APX it is hydrogen bonded to the heme and mutations here may lead to destabilisation of the heme. Ser69 is 6 Å away from the proposed guaiacol binding site but is equivalent to Phe68 in HRP, which is thought to provide a hydrophobic pocket for guaiacol binding in HRP [32] and the introduction of an aromatic residue at Ser69 may increase aromatic oxidation by aiding guaiacol binding. Asp133 is equivalent to Phe142 in HRP and may help to create a hydrophobic environment for guaiacol binding in HRP; mutations at this residue may also increase the rate of aromatic oxidation.

From the analysis of the model two residues were chosen to be subjected to saturated mutagenesis; Ser69 and Asp133 (Figure 5.3(B)). A separate library was created for each in order to minimize the amount of screening needed. The saturated mutagenesis libraries were created using Quikchange® site-directed mutagenesis kit

(Stratagene) and oligonucleotides with a degenerate NNS codon at the point of mutation, where N is equal amounts of all four bases and S is guanine and cytosine in equal amounts, were used. The best mutations from each of the saturated mutagenesis libraries, selected via the guaiacol screen, (see section 5.2.2.1) were used as a template for a second round of saturated mutagenesis producing two saturated mutagenesis libraries: S69P/D133X and S69X/D133R.

### *5.2.1.2 Random mutagenesis*

#### 5.2.1.2 (a) Random mutagenesis via error prone PCR using GeneMorph® and Taq polymerase

Mutazyme® DNA polymerase in the GeneMorph® kit produces a unique spectrum of mutations compared to Taq DNA polymerase, both generate all possible nucleotide substitutions but the frequency of incorporating each type of mutation is different. For example Mutazyme® preferentially replaces Gs or Cs with As or Ts whereas Taq polymerase tends to replace As or Ts with Cs or Gs. Because the production of representative mutant libraries is desired, in which all types of mutation are equally likely, two types of random mutagenesis library were produced: one using Taq polymerase and the other using Mutazyme®

For the creation of the library using Mutazyme® the PCR conditions were optimized to give the strongest band in agarose gel. Only the gene was amplified and the PCR product was religated into empty pQE30 vector. The level of template used (31.25 ng) should have led to mutation levels of 3-7 mutations per gene. This was confirmed by sequencing of random colonies of XL1-Blue cells. The DNA was extracted from XL1-Blue cells and transformed into SG 1300 cells in order to create a protein library ready for screening, called Mut.

The creation of the Taq polymerase error prone PCR library was carried out with the aid of Dr. L. G. Otten and Dr. Florian Hollfelder (Department of Biochemistry, Cambridge University). The PCR was optimised using various amounts of $Mn^{2+}$ cofactor to give different levels of mutagenesis. Again, using the forward and reverse pQE30 sequencing primers in the PCR meant that just the APX gene was amplified so it was necessary to reinsert the gene into the vector before transformation into XL1-Blue cells. Two libraries were created: one with 0.1 mM $Mn^{2+}$ giving average mutation levels of two nucleotide changes per gene, and the other with 0.3

mM $Mn^{2+}$ giving average mutation levels of four nucleotide changes per gene: mutation levels were confirmed by sequencing of random colonies. DNA was extracted from XL1-Blue cells and transformed into SG 1300 cells to produce two protein libraries ready for screening; ep0.1 and ep0.3.

#### 5.2.1.2(b) Random mutagenesis using DNA repair pathway deficient *E. coli*

The pQE30 vector containing APX was extracted from XL1-Blue cells and transformed into commercially available XL1-Red cells (Stratagene). XL1-Red cells are deficient in DNA repair so as they replicate the plasmid naturally occurring errors, that are normally repaired, are ignored to produce mutated plasmids. After ~72 hours of growth, monitored by UV-visible spectroscopy, the plasmid was extracted and retransformed into fresh XL1-Red cells; this process was repeated four times. According to Stratagene (www.stratagene.co.uk) the mutation rate of XL1-Red cells is 1 mutation per 2000 nucleotides per 24 hours of growth. After the four rounds of extraction, transformation and growth each colony should contain an APX gene that had ~11 point mutations. Random colonies were chosen and the DNA extracted and sequenced, all the chosen colonies contained wild type APX. A possible reason for this is that the XL1-Red cells themselves are evolving; those that have more efficient DNA repair are more likely to survive, hence the cells revert back to wild type cells and mutation is no longer carried out.

## *5.2.2 The screen for directed evolution*

### *5.2.2.1 Sharp guaiacol screen*

This screen was developed by K. H. Sharp [30] in collaboration with Dr. T. Fleming and Prof. N. Turner (Chemistry department, University of Edinburgh) and is based on a screen to detect $H_2O_2$ production by monoamine oxidase (MAO-N) [33]. The colorimetric screen detects formation of red tetraguaiacol (Figure 5.5).

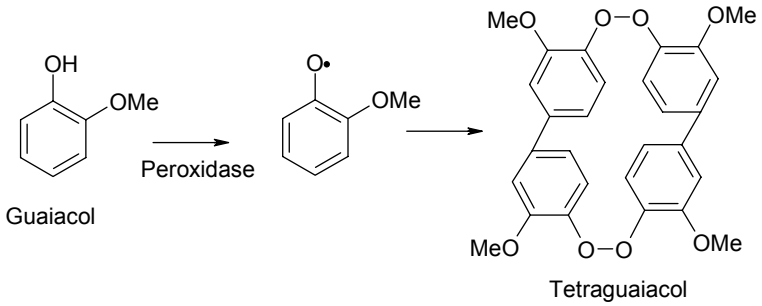


**Figure 5.4: The formation of tetraguaiacol**

Four molecules of oxidised guaiacol come together to form red tetraguaiacol.

Protein libraries contained within SG 1300 supercompetent cells were grown up on nitrocellulose membranes and expression of APX was induced using isopropyl-β-D thiogalactopyanside (IPTG). The membranes were then frozen at -80 ºC to partially lyse the cells and to allow APX to interact with guaiacol whilst ensuring that live cells remained within each colony for later growth. Molten agar containing guaiacol and $H_2O_2$ was poured directly over the membrane.

Colonies containing wild type APX take approximately 45 minutes to stain red and any colonies containing APX mutants with enhanced activity should stain red quicker than this (Figure 5.6). DNA was extracted from the selected colonies and sequenced in order to identify the mutations.

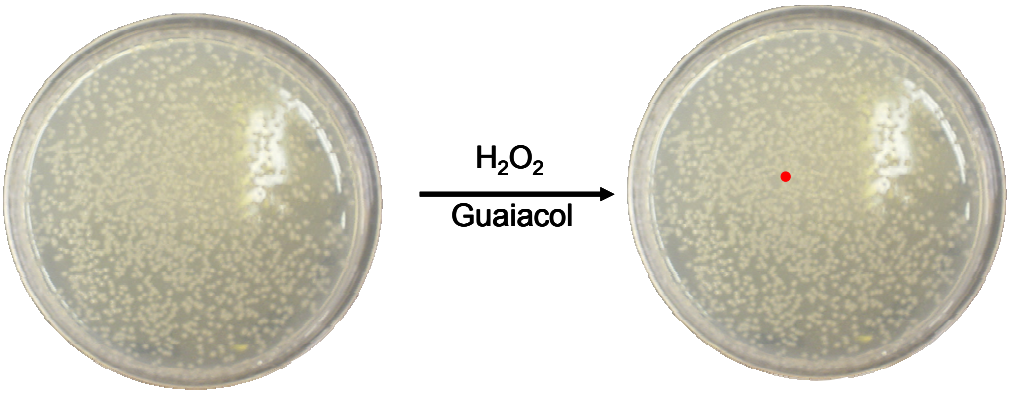


**Figure 5.5:Representation of the guaiacol screen [30]**

The red dot indicates a colony containing an APX mutant with increased activity towards guaiacol.

The screen presented above is very efficient and the colour producing reaction is directly coupled to the desired activity so the screen will not give false positives,

however the depth of the agar above the colonies means that the colour change of the colonies upon guaiacol oxidation is minimal and can be difficult to detect. The tetraguaiacol produced is soluble and quickly diffuses into the agar meaning that the colour change is time sensitive and must be monitored very closely.

#### *5.2.2.2 Iffland guaiacol screen*

The screen proposed by Iffland *et al* [26] utilises the same colorimetric principles as the Sharp screen with a few simple changes. The main change is that instead of pouring molten agar over the membrane, membranes displaying protein libraries were placed on filter paper that had been soaked in guaiacol/$H_2O_2$ solution. Colonies containing wild type APX stained red after approximately seven minutes, the colour change was more pronounced, and tetraguaiacol once formed did not diffuse from the colony that produced it.

A second difference is that the cells are partially lysed by dipping the membranes displaying the library briefly into liquid $N_2$ and allowing to air dry. This speeds up the screening process and still leaves viable cells in the colonies.

### *5.2.3 Summary of enhanced variants*

#### *5.2.3.1 Enhanced variants from saturated mutagenesis*

Approximately 200 colonies were screened containing the S69X saturated mutagenesis library, many of the colonies stained red faster than colonies containing wild type APX. The five colonies which stained red quickest were picked from the screen and grown up overnight. DNA sequencing was carried out to determine the mutations. Three out of the five colonies chosen, including the two fastest had a proline residue instead of the serine residue at position 69. The two others had either threonine or glutamine at position 69.

Approximately 200 colonies were screened containing the D133X saturated mutagenesis library, again there was variation in the rate at which the colonies stained red and the five quickest staining colonies were grown up overnight and their DNA extracted and sequenced; three of the colonies had an arginine residue at position 133, the other two had either glutamate or glutamine at position 133.

Screening of 200 colonies from each of the saturated mutagenesis libraries containing the double mutants (one library with proline at position 69 and all 20 possible amino acids at position 133, the other library with arginine at position 133 and all 20 possible amino acids at position 69) was carried out. The five quickest staining colonies from the S69P/D133X library were grown up and their DNA extracted and sequenced; all five had an asparigine at position 133.

From the S69X/D133R library just two colonies were chosen from the screen and grown up overnight and both were found to contain a threonine residue at position 69. A summary of the mutants and the saturated mutagenesis library they were selected from is shown in Table 5.1.

**Table 5.1: Summary of mutants selected from saturated mutagenesis libraries**

| *Saturated Mutagenesis library* | *Mutant selected from the screen* |
|---|---|
| **S69X** | S69P |
| | S69T |
| | S69Q |
| **D133R** | D133R |
| | D133N |
| | D133E |
| **S69P D133X** | S69P/D133N |
| **S69X D133R** | S69T/D133R |

### *5.3.1.2 Enhanced variants from random mutagenesis*

Each of the random mutagenesis libraries produced were spread onto ten nitrocellulose membranes, each membrane displayed approximately 100 colonies, meaning that 1000 colonies were screened for each of the three libraries created. From all of the screens 8 colonies were chosen in total which all stained red faster than the other colonies on the membrane. Three colonies were chosen from the library created using Taq polymerase and 0.1 mM $Mn^{2+}$, they were grown up overnight and their DNA extracted. DNA sequencing revealed that two of the colonies chosen contained D133R APX and the third contained the mutation D133R plus an additional mutation

at position 105 where valine was replaced with isoleucine giving the double mutant V105I/D133R.

Three colonies were also chosen from the random mutagenesis library created using Taq polymerase and 0.3 mM $Mn^{2+}$. The DNA extracted from these colonies all had different mutations, they all contained the D133R mutation; one had no additional mutations; one had an additional mutation where glycine at position 50 was replaced by aspartate and the other where valine at 105 was again replaced by isoleucine to give the double mutants G50D/D133R and V105I/D133R respectively. Two colonies were chosen from the random mutagenesis library created using Mutazyme®. The colonies were again grown up overnight and the DNA extracted. Sequencing revealed that both colonies selected contained APX with a single mutation; one had the recurring D133R mutation and the other contained the mutation D133N.The mutants and the random mutagenesis library they were selected from are summarised in Table 5.2.

**Table 5.2: Summary of mutants selected from random mutagenesis libraries**

| *Random Mutagenesis library* | *Variants selected from the screen* |
|---|---|
| **Ep0.1** | D133R |
| | V105I/D133R |
| **Ep0.3** | D133R |
| | G50D/D133R |
| | V105I/D133R |
| **Mut** | D133R |
| | D133N |

# 5.3 Expression of selected variants

## *5.3.1 Expression of variants*

Samples of APX variants were prepared from *E. coli* SG 1300 supercompetent cells (containing the pREP4 vector) incorporating a pQE30-APX construct and purified as described in Chapter 3. Samples with $R_z$ values of greater than two were considered pure. Five mutant variants were selected for protein preparation, S69P,

D133R, D133N, S69P/D133N and G50D/D133R which were all compared to wild type APX.

#### *5.3.1.1 Electronic absorption spectra*

Electronic absorption spectra were obtained for the five selected variants produced. Analysis reveals wavelength maxima ($\lambda_{max}$/nm) at 407, 506, 540$^{(sh)}$ and 636 in all cases. There were no significant differences between the wild type protein and the five mutants.

## 5.4 Steady state kinetics

In order to ensure that the screen is enabling selection of mutations that really do confer enhanced aromatic activity, steady state analysis was carried out on the five fastest mutants selected from all seven protein libraries. Standard guaiacol assays were carried out, however, the results from the standard assay did not show a significant enhancement of guaiacol oxidation by the mutants chosen from the screen, in order to confirm these results assays were carried out using stopped-flow spectrophotometry. A single-mixing experiment was carried out at a single wavelength (470 nm), one syringe contained $H_2O_2$ solution to initiate the peroxidase reaction; the other contained a pre-mixed solution of APX and guaiacol. The concentrations of enzyme and $H_2O_2$ were kept constant and the concentration of guaiacol was varied as in the standard guaiacol assay. The solutions were shot into the cell and the increase in absorption at 470 nm measured as a function of time over a period of 10 seconds, the stopped-flow apparatus has a dead time of just 1 ms meaning that it is possible to measure the initial part of the reaction even at high guaiacol concentrations. The rate of tetraguaiacol production was determined by fitting the initial part of the curve to a linear plot and calculating the gradient.

The assay was carried out for the five mutant enzymes produced and the wild type, but inconsistent data were obtained that had a large decrease in activity at higher concentrations of guaiacol. In order to overcome this the assay was carried out as it is in the screen *i.e.* to pre-mix $H_2O_2$ and guaiacol and initiate the reaction by addition of enzyme, this may prevent the enzyme being inhibited by saturation with guaiacol. Three independent assays were carried out for each of the mutants and wild type APX and the initial rate of reaction plotted versus substrate concentration (Figure 5.7), $k_{cat}$

and $K_M$ were determined by fitting the plots to the Michaelis-Menten equation as seen previously. The steady state kinetic data for wild type APX and the five mutants examined are compared in Table 5.3.

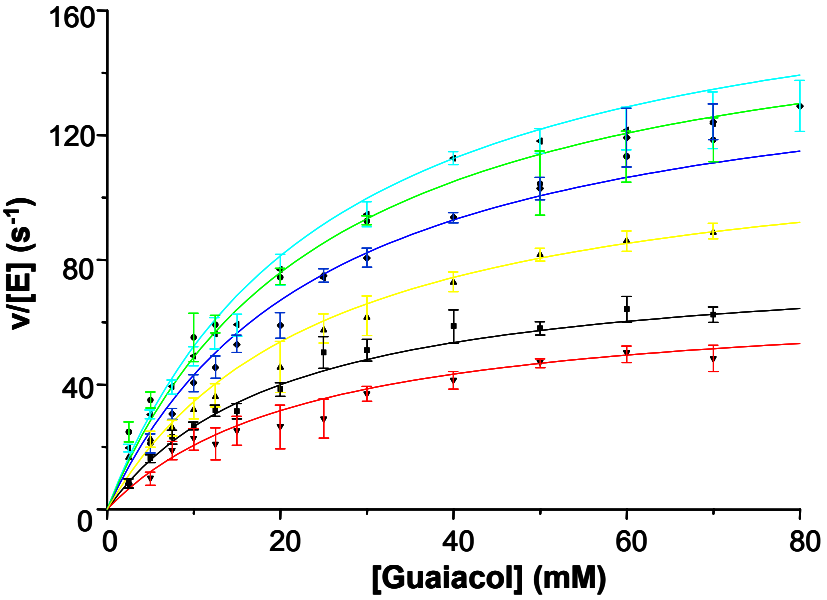


**Figure 5.6: Steady state oxidation of guaiacol by mutants examined in this Chapter**

Conditions: [Enzyme] = 100 nM, 25 ºC, 100 mM KPi, pH 7.0. The lines represent a fit of the data to the Michaelis-Menten equation. Wild type APX (black), S69P (red), G50D/D133R (yellow), D133N (blue), D133R (green), S69P/D133R (cyan). Average values of three independent measurements are shown; error bars represent standard deviation.

**Table 5.3: Steady state kinetic data for guaiacol oxidation**

Values are shown for wild type APX and five mutants selected using the guaiacol screen. Each value is an average of at least three independent measurements.

| *APX* | $k_{cat}$ ($s^{-1}$) | $K_M$ (mM) | $k_{cat}/K_M$ ($s^{-1}$ $mM^{-1}$) |
|---|---|---|---|
| **Wild type APX** | 82.1 ± 2.8 | 20.3 ± 2.0 | 4.0 |
| **D133R** | 175.5 ± 7.2 | 26.2 ± 2.4 | 6.7 |
| **G50D/D133R** | 142.4 ± 4.3 | 24.5 ± 1.3 | 5.8 |
| **S69P/D133N** | 182.2 ± 3.6 | 26.6 ±1.2 | 6.9 |
| **S69P** | 68.3 ± 3.6 | 23.6 ± 2.9 | 2.9 |
| **D133N** | 150.9 ± 5.1 | 28.7 ± 2.6 | 5.3 |

## 5.5 Discussion

The main aim of the Chapter was to use directed evolution to enhance the activity of APX towards aromatic compounds. The two steps in the directed evolution experiment, namely the creation of diversity and the selection of improved mutants has been carried out efficiently but has failed to produce a mutant with a significantly enhanced rate (i.e >10-fold) compared to wild type APX. Sequencing of mutanst produced by saturated mutagenesis showed that this protocol gave a high level of success. The D133R mutant was selected consistently from the screen, sometimes as a single mutation and other times in combination with other mutations such as G50D and V105I. The change from an aspartate residue to an arginine residue, Figure 5.8, is a charge reversal and would not have been considered during a rational design experiment.

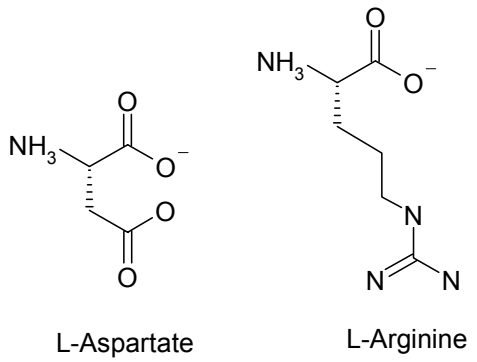


**Figure 5.7: Structures of aspartate and arginine**

Steady state kinetic analysis of D133R and D133N along with the double mutant G50D/D133R showed no significant increase in the rate of guaiacol oxidation with a comparable $k_{cat}$ to wild type APX. The reason that this mutant was selected consistently from the screen remains unclear. The $K_M$ is not significantly altered and so it is unlikely that the mutations at this position lead to an increased ability to bind guaiacol. Crystal structures or molecular modelling of guaiacol into a model of the mutated active site may provide further insights into this, however, crystallisation was not achieved.

A second mutation consistently selected from the screen was S69P and again steady-state kinetic analysis of this mutant showed no significant increase in activity towards guaiacol. In any screen there is a certain amount of phenotypic variation between colonies, for example, a screen of a membrane displaying only wild type

colonies will show some variation in the time each colony takes to stain red. Typically in the Sharp screen wild type colonies will all stain red within approximately seven minutes of each other. This phenotypic variation is a result of factors such as colony size, protein expression levels within each colony and time taken for substrate to become available to each colony. However, the S69P and D133R mutants were consistently selected from the screen independently of which mutagenesis process was used to create the variation. In the Iffland screen (seven minutes) colonies containing these mutations stained red within two minutes, faster than even the most active wild type colony. A proline at position 69 is not an obvious choice to allow enhanced aromatic oxidation and, as shown by the steady state kinetics, appears to have no affect on the rate of aromatic oxidation. A possible reason that these mutants are selected from the screen is that they may have enhanced levels of heme uptake, meaning that colonies containing them have a higher percentage of holoenzyme than other colonies and so stain quicker, in order to prove this hypothesis the $R_z$ value of purified protein before hemin reconstitution could be compared to that of the wild type. Expression levels may also have been increased by the introduction of mutations at D133 and S69 although this is unlikely.

Although directed evolution has been shown to be a powerful tool in enhancing rates of enzymatically catalysed reactions, protein stability, and the range of substrates utilised by an enzyme [3, 6], the system to which it is applied needs to be suitable. In this case the natural rate of guaiacol oxidation by APX is high ($k_{cat}$ = 82.1 ± 2.8 $s^{-1}$) and a screen is needed which can distinguish between variants with a faster rate than that of the wild type. The screen used in this Chapter, although suitable for early rounds of directed evolution where the wild type protein has little latent activity towards the substrate, was not powerful enough to allow true selection of enhanced variants. Perhaps a more efficient way of screening mutants with enhanced guaiacol binding properties would have been to screen for mutants that possessed a lower $K_M$, for example by screening for colonies that turned red even in the presence of low guaiacol concentrations or competitive inhibitors such as isoniazid. Evolutionary strategies for creating enhanced enzymes require elaborate technical equipment and so to further study aromatic oxidation in APX using this method a screen needs to be devised which removes some of the factors hindering the efficiency of the screen used here. Controls need to be applied to colony size, levels of expression and availability of substrates in order to quantitatively assess the ability of a single variant to oxidise

aromatic substrates. This would require a vast amount of screening with a higher degree of accuracy which in turn would require a higher degree of automatization.

## 5.6 References


1. Otten, L.G. and Quax, W.J., *Directed evolution: selecting todays biocatalysts.* Biomol. Eng., 2005. **22**: 1-9.
2. Darwin, C., *The origin of the species*. 1859: Penguin.
3. Bornscheuer, U.T. and Pohl, M., *Improved biocatalysts by directed evolution and rational protein design.* Curr. Opin. Chem. Biol., 2001. **5**: 137-143.
4. Johannes, T.W. and Zhao, H., *Directed evolution of enzymes and biosynthetic pathways.* Curr. opin. Mol., 2006. **9**: 1-7.
5. Baker, K., Bleczinski, C., Lin, H.N., Salazar-Jimenez, G., Sengupta, D., Krane, S., and Cornish, V.W., *Chemical complementation: A reaction-independent genetic assay for enzyme catalysis.* Proc. Natl. Acad. Sci. USA, 2002. **99**(26): 16537-16542.
6. Brakmann, S., Johnsson, K (Eds.), *Directed molecular evolution of proteins or how to improve enzymes for biocatalysis*. 2002, Weinheim: Wiley-VCH. 357 Pages.
7. Voigt, C.A., Kauffman, S., and Wang, Z.-G., *Rational evolutionary design: The theory of in vitro protein evolution.* Adv. Prot. Chem., 2001. **55**: 79-155.
8. Pluckthun, A., Schaffitzel, C., Hanes, J., and Jermutus, L., *Methods in enzymology*. Vol. 1. 367-429. 1991: Academic Press Inc.
9. Kazlauskas, R., *Enzymes in focus.* Nature, 2005. **436**: 1096-1097.
10. Neylon, C., *Chemical and biochemical strategies for the randomization of protein encoding DNA sequences: library construction methods for directed evolution.* Nucleic Acids Res., 2004. **32**(4): 1448-1459.
11. You, L. and Arnold, F.H., *Directed evolution of of subtilisin E in Bacillus Subtilis to enhance total activity in aqueous dimethylformamide.* Protein Eng., 1996. **9**: 77-83.
12. Parikh, M.R. and Matsumara, I., *Site-saturation mutagenesis is more efficient than DNA shuffling for the directed evolution of beta-Fucosidase from beta-galactosidase.* J. Mol. Biol., 2005. **32**: 1-8.
13. Bornscheuer, U.T., Altenbuchner, J., and Meyer, H.H., *Directed evolution of an esterase: screening of enzyme libraries based on pH-indicators and a growth assay.* Bioorg. Med. Chem., 1999. **7**: 2169-2173.
14. Cadwell, R.C. and Joyce, G.F., *Randomization of genes by PCR mutagenesis.* PCR Meth. Appl., 1992. **2**: 28-33.
15. Shultz, S.C. and Richards, J.H., *Site-saturation studies of beta-lactamase: Production and characterization of mutant beta-lacatamase with all possible amino acid substitutions at residue 71.* Biochemistry, 1986. **83**: 1588-1592.
16. Miyazaki, K. and Arnold, F.H., *Exploring nonnatural evolutionary pathways by saturation mutagenesis: Rapid improvement of protein function.* J. Mol. Evol., 1999. **49**(6): 716-720.
17. Stemmer, W.P., *Rapid evolution of a protein in vitro by DNA shuffling.* Nature, 1994. **370**: 389.
18. Wilming, M., Iffland, A., Tafelmeyer, P., Arrivoli, C., Saudan, C., and Johnsson, K., *Examining reactivity and specificity of cytochrome c peroxidase by using combinatorial mutagenesis.* Chembiochem, 2002. **3**(11): 1097-1104.
19. Coco, W.M., Levinson, W.E., Crist, M.J., Hektor, H.J., Darzins, A., Pienkos, P.T., Squires, C.H., and Monticello, D.J., *DNA shuffling methods for creating*

*highly recombined genes and evolved enzymes.* Nat. Biotechnol., 2001. **19**: 354-359.
20. Ostermeier, M., S., L., and Benokovic, S.J., *Rapid generation of incremental truncation libraries for protein engineering using alpha-phosphotioate nucleotides.* Nucleic Acids Research, 2001. **29**(16).
21. Ahoroni, A., Griffiths, A.D., and Tawfik, D.S., *High-throughput screens and selections of enzyme-encoding genes.* Curr. Opin. Chem. Biol., 2005. **9**: 210-216.
22. Schmidt-Dannert, C. and Arnold, F.H., *Directed evolution of industrial enzymes.* Trends. Biotech., 1999. **17**: 135-136.
23. Matsuura, T., Yomo, T., Trakulnaleamsai, S., Ohashi, Y., Yamamoto, K., and Urabe, I., *Nonadditivity of mutational effects on the properties of catalse I and its application to efficient directed evolution.* Protein Eng., 1998. **11**: 789-795.
24. Li, Q.S., Schwaneberg, U., Fisher, P., and Schmid, R.D., *Directed evolution of the fatty acid hydroxylase P450BM-3 into an indole-hydroxylating catalyst.* Chem. Eur. J., 2000. **6**: 1531-1536.
25. Wan, L., Twitchett, M., Eltis, L., Mauk, G., and Smith, M., *In vitro evolution of horse heart myoglobin to increase peroxidase activity.* Proc. Natl. Acad. Sci. USA, 1998. **95**: 12825-12831.
26. Iffland, A., Tafelmeyer, P., Saudan, C., and Johnsson, K., *Directed molecular evolution of cytochrome c peroxidase.* Biochemistry, 2000. **39**(35): 10790-10798.
27. Cherry, J.R., *Directed evolution of microbial oxidative enzymes.* Curr. Opin. Biotech., 2000. **11**(3): 250-254.
28. Morawski, B., Lin, Z.L., Cirino, P., Joo, H., Bandara, G., and Arnold, F.H., *Functional expression of horseradish peroxidase in saccharomyces cerevisiae and pichia pastoris.* Protein Eng., 2000. **13**: 377-384.
29. Sharp, K.H., Moody, P.C.E., Brown, K.A., and Raven, E.L., *Crystal Structure of the Ascorbate Peroxidase-Salicylhydroxamic Acid Complex.* Biochemistry, 2004. **43**: 8644-8651.
30. Sharp, K.H., *Substrate Binding Interactions in Ascorbate Peroxidase*, in *Chemistry*. 2005, University of Leicester: Leicester.
31. Delano, W.L., *The PyMOL Molecular Graphics System*. 2002, DeLano Scientific: San Carlos, CA.
32. Henriksen, A., Schuller, D.J., Meno, K., Welinder, K.G., Smith, A.T., and Gajhede, M., *Structural interactions between horseradish peroxidase C and the substrate benzhydroxamic acid determined by X-ray crystallography.* Biochemistry, 1998. **37**(22): 8054-8060.
33. Alexeeva, M., Carr, R., and Turner, N.J., *Directed evolution of enzymes: New biocatalysts for asymmetric synthesis.* Org. Mol. Chem., 2003. **1**: 4133-4137.

# Chapter 6

## *Neutron Diffraction Studies of Cytochrome c Peroxidase*

# 6.1 Introduction

A discussion of the chemistry of an enzyme requires an understanding of the protonation states of both the protein and any cofactors involved. The significance of the contribution of X-ray crystallography to the understanding of enzyme mechanism cannot be underestimated; however the requirement for electrons to scatter X-rays means that hydrogen atoms are usually invisible and can only be seen in crystal structures determined to ultra-high resolutions(< 1.0 Å) [1]. In many cases the positions of hydrogen atoms can be extrapolated from either bonded heavy atoms or deduced, however neutron diffraction can provide direct evidence for the protonation state of ionisable groups.

Neutron diffraction, along with X-ray crystallography and nuclear magnetic resonance (NMR), is a method used to determine macromolecular structure. It originated from the Manhattan Project that produced the atom bomb in 1945 [2], during pioneering work by Clifford G. Shull. Shull said "Scientists at Oak Ridge were very anxious to find real honest-to-goodness scientific uses for the information and technology that had been developed during the war at Oak Ridge and at other places associated with the wartime Manhattan Project." [3], he later received the Nobel prize "for the development of the neutron diffraction technique" [3].

A neutron diffraction experiment requires a neutron source, such as a nuclear reactor, and a neutron-sensitive detector. Like X-ray diffraction, neutron diffraction is a form of elastic scattering, where the neutrons exiting the sample have approximately the same energy as the incident neutrons, however, neutrons are scattered by atomic nuclei rather than electron clouds. Every electron has the same scattering length meaning that each element scatters X-rays proportionally according to its number of electrons, in contrast, for neutrons, each element has a characteristic scattering length which shows no regularity across the periodic table and can even be negative (*i.e.* for hydrogen). Coherent scattering, where the phase of the incident beam is preserved, gives rise to neutron diffraction patterns which can be mathematically inverted in order to derive the molecular structure of the sample in exactly the same way as an X-ray diffraction pattern. The scattering length of some biologically important elements are shown in Table 6.1 [1].

**Table 6.1:** Neutron Coherent scattering length and incoherent cross-sections

| *Element* | *No. of electrons* | *Incoherent cross-section (barns)* | *Coherent scattering length ($10^{-12}$ cm)* |
|---|---|---|---|
| $^{1}$**H** | 1 | 80.27 | -0.374 |
| $^{2}$**D** | 1 | 2.05 | 0.667 |
| $^{12}$**C** | 6 | 0.00 | 0.665 |
| $^{14}$**N** | 7 | 0.49 | 0.937 |
| $^{16}$**O** | 8 | 0.00 | 0.580 |
| $^{32}$**S** | 16 | 0.00 | 0.280 |
| $^{56}$**Fe** | 26 | 0.00 | 1.012 |

There are two important things to note from Table 6.1, first the scattering length of nitrogen is larger than that of carbon and oxygen, this means that the orientation of asparagine, glutamine and histidine can be readily determined using neutron diffraction. Second the incoherent scattering of hydrogen is anomalously large, giving rise to large amounts of background, this can be overcome in two ways: partially, by soaking crystals in $D_2O$, or fully by preparing perdeuterated proteins. Soaking crystals in $D_2O$ allows exchangeable protons to be replaced by deuterium, for full deuteration, expression systems are adapted to grow in $D_2O$ and use a deuterated carbon source. Deuteration is also important because the coherent scattering length of hydrogen is negative, this means that it can cancel out the scattering of heavy atoms that it is bound to at low resolution, for example $CH_2$ groups are often not visible (Figure 6.1).

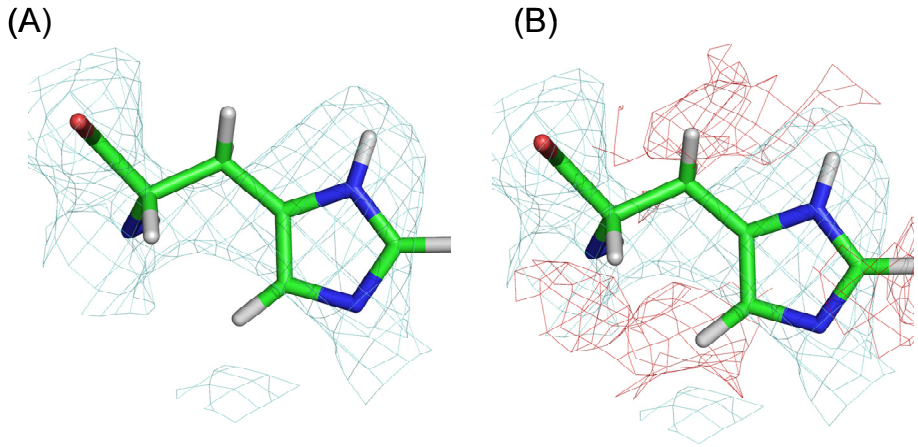


**Figure 6.1: Negative scattering by hydrogen**

(A) The $2F_o$-$F_c$ nuclear density of a histidine residue, the negative scattering of hydrogen means that scattering from $C_\beta$ is cancelled out. (B) The $F_o$-$F_c$ density is shown in red revealing the hydrogen atoms.

Neutron diffraction is a powerful technique for locating hydrogen atoms and is used to provide information on the protonation states of amino acid residues, the identity of solvent molecules, and the nature of bonds involving hydrogen, as recently reviewed [4]. Neutron diffraction can also be used to identify hydrogen atoms that are exchanged with deuterium and the extent of this replacement, thus providing a tool for identifying isotopically labelled structural features and for studying solvent accessibility and macromolecular dynamics, complementary to NMR techniques.

The Laue method, in which a single crystal is fixed in an incident beam containing a wide range of wavelengths (often referred to as the "white beam" method), is commonly employed in neutron crystallography experiments. The Laue method provides a much more rapid scan of reciprocal space allowing larger numbers of reflections to be recorded over a shorter time. The disadvantages of using a full "white beam" include the higher complexity of data processing and the increased background seen on the detector, these can be somewhat over come by using quasi-Laue methods, where the spectral wavelength of neutron beams is restricted. Recently an upgraded neutron Laue diffractometer, LADI-III, has been installed at the *Institut Laue-Langevin* (ILL). The LADI-III instrument replaces the LADI-I instrument previously used to collect data for human Aldose Reductase [5, 6], Xylose Isomerase [7] and concanavalin A [8] from perdeuterated crystals as small as 0.15mm$^3$. Operational since March 2007, the instrument uses a large cylindrical area detector composed of neutron-sensitive image-plates (NIPs) which completely surround the sample and allows large numbers of Bragg reflections to be recorded simultaneously. Data is collected using a quasi-Laue method in order to provide a rapid survey of reciprocal space, while reducing the background on the detector compared to use of the full white beam. The quasi-Laue method restricts the wavelength of the incident beam to between 3.2 and 4.2 Å.

Single crystal neutron diffraction is currently not a commonly used technique, hence to date there are only ~ 30 protein crystals for which neutron data have been collected [1]. The relative lack of neutron crystal structures available is due to a number of reasons. First, relatively large samples and large single crystals required for available neutron sources, which are often difficult to obtain. The scarcity of neutron beams and the time taken for data to be collected is another factor affecting the use of this method. Even using Laue neutron beams data collection needs to be carried out

for much longer than when using X-rays in order to compensate for the low flux of neutrons ($10^6$ $cm^{-2}$ $s^{-1}$, compared to $10^{12}$ $mm^{-2}$ $s^{-1}$ for X-rays).

As discussed throughout this Thesis, due to the availability of large quantities of protein and the crystal structure, C*c*P became *the* benchmark against which all other peroxidases were compared, and has become the subject of much investigation into both enzymatic mechanism and the electron transfer pathway. The hydrogen bonding network around the active site of C*c*P helps to define the reactivity of the heme, unambiguous identification of the hydrogen bonding patterns will lead to insights into enzymatic mechanism as well as the structural features that determine the properties of the heme.

This Chapter presents the neutron diffraction structure of C*c*P along with a jointly refined neutron/X-ray structure which has allowed the determination of the protonation states of important catalytic residues. Preliminary neutron Laue diffraction data to 2.4 Å resolution has been collected of wild type C*c*P at room temperature (from a crystal grown in $D_2O$) on the LADI-III instrument at the ILL. Room temperature X-ray data have been collected on a rotating anode source from similar crystals and a joint neutron/X-ray refinement of the 'native' structure has been carried out. This preliminary study indicates that the sample volume (0.8 $mm^3$) available is sufficient to collect the high resolution neutron data required in order to examine the nature of the ground state of the enzyme.

# 6.2 Results

## *6.2.1 Crystallisation of CcP for neutron diffraction*

Crystals for neutron diffraction were grown as previously described (Chapter 2, Section 2.2.3). Once grown the crystals were redissolved in potassium phosphate buffer (500 mM) which had been produced using $D_2O$ instead of $H_2O$, and dialysed against 50 mM potassium phosphate buffer containing 30% 2-methyl-2,4-pentanediol by volume which had also been produced using $D_2O$.

### *6.2.2 Collection of neutron diffraction data*

Neutron diffraction data were collected by Matthew Blakeley and Peter Moody at the European Molecular Biology Laboratory (EMBL) in Grenoble at the ILL neutron Laue diffractometer, LADI. A $D_2O$-soaked C*c*P crystal (0.8 $mm^3$ volume) was mounted in a quartz capillary and sealed with wax for data collection. Neutron Laue diffraction data were collected at room temperature using the LADI-III instrument installed on cold neutron guide H142. Data were recorded in a series of 9 contiguous Laue images using 15h exposures and spots were observed up to 2.2 Å resolution with data processed to 2.4 Å resolution (Figure 6.2).

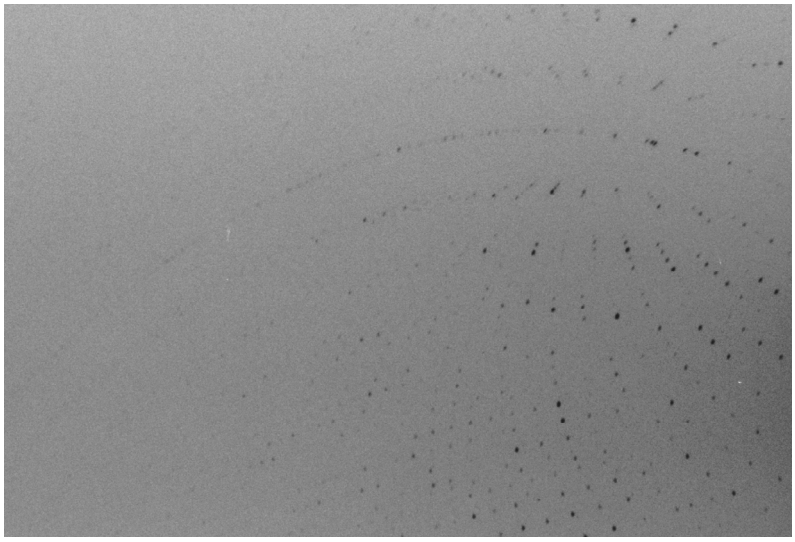

**Figure 6.2: Close-up of part of a neutron Laue diffraction pattern from C*c*P**

Neutron Laue data were indexed and integrated using the Daresbury Laboratory LAUEGEN software suite [9, 10], modified for the cylindrical geometry of the LADI-III detector [11]. The LSCALE program [12] was used to derive the wavelength-normalization curve using the intensities of symmetry-equivalent reflections measured at different wavelengths. No account was made for crystal damage since neutrons do not induce detectable radiation damage and no explicit absorption corrections were applied. SCALA [13] was used to combine and merge the 21637 observed reflections. Relevant statistics of diffraction data are shown in Table 6.2.

**Table 6.2:** Summary of 2.4 Å room temperature neutron Laue diffraction data from C*c*P

| $D_{min}$ (Å) | $N_{meas}$ | $N_{ref}$ | $R_{merge}$ (%) | I/sigma(I) | %complete | Multiplicity |
|---|---|---|---|---|---|---|
| 7.59 | 720 | 412 | 8.0 | 6.3 | 74.1 | 1.7 |
| 5.37 | 2030 | 854 | 10.5 | 6.9 | 88.4 | 2.4 |
| 4.38 | 2722 | 1094 | 12.3 | 6.9 | 88.8 | 2.5 |
| 3.79 | 2985 | 1256 | 12.9 | 6.6 | 87.8 | 2.4 |
| 3.39 | 2833 | 1315 | 13.4 | 5.9 | 82.4 | 2.2 |
| 3.10 | 2566 | 1296 | 14.0 | 5.1 | 72.8 | 2.0 |
| 2.87 | 2250 | 1201 | 15.4 | 4.5 | 62.6 | 1.9 |
| 2.68 | 1964 | 1102 | 15.9 | 3.9 | 54.2 | 1.8 |
| 2.53 | 1762 | 1045 | 16.5 | 3.3 | 48.0 | 1.7 |
| 2.40 | 1805 | 1048 | 17.0 | 3.1 | 45.1 | 1.7 |
| Overall | 21637 | 10623 | 13.0 | 5.2 | 66.1 | 2.0 |

### *6.2.3 Neutron diffraction structure of CcP*

Initial refinement clearly shows the protonation state of four of the six histidine residues (Figure 6.3), the orientation of the asparagine (Figure 6.4) and glutamine residues and the dual conformation of Arg48.

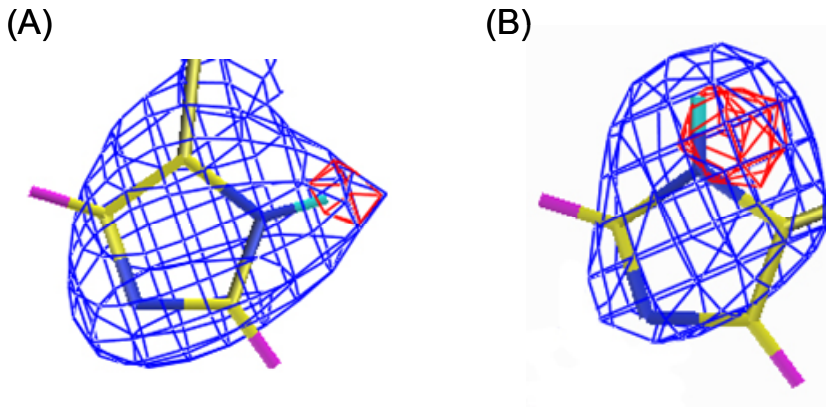


**Figure 6.3: Example of C*c*P nuclear density; histidine protonation state determination**

$2F_o$-$F_c$ nuclear density is shown in blue at 1.5 r.m.s. and $F_o$-$F_c$ nuclear density shown in red at 2.5 σ (calculated without the D-atoms included in the model). (A) His181 showing only $N_\delta$ is deuterated. (B) His52 showing only $N_\delta$ is deuterated.

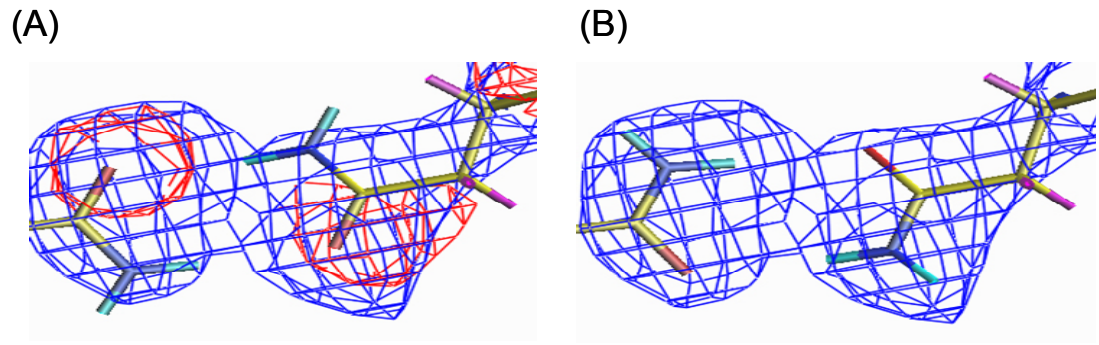


**Figure 6.4: Example of C*c*P nuclear density; asparagine orientation determination**

$2F_o$-$F_c$ nuclear density is shown in blue at 1.5 r.m.s. and $F_o$-$F_c$ nuclear density shown in red at 2.5σ. (A) Shows the orientations of the side chains of Asn24 and Asn292 as found in the X-ray starting model. Clear $F_o$-$F_c$ density (red) is observed for the $N_\delta 2$ groups of each residue indicating the orientation is not correct. (B) Shows the same residues after they have been flipped, no $F_o$-$F_c$ density is observed showing that they are now in the correct orientation.

### *6.2.4 X-ray data collection at room temperature*

In neutron diffraction the addition of hydrogen and deuterium atoms into the model means that the number of atoms being refined is typically twice the number of atoms in an X-ray refinement [14]. The increased number of atoms increases the number of parameters and reduces the data-to-parameter ratio, a problem which is increased with the medium resolution of the neutron structure (2.4 Å). This higher data-to-parameter ratio means there is a danger of over fitting the data, decreasing the accuracy of the model [15]. A joint refinement using both the neutron data and X-ray data increases the data-to-parameter ratio leading to a more accurate refinement. Another advantage of the joint neutron/X-ray refinement is that displaying both the X-ray and neutron density maps together allows easier interpretation of the model (Figure 6.5). Showing both maps allows more accurate interpretation of the positions of $CH_2$ groups, which may be difficult to visualize using the neutron density maps due to the negative scattering of the hydrogen atoms.

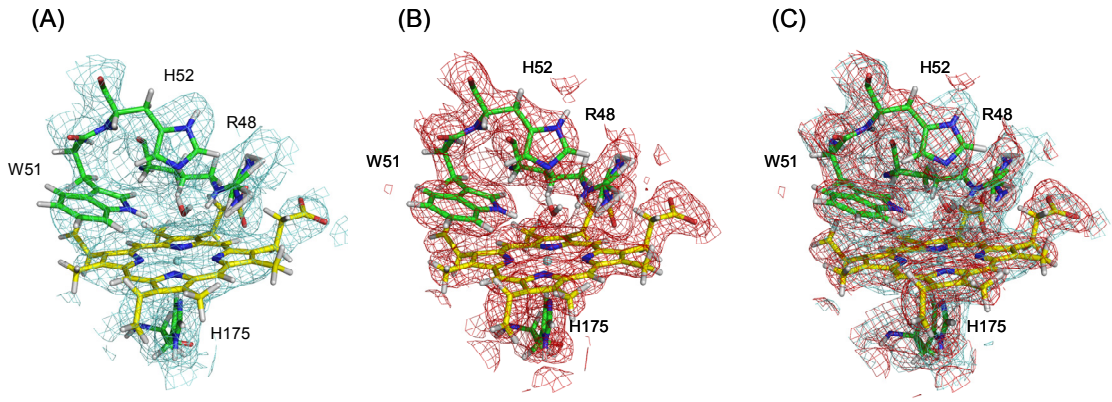


**Figure 6.5: The active site of C*c*P showing the difference between nuclear and electron density**

(A) The refined $2F_o$-$F_c$ nuclear density, the negative scattering of the hydrogen atoms can be seen by the lack of density around the $CH_2$ group of H52. (B) The refined $2F_o$-$F_c$ electron density, the deuteration at position $N_\delta$ of H52 cannot be seen. (C) Both nuclear (aqua) and electron density (red) allow for a more accurate interpretation of the structure.

In order for comparison and scaling between the neutron diffraction structure and the X-ray crystal structure of wild type C*c*P to be carried out, it was necessary to produce a crystal structure of wild type C*c*P at room temperature. As protein crystals are ~ 50 % water they need to be kept in mother liquor so that they won't dry out in the X-ray beam, this is achieved by mounting the crystals using a glass capillary tube, which is sealed with wax. At room temperature the crystal is not protected from the damaging X-rays and so, in this case, after approximately 30 degrees of collection (60 images) resolution is clearly lost (Figure 6.6). There were 60 images collected per crystal and the data from six individual crystals was combined to give a single merged data set.

The crystal structure of wild type C*c*P refined with room temperature data showed no differences with the structure of C*c*P refined with data collected under cryogenic conditions with r.m.s deviation in Cα positions of 0.111 Å. Refinement statistic for the data collected at room temperature are shown in Table 6.3.

(A) (B) (C)

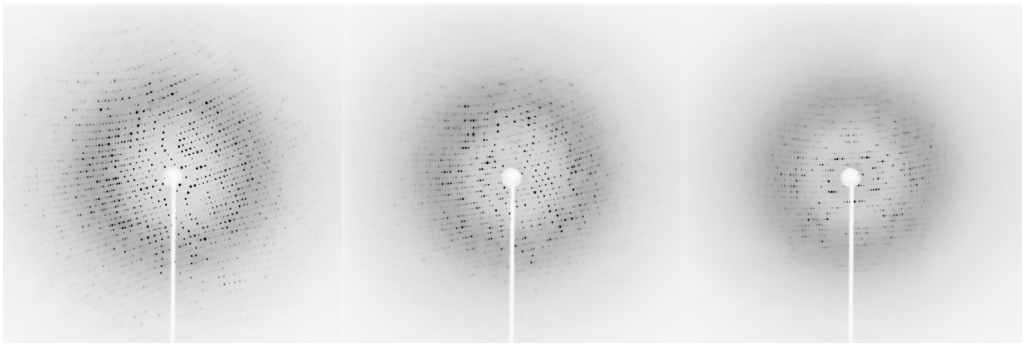

**Figure 6.6: Effects of damaging X-rays on wild type C*c*P crystal diffraction pattern at room temperature**

The diffraction pattern of wild type C*c*P at different stages during data collection at room temperature; (A) 1st image, (B) after 20 degrees and (C) after 30 degrees.

**Table 6.3:** Data Collection and refinement statistics for wild type C*c*P collected at room temperature

| Protein | wild type C*c*P |
|---|---|
| **Data Collection** | |
| Space group | $P2_12_12_1$ |
| Unit Cell (Å) | |
| A | 51.547 |
| B | 76.655 |
| C | 107.078 |
| Resolution (Å) | 43.90-2.01 (2.12-2.01) |
| Total observations | 78178 (10136) |
| Unique reflections | 26005 (3550) |
| $I/\sigma I$ | 18.7 (2.0) |
| $R_{merge}$ | 0.076 (0.671) |
| Completeness (%) | 90.5 (86.9) |
| **Refinement statistics** | |
| $R_{work}$ | 0.16291 |
| $R_{free}$ | 0.20011 |
| R.M.S.D | |
| Bonds (Å) | 0.017 |
| Angles (°) | 1.523 |

### *6.2.5 Combined X-ray and neutron structure*

The joint neutron/X-ray refinement of the native C*c*P structure used newly developed software '*nCNS'* [16] which combines, for the first time, global X-ray data, neutron data and energy refinement with cross-validated maximum likelihood simulated annealing refinement. This combined neutron/X-ray refinement allowed the assignment of the orientation and protonation states of the remaining histidine, asparagine and glutamine residues and allows a description of key residues in the ground state. The active site bonding network of C*c*P is shown in Figure 6.7.

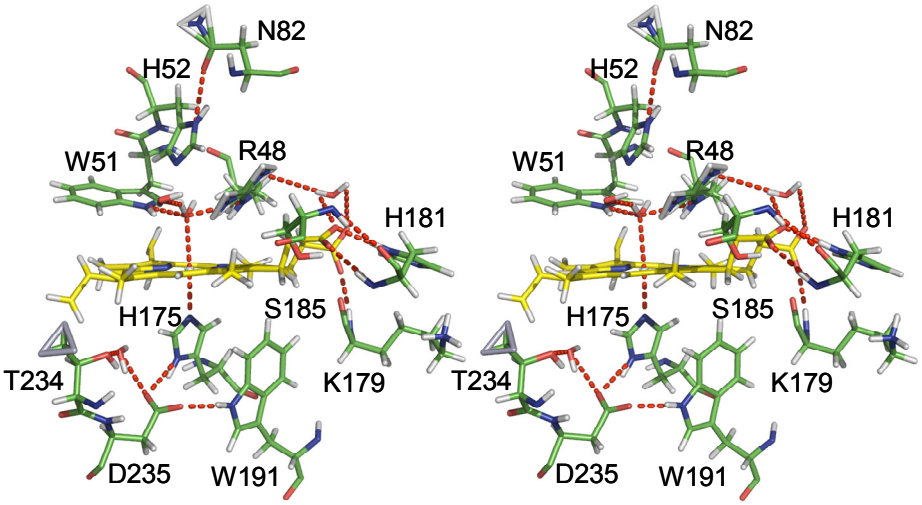


**Figure 6.7 The bonding network in the active site of C*c*P**

Stereo representation, produced from the joint neutron/X-ray structure, of the bonding network of the active site of C*c*P, the heme is shown in yellow and bonds are represented by red dashes.

The distal histidine (His52) has been shown to be critical for the rapid formation of compound I [17], the structure shows only the $N_\delta$ of the imidazole is deuterated and this forms a hydrogen bond to $O_\delta$ of Asn82. The $N_\varepsilon$ is 2.7 Å from the oxygen of the water bound above the heme iron, but the nuclear density of this water is not well enough defined to place its hydrogen atoms with certainty. The adjacent tryptophan (Trp51, implicated in the stabilization of bound peroxide and Compound I

[18], is deuterated on the indole nitrogen ($N_\varepsilon$) and is 2.9 Å away from the water bound above the heme, with the hydrogen atom almost in line with the water oxygen, consistent with the formation of a hydrogen bond. However, the angle formed by the Trp51 indole nitrogen-water-imidazole nitrogen of His52 is acute (78°), and therefore it is unlikely that both nitrogens are involved in hydrogen bonding to the water simultaneously (Figure 6.8).

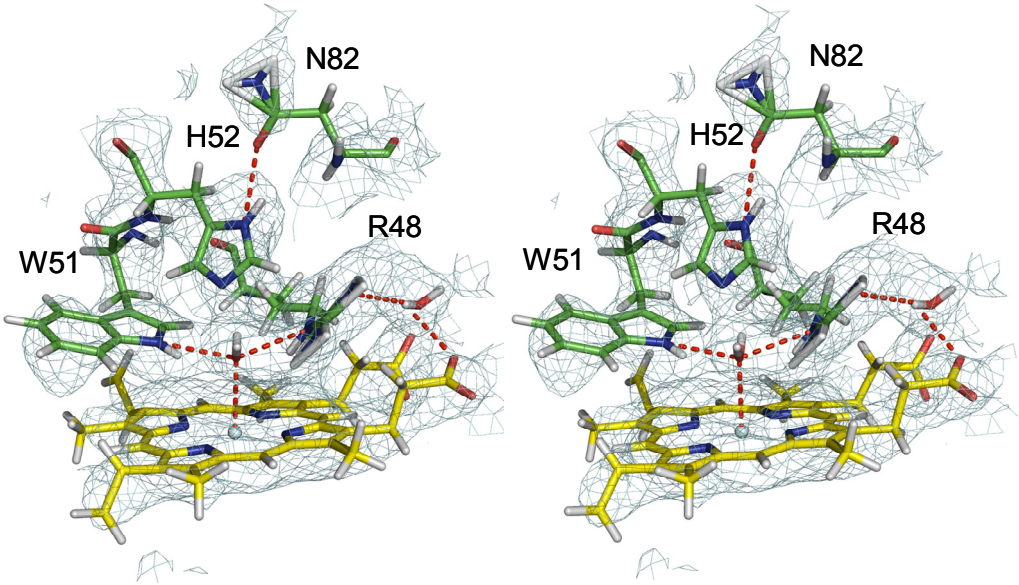


**Figure 6.8: Joint neutron/X-ray structure of the distal heme pocket**

Stereo representation of the distal heme pocket produced from the joint neutron/X-ray structure. The heme is shown in yellow with hydrogen bonds represented by red dashes. The $2F_o$-$F_c$ nuclear density is shown in aquamarine.

The orientation of the proximal histidine (His175) side chain, is clearly seen, as expected the $N_\varepsilon$, which co-ordinates to the heme iron 2.3 Å away, is not deuterated whereas the $N_\delta$ is deuterated and hydrogen bonds to $O_\delta 2$ of the acid group of Asp235, whose other oxygen in turn hydrogen bond to the deuterated $N_\varepsilon$ of Trp191. $O_\delta 2$ of Asp235 also hydrogen bonds to a water molecule (2.7 Å) which in turn hydrogen bonds to $O_\gamma 1$ of Thr234 (Figure 6.9).

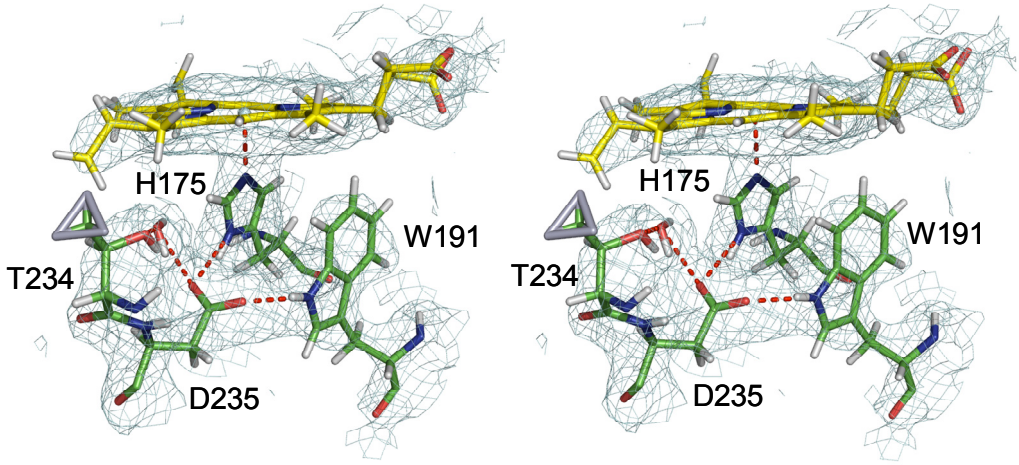


**Figure 6.9: Joint neutron/X-ray structure of the proximal heme pocket**

Stereo representation of the proximal heme pocket produced from the joint neutron/X-ray structure. The heme is shown in yellow with hydrogen bonds represented by red dashes. The $2F_o$-$F_{c\ nuclear}$ density is shown in aquamarine.

The ligation of proximal histidine (His175) controls the catalytic activity of the heme [19-21], hence, the hydrogen bonding network surrounding the histidine also plays a role in controlling the activity of the heme. Asp235 has been shown to control the properties of His175 as a heme ligand, to influence the electrochemical properties of the heme, and to modulate the coupling between the heme and the Trp191 radical [22-24]. It is also reasonable that the buried charge of Asp235 may stabilize the formation of the Trp191 radical by an electrostatic charge-pair interaction and may also be involved in stabilizing the higher oxidation states of the peroxidase that form transiently during catalysis. Trp191 forms an indolyl radical as Compound I is formed, and its substitution with phenylalanine reduced the rate of Compound I formation by a factor of at least 10,000 [25].

His181 forms two hydrogen bonds with the deprotonated heme 7-propionate; one between the deuterated $N_\delta$ of the histidine side chain and one between the backbone amide. His181 is connected to the distal histidine, His175, via a six residue loop and is proposed to anchor the heme in place, strengthening the proximal heme linkage [26]. The heme 7-propionate is also close to the side chain of Ser185; however the geometry is poor for hydrogen bond formation (Figure 6.10).

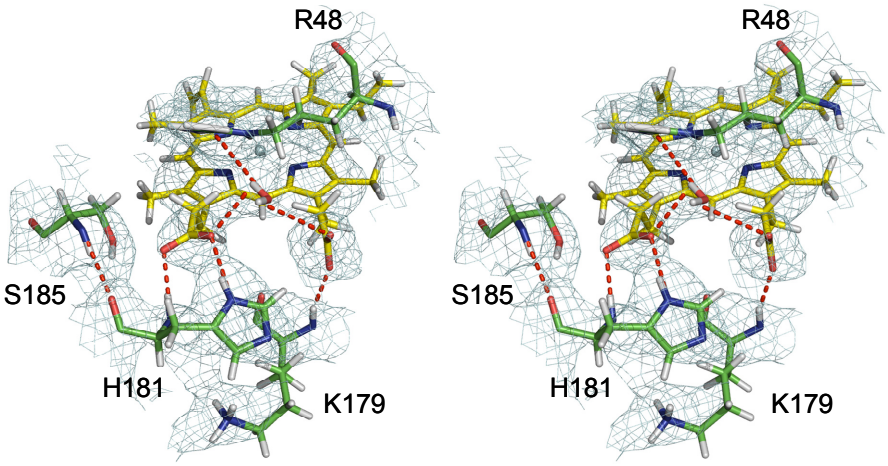


**Figure 6.10: Joint neutron/X-ray structure of bonding involving the heme propionates**

Stereo representation of the heme active site produced from the joint neutron/X-ray structure showing the hydrogen bonding networks involving the heme propionates. The heme is shown in yellow with bonds represented by red dashes. The $2F_o$-$F_c$ nuclear density is shown in aquamarine.

One oxygen of the heme 6-propionate is seen to hydrogen bond to the main chain nitrogen of Lys179, the other oxygen appears to interact with the same water molecule which bridges the heme propionates to the motile guanidinium of Arg48 [27] (Figure 6.10). Arg48 forms part of the distal catalytic triad and is important in the stabilisation of Compound I [17, 28, 29].

## 6.3 Discussion

A detailed description of the resting C*c*P enzyme has been produced, the neutron data and joint refinement have added to the previously published crystal structure by allowing determination of the protonation states of histidine residues and the orientations of asparagine and glutamine side chains. It has allowed a detailed description of the hydrogen bonding network within the active site of C*c*P, which is important in controlling the overall activity of the enzyme.

Over the past decade there have been a number of crystal structures obtained for the Compound I intermediate of C*c*P clearly showing the [Fe(IV) – O]] centre. There has been much debate into the exact nature of the Compound I [Fe(IV) – O]

centre. Early EXAFS work [30, 31] on C*c*P estimated Fe-O bond lengths to be in the region of 1.6 Å indicating a [Fe(IV) = O] species. Whereas the high resolution crystal structure obtained by Poulos [32] showed an Fe-O bond length of 1.87 Å which they characterised as a ferryl bound hydroxyl species [Fe(IV) - OH] claiming that in the cytochrome P450's that substrate oxidation occurs through a direct hydroxyl transfer mechanism from the transient Compound I.

Given the ambiguities of the chemical and spectroscopic experiments reported so far, it would be interesting to unambiguously resolve the question of the protonation state of Compound I in C*c*P; neutron diffraction could be used to do this as the negative scattering length of a proton should show this up clearly. The generation of X-ray induced electrons during diffraction data acquisition may mean that the oxyferryl centre in Compound I is subject to radiolytic reduction [33], therefore, the structure obtained may not be a true Compound I intermediate and data collection needs to be followed closely using single crystal microspectrophotometry in order to be certain that the correct intermediate has been formed. Neutron diffraction also offers the advantage that neutrons do not cause radiation damage and so will not affect the oxyferryl centre in Compound I.

In the peroxidases, in particular C*c*P, the [Fe(IV) – O] centre is remarkably stable ($t_{1/2} \approx$ several hours) thus the intermediate can easily be trapped in the crystalline state allowing detailed characterization studies to be undertaken. However, the experiments would need to be conducted in cryogenic conditions to preserve Compound I. Data collection at cryogenic temperatures is a challenge when using the large protein crystals used for neutron diffraction since the solvent must be rapidly (flash)-cooled to a vitreous glass in order to avoid ice formation that disrupts the crystal lattice. Protocols for cryogenic neutron diffraction have been developed at the *Institut Laue-Langevin* (ILL) to cool and maintain large protein crystals (1-5 $mm^3$) at cryogenic temperatures (~15 K). Data have been previously collected at 15 K on the LADI-I instrument at the ILL for lysozyme [34] and concanavalin A [35].

The neutron diffraction studies presented in this Chapter show that sufficient crystal volumes of C*c*P would be available in order to determine the neutron diffraction structure of Compound I of C*c*P and to unambiguously assign the protonation state of this important intermediate.

## 6.4 References


1. Myles, D., *Neutron protein crystallography: current status and a brighter future.* Curr. Opin. Struc. Biol., 2006. **16**: 630-637.
2. Bradshaw, J.P., *Neutron Diffraction*. Encyclopedia of Life Sciences. 2001: John Wiley & Sons.
3. Thomson, E.A., *Shull joins ranks of MIT's Nobelists*, in *MIT tech talk*. 1994: Massachussets.
4. Niimura, N. and Bau, R., *Neutron protein crystallography: beyond the folding structure of biological macromolecules.* Acta Crystallogr. A, 2008. **64**: 12-22.
5. Blakeley, M.P., Ruiz, F., Cachau, R., Hazemann, I., Meilleur, F., Mitschler, A., Ginell, S., Afonine, P., Ventura, O.N., Cousido-Siah, A., Haertlein, M., Joachimiak, A., Myles, D., and Podjarny, A., *Quantum model of catalysis based on a mobile proton revealed by subatomic x-ray and neutron diffraction studies of h-aldose reductase.* Proc. Natl. Acad. Sci. USA., 2008. **105**(6): 1844-1848.
6. Hazemann, I., Dauvergne, M.T., Blakeley, M.P., Meilleur, F., Haertlein, M., Van Dorsselaer, A., Mitschler, A., Myles, D.A.A., and Podjarny, A., *High-resolution neutron protein crystallography with radically small crystal volumes: application of perdeuteration to human aldose reductase.* Acta Crystallogr., Sect. D. Biol. Crystallogr., 2005. **61**: 1413-1417.
7. Meilleur, F., Snell, E.H., Van Der Woerd, M.J., Judge, R.A., and Myles, D.A.A., *A quasi-Laue neutron crystallographic study of D-xylose isomerase.* Eur. Biophys. J., 2006. **35**(7): 601-609.
8. Ahmed, H.U., Blakeley, M.P., Cianci, M., Cruickshank, D.W.J., Hubbard, J.A., and Helliwell, J.R., *The determination of protonation states in proteins.* Acta Crystallogr., Sect. D. Biol. Crystallogr., 2007. **63**: 906-922.
9. Campbell, J.W., *LAUEGEN, an X-windows-based program for the processing of Laue diffraction data.* J. Appl. Crystallogr., 1995. **28**: 228-236.
10. Helliwell, J.R., *The recording and analysis of synchrotron x-radiation Laue diffraction photographs.* J. Appl. Crystallogr., 1989. **22**: 483-497.
11. Campbell, J.W., Hao, Q., Harding, M., Nguti, N.D., and Wilkinson, C., *LAUEGEN, an X-windows-based program for the processing of Laue diffraction data.* J. Appl. Crystallogr., 1998. **31**: 496-502.
12. Arzt, S., Campbell, J.W., Harding, M.M., Hao, Q., and Helliwell, J.R., *LSCALE - the new normalization, scaling and absorption correction program in the Daresbury Laue software suite.* J. Appl. Crystallogr., 1999. **32**: 554-562.
13. Bailey, S., *The CCP4 Suite - Programs for protein crystallography.* Acta Crystallogr., Sect. D. Biol. Crystallogr., 1994. **50**: 760-763.
14. Coates, L., Han-Fang, T., Tomanicek, S., Kovalevsky, A., Mustyakimov, M., Erskine, P., and Cooper, J., *The catalytic mechanism of an aspartic proteinase explored with neutron and X-ray diffraction.* J. Am. Chem. Soc., 2008. **130**: 7235-7237.
15. Fisher, S., Anderson, S., Henning, R., Moffat, K., Langan, P., Thiyagarajan, P., and Schultz, A., *Neutron and X-ray structural studies of short hydrogen bonds in photoactive yellow protein (PYP).* Acta Crystallogr., Sect. D. Biol. Crystallogr., 2007. **63**(11): 1178-1184.
16. Mustyakimov, M., Afonine, P., Adams, P.D., and Langan, P., *nCNS, a patch for CNS*. 2007: Los Alamos National Security, LL. p. Copyright (C-06, 104).

17. Erman, J.E., Vitello, L.B., Miller, M.A., and Kraut, J., *Active-site mutations in cytochrome c peroxidase - a critical role for histidine-52 in the rate of formation of Compound I.* J. Am. Chem. Soc., 1992. **114**(16): 6592-6593.
18. Miller, M.A., Shaw, A., and Kraut, J., *2.2 Angstrom structure of oxy-peroxidase as a model for the transient enzyme peroxide complex.* Nat. Struct. Biol., 1994. **1**(8): 524-531.
19. Choudhury, K., Sundaramoorthy, M., Hickman, A., Yonetani, T., Woehl, E., Dunn, M.F., and Poulos, T.L., *Role of the proximal ligand in peroxidase catalysis - Crystallographic, kinetic, and spectral studies of cytochrome c peroxidase proximal ligand mutants.* J. Biol. Chem., 1994. **269**(32): 20239-20249.
20. Choudhury, K., Sundaramoorthy, M., Mauro, J.M., and Poulos, T.L., *Conversion of the proximal histidine ligand to glutamine restores activity to an inactive mutant of cytochrome c peroxidase.* J. Biol. Chem., 1992. **267**(36): 25656-25659.
21. Sundaramoorthy, M., Choudhury, K., Edwards, S.L., and Poulos, T.L., *Crystal-structure and preliminary functional-analysis of the cytochrome c peroxidase His175gln proximal ligand mutant.* J. Am. Chem. Soc., 1991. **113**(20): 7755-7757.
22. Dasgupta, S., Rousseau, D.L., Anni, H., and Yonetani, T., *Structural characterization of cytochrome c peroxidase by resonance raman-scattering.* J. Biol. Chem., 1989. **264**(1): 654-662.
23. Satterlee, J.D., Erman, J.E., Mauro, J.M., and Kraut, J., *Comparative proton NMR analysis of wild type cytochrome c peroxidase from yeast, the recombinant enzyme from Escherichia Coli, and an Asp235Asn mutant.* Biochemistry, 1990. **29**(37): 8797-8804.
24. Goodin, D.B. and Mcree, D.E., *The Asp-His-Fe triad of cytochrome c peroxidase controls the reduction potential, electronic-structure, and coupling of the tryptophan free-radical to the heme.* Biochemistry, 1993. **32**(13): 3313-3324.
25. Miller, M.A., Vitello, L., and Erman, J.E., *Regulation of interprotein electron-transfer by Trp191 of cytochrome c peroxidase.* Biochemistry, 1995. **34**(37): 12048-12058.
26. Smulevich, G., Miller, M.A., Kraut, J., and Spiro, T.G., *Conformational change and histidine control of heme chemistry in cytochrome c peroxidase - resonance Raman evidence from Leu52 and Gly181 mutants of cytochrome c peroxidase.* Biochemistry, 1991. **30**(39): 9546-9558.
27. Metcalfe, C., Macdonald, I.K., Murphy, E.J., Brown, K.A., Raven, E.L., and Moody, P.C.E., *The tuberculosis prodrug isoniazid bound to activating peroxidases.* J. Biol. Chem., 2008. **283**(10): 6193-6200.
28. Bujons, J., Dikiy, A., Ferrer, J.C., Banci, L., and Mauk, A.G., *Charge reversal of a critical active-site residue of cytochrome-c peroxidase - Characterization of the Arg48->Glu variant.* Eur.J. Biochem., 1997. **243**(1-2): 72-84.
29. Vitello, L.B., Erman, J.E., Miller, M.A., Mauro, J.M., and Kraut, J., *Effect of Asp-235-Asn substitution on the absorption-spectrum and hydrogen-peroxide reactivity of cytochrome c peroxidase.* Biochemistry, 1992. **31**(46): 11524-11535.
30. Chance, B., Powers, L., Ching, Y., Poulos, T., Schonbaum, G.R., Yamazaki, I., and Paul, K.G., *X-Ray absorption studies of intermediates in peroxidase-activity.* Arch. Biochem. Biophys., 1984. **235**(2): 596-611.

31. Penner-Hahn, J.E., Mcmurry, T.J., Renner, M., Latosgrazynsky, L., Eble, K.S., Davis, I.M., Balch, A.L., Groves, J.T., Dawson, J.H., and Hodgson, K.O., *X-Ray absorption spectroscopic studies of high valent iron porphyrins - horseradish-peroxidase Compound I and Compound II and synthetic models.* J. Biol. Chem., 1983. **258**(21): 2761-2764.
32. Bonagura, C.A., Bhaskar, B., Shimizu, H., Li, H.Y., Sundaramoorthy, M., Mcree, D.E., Goodin, D.B., and Poulos, T.L., *High-resolution crystal structures and spectroscopy of native and Compound I cytochrome c peroxidase.* Biochemistry, 2003. **42**(19): 5600-5608.
33. Berglund, G.I., Carlsson, G.H., Smith, A.T., Szoke, H., Henriksen, A., and Hajdu, J., *The catalytic pathway of horseradish peroxidase at high resolution.* Nature, 2002. **417**(6887): 463-468.
34. Meilleur F, B.M., Myles Da. , *Neutron Laue analysis of hydrogen and hydration in protein structure*. Hydrogen and hydration sensitive structural biology pages 75-85. 2005.
35. Blakeley, M.P., Kalb, A.J., Helliwell, J.R., and Myles, D.A.A., *The 15-K neutron structure of saccharide-free concanavalin A.* Proc. Natl. Acad. Sci. USA., 2004. **101**(47): 16405-16410.

# Chapter 7

## *Summary*

## 7.1 Substrate binding in heme peroxidases: evolution of the consensus

In many heme proteins substrate binding occurs in the distal heme pocket where the substrate has access to the activated oxygen provided by the heme. For the oxygenase enzymes such as the P450s and heme dioxygenases, the reactive intermediate, either Compound I or the ferrous-oxy complex , needs to be close to the bound substrate so that reaction (*i.e.* insertion of oxygen) can occur. In contrast, the reactive intermediate of peroxidases functions as an oxidant rather than an oxygen donor and it is necessary for the protein to shield the substrate from the reactive oxy-ferryl species in order to ensure that peroxidase, rather than oxygenase, activity occurs. The requirement for access to the oxygen for P450s and shielding from the oxygen for peroxidases has been shown by phenylhydrazine experiments; all heme proteins with an accessible heme iron, such as the P450s, form phenyl-iron complexes when reacted with phenylhydrazines [1], peroxidases do not [2-4]. Since direct contact between the activated oxygen and the substrate is not required for peroxidases, the distance between the bound substrate and the active site is controlled only by the need for a mechanism by which electrons can be transferred from the substrate to the heme iron. This means that the location of the substrate binding site in peroxidases can be more flexible than that of other heme proteins and provides a protein framework that is capable of utilising different binding sites depending on the nature of the substrate.

As discussed throughout this Thesis, until recently it was generally believed that peroxidases bound and oxidised substrates at the δ-heme edge. A "one-site fits all" model was proposed and backed up by chemical evidence [2, 5, 6], structural evidence [7-9], and site-directed mutagenesis [10]. The two exceptions to this rule were the C*c*P-cytochrome *c* complex [11], which binds cytochrome *c* on the surface, and the MnP-$Mn^{2+}$ complex [12] which uses the γ-heme edge; both of these proteins have unusual substrates so were not thought to describe a general mode of substrate binding in heme peroxidases. The crystal structure of the APX-ascorbate complex [13] showed that the γ-heme edge may provide a more general site for substrate oxidation. This is helpful for the protein in terms of its ability to oxidise different types of substrate because oxidation of different *types* of substrate can be

accommodated within the *same* protein framework, for example, in the case of ascorbate peroxidase where (hydrophobic) aromatic substrates and (hydrophilic) ascorbate are oxidised at different sites [13, 14].

The presence of an efficient binding site is not necessarily enough to confer the catalytic activity seen at the γ-heme edge of APX. As seen in Chapter 2, although ascorbate binds at a site created at the γ-heme edge of C*c*P, mimicking that of APX, the oxidation of ascorbate at this site is not catalytically efficient. In this case it is the combination of efficient substrate binding, together with the formation of a suitably stable porphyrin π-cation radical, that seems to be the key to rapid substrate oxidation. The inadequacy of the presence of a binding site alone is also seen in Chapter 4, where crystal structures reveal aromatic substrate binding at sites which were shown by inhibition studies to be catalytically inactive. In this case it is likely that electron transfer pathways between the substrate and the heme do not exist and the binding sites are adventitious.

In Chapter 3, the crystal structure of an aromatic substrate (isoniazid, INH) binding at the γ-heme edge has been presented, this strengthens the idea that that substrate oxidation can occur at *both* the δ- and γ-heme edges, which allows the use of more than one electron transfer pathway. In addition the structures have provided unambiguous evidence for the location of INH binding in the class I peroxidises, C*c*P and APX. These data expand on previous predictions and provide a molecular understanding of prodrug binding and activation. Furthermore, by comparing mutations engineered into peroxidase models with naturally occurring INH-resistant variants of *M. tuberculosis*, three separate means of drug resistance have been identified: steric hindrance of the δ-heme edge INH binding site, direct binding to the heme iron (and consequent inhibition of Compound I formation), and the loss of peroxidatic activity due to the mutation of essential catalytic residues. These observations provide a fundamental platform upon which our understanding of the enzyme-catalyzed activation of this prodrug can now be developed for more effective tuberculosis therapies in the future and show the true importance of obtaining a detailed understanding of substrate binding.

This Thesis has shown that heme peroxidases have an inherent flexibility in the location at which they bind and oxidise substrates, the key requirements for rapid oxidation being a suitable binding site *and* an efficient mechanism for electron/proton

transfer. The ability to use long range electron transfer such as that seen in the C*c*P-cytochrome *c* complex, which involves different protein residues carrying an electron from a distant binding site to the heme, along with the ability to transfer electrons directly, as in the case of the APX-ascorbate and MnP-$Mn^{2+}$ complexes, via an interaction with the heme propionates, provides this flexibility and allows oxidation of different types of substrate within the same protein framework.

As substrate binding is not the only determinant of catalytic activity in the heme peroxidases, more research into the nature of electron and proton transfer needs to be undertaken. Determination of the neutron diffraction structure of C*c*P (Chapter 6) has allowed a detailed description of the resting ferric enzyme and has shown that the sample volume available (0.8 $mm^3$) is sufficient to collect high resolution data. Determining the structures of key intermediates in the catalytic cycle, for example by obtaining the neutron diffraction structure of Compound I, will lead to a better understanding of the electron/proton transfer mechanisms utilised by peroxidases and, in turn, the structural features necessary to confer function.

## 7.2 References


1. De Montellano, P.R.O., *Control of the catalytic activity of prosthetic heme by the structure of hemoproteins.* Acc. Chem. Res., 1987. **20**: 289-294.
2. Depillis, G.D., Wariishi, H., Gold, M.H., and Demontellano, P.R.O., *Inactivation of lignin peroxidase by phenylhydrazine and sodium-azide.* Arch. Biochem.and Biophys., 1990. **280**(1): 217-223.
3. Harris, R.Z., Wariishi, H., Gold, M.H., and De Montellano, P.R.O., *The catalytic site of manganese peroxidase. Regiospecific addition of sodium azide and alkylhydrazines to the heme group.* J. Biol. Chem., 1991. **266**: 8751-8758.
4. Depillis, G.D. and De Montellano, P.R.O., *Substrate oxidation by the heme edge of fungal peroxidases. Reactions of Coprinus macrorhizus peroxidase with hydrazines and sodium azide.* Biochemistry, 1989. **28**: 7947-7952.
5. Sakurada, J., Takahashi, S., and Hosoya, T., *NMR studies on the spatial relationship of aromatic donor molecules to the heme iron of horseradish peroxidase.* J. Biol. Chem., 1986. **261**(21): 9657-9662.
6. Ator, M.A., David, S.K., and De Montellano, P.R.O., *Structure and catalytic mechanism of horseradish peroxidase: Regiospecific meso-alkylation of the prosthetic heme group by alkylhydrazines.* J. Biol. Chem., 1987. **262**(31): 14954-14960.
7. Henriksen, A., Schuller, D.J., Meno, K., Welinder, K.G., Smith, A.T., and Gajhede, M., *Structural interactions between horseradish peroxidase C and the substrate benzhydroxamic acid determined by X-ray crystallography.* Biochemistry, 1998. **37**(22): 8054-8060.
8. Tsukamoto, K., Itakura, H., Sato, K., Fukuyama, K., Miura, S., Takahashi, S., Ikezawa, H., and Hosoya, T., *Binding of salicylhydroxamic acid and several aromatic donor molecules to Arthromyces ramosus peroxidase, investigated by X-ray crystallography, optical difference spectroscopy, NMR relaxation, molecular dynamics, and kinetics.* Biochemistry, 1999. **38**(39): 12558-12568.
9. Henriksen, A., Smith, A.T., and Gajhede, M., *The Structures of the Horseradish Peroxidase C-Ferulic Acid Complex and the Ternary Complex with Cyanide Suggest How Peroxidases Oxidize Small Phenolic Substrates.* J. Biol. Chem., 1999. **274**(49): 35005-35011.
10. Adak, S., Mazumder, A., and Banerjee, R.K., *Probing the active site residues in aromatic donor oxidation in horseradish peroxidase: Involvement of an arginine and a tyrosine residue in aromatic donor binding.* Biochem. J., 1996. **314**: 985-991.
11. Pelletier, H. and Kraut, J., *Crystal-structure of a complex between electron-transfer partners, cytochrome c peroxidase and cytochrome c.* Science, 1992. **258**(5089): 1748-1755.
12. Sundaramoorthy, M., Youngs, H.L., Gold, M.H., and Poulos, T.L., *High-resolution crystal structure of manganese peroxidase: Substrate and inhibitor complexes.* Biochemistry, 2005. **44**(17): 6463-6470.
13. Sharp, K.H., Mewies, M., Moody, P.C.E., and Raven, E.L., *Crystal structure of the ascorbate peroxidase-ascorbate complex.* Nat. Struct. Biol., 2003. **10**(4): 303-307.
14. Sharp, K.H., Moody, P.C.E., Brown, K.A., and Raven, E.L., *Crystal structure of the ascorbate peroxidase-salicylhydroxamic acid complex.* Biochemistry, 2004. **43**(27): 8644-8651.

# Chapter 8

## *Experimental*

# 8.1 General

## *8.1.1 Materials and stock solutions*

All chemicals were obtained from Sigma Aldrich Co. (unless otherwise stated) and were used without further purification. All buffers, media and solutions (listed in Appendix A) were prepared using double deionised water (Elga classic DI) and glycerol was sterilised before use.

## *8.1.2 DNA preparation*

### *8.1.2.3 DNA preparation from XL1-Blue cells*

DNA was extracted from XL1-Blue cells for transformation into SG 1300 cells, BL21 DE3 Gold cells or for sequencing using a QIAprep Spin Miniprep kit (Qiagen, catalogue no. 27104). The protocol from the kit handbook (page 22) was undertaken as follows: overnight grow-ups were centrifuged at 3000 rpm for 30 minutes in order to pellet the cells and the supernatant discarded. The cells were resuspended in 250 µl of P1 buffer (Appendix A) (RNase added, stored at 4 ºC) and transferred to a microcentrifuge tube. Lysis buffer (250 µl, P2 (Appendix A)) was added and the tube gently inverted 4-6 times. Neutralization buffer (350 µl, P3 (Appendix A)) was added to stop the lysis reaction and the tube inverted immediately but gently 4-6 times leading to the formation of a white precipitate. The tube was centrifuged at 13,000 rpm for 10 minutes in order to pellet the white precipitate and the supernatant containing DNA transferred to a QIAprep spin column. The spin column was centrifuged at 13,000 rpm for 60 seconds and the flow through discarded. PB wash buffer (500 µl, Appendix A) was added to the column and the column centrifuged for 60 seconds at 13,000 rpm, the flow through was discarded and PE wash buffer (750 µl, Appendix A) with ethanol added was placed in the column. After centrifuging for 60 seconds, discarding the flow through and centrifuging for a further 60 seconds the column was transferred to a clean microcentrifuge tube. Sterile water (50 µl) was added directly to the column and the column allowed to stand for four minutes before centrifuging at 13,000 rpm to elute the DNA bound to the column. The DNA prepared

was stored at -20 ºC ready for transformation into expression cells, sequencing or use as a template for PCR.

### *8.1.2.3 DNA preparation of DNA using Qiagen midi spin kit*

Qiagen midi spin kit can be used to purify 100 µg of plasmid DNA from 25 ml overnight cultures. The protocol was followed as on page 17 of the Qiagen plasmid purification handbook. Cells from an overnight culture (25 ml) were pelleted by centrifuging the culture at 6000 rpm for 15 minutes at 4 ºC and the supernatant discarded. The pellet was resuspended in P1 buffer (4 ml) and P2 buffer (4 ml) was added followed by gentle mixing. P3 buffer (4ml) was added and the tube mixed gently but immediately before being incubated on ice for 15 minutes.

The mixture was centrifuged at 20,000 rpm for 30 minutes at 4 ºC; while the centrifugation was being carried out a QIAtip100 was calibrated by applying QBT buffer (4 ml, Appendix A) and allowing the column to empty by gravity flow. The supernatant was applied to the QIAtip and once it had drained through the QIAtip was washed twice with QC buffer (10 ml, Appendix A). The DNA was eluted with QF buffer (5 ml, Appendix A) and the eluant separated into 6x 1.5 ml microcentrifuge tubes. Isopropanol (583 µl) was added to each tube and the tubes centrifuged at 15,000 rpm for 30 minutes at 4 ºC. The supernatant was decanted, 70% ethanol solution (333 µl) was added to each tube and the tubes centrifuged for a further 10 minutes at 15,000 rpm. The supernatant was decanted and the pellet air-dried before being resuspended in 10 mM TrisCl, pH 8.5.(200 µl)

### *8.1.2.4 DNA preparation by gel extraction*

Gel extraction was carried out as per page 23 of the QIAquick spin handbook. Agarose gel was visualised under UV light and the desired band (as determined by comparison with a DNA ladder) was carefully cut from the gel using a sterile scalpel. The gel slice was weighed and three gel volumes of QG buffer (Appendix A) was added (300 µl per 100 mg of gel). The gel slice was dissolved in the QG buffer by heating at 50 ºC and vortexing occasionally. One gel volume of isopropanol was added to the tube (100 µl per 100 mg of gel) and the tube gently mixed before adding the mixture to a spin column. The spin column was centrifuged for 60 seconds and the flow through discarded. PE buffer (750 µl) was added and the column centrifuged for

60 seconds, the flow through was discarded and the column centrifuged for a further 60 seconds. The column was placed in a clean 1.5 ml microcentrifuge tube and the DNA eluted by addition of EB buffer (50 µl, Appendix A) directly to the membrane followed by a 60 second centrifugation. All centrifuge steps were carried out at 13,000 rpm and 4 ºC.

#### *8.1.2.5 Agarose gel electrophoresis*

Agarose (1.4 g) was dissolved in 1x TAE buffer (200 ml, Appendix A) by heating in the microwave for approximately two minutes. After allowing to cool slightly ethidium bromide solution (20 µl, 10 mg/ml, stored at 4 ºC) was added carefully and the gel swirled. A horizontal bed with a well comb was set up in an electrophoresis tank to which the gel was added and allowed to set. Once the gel had set fully 1x TAE buffer was poured over the gel and into the electrophoresis tank so that the gel was completely covered and the comb removed. The first well was loaded with 6 µl of a 1 kb DNA ladder (Fermentas, generuler™) and DNA samples prepared by mixing 10 µl DNA with 2 µl of loading buffer (Fermentas). The samples were loaded into separate wells and the gel run by applying a 100 mA current for approximately 1 hour. Positively charged DNA moves from the positive terminal to the negative terminal upon applying electrical current. Gels were visualised by placing under a UV light, this shows up ethidium bromide that has chelated to DNA.

#### *8.1.2.6 DNA sequencing*

The Protein and Nucleic Acid Chemistry Laboratory (PNACL) at the University of Leicester carried out all DNA sequencing. It was performed by automated fluorescent sequencing on an Applied Biosystems 373-Stretch machine and the data analysed using the program SeqED (Applied Biosystems). Purified DNA (20 µl) was supplied to PNACL along with 10 µl of the pQE30 forward sequencing primer and pQE30 reverse sequencing primer for APX. C*c*P was sequenced using a standard T7 sequencing primer supplied by PNACL.

## *8.1.3 Transformations*

### *8.1.3.1 Transformation into XL1-Blue cells*

XL1-Blue supercompetent cells (stored at -80 ºC) were gently thawed on ice. *Dpn*I-treated PCR product (1 µl) was added to a pre-chilled 14 ml Falcon 2059 polypropylene tube. To the DNA was added 100 µl of thawed cells and the mixture swirled before being incubated on ice for 30 minutes. The reaction was heat shocked in a water bath at 42 ºC for 45 seconds and stored on ice for a further 2 minutes. LB media (5 ml) to which had been added 1 M $MgCl_2$ (70 µl) and 1 M $MgSO_4$ (70 µl) was preheated to 42 ºC in a water bath and 500 µl of this added to the reaction. The reaction was then incubated at 37 ºC for 1 hour with shaking at 225-250 rpm. The cells were pelleted by centrifugation at 1500 rpm for 10 minutes, 250 µl of the supernatant removed and the cells resuspended in the remaining supernatant. 100 µl of the reaction mixture was spread onto an agar plate containing 100 µg/ml ampicillin which was incubated overnight at 37 ºC

### *8.1.3.2 Transformation into SG 1300 cells*

Transformation into SG 1300 cells was carried out according to a protocol based on the one found on page 40 of the QIAexpressionist. XL1-Blue DNA (1 µl) was placed in a pre-chilled Falcon tube and gently thawed SG 1300 cells (100 µl) were added, the reaction mixture was swirled and incubated on ice for 20 minutes. The reaction was heat shocked in a water bath at 42 ºC for 90 seconds and placed back on ice for 3 minutes. LB media (500 µl) containing 70 µl/5 ml each of 1 M $MgCl_2$ and 1 M $MgSO_4$ was added to the reaction and the reaction incubated at 37 ºC with shaking (225-250 rpm) for 90 minutes. The reaction was streaked on LB plates containing 100 µg/ml ampicillin and 30 µg/ml kanamycin and incubated at 37 ºC overnight.

### *8.1.3.3 Transformation into BL21 DE3 Gold cells*

BL21 DE3 Gold cells (100 µl) were gently thawed in a pre-chilled 14 ml Falcon tube. β-mercaptoethanol (1.8 µl) was added, in order to aid DNA uptake, along with 5 µl of DNA prepared from XL1-Blue cells. The reaction was kept on ice for 30

minutes with gentle swirling every 5 minutes. The reaction was heat shocked at 42 ºC for 60 seconds before being returned to ice for a further 2 minutes. LB media (900 µl containing 1 M $MgCl_2$ (70 µl) and 1 M $MgSO_4$ (70 µl) was added to the reaction followed by incubation at 37 ºC for 1 hour. Cells were spun at 1000 rpm for 10 minutes and 900 µl of supernatant was removed, the pellet was resuspended in the remaining 100 µl and this was plated on an LB plate containing 100 µg/ml ampicillin, which was then incubated at 37 ºC overnight.

### *8.1.4 Polymerase chain reaction*

All reactions were carried out using either a Perkin-Elmer 480 DNA Thermocycler or an Eppendorf Mastercycler gradient. PCR products were purified using QIAquick PCR purification kit, the protocol followed was as on page 18 of the QIAquick Spin Handbook. PB buffer was added (five volumes per volume of PCR product) and the mixture was applied to a spin column, centrifuged for 60 seconds and the flow through discarded. PE buffer (750 µl) was then added to the column and centrifuged for a further 60 seconds before discarding the flow through, a second 60 seconds centrifugation removed residual buffer. The column was transferred to an empty microcentrifuge tube and EB buffer (50 µl) was added directly to the membrane. The PCR product was eluted by centrifuging for 60 seconds.

## 8.2 Protein expression and purification

### *8.2.1 Expression of cytochrome c peroxidase (CcP)*

The C*c*P construct (a kind gift from Prof. Mauk, University of British Columbia) was transformed into XL1-Blue supercompetent cells (Stratagene) and an overnight culture (5 ml) was grown and used to prepare DNA. BL21 DE3 Gold cells (Stratagene) were freshly transformed with the sequenced DNA and colonies were grown on an LB plate containing 100 µg/ml ampicillin, at 37 ºC for 12 hours. A single colony was picked and used to inoculate LB broth (50 ml) containing 100 µg/ml ampicillin, which was grown at 37 ºC with shaking at 225 rpm for 12 hours. 8x 1 L flasks of LB broth containing 100 µg/ml ampicillin were inoculated with 1 ml of the overnight culture and left to incubate at 37 ºC for ~8 hours with shaking at 225 rpm until the absorbance at 600 nm ($A_{600}$) reached 2.0 after which they were induced with

IPTG and left at 20 ºC for 18 hours with shaking at 225 rpm. The cells were harvested by centrifugation giving large red pellets which were stored at -80 ºC to aid lysis.

## *8.2.2 Purification of CcP*

### *8.2.2.1 Cell lysis*

The cell pellets were resuspended in lysis buffer (0.1M KPi, 1 mM EDTA, pH 6.0) (100 ml) along with hemin (10 mg dissolved in 1 ml 0.1 M KOH) (1 ml) and PMSF to a 1 mM final concentration. Once resuspended the cells were sonicated by 8x 1 minute bursts at high frequency with cooling for 30 seconds in between each burst. After sonication the lysate was left at 4 ºC for 1 hour in order to allow for reconstitution with hemin. The cell debris was removed by centrifugation at 20,000 rpm for 40 minutes. The cell free extract was then diluted to a total volume of 500 ml and readjusted to pH 6.0 before further purification.

### *8.2.2.2 Ion exchange chromatography*

The crude cell lysate was slowly loaded onto a 5 x 2 cm DEAE sepharose ion exchange column which had been pre equilibrated with 0.1 M KPi, pH 6.0. The column was then washed with 1 L of 0.1 M KPi buffer, pH 6.0 and eluted as a single red band with a minimum amount of 0.5 M KPi buffer, pH 6.0.

### *8.2.2.3 Gel filtration chromatography*

After elution from the ion exchange column the crude protein was diluted to a total volume of 100 ml using deionised water. The pH was adjusted to pH 5.0 and left at 4 ºC for 1 hour allowing an unidentified protein which coelutes with C*c*P to form a white precipitate, which was removed by centrifugation at 10,000 rpm for 10 minutes. The protein solution was concentrated to 10 ml and slowly loaded onto a 150 x 3 cm G50 gel filtration column which had been pre equilibrated with 0.1 M KPi, pH 6.0. The protein was slowly eluted over 8 hours and the centre of the large red band was collected for further purification.

#### *8.2.2.4 Recrystallisation*

The protein was placed in dialysis tubing and dialysed against 5 L of deionised water. After 4 days the crude crystals which formed were collected by centrifugation at 20,000 rpm for 10 minutes, washed with deionised water and redissolved in 0.1 M KPi buffer pH 6.0. The redissolved protein was then redialysed against water overnight and the process repeated 3 times. The protein was stored at -80 ºC as a crystalline suspension in water.

### *8.2.3 Expression of ascorbate peroxidase (APX)*

Recombinant soybean cytosolic APX (rsAPX) was prepared from *E. coli* SG 1300 cells (Qiagen) which contain pREP4 vector conferring kanamycin resistance. Cells also contained pQE30-rsAPX construct conferring ampicillin resistance, all media and plates used in the grow-up process contained kanamycin (30 μg/ml) and ampicillin (100 μg/ml). Agar plates were streaked with SG glycerol stocks stored at -80 ºC. The plates were inverted and incubated overnight at 37 ºC. A single colony was used to inoculate 400 ml LB media which was incubated overnight at 37 ºC with shaking at 225-250 rpm to form a starter culture. 50 ml of the starter culture was added to each of 8x 1 litre flasks of LB media. The flasks incubated at 37 ºC with shaking (225-250 rpm) until the absorbance at 600 nm ($A_{600}$) of the culture reached 1.0 (approximately 2 hours), at this point 1 M IPTG (1 ml) was added to each flask to induce protein expression and the flasks incubated at 27 ºC overnight with shaking at 225-250 rpm. Cells were harvested from the 8x 1 litre cultures by centrifugation at 8000 rpm for 5 minutes at 5 ºC. The cell pellets were frozen overnight at -80 ºC to aid lysis.

### *8.2.4 Purification of APX*

#### *8.2.4.1 Cell lysis*

The cell pellets were thawed in sonication buffer (200 ml). PMSF (50 mg in 2 ml isopropanol) was added to the cell suspension along with egg white lysozyme (~ 5 mg) and the suspension was stirred at room temperature for 20 minutes. DNase (50 μl of 1 mg/ml solution) was added to the viscous cell suspension, which was stirred for a

further 10 minutes until it became more fluid. The mixture was sonicated at maximum power in 4x 1 minute bursts, and kept on ice during the process. The cell debris was pelleted by centrifugation (20,000 rpm for 40 minutes at 4 ºC) and the supernatant (cell free extract) was collected and stored on ice for purification.

#### *8.2.4.2 Purification by nickel resin chromatography*

A $Ni^{2+}$- nitriloacetic acid (NTA) agarose column (Qiagen) was used to isolate rsAPX from the cell free extract by means of binding the His-tag on rsAPX. A column was packed with 5 ml Ni-NTA super flow resin (Qiagen) and washed with water (100 ml). The resin was equilibrated with sonication buffer (100 ml) and the cell free extract loaded slowly onto the column. The column was washed with sonication buffer until the flow through had an $A_{280}$ of <0.03 (~ 700 ml) indicating all the protein had been removed from the column. The column was then washed further using wash buffer (600 ml). The bound APX was eluted using a minimum amount of elution buffer (~ 200 ml) and the pH of the eluant adjusted to pH 6.0 for reconstitution.

#### *8.2.4.3 Reconstitution*

Hemin solution (5 mg/ml in 0.1 M KOH) was prepared and added to the Ni-NTA column eluant in aliquots of 20 µl, the eluant was stirred at 4 ºC for ~30 minutes between each addition and the $R_z$ value calculated using the Soret absorbance and the absorbance at 280 nm. Once the $R_z$ had reached ~ 2, 100 µl of the hemin solution was added and the protein solution dialysed against FFQ buffer overnight at 4ºC.

#### *8.2.4.4 FFQ chromatography*

Excess hemin was removed using a column (2.5 cm diameter and 20 cm long) packed with Q Sepharose fast flow (FFQ) resin. The column was washed with water (100 ml) and equilibrated with FFQ buffer (200 ml) the dialysed protein and hemin solution was centrifuged at 8000 rpm for 10 minutes and the supernatant loaded onto the column at a maximum flow rate. The column was then washed with FFQ buffer (100 ml). The protein was eluted using FFQ elution buffer (50 ml) and concentrated using an amicon device (Amicon, Bioseparations, Millipore) with nitrogen under pressure using an ultra filtration regenerated cellulose membrane (MW cut off 10,000,

Amicon) to a minimum volume of 20 ml. The protein was exchanged into deionised water 5 times using an amicon and concentrated to ~1 ml using a centricon (Amicon, Bioseparations, Millipore). The protein was pipetted into small eppendorfs (100 µl aliquots), snap frozen using dry ice and ethanol and stored at -80 ºC.

### *8.2.4.5 SDS-page*

To follow the progress of APX and C*c*P purification and to confirm the purity of the protein, SDS-PAGE was carried out for all proteins. Discontinuous polyacrylamide gels (15%) containing 0.1% SDS and 4% polyacrylamide stacking gel and a mini-Protean II gel system at 0.75 mm thickness were used. Samples were prepared by adding an equal volume of sample buffer and boiling for five minutes. The gels were run in SDS running buffer at 150 V until the dye front reached the end of the gel. Gels were soaked in stain for thirty minutes, then excess stain was removed by soaking in destain solution overnight. A typical SDS-PAGE gel of samples taken at various stages during the expression process is shown in Figure 8.1.

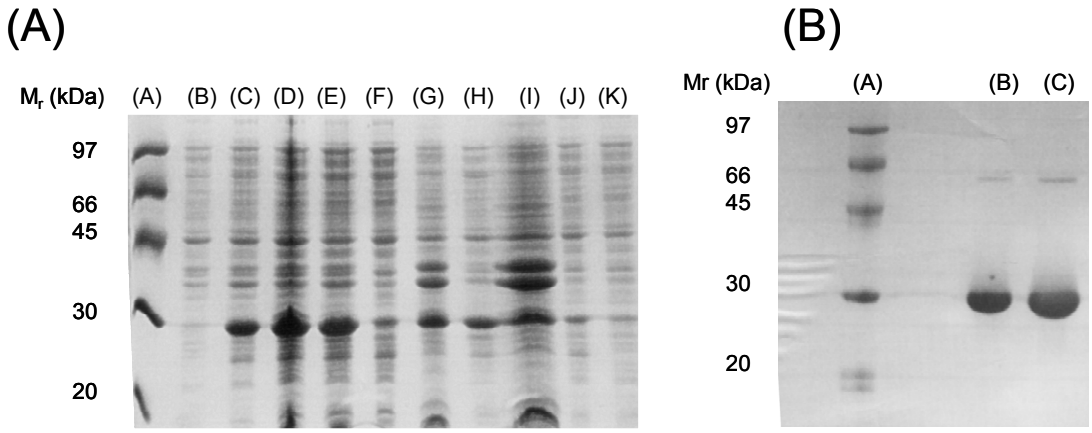


**Figure 8.1: SDS-page**

**(A)** SDS-PAGE of samples taken during the purification of rsAPX. Lane (A) denotes the marker standards. Lanes (B) to (K) are samples taken at different stages of the purification process. The stages are: (B) before induction; (C) before harvesting; (D) cell pellet with lysozyme; (E) primary lysis (after sonication); (F) cell free extract; (G) cell pellet; (H) second cell free extract; (I) final cell pellet; (J) and (K) the cell-free extract after the His-binding nickel column. **(B)** SDS-PAGE of purified rsAPX, (A) is the marker (B) is rsAPX before FPLC and (C) is rsAPX after FPLC.

# 8.3 Mutagenesis

## *8.3.1 Site directed mutagenesis*

Site-directed mutagenesis on C*c*P and APX was performed according to the Quikchange™ protocol (Stratagene Ltd, Cambridge, UK). Mutations were confirmed by DNA sequencing as reported previously [1]. Standard reactions volumes are shown in Appendix C, Table 1 and reagents were added in the order shown. Thermocycler programmes are shown in Appendix C, Table 2 and complementary oligonucleotides for the generation of ascorbate binding site C*c*P mutants (Chapter 2) are shown in Appendix B, Table 1. Seven C*c*P mutants were made in total: Y36A, N184R, W191F, Y36A/N184R, Y36A/W191F, N184R/W191F, and Y36A/N184R/W191F. Wild type C*c*P was used as a template for the single variants, Y36A was used as a template for Y36A/N184R and Y36A/W191F, N184R was used as a template for N184R/W191F and Y36A/W191F was used as a template for Y36A/N184R/W191F. Oligonucleotides used to produce the C*c*P aromatic binding site mutants, M119W and S81W (Chapter 4) are shown in Appendix B, Table 2. Oligonucleotides used to produce H42A for the isoniazid binding work (Chapter 3) are shown in Appendix B, Table 3. Optical density (OD) is used as a measure of oligonucleotide concentration and is the absorbance of the oligonucleotides at 260 nm.

# 8.4 Directed evolution

## *8.4.1 Saturated mutagenesis*

Complementary oligonucleotides were designed by K. H. Sharp [2] to have approximately 15 bases either side of the codon for the residue to be mutated and end in G or C. The oligonucleotides were designed for saturated point mutagenesis at either Ser69 or Asp133 in APX and were prepared by Invitrogen, their sequences are shown in Appendix B, Table 4.

The saturated mutagenesis libraries were created using the Quikchange™ mutagenesis kit (Stratagene). Using the appropriate primers two individual libraries were made; S69X and D133X. Reactions were set up as shown in Appendix C, Table 5. *Pfu Ultra* is a DNA polymerase supplied with the Quikchange® kit along with 10x

reaction buffers. The water and glycerol used were both sterile and $MgCl_2$ (25 mM) was prepared using sterile water. The template used was pQE30 vector (Qiagen) containing the rsAPX gene (25 ng/µl), a total of 50ng of template DNA was present in each reaction. Absorbance values of the primers (260 nm) were S69XF (10) S69XR (10), D133XF (12.4), D133XR (7.8). The dNTP mix contained equal amounts of dATP, dTTP, dCTP and dGTP with a total dNTP concentration of 40 mM.

With the exception of *Pfu Ultra,* chemicals were added to thin walled PCR tubes and were centrifuged for 10 s at 13,000 rpm. The reactions were carried out in a Perkin-Elmer 480 DNA Thermocycler with programs set as in Appendix C, Table 4. The Thermocycler was turned on and when it reached 94 ºC the *Pfu Ultra* was added to each reaction along with a drop of nujol oil and the tubes put in.

Bands were seen for the primers in the agarose electrophoresis of each of the reactions but in addition faint bands were seen at 4.7 kb (desired product) for S69X reactions 3 and 4 and D133X reactions 3 and 4 (see Table 5, Appendix C for reaction volumes). These reactions were treated with *Dpn*I (1 µl) (also supplied in the Quikchange™ kit) and incubated at 37 ºC for 1 hour in order to digest template DNA before being transformed into XL1-Blue cells for amplification of the DNA libraries. A second round of saturated mutagenesis was carried out in the exact same way as the first round using either S69P rsAPX or D133R rsAPX as the template DNA to create two new libraries, S69P/D133X and S69X/D133R respectively.

The protocol followed was the same as in the first round of saturated mutagenesis, the reactions were set up as shown in Appendix C, Table 5 (S69P/D133X) and Table 6 (S69X/D133R) and the Thermocycler programmed as shown in Appendix C, Table 7. The Templates used were S69P rsAPX (116 ng/µl) and D133R rsAPX (62.5 ng/µl). The primers were of the same optical density and the DNA polymerase used was *Pfu Ultra* from the Quikchange™ kit, as for the first round of saturated mutagenesis.

Bands corresponding to the product of the PCR (4.7 kb) were seen on agarose gels for reactions 1, 3 and 4 for S69P/D133X and reactions 2, 3 and 4 for S69X/D133R. Reactions 4 were chosen for each library, treated with *Dpn*I (1 µl) and incubated at 37 ºC for 1 hour before being transformed into XL1-Blue cells to amplify the two libraries.

## *8.4.2 Random mutagenesis*

### *8.4.2.1 Random mutagenesis using Genemorph® random mutagenesis kit (Stratagene)*

The primers used were pQE30 forward and reverse primers; this allowed amplification of the rsAPX gene via PCR and not the whole pQE30-rsAPX construct, in turn allowing for levels of mutagenesis to be more accurately controlled. The primers were prepared by Invitrogen and their sequences are shown in Appendix B, Table 5.

The template used was wild type rsAPX prepared from XL1-Blue cells (16.5 ng/µl). By varying the amount of template used the mutation levels can be varied; the lower the concentration of the template, the higher the mutation frequency. Four reactions were set up in total with final template amounts of 12.5 ng, 31.25 ng, 50 ng, and 62.5 ng. The DNA polymerase used was Mutazyme® (5 U/µl), the buffer used was 10x Mutazyme® reaction buffer, the dNTP mix contained equal amounts of dATP, dCTP, dGTP and dGTP with a concentration of 10 mM per dNTP all of which were supplied in the Genemorph® kit. The $MgCl_2$ used had a concentration of 25 mM and was filter sterilised before use. Reagents were added to thin walled PCR tubes in the order shown in Appendix C Table 8. The optical density of both pQE30F and pQE30R was 10.The Thermocycler used was an Eppendorf Mastercycler gradient. Four different annealing temperatures were tried for each reaction (48 ºC, 51.2 ºC, 61.5 ºC and 68.5 ºC). The Thermocycler was programmed as shown in Appendix C, Table 9.

The product from each reaction with varying levels of template and different annealing temperatures (16 reactions in total) were examined by agarose gel electrophoresis after *Dpn*I degradation of the template. The expected product band should be seen at approximately 1050 bp. Reactions with 1 µl of template showed no band at any annealing temperature. Reactions with 5 µl template showed very strong bands but this has the lowest mutation frequency so much of the product can be expected to be wild type rsAPX. The cleanest bands seen were for reactions containing 2.5 µl of template (31.25 ng per 50 µl reaction) with an annealing temperature of 61.5 ºC. This PCR product was purified (section 8.1.4), religated into

empty pQE30 vector and transformed into XL1-Blue cells to create a random mutagenesis DNA library, named Mut.

### *8.4.2.2 Random mutagenesis using error prone PCR (Taq DNA polymerase)*

Taq DNA polymerase (5 U/µl) (Stratagene) was used for error prone PCR with varying amounts of $MnCl_2$ (2.5 mM) to decrease the efficiency of replication. The template used was wild type rsAPX (16.5 ng/µl) prepared from XL1-Blue cells and as in the random mutagenesis using Mutazyme® pQE30 forward and reverse sequencing primers were used (Appendix B, Table 5) meaning that only the rsAPX gene is amplified in the PCR, both primers had an optical density of 10. $MnCl_2$ and $MgCl_2$ (50 mM) were both filter sterilised before use. The buffer used was 10x Taq reaction buffer (Stratagene) and the dNTP mix used had equal amounts of dATP, dCTP, dGTP and dTTP with a total dNTP concentration of 40 mM. Reagents were added to thin walled PCR tubes in the order shown in Appendix C, Table 10. The Thermocycler used was an Eppendorf Mastercycler gradient. Four different annealing temperatures were tried for each reaction (48 ºC, 51.2 ºC, 61.5 ºC and 68.5 ºC). The Thermocycler was programmed in the same way as for random mutagenesis using Mutazyme and is shown in Appendix C, Table 9.

The products from all 24 reactions were treated with *Dpn*I (1 µl) and incubated at 37 ºC for one hour before being examined by agarose gel electrophoresis. No product was seen at 1050 bp for annealing temperature of 68 ºC. No product was seen at concentrations of $MnCl_2$ less than 0.3 and very little product is seen for reactions with 0.5 mM $MnCl_2$. Experiments were repeated using 0.1 mM and 0.3 mM $MnCl_2$ and lower $MgCl_2$ concentrations (2.5 mM instead of 5 mM), the annealing temperature used was 61 ºC. The two products from the repeated PCR experiments were purified (Section 8.1.4) and religated in empty pQE30 vector before being transformed into XL1-Blues to create two error prone PCR libraries, Ep 0.1 and Ep 0.3 respectively.

### *8.4.2.3 Insertion of PCR product into pQE30 vector*

The PCR products were purified and restricted with *Bam*HI and *Kpn*I, reactions were made up as in Appendix C, Table 11 and incubated at 37 ºC for 3 hours. Both restriction enzymes, Bovine Serum Albumin (BSA) and NEB2 buffer were obtained

from New England Biosciences. The 85 and 81 kb fragments were removed by PCR purification.

pQE30-rsAPX construct prepared using Qiagen midi spin kit was used to create empty vector for insertion of the PCR products. A restriction was set up as in Appendix C, Table 12 and incubated at 37 ºC for 3 hours. The 900 kb fragment was too large to be removed by PCR purification and so the desired 3444 kb product was extracted from an agarose gel after electrophoresis. The DNA from the gel extraction was treated with Calf Intestinal Alkaline Phosphatase (CIAP, New England Biosciences) before ligation to prevent self ligation. CIAP (1 µl) was added to the DNA and the reaction incubated at 37 ºC for 1 hour, before being removed by PCR purification.

Ligation reactions were set up as shown in Appendix C, Table 13 using a 5:1 vector: insert ratio based on the amount of DNA used in the reaction. The reactions were incubated at room temperature for 1 hour before being transformed into *E. coli*. T4 DNA ligase and reaction buffer were obtained from New England Biosciences. The concentration of vector was 37.5 ng/µl, Ep 0.1 PCR product 37 ng/µl, Ep0.3 PCR product 13 ng/µl and Mut PCR product 33 ng/µl. Each ligation mixture (5 µl) was transformed into XL1-Blue cells and plated on agar plates containing ampicillin (100 µg/ml) which were incubated overnight at 37 ºC. The plate with cells transformed with the self ligation mixture showed no colonies. Therefore the colonies on the other plate were likely to be due only to uptake of plasmids containing PCR product.

#### *8.4.2.4 Random mutagenesis by DNA repair pathway deficient E. coli*

XL1-Red competent cells (Stratagene) which were stored at -80 ºC were gently thawed on ice. The cells (100 µl) were added to pre-chilled 14 ml Falcon 2059 tubes along with β-mercaptoethanol (1.7 µl, 1.42 M), the tubes were swirled and kept on ice for 10 minutes, swirling gently every two minutes. rsAPX DNA (~ 50 ng) from XL1-blue cells was added and after gently swirling the tubes were incubated on ice for 30 minutes. The tubes were heat shocked at 42 ºC for 45 seconds in a water bath then put back on ice for a further 2 minutes. LB-media (5 ml) containing $MgCl_2$ (70 µl, 1 M) and $MgSO_4$ (70 µl, 1 M) was preheated to 42 ºC and added to the Falcon tube (500 µl) and the tube incubated at 37 ºC for 1 hour with shaking at 225-250 rpm.

The cell solution was added to 10 ml LB-media containing ampicillin (100 μg/ml) and incubated at 37 ºC until the absorbance of the solution at 600 nm ($A_{600}$) was >1.5, indicating that late log phase had been reached (~ 48 hours). Fresh ampicillin (100 μg/ml) was added after 24 hrs. This two day grow-up (100 μl) was added to LB-media (10 ml containing ampicillin (100 μg/ml)) and incubated again until late log phase was reached (~ 48 hours). The DNA was extracted from the cells and re-transformed into XL1-Red cells and the process repeated four times before screening.

## *8.4.4 Screening*

### *8.4.4.1 K.H. Sharp guaiacol screen*

The screen used to screen for enhanced guaiacol activity was developed by K.H. Sharp [2]. SG glycerols containing the libraries to be screened were diluted in LB media (1/1000) and spread on kanamycin (30 μg/ml)/ampicillin (100 μg/ml) agar plates which had been over laid with a nitrocellulose membrane (Hybond-C extra, Amersham biosciences, Catalogue no. RPN82E). The plates were incubated inverted overnight at 37 ºC. Using tweezers the membranes were carefully transferred to agar plates containing kanamycin (30 μg/ml)/ampicillin (100 μg/ml) which had been spread with 1 M IPTG (20μl). The plates were incubated at 27 ºC for 4 hours before the membranes were carefully transferred to an empty Petri dish and frozen overnight at -80 ºC to partially lyse the cells.

The membranes were allowed to thaw for 1 hour at room temperature before screening. A 2% agar solution in sterile water was melted and placed in a water bath at 50 ºC in aliquots of 10 ml for each membrane to be screened. A guaiacol (250 μM) and hydrogen peroxide (125 μM, assessed by UV-visible spectroscopy)) solution was made in 0.1 M KPi buffer, pH 7.0 and stored in aliquots of 10 ml in a 50 ºC water bath. A 10 ml aliquot of agar was mixed with 10 ml of the guaiacol and hydrogen peroxide solution and poured over each membrane. The membranes were monitored for 1 hour to detect any colour change in the colonies. Red colonies were removed using a pipette and placed in 10 ml LB media containing kanamycin (30 μg/ml) and ampicillin (100 μg/ml); this was incubated overnight at 37 ºC with shaking (225-250 rpm). DNA was prepared from the overnight culture for sequencing.

#### *8.4.4.2 Iffland et al guaiacol screen*

The second type of screen used was developed by I*ffland et al* [3] during there work on enhancing the guaiacol activity of C*c*P. SG glycerols containing the libraries to be screened were grown up at 37 ºC overnight on nitrocellulose membranes as in the Sharp screen. Protein expression was also induced in the same way by transferring the membranes to agar plates which had been spread with 1 M IPTG. In order to partially lyse the cells the membranes were dipped in liquid $N_2$ for ~3 seconds and allowed to air dry. The screen was carried out by placing the membranes on 4x filter papers that had been soaked in a guaiacol and hydrogen peroxide solution (7.5 ml, 1 mM guaiacol and 0.5 mM $H_2O_2$ in 0.1 M KPi, pH 7.0). Positive colonies were picked using pipettes and grown-up overnight in LB media containing kanamycin (30 µg/ml) and ampicillin (100 µg/ml). DNA was prepared from the overnight grow-ups for sequencing.

## 8.5 Spectroscopy

### *8.5.1 Electronic absorption spectroscopy*

UV-visible spectra were recorded on variable slit Perkin-Elmer Lambda 14, Lambda 35 or Lambda 40 each had a 1 mm slit width and 10 mm path length. Where temperature was controlled, a Perkin-Elmer Lambda 35 was used which was fitted with a Peltier device (Perkin-Elmer, Peltier thermostated reference holder, BS0510412).

### *8.5.2 Determination of absorption coefficients*

In order to determine the absorption coefficients for the mutant APX and C*c*P proteins produced, an average of three heme contents were measured using the pyridine hemochromogen assay [4]. Purified protein (10 µl) was diluted to 1 ml using sterile water and the absorbance at the Soret ($A_{Soret}$) was measured, this was used to calculate the amount of protein required to make a solution with an absorbance of 3.0 at $A_{Soret}$ ($3_{OD}$ solution). The $3_{OD}$ solution (50 µl) was diluted to 500 µl using sterile water and the $A_{Soret}$ obtained. The $3_{OD}$ solution (300 µl) was then mixed with pyridine base solution (Appendix A) (600 µl) in a cuvette and allowed to stand for five minutes

resulting in oxidised hemochromogen. Sodium dithionate (2-3 grains) was added and a UV-visible spectrum of the unstable reduced hemochromogen recorded over the wavelength range 650-450 nm (Figure 8.2). The exact concentration of the protein stock is determined from the concentration of the haemochromogen formed in the reaction. The absorption coefficient of the proto-heme reduced pyridine-haemochromogen at 557 nm is 32 $mM^{-1}$ $cm^{-1}$ and permits calculation of the concentration using the Beer-Lambert law. Once the exact concentration of the protein sample is known the absorption coefficient at $A_{Soret}$ can be calculated again using the Beer-Lambert law.

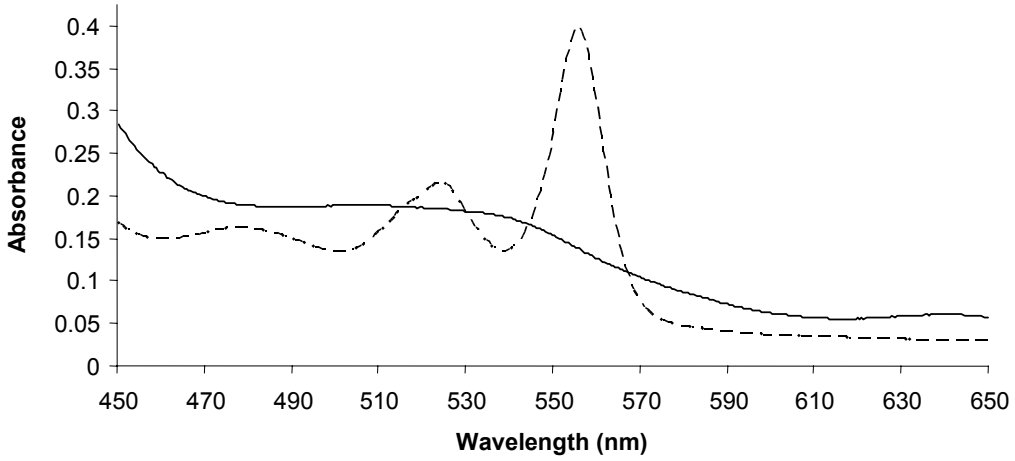


**Figure 8.2: Pyridine hemochromogen**.

Spectra of rsAPX before the addition of alkaline pyridine and sodium dithionite (solid line) and the reduced pyridine-haemochromogen complex (dashed line).

# 8.6 Transient state kinetics

For Chapter 2 transient state kinetics were performed using a SX.18 MV stopped-flow spectrophotometer (Applied Photophysics Ltd) in 100 mM potassium phosphate, pH 6.0 at 10 °C. Time-dependent spectral changes occurring upon reaction of C*c*P with $H_2O_2$ were monitored using a photodiode array detector and X-SCAN software (Applied Photophysics Ltd). In these experiments the protein (concentration = 2 μM) was mixed with either a stoichiometric or 10-fold molar excess of $H_2O_2$ (reaction cell concentrations). Spectral deconvolution was performed by global analysis and numerical integration methods using PROKIN software (Applied Photophysics Ltd).

Oxidation of L-ascorbate by the W191F and W191F/N184R variants of C*c*P was measured using the sequential mixing mode of the stopped-flow apparatus: 4 μM of mutant C*c*P was mixed with 6 μM $H_2O_2$ and the solution allowed to age for 20 ms (enabling formation of the porphyrin π-cation radical intermediate) prior to mixing with ascorbate. Oxidation of ascorbate was monitored at 423 nm at a range of ascorbate concentrations between 100 and 1000 μM.

## 8.6 Steady-state kinetics

### *8.6.1 Oxidation of guaiacol by APX*

#### *8.6.1.1 Standard assay*

Three stock solutions were made: a 100 mM guaiacol solution (70 μl guaiacol, 1.5 ml ethanol and 3.43 ml 0.1 M KPi buffer pH 7.0); a 10 mM hydrogen peroxide solution in 0.1 M KPi buffer pH 7.0; and an enzyme solution also in 0.1 M KPi buffer pH 7.0. The concentration of the hydrogen peroxide solution and the enzyme solution were assessed using UV-visible spectroscopy using an absorption coefficient of 39.4 $M^{-1}cm^{-1}$ for $H_2O_2$. The concentration of the enzyme solution was ~ 5 μM; the exact final concentration was used when calculating v/[E] values. A fixed amount of enzyme was mixed with buffer and various amounts of guaiacol solution up to a final volume of 990 μl in a 1 cm path length cuvette. Hydrogen peroxide solution (10 μl) was added to initiate the reaction and the formation of tetraguaiacol was measured at 470 nm on a UV-visible spectrophotometer. The initial rate was measured as a function of time using the Kinlab program. Initial rates (v/[E] ($s^{-1}$)) were plotted against guaiacol concentration and the data fitted to the Michaelis-Menten equation using kaleidagraph 3.0 to obtain $k_{cat}$ and $K_M$ for the oxidation of guaiacol.

#### *8.6.1.2 Using Stopped –flow*

An Applied Photophysics RX.2000 stopped-flow was used for measuring the rate of tetraguaiacol production at 470 nm. The apparatus was set up for single wavelength experiments (470 nm) and single mixing. The temperature of the water bath was set at 25 ºC, the pressure of the $N_2$ cylinder was set and 8 Barr and the lamp

switched on 30 minutes before use. Datum were collected over 10 seconds for each guaiacol concentration and fitted to a linear plot to get the initial rate of tetraguaiacol formation. The solutions in the syringes were double the concentration of the final desired concentration. One syringe contained a 0.02 μM rsAPX solution; the other contained a solution with 0.02 mM $H_2O_2$ and various concentrations of guaiacol ranging from 5 mM to 80 mM. At least five initial rates were found for each guaiacol concentration and the average taken. Initial rates (v/[E] ($s^{-1}$)) were plotted against guaiacol concentration and the data fitted to the Michaelis-Menten equation using kaleidagraph 3.0 to obtain $k_{cat}$ and $K_M$ for the oxidation of guaiacol as for the assays carried out using standard assay techniques. Three independent assays were carried out for the wild type and each mutant to give average values of $k_{cat}$ and $K_M$.

### *8.6.2 Oxidation of cytochrome c by CcP*

Steady-state oxidations of horse heart cytochrome *c* were carried out using reduced cytochrome *c*. Reduction of cytochrome *c* was carried out as reported previously [5] by adding a single grain of sodium dithionite to horse heart cytochrome *c* (Sigma). UV-visible spectra were recorded before and after addition of the reducing agent (Figure 8.3) and excess sodium dithionite was removed using a G50-sephadex gel filtration column.

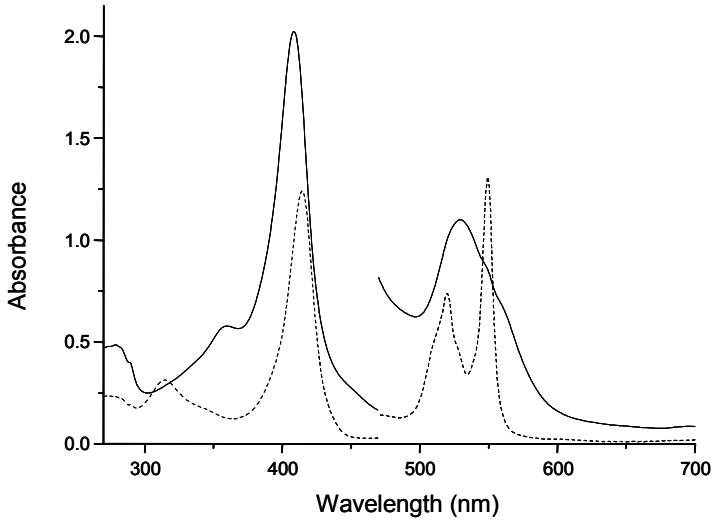


**Figure 8.3: Reduction of horse heart cytochrome *c***

Spectrum of oxidised cytochrome *c* (solid line) and reduced cytochrome *c* (dashed line).

A $H_2O_2$ stock solution (100 mM) was made in 0.1 M KPi buffer, pH 6.0, the concentration of which was assessed spectroscopically. An ~ 5 μM solution of enzyme was made up in 0.1 M KPi, pH 6.0, the exact final concentration was used when calculating v/[E] values. A fixed amount of enzyme was mixed with buffer and varying volumes of cytochrome *c* were added, the final concentration of cytochrome *c* was then calculated using $\varepsilon_{550}$ = 27.7 $mM^{-1}cm^{-1}$ for cytochrome *c*. $H_2O_2$ solution (20 μl giving a final concentration of 200 μM) was added to initiate the reaction. A final volume of 1 ml was used in a cuvette with a 1 cm path length. The reaction followed the decrease in absorbance at 550 nm as cytochrome *c* was oxidised. The initial rate was measured as a function of time using the Kinlab program. Initial rates (v/[E] ($s^{-1}$)) were plotted against cytochrome *c* concentration and the data fitted to the Michaelis-Menten equation using kaleidagraph 3.0 to obtain $k_{cat}$ and $K_M$ for the oxidation of cytochrome *c*. All measurements were carried out at 25 ºC.

### *8.6.3 Oxidation of ascorbate by CcP*

Steady-state measurements for oxidation of ascorbic acid were carried by following the time-dependent decrease in absorption at 270 nm which corresponds to s decrease in ascorbate concentration. Stock solutions were made up in 0.1 M KPi buffer, pH 6.0. Enzyme (~ 5 μM) and $H_2O_2$ (100 mM) concentrations were calculated as described previously (section 8.6.2), with an exact final enzyme concentration being used to calculate v/[E]. A final assay volume of 500 μl was used with a cuvette that had a 0.2 cm path length. Ascorbate concentrations were calculated using the absorption coefficient $\varepsilon_{290}$ = 2.8 $mM^{-1}cm^{-1}$ [6]. Enzyme and buffer were mixed with ascorbate, the initial absorption taken in order to calculate the final ascorbate concentration, and the reaction initiated with $H_2O_2$.Initial rates were multiplied by a factor of two to allow for disproportionation of the monodehyroascorbate radical [7]. Data were fitted to the Michaelis-Menten equation as previously described [7, 8]. All measurements were carried out at 25 ºC

### *8.6.4 Oxidation of guaiacol by CcP*

Steady-state oxidations of guaiacol in 100 mM KPi buffer, pH 6.0, 25°C, were carried out according to published protocols [8] using the standard assay as detailed in guaiacol oxidation by APX (section 8.6.1.1).

#### *8.6.4.1 INH inhibition of cytochrome c oxidation by CcP*

Steady-state oxidation of cytochrome *c* was measured as described previously (section 8.6.2) in the presence of various concentrations of INH. Enzyme and cytochrome *c* were mixed with buffer and a fixed concentration of INH solution (100 mM, 0.1 M KPi buffer, pH 6.0) was added to a final volume of 1 ml in a cuvette with a 1 cm path length. $H_2O_2$ was added to a final concentration of 200 μM in order to initiate the reaction. Steady-state oxidation was measured at four final INH concentrations: 1 mM, 2.5 mM, 5 mM and 10 mM. Data were fitted to the Michaelis-Menten equation.

#### *8.6.4.2 INH inhibition of guaiacol oxidation by CcP*

Steady-state guaiacol oxidation was measured as described previously (section 8.6.1.1). As for inhibition experiments where cytochrome *c* was the substrate (section 8.6.4.1), steady-state experiments were carried out in the presence of four final concentrations of INH (1 mM, 2.5 mM, 5 mM and 10 mM).

#### *8.6.4.3 Calculation of $K_i$*

The dissociation constant for the binding of INH to C*c*P, $K_i$, was calculated using reciprocal (Lineweaver-Burk) plots of the steady-state data at various INH concentrations. The slope of the reciprocal plot is given by Equation 8.1.

$$Slope = \frac{K_M}{V_{max} K_i}[I] + \frac{K_M}{V_{max}} \qquad \textbf{(8.1)}$$

Where [I] is the concentration of inhibitor. Hence a plot of the slope of the reciprocal plot against [I] will give a straight line with a slope of $K_m/V_{max}K_i$, a y-axis intercept of $K_M/V_{max}$ and, in the case of competitive inhibition, an x-axis intercept of $-K_i$.

# 8.7 X-ray crystallography

## *8.7.1 Crystallisation of APX*

Crystallisation of the H42A variant of rsAPX was carried out using the sitting drop method in 24 well plates (4x 6 Cryschem plates with 1 ml reservoirs, Hampton Research). The plates were set up in a temperature controlled room at 19 ºC and the area dusted before use. The protein solution (10 mg/ml in deionised water) was kept on ice throughout. Reservoirs contained 1 ml of solution (2.25 M $LiSO_4$, 0.1 M Hepes, pH 8.3). Protein solution (2 µl) and reservoir solution (2 µl) were added to each well and the plates sealed carefully with clear postal tape ensuring no bubbles were present. After 2 days crystals that appeared well ordered were seen in most of the wells (Figure 8.4).

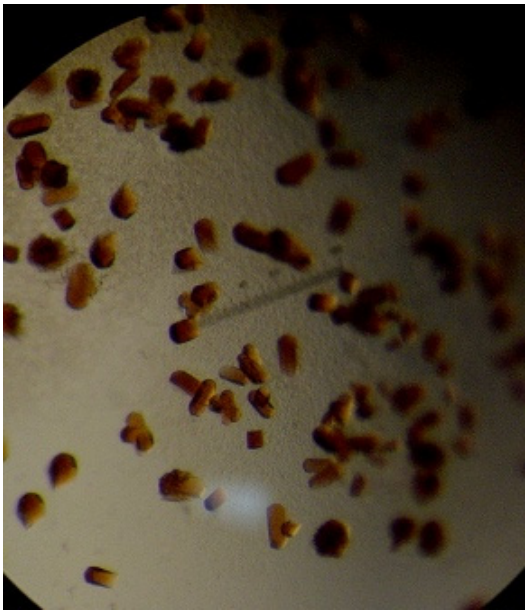

**Figure 8.4: Crystals of APX (magnified)**

## *8.7.2 Crystallisation of Cc*P

Crystals of C*c*P were prepared by microdialysis with 100 µl of a 10-30 mg/ml solution of C*c*P in 500 mM potassium phosphate, pH 6.0 against 10 ml of 50 mM potassium phosphate, pH 6.0 containing 30% 2-methyl-2,4-pentanediol by volume. The crystals were grown at 4 ºC and after approximately 2 days (dependant on the variant) large bright red crystals were seen (Figure 8.5).

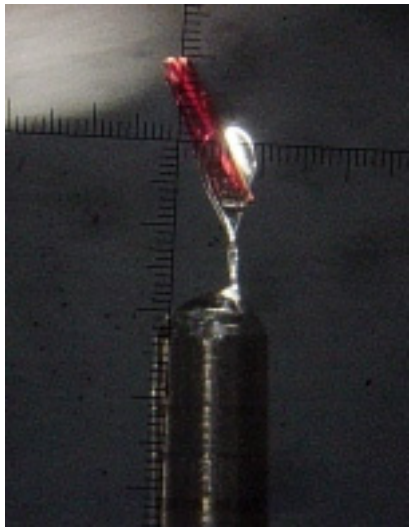

**Figure 8.5: Crystal of C*c*P mounted in cryostream (magnified).**

### *8.7.3 Ascorbate, INH, guaiacol and phenol soaks*

Crystals of APX and C*c*P were soaked to obtain the substrate- or inhibitor-bound forms. The soaks were carried out using a glass plate with 0.5 ml wells, 20 µl of soaking solution was pipetted into a well. A mounting loop (Hampton research, crystalcap copper™) was used to lift crystals out of their mother liquor and hold them in the various soaking solutions for a defined amount of time. The crystals were then frozen either by placing them directly in a cryostream or by placing in liquid nitrogen. For the ascorbate-C*c*P structure the crystal were soaked in mother liquor containing 100 mM ascorbate for five minutes before rapid cooling to 100 K. For the C*c*P-INH structure, the crystals were soaked in mother liquor saturated with isoniazid (INH) for 5 minutes before rapid cooling to 100K. For the various C*c*P-guaiacol structures, the crystals were soaked in 150 mM guaiacol solution for 10 minutes, the guaiacol was solubilised in 20% methanol before being added to mother liquor. For the C*c*P-phenol structures, crystals were soaked in 100 mM phenol solution for 10 minutes.

### *8.7.4 Data collection and refinement*

Diffraction data were collected for all variants of C*c*P in house using a Rigaku RU2HB X-ray generator with copper anode and Xenocs multilayer optics and an R-Axis IV detector. All data were collected at 100 K. Diffraction data for rsAPX H42A and the rsAPX H42A-INH complex were collected at ESRF (Grenoble, France) using ID14-1 and an ADSC Q4R detector. All data were collected at 100 K. Data were indexed, integrated and scaled using MOSFLM [9] and SCALA [10]. Data Collection

statistics for H42A rsAPX and the H42A-INH complex (Chapter 3) are shown in Appendix D, Table 1, data collection statistics for ascorbate binding C*c*P variants (Chapter 2) are shown in Appendix D, Table 2 and data collection statistics for aromatic binding C*c*P variants (Chapter 4) are shown in Appendix D, Table 3. In all cases 5 % of the data were flagged for the calculation of $R_{free}$ and excluded from subsequent refinement. The structures were refined from the 1.70 Å wild type C*c*P structure [11] (Protein data bank entry 2CYP) or the 1.60 Å wild type rsAPX structure [12] (Protein data bank entry 1OAG). All refinement used REFMAC [13] from the CCP4 suite [10]. COOT [14] was used throughout for manual adjustment, ligand fitting and interpretation of the water structure.

### *8.7.5 Neutron diffraction*

Partially deuterated conditions were used in order to obtain wild type C*c*P crystals for neutron diffraction. Protein was grown and purified as described in Sections 8.2.1 and 8.2.2. However instead of exchanging crude crystals into water crystals were exchanged into $D_2O$. Diffraction quality crystals were produced by dialysing 100 µl of a 10-30 mg/ml solution of C*c*P in 500 mM potassium phosphate, pH 6.0 against 10 ml of 50 mM potassium phosphate, pH 6.0 containing 30% 2-methyl-2,4-pentanediol by volume. All solutions and buffers were made with $D_2O$ instead of $H_2O$. The crystals were grown at 4 ºC and the deuterium appeared to have no effect on the length of time taken for crystals to grow or their quality/size. Neutron diffraction data were collected by Matthew Blakeley and Peter Moody at the European Molecular Biology Laboratory (EMBL) in Grenoble on the *Institut Laue Langevin* (ILL) neutron Laue diffractometer, *LADI.* A wild type C*c*P crystal with an approximate volume of 1.5 $mm^3$ was mounted in a quartz capillary which was sealed with wax. Neutron Laue diffraction were collected at room temperature using the LADI-III instrument installed on cold neutron guide H142 at the ILL. An Ni/Ti Multilayer band-pass filter was used to select a restricted neutron wavelength range ($\delta\lambda/\lambda \approx 25\%$) centred at 3.7 Å and extending from 3.2 to 4.2 Å. Data were recorded in a series of 9 contiguous Laue images using 15 hour exposures with a step separation of $\varphi = 14^{\circ}$ around the vertical rotation axis of the detector. Spots were observed up to 2.2 Å resolution with data processed up to 2.4 Å. Neutron Laue data were indexed and integrated using the Daresbury Laboratory LAUGEN software suite [15, 16] modified

for the cylindrical geometry of the LADI-III detector. The LSCALE programme [17] was used to derive the wavelength-normalization curve using the intensities of symmetry-equivalent reflections measured at different wavelengths. Reflections were scaled using SCALA [10] and relevant statistics of data collection are shown in Appendix D, Table 4.

### *8.7.7 Collecting room temperature diffraction data*

A single wild type C*c*P crystal was pulled into a 0.7 mm diameter glass capillary tube (Glaskapillaren, Astrophysics research limited). Excess mother liquor was removed by carefully inserting fine strips of filter paper into the capillary tube each end of which was then sealed with melted wax. Data were collected in the same way as under cryogenic conditions using a Rigaku RU2HB X-ray generator with copper anode and Xenocs multilayer optics and an R-Axis IV detector. As a result of damaging effects of the X-ray beam, data were collected from 6 individual crystals, with 30 degrees of data (60 images) collected on each. The individual data sets were integrated using MOSFLM [9] and the mtz files produced combined in the CCP4 suite [10] before the resulting single mtz file was scaled using SCALA [10]. Further refinement was carried out as detailed in section 8.7.4. Refinement statistics are shown in Appendix D, Table 5.

## 8.8 References


1. Metcalfe, C.L., Ott, M., Patel, N., Singh, K., Mistry, S.C., Goff, H.M., and Raven, E.L., *Autocatalytic formation of green heme: Evidence for $H_2O_2$-dependent formation of a covalent methionine-heme linkage in ascorbate peroxidase.* J. Am. Chem. Soc., 2004. **126**(49): 16242-16248.
2. Sharp, K.H., *Substrate Binding Interactions in Ascorbate Peroxidase*, in *Chemistry*. 2005, University of Leicester: Leicester.
3. Iffland, A., Tafelmeyer, P., Saudan, C., and Johnsson, K., *Directed molecular evolution of cytochrome c peroxidase.* Biochemistry, 2000. **39**(35): 10790-10798.
4. Antonini, M., and Brunori, E. , *Hemogloblin and Myoglobin and their Reactions with Ligands*. North-Holland Research Monographs Frontiers of Biology, ed. A. Neuberger and E.L. Tatum. Vol. 21. 1971, Amsterdam, London.: North Holland Publishing company.
5. Yonetani, T., and Ray, G. S, *Studies on Cytochrome c Peroxidase: Purification and some properties.* J. Biol. Chem., 1965. **240**: 4503-4514.
6. Asada, K., Methods in Enzymology, 1984. **105**: 422-427.
7. Lad, L., Mewies, M., and Raven, E.L., *Substrate binding and catalytic mechanism in ascorbate peroxidase: Evidence for two ascorbate binding sites.* Biochemistry, 2002. **41**(46): 13774-13781.
8. Lad, L., Mewies, M., Basran, J., Scrutton, N.S., and Raven, E.L., *Role of histidine 42 in ascorbate peroxidase - Kinetic analysis of the H42A and H42E variants.* Eur. J. Biochem., 2002. **269**(13): 3182-3192.
9. Leslie, A.G.W., *Joint CCP4 + ESF-EAMCB Newsletter on Protein Crystallography.* 1992. **No. 26**.
10. Bailey, S., *The CCP4 Suite - Programs for protein crystallography.* Acta Crystallogr., Sect. D. Biol. Crystallogr., 1994. **50**: 760-763.
11. Finzel, B.C., Poulos, T.L., and Kraut, J., *Crystal structure of yeast cytochrome c peroxidase refined at 1.7 angstrom resolution.* J. Biol. Chem., 1984. **259**(21): 3027-3036.
12. Sharp, K.H., Mewies, M., Moody, P.C.E., and Raven, E.L., *Crystal structure of the ascorbate peroxidase-ascorbate complex.* Nat. Struct. Biol., 2003. **10**(4): 303-307.
13. Murshudov, G.N., Vagin, A.A., and Dodson, E.J., *Refinement of macromolecular structures by the maximum-likelihood method.* Acta Crystallogr., Sect. D. Biol. Crystallogr., 1997. **53**: 240-255.
14. Emsley, P. and Cowtan, K., *COOT: model-building tools for molecular graphics.* Acta Crystallogr., Sect. D. Biol. Crystallogr., 2004. **60**: 2126-2132.
15. Campbell, J.W., Clifton, I.J., Harding, M.M., and Hao, Q., *The Laue-Data-Module (Ldm) - a Software-Development for Laue X-Ray-Diffraction Data-Processing.* J. Appl. Crystallogr., 1995. **28**: 635-640.
16. Helliwell, J.R., Habash, J., Cruickshank, D.W.J., Harding, M.M., Greenhough, T.J., Campbell, J.W., Clifton, I.J., Elder, M., Machin, P.A., Papiz, M.Z., and Zurek, S., *The Recording and Analysis of Synchrotron X-Radiation Laue Diffraction Photographs.* J. Appl. Crystallogr., 1989. **22**: 483-497.
17. Arzt, S., Campbell, J.W., Harding, M.M., Hao, Q., and Helliwell, J.R., *LSCALE - the new normalization, scaling and absorption correction program in the Daresbury Laue software suite.* J. Appl. Crystallogr., 1999. **32**: 554-562.

# Appendix A

## *Buffers and Solutions*

**Antidenaturation Buffer**

50 mM potassium phosphate buffer pH 7.0

**Destain (SDS-PAGE)**

7.5% acetic acid

5% methanol

**Elution Buffer**

50 mM sodium phosphate buffer pH 4.2

0.3 M sodium chloride

10% glycerol

**FFQ Buffer**

10 mM potassium phosphate buffer pH 7.0

**LB Media (Fisher or Sigma)**

10 g NaCl

10 g tryptone

5 g yeast extract

Adjust to pH 7.0 with 5 N NaOH

Make up to 1.0 l with deionised water

Autoclave

**Mother Liquor (rsAPX Crystallisation)**

2.25 M lithium sulphate

0.1 M Hepes pH 8.3

**Reconstitution Buffer**

0.1 M potassium phosphate buffer pH 6.5

**Sample Buffer (SDS-PAGE)**

125 mM Tris-HCl, pH 6.8

4% SDS

20% w/v glycerol

0.002% bromophenol blue

**SDS Running Buffer (SDS-PAGE)**

25 mM Tris-HCl

192 mM glycerine

0.1% w/v SDS

**SOC Media**

2 g tryptone

0.5 g yeast extract

0.05 g NaCl

0.4 g glucose

Make up to 100 ml with deionised water

Autoclave

Add 1 ml of filter sterilised 1 M $MgCl_2$

Add 1 ml of filter sterilised 1 M $MgSO_4$

**Sonication Buffer**

50 mM sodium phosphate buffer pH 8.0

0.3 M sodium chloride

**Stain (SDS-PAGE)**

30% v/v methanol

12% w/v trichloroacetic acid

0.01% w/v Coomassie Blue R

10% w/v sulphosalicyclic acid

**50x TAE Buffer (Agarose gel electrophoresis)**

242 g Tris base

37.1 g glacial acetic acid

100 ml of 0.5 M EDTA

900 ml deionised water

**Wash Buffer**

50 mM sodium phosphate buffer pH 6.0

0.3 M sodium chloride

10% glycerol

**Pyridine Base Solution**

1.2 ml pyridine

4 ml NaOH (1 M)

6.8 ml $H_2O$

# Appendix B

## *Oligonucleotides for mutagenesis*

**Table 1: Oligonucleotides used to create C*c*P mutants used in Chapter 2.**

| Primer | Sequence |
|---|---|
| Y36A Forward | 5’ AGG GAA GAT GAC GAA **GCA** GAC AAC TAT 3’ |
| Y36A Reverse | 5’ ATA GTT GTC **TGC** TTC GTC ATC TTC CCT 3’ |
| N184R | 5’ G GGC AAG ACC CAC TTG AAG **CGT** TCT GGA TAC GAA CCG |
| N184R Reverse | 5’ GG CGG TTC GTA TCC AGA **ACG** CTT CAA GTG GGT CTT GCC |
| W191F | 5’ C GAA GGG CCA **TTT** GGA GCC GCT AA 3’ |
| W191F | 3’ TT AGC GGC TCC **AAA** TGG CCC TTC G 5’ |

**Table 2: Oligonucleotides used to create C*c*P mutants used in Chapter 4.**

| Primer | Sequence |
|---|---|
| M119W Forward | 5' GCT GTG CAG GAA **TGG** CAG GGT CCC 3' |
| M119W Reverse | 5' GGG ACC CTG **CCA** TTC CTG CAC AGC 3' |
| S81W Forward | 5' GAG TTT AAC GAT CCA **TGG** AAT GCG GGC 3' |
| S81W Reverse | 5' GCC CGC ATT **CCA** TGG ATC GTT AAA CTC 3' |

**Table 3: Oligonucleotides used to create the H42A mutant of APX, Chapter 3.**

| Primer | Sequence |
|---|---|
| H42A Forward | 5’ CGT TTG GCA TGG **GCT** TCT GCT GGT AC 3’ |
| H42A Reverse | 5’GT ACC AGC AGA **AGC** CCA TGC CAA ACG 3’ |

**Table 4: Oligonucleotides used to create saturated point mutagenesis libraries at S69 and D133 in APX, N is a mixture of A, C, G and T and S is G or C.**

| Primer | Sequence |
|---|---|
| S69X Forward | 5’ CGA ACT GGC TCA **CNN** SGC TAA CAA CGG TCT TG 3’ |
| S69X Reverse | 3’ GCT TGA CCG AGT **GNN** SCG ATT GTT GCC AGA AC 5’ |
| D133X Forward | 5’ GAG GGT CGC TTG CCC **NNS** GCC ACT AAG GCT TCT G 3’ |
| D133X Reverse | 3’ CTC CCA GCG AAC GGG **NNS** CGG TGA TTC CCA AGA C 5’ |

**Table 5: Oligonucleotides used to create random mutagenesis libraries in APX, both by use of Mutazyme® DNA polymerase and Taq DNA polymerase.**

| Primer | Sequence |
|---|---|
| pQE30 Forward | 5’ CCC GAA AAG TGC CAC CTG 3’ |
| pQE30 Reverse | 3’ GGG CTT TTC CAG GTG GAC 5’ |

# Appendix C

## *Reaction Volumes and Thermocycler Programmes*

**Table 1: Standard reaction volumes for site-directed mutagenesis.**

| | *1* | *2* | *3* | *4* |
|---|---|---|---|---|
| **Water (µl)** | 29 | 28 | 27 | 26 |
| **10x buffer (µl)** | 5 | 5 | 5 | 5 |
| **$MgSO_4$ (25 mM) (µl)** | 2 | 2 | 2 | 2 |
| **DMSO (100%)** | 1 | 1 | 1 | 1 |
| **Template DNA (µl)** | 1 | 2 | 3 | 4 |
| **Forward Primer (10 $_{OD}$) (µl)** | 3 | 3 | 3 | 3 |
| **Reverse Primer (10 $_{OD}$)(µl)** | 3 | 3 | 3 | 3 |
| **dNTP mix (2.5 mM) (µl)** | 5 | 5 | 5 | 5 |
| **KOD polymerase (µl)** | 1 | 1 | 1 | 1 |

**Table 2: Standard thermocycler programme for site-directed mutagenesis.**

| *Number of cycles* | *Temperature (ºC)* | *Time (s)* |
|---|---|---|
| **1** | 96 | 180 |
| **30** | 96 | 30 |
| | $T_m$ -5 ºC | 60 |
| | 72 | 600 |
| **1** | 72 | 600 |
| **Hold** | 4 | - |

**Table 3: Reaction volumes used for saturated mutagenesis PCR.**

| | ***S69X*** | | | | ***D133X*** | | | |
|---|---|---|---|---|---|---|---|---|
| | 1 | 2 | 3 | 4 | 1 | 2 | 3 | 4 |
| **Water (µl)** | 13.5 | 12.8 | 12 | 11.3 | 13.85 | 13.6 | 13.35 | 13.1 |
| **Glycerol (µl)** | 2.5 | 2.5 | 2.5 | 2.5 | 2 | 2 | 2 | 2 |
| **10X buffer (µl)** | 2.5 | 2.5 | 2.5 | 2.5 | 2.5 | 2.5 | 2.5 | 2.5 |
| **$MgCl_2$ (µl)** | 2 | 2 | 2 | 2 | 2 | 2 | 2 | 2 |
| **Template DNA (µl)** | 2 | 2 | 2 | 2 | 2 | 2 | 2 | 2 |
| **Forward Primer (µl)** | 0.5 | 0.75 | 1 | 1.25 | 0.5 | 0.5 | 0.5 | 0.5 |
| **Reverse Primer (µl)** | 0.5 | 0.75 | 1 | 1.25 | 0.65 | 0.65 | 0.65 | 0.65 |
| **dNTP mix (µl)** | 1 | 1 | 1 | 1 | 1 | 1 | 1 | 1 |
| ***Pfu Ultra* (µl)** | 1 | 1 | 1 | 1 | 0.5 | .75 | 1 | 1.25 |

**Table 4: Thermocycler program for first round of saturated mutagenesis.**

| *S69X* | | | *D133X* | | |
|---|---|---|---|---|---|
| **Number of cycles** | **Temperature (ºC)** | **Time (s)** | **Number of cycles** | **Temperature (ºC)** | **Time (s)** |
| **1** | 96 | 180 | **1** | 96 | 180 |
| **30** | 96 | 30 | **30** | 96 | 30 |
| | 62 | 60 | | 66 | 60 |
| | 72 | 600 | | 72 | 600 |
| **1** | 72 | 600 | **1** | 72 | 600 |
| | 4 | 30 | | 4 | 30 |

**Table 5: Reaction volumes for the second round of saturated mutagenesis; creation of S69P/D133X library.**

| | *1* | *2* | *3* | *4* |
|---|---|---|---|---|
| **Water (µl)** | 14.65 | 13.65 | 12.65 | 10.15 |
| **Glycerol (µl)** | 2.5 | 2.5 | 2.5 | 2.5 |
| **10x buffer (µl)** | 2.5 | 2.5 | 2.5 | 2.5 |
| **$MgCl_2$ (µl)** | 1 | 2 | 3 | 4 |
| **Template DNA (S69P rsAPX) (µl)** | 1.7 | 1.7 | 1.7 | 1.7 |
| **Forward Primer (D133XF) (µl)** | 0.5 | 0.5 | 0.5 | 0.5 |
| **Reverse Primer (D133XR) (µl)** | 0.65 | 0.65 | 0.65 | 0.65 |
| **dNTP mix (µl)** | 0.5 | 0.5 | 0.5 | 0.5 |
| ***Pfu Ultra* (µl)** | 1 | 1 | 1 | 1 |

**Table 6: Reaction volumes for the second round of saturated mutagenesis; creation of S69X/D133R library.**

| | *1* | *2* | *3* | *4* |
|---|---|---|---|---|
| **Water (µl)** | 14.65 | 13.65 | 12.65 | 10.15 |
| **Glycerol (µl)** | 2.5 | 2.5 | 2.5 | 2.5 |
| **10x buffer (µl)** | 2.5 | 2.5 | 2.5 | 2.5 |
| **$MgCl_2$ (µl)** | 2 | 2 | 2 | 2 |
| **Template DNA (D133R rsAPX) (µl)** | 0.5 | 0.5 | 0.5 | 0.5 |
| **Forward Primer (S69XF) (µl)** | 0.9 | 0.9 | 0.9 | 0.9 |
| **Reverse Primer (S69XR) (µl)** | 0.65 | 0.65 | 0.65 | 0.65 |
| **dNTP mix (µl)** | 0.5 | 0.5 | 0.5 | 0.5 |
| ***Pfu Ultra* (µl)** | 1 | 1 | 1 | 1 |

**Table 7: Thermocycler program for second round of saturated mutagenesis.**

| ***S69P/D133X*** | | | ***S69X/D133R*** | | |
|---|---|---|---|---|---|
| **Number of cycles** | **Temperature (ºC)** | **Time (s)** | **Number of cycles** | **Temperature (ºC)** | **Time (s)** |
| **1** | 96 | 180 | **1** | 96 | 180 |
| **30** | 96 | 30 | **30** | 96 | 30 |
| | 62 | 60 | | 66 | 60 |
| | 72 | 600 | | 72 | 600 |
| **1** | 72 | 600 | **1** | 72 | 600 |
| | 4 | 30 | | 4 | 30 |

**Table 8: Reaction volumes for random mutagenesis PCR using Mutazyme® DNA polymerase.**

| | *1* | *2* | *3* | *4* |
|---|---|---|---|---|
| **Water (µl)** | 35 | 33.5 | 32 | 31 |
| **10x buffer (µl)** | 5 | 5 | 5 | 5 |
| **$MgCl_2$ (µl)** | 2.5 | 2.5 | 2.5 | 2.5 |
| **Template DNA (rsAPX) (µl)** | 1 | 2.5 | 4 | 5 |
| **Forward Primer (pQE30F) (µl)** | 1 | 1 | 1 | 1 |
| **Reverse Primer (pQE30R) (µl)** | 1 | 1 | 1 | 1 |
| **dNTP mix (µl)** | 4 | 4 | 4 | 4 |
| **Mutazyme® (µl)** | 0.5 | 0.5 | 0.5 | 0.5 |

**Table 9: Thermocycler program for random mutagenesis using Mutazyme® DNA polymerase.**

| Number of cycles | Temperature (ºC) | Time (s) |
|---|---|---|
| **1** | 96 | 180 |
| **40** | 96 | 45 |
| | 48 ºC, 51.2 ºC, 61.5 ºC or 68.5 ºC | 30 |
| | 72 | 120 |
| **1** | 72 | 600 |
| | 18 | 30 |

**Table 10: Reaction volumes for random mutagenesis PCR using Taq polymerase and $MnCl_2$ (Numbers in parenthesis indicate final concentration of $MnCl_2$ (mM) in reaction).**

| | *1* | *2* | *3* | *4* | *5* | *6* |
|---|---|---|---|---|---|---|
| **Water (µl)** | 31 | 29 | 27 | 25 | 23 | 21 |
| **$MnCl_2$ (µl)** | 0 (0) | 2 (0.1) | 4 (0.2) | 6 (0.3) | 8 (0.4) | 10 (0.5) |
| **10x buffer (µl)** | 5 | 5 | 5 | 5 | 5 | 5 |
| **$MgCl_2$ (µl)** | 2.5 | 2.5 | 2.5 | 2.5 | 2.5 | 2.5 |
| **Template DNA (rsAPX) (µl)** | 5 | 5 | 5 | 5 | 5 | 5 |
| **Forward Primer (pQE30F) (µl)** | 1 | 1 | 1 | 1 | 1 | 1 |
| **Reverse Primer (pQE30R) (µl)** | 1 | 1 | 1 | 1 | 1 | 1 |
| **dNTP mix (µl)** | 4 | 4 | 4 | 4 | 4 | 4 |
| **Taq Polymerase (µl)** | 0.5 | 0.5 | 0.5 | 0.5 | 0.5 | 0.5 |

**Table 11: Reaction volumes for restriction of PCR products.**

| | ***Ep 0.1*** | ***Ep 0.3*** | ***Mut*** |
|---|---|---|---|
| **DNA (µl)** | 40 | 25 | 40 |
| **Buffer NEB2 (µl)** | 6 | 4 | 6 |
| **BSA 10X (µl)** | 6 | 4 | 6 |
| **Water (µl)** | 3 | 2 | 3 |
| ***Bam*HI (µl)** | 2 | 2 | 2 |
| ***Kpn*I (µl)** | 3 | 3 | 3 |
| **Total volume (µl)** | 60 | 40 | 60 |
| **Expected fragments (kb)** | 892, 85, 81 | 892, 85, 81 | 892, 85, 81 |

**Table 12: Reaction volumes for restriction of pQE30-rsAPX.**

| | ***pQE30*** |
|---|---|
| **DNA (µl)** | 198 |
| **Buffer NEB2 (µl)** | 26 |
| **BSA 10X (µl)** | 26 |
| ***Bam*HI (µl)** | 4 |
| ***Kpn*I (µl)** | 6 |
| **Total volume (µl)** | 260 |
| **Expected fragments (kb)** | 3444, 900 |

**Table 13: Reaction volumes for ligation of PCR products into empty pQE30 Vector.**

| | *Ep 0.3* | *Ep 0.1* | *Mut* | *Self ligation* |
|---|---|---|---|---|
| **Vector (µl)** | 5 | 5 | 5 | 5 |
| **PCR product (µl)** | 2.89 | 1.02 | 1.14 | 2 |
| **Buffer (µl)** | 2 | 2 | 2 | 2 |
| **T4 DNA ligase (µl)** | 1 | 1 | 1 | 1 |
| **Water (µl)** | 9.11 | 10.98 | 10.86 | 12 |

# Publications

THE JOURNAL OF BIOLOGICAL CHEMISTRY VOL. 283, NO. 10, pp. 6193–6200, March 7, 2008


# The Tuberculosis Prodrug Isoniazid Bound to Activating Peroxidases*

Received for publication, September 4, 2007, and in revised form, October 29, 2007 Published, JBC Papers in Press, December 5, 2007, DOI 10.1074/jbc.M707412200

**Clive Metcalfe[‡], Isabel K. Macdonald[‡1], Emma J. Murphy[‡], Katherine A. Brown[§], Emma Lloyd Raven[‡], and Peter C. E. Moody[¶2]**

*From the Departments of [‡]Chemistry and [¶]Biochemistry, University of Leicester, Lancaster Road, Leicester LE1 9HN and [§]Department of Life Sciences, Division of Cell and Molecular Biology, Centre for Molecular Microbiology and Infection, Imperial College, Exhibition Road, London SW7 2AZ, United Kingdom*

**Isoniazid (INH, isonicotinic acid hydrazine) is one of only two therapeutic agents effective in treating tuberculosis. This prodrug is activated by the heme enzyme catalase peroxidase (KatG) endogenous to *Mycobacterium tuberculosis* but the mechanism of activation is poorly understood, in part because the binding interaction has not been properly established. The class I peroxidases ascorbate peroxidase (APX) and cytochrome *c* peroxidase (C*c*P) have active site structures very similar to KatG and are also capable of activating isoniazid. We report here the first crystal structures of complexes of isoniazid bound to APX and C*c*P. These are the first structures of isoniazid bound to any activating enzymes. The structures show that isoniazid binds close to the δ-heme edge in both APX and C*c*P, although the precise binding orientation varies slightly in the two cases. A second binding site for INH is found in APX at the γ-heme edge close to the established ascorbate binding site, indicating that the γ-heme edge can also support the binding of aromatic substrates. We also show that in an active site mutant of soybean APX (W41A) INH can bind directly to the heme iron to become an inhibitor and in a different mode when the distal histidine is replaced by alanine (H42A). These structures provide the first unambiguous evidence for the location of the isoniazid binding site in the class I peroxidases and provide rationalization of isoniazid resistance in naturally occurring KatG mutant strains of *M. tuberculosis*.**

Isoniazid (isonicotinic acid hydrazide, INH,[3]) (Scheme 1) is a prodrug that has been extensively used as a frontline chemotherapeutic to treat tuberculosis for many years (1). More than 8 million people per year are diagnosed with tuberculosis in both developed and developing nations, resulting in more than 2 million deaths per year (2). However, despite the worldwide success of INH in treating tuberculosis since the 1950s, very little is understood about the mode of action or the mechanism of activation of this prodrug. In recent times the emergence of INH- and multidrug-resistant strains of tuberculosis and the scale of the tuberculosis epidemic has highlighted the need for this fundamental lack of knowledge to be addressed with a view to discovering new antimicrobial targets and treatment regimens.

*In vitro* and *in vivo* studies have established that a catalase peroxidase, KatG, which is endogenous to *M. tuberculosis* (the principal causative agent of tuberculosis), is essential for prodrug activation (3). KatGs are bifunctional heme enzymes that exhibit both catalase activity and broad spectrum peroxidatic activity comparable with monofunctional peroxidases (4, 5). The peroxidatic activity involves the formation of an oxidized ferryl intermediate (Equation 1, *Compound I*) that is subsequently reduced by substrate. This reduction usually occurs in two successive single-electron transfer steps as follows (Equations 2 and 3) (where $P$ = peroxidase, $HS$ = substrate, $S^{\cdot}$ = 1-electron oxidized form of substrate).

$$P + H_2O_2 \xrightarrow{k_1} \text{Compound I} + H_2O \qquad \text{(Eq. 1)}$$

$$\text{Compound I} + HS \xrightarrow{k_2} \text{Compound II} + S^{\cdot} \qquad \text{(Eq. 2)}$$

$$\text{Compound II} + HS \xrightarrow{k_3} P + S^{\cdot} + H_2O \qquad \text{(Eq. 3)}$$

KatG is a dimeric heme-containing enzyme of ~160-kDa molecular mass; its structure (Fig. 1*A*) (6) and function place it in the class I superfamily of peroxidases along with cytochrome *c* peroxidase (C*c*P) (Fig. 1*B*) and ascorbate peroxidase (APX) (Fig. 1*C*) (7). The determination of the crystal structure of *M. tuberculosis* KatG (6) provided a major breakthrough in understanding the molecular mechanism of INH activation and highlighted the remarkable structural similarity both in the overall structures and at the active sites of KatG and the monofunctional class I peroxidases such as C*c*P (8) and APX (9), both of

* This work was supported by Biotechnology and Biological Sciences Research Council Grants BBC/0011841 (to E. L. R. and P. C. E. M.), 91/B19083 (to E. L. R.), and BBS/S/A/2004/12421 (to E. L. R.). The costs of publication of this article were defrayed in part by the payment of page charges. This article must therefore be hereby marked "*advertisement*" in accordance with 18 U.S.C. Section 1734 solely to indicate this fact.

*The atomic coordinates and structure factors (codes 2V23, 2V2E, 2VCF, 2VCN, and 2VCS) have been deposited in the Protein Data Bank, Research Collaboratory for Structural Bioinformatics, Rutgers University, New Brunswick, NJ (http://www.rcsb.org/).*

[1] Present address: The Edward Jenner Inst. for Vaccine Research, Compton, Newbury, Berkshire RG20 7NN, UK.

[2] To whom correspondence should be addressed. Tel.: 44-116-229-7097; Fax: 44-116-229-7084; E-mail: peter.moody@le.ac.uk.

[3] The abbreviations used are: INH, isonicotinic acid hydrazine; C*c*P, cytochrome *c* peroxidase; APX, ascorbate peroxidase; sAPX, soybean APX; SHA, salicylhydroxamic acid.

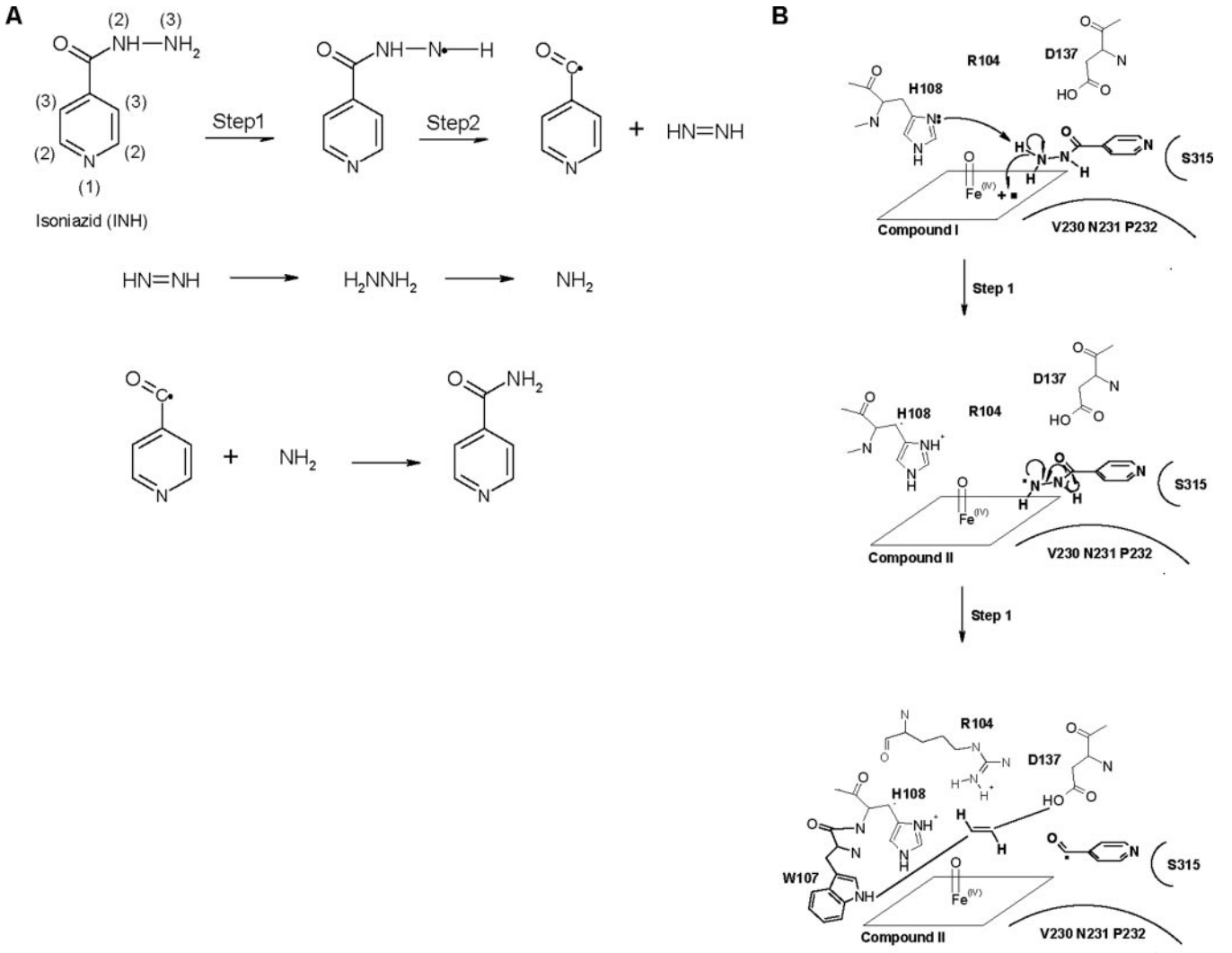


SCHEME 1. *A*, the proposed catalytic mechanism of INH oxidation by the class 1 peroxidases. The first stage (*steps 1* and *2*) forms the isonicotinoyl radical, which is then thought to react with the liberated hydrazine to form the primary product isonicotinamide (38). The INH numbering scheme is also shown. *B*, the active site residues of KatG that are proposed to be involved in the catalytic mechanism of INH oxidation (1). Possible stabilizing interactions are shown as *dotted lines*, and the heme is represented as a *rhombus*. The equivalent residues in CcP and sAPX are as follows: Arg-104 ≡ Arg-48, Arg-38; Trp-107 ≡ Trp-51, Trp-41; His-108 ≡ His-52, His-42; Asp-137 ≡ Ser-81, Ala-70. Asp-137 of KatG is thought to play a major role in stabilizing the catalytic intermediate of INH oxidation.

which can also activate INH (1) (Fig. 1). Mechanistic studies show INH is activated by both KatG and the class III peroxidase horseradish peroxidase in the typical two-step peroxidatic process, again indicating a universal mechanism of INH oxidation in peroxidases (1) (Scheme 1). In most peroxidases, aromatic substrates similar in structure to INH, such as salicylhydroxamic acid (SHA) (10) and benzhydroxamic acid (11), bind and react at the δ-heme edge. However, there is no direct structural information for INH binding from any of the INH-activating enzymes. The best information available on the INH binding site in peroxidases comes from an NMR model of INH bound to horseradish peroxidase. These NMR data were used as a basis for energetic grid calculations from which a set of models describing the INH binding site in KatG and other class I peroxidases were constructed. In all of these models the INH binding site was placed at the δ-heme edge in what is commonly referred to as the hydrophobic pocket (1).

To fully elucidate the mechanism of INH activation in KatG and other INH-activating peroxidases, the binding site of INH has to be accurately described. Only then can the fine molecular details of catalysis be unraveled. Here we report the first crystal structures of INH bound to *Saccharomyces cerevisiae* CcP and soybean ascorbate peroxidase (sAPX), both of which are known activators of INH (1). We establish that the INH occupies the δ-meso edge of the heme, and we also show that in an active site mutant of sAPX (W41A) INH can bind directly to the heme iron to become an inhibitor. Furthermore, we show in a complex of INH and the H42A mutant of sAPX that the indole nitrogen of Trp-41 is important for ligand orientation. The data are discussed in the context of our current understanding of INH binding and activation and provide an explanation for the molecular mechanism of mutation-acquired resistance.

## EXPERIMENTAL PROCEDURES

*Enzyme Expression and Purification*—The Y39A/N184R mutant of recombinant CcP from Baker's yeast (optimized for crystallization) was prepared and isolated with modifications to

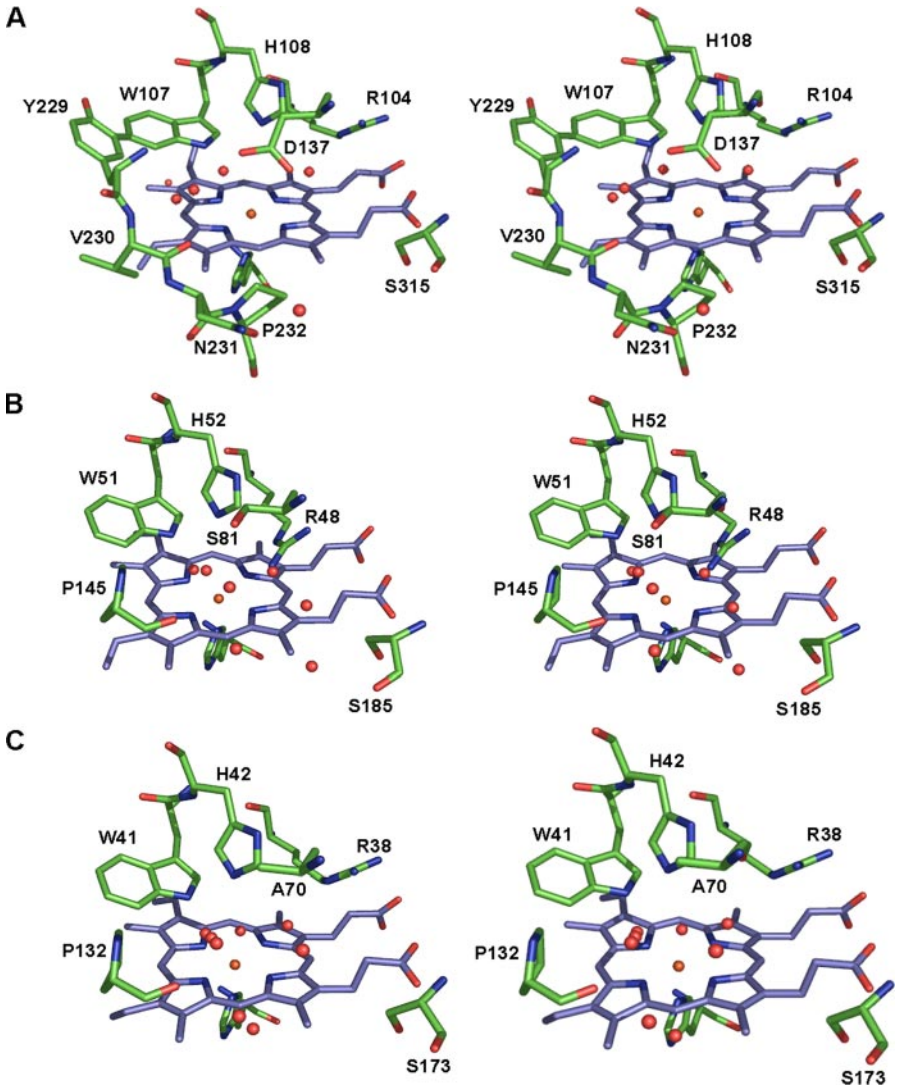


FIGURE 1. **Stereo diagrams of the key active site residues, δ-heme edge hydrophobic binding pocket, and bound waters of the unliganded class I peroxidases discussed in this study.** KatG (6) (*A*), C*c*P (*B*), and sAPX (9) (*C*). The protein residues are shown in *green*, the heme group in *blue*, and waters are represented as *red spheres*.

published procedures (12). Recombinant cytosolic sAPX and the W41A and H42A mutants were prepared and isolated according to published procedures (13, 14). All protein preparations were checked for homogeneity by SDS-PAGE.

*Protein Crystallography*—Crystals of C*c*P were prepared by microdialysis with 100 μl of a 10–30 mg/ml solution of C*c*P in 500 mM potassium phosphate, pH 6.0, against 10 ml of 50 mM potassium phosphate, pH 6.0, containing 30% 2-methyl-2,4-pentanediol by volume. Crystals were grown at 4 °C. Once formed, the crystals of C*c*P were soaked in mother liquor saturated with INH for 5 min prior to rapid cooling to 100 K.

Crystals of sAPX, sAPX (W41A), and sAPX (H42A) were prepared as described previously (9). Once formed, crystals were soaked in mother liquor containing INH (100 mM) overnight prior to freezing in liquid nitrogen for storage and transport.

*Data Collection and Refinement*—Diffraction data were collected for the C*c*P·INH complex in-house using a Rigaku RU2HB x-ray generator with copper anode and Xenocs multilayer optics and an R-Axis IV detector. Diffraction data were collected for sAPX·INH and sAPX (W41A) INH complexes

**TABLE 1**
**Data collection and refinement statistics**
Values in parentheses are for the outer shell.

| Data collection | C*c*P[a] | C*c*P·INH[a] | sAPX·INH | sAPX·(W41A)·INH | sAPX·(H42A)·INH[a] |
|---|---|---|---|---|---|
| Space group | $P2_12_12_1$ | $P2_12_12_1$ | $P4_22_12$ | $P4_22_12$ | $P4_22_12$ |
| **Unit cell (Å)** | | | | | |
| a | 51.15 | 51.15 | 82.24 | 82.13 | 81.74 |
| b | 75.38 | 75.13 | 82.24 | 82.13 | 81.74 |
| c | 107.23 | 106.86 | 74.97 | 75.16 | 74.94 |
| Resolution (Å) | 30.2-1.68 (1.77-1.68) | 30.28-1.68 (1.77-1.68) | 27.11-1.80 (1.90-1.80) | 37.58-1.20 (1.26-1.20) | 27.62-1.68 (1.77-1.68) |
| Total observations | 101429 (1628) | 129214 (1652) | 170464 (24801) | 732420 (82637) | 103919 (1437) |
| Unique reflections | 37067 (1317) | 38990 (1367) | 24461 (3497) | 78730 (11128) | 24816 (1102) |
| $I/\sigma I$ | 23.2 (3.3) | 27.4 (5.8) | 17.4 (4.7) | 17.2 (2.5) | 31.2 (2.5) |
| $R_{merge}$ | 0.036 (0.238) | 0.031 (0.133) | 0.091 (0.378) | 0.063 (0.687) | 0.032 (0.209) |
| Completeness (%) | 77.7 (19.7) | 81.9 (20.3) | 100 (100) | 97.9 (96.0) | 84.0 (26.8) |
| **Refinement statistics** | | | | | |
| $R_{work}$ | 0.159 | 0.156 | 0.154 | 0.192 | 0.165 |
| $R_{free}$ | 0.192 | 0.180 | 0.188 | 0.209 | 0.209 |
| **Root mean square deviations from ideal** | | | | | |
| Bonds (Å) | 0.012 | 0.010 | 0.012 | 0.007 | 0.010 |
| Angles (°) | 1.208 | 1.157 | 1.234 | 1.151 | 1.174 |
| Protein Data Bank code | 2V23 | 2V2E | 2VCF | 2VCN | 2VCS |

[a] These figures are for data measured into the corners of the square detector and used for refinement. In the case of C*c*P, C*c*P·INH, and sAPX (H42A) INH, the completeness to 2.0 Å is, respectively, 92.9, 99.3, and 99.6%.

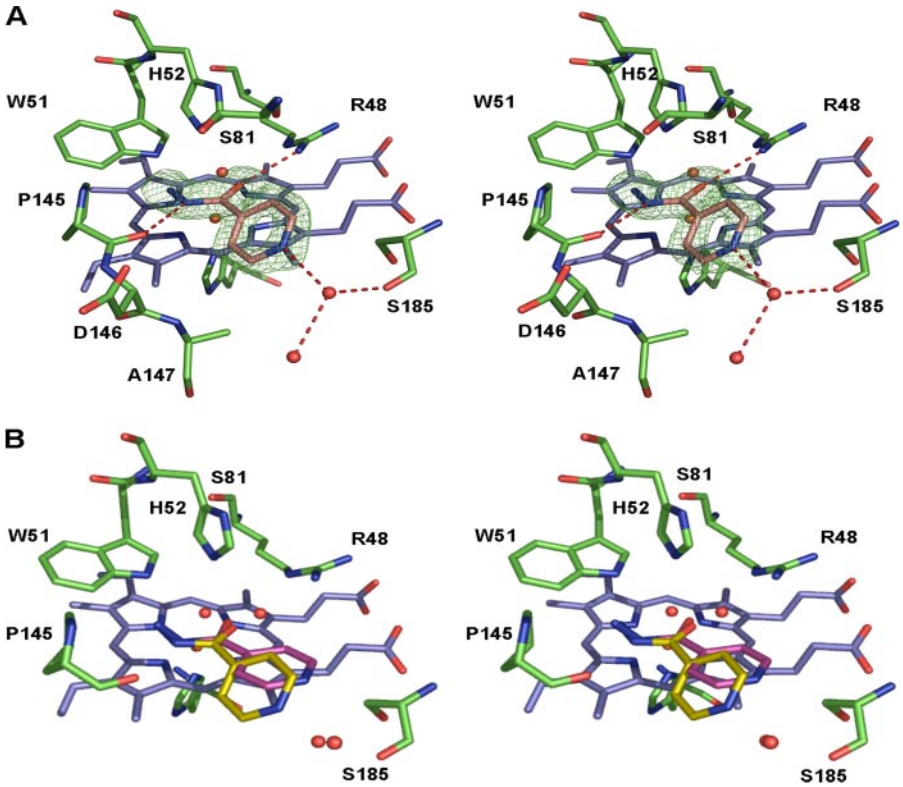


FIGURE 2. **Stereo diagrams showing INH bound in place of waters in the δ-heme edge hydrophobic binding pocket of CcP.** *A*, observed $F_o - F_c$ difference density is shown in *green* (contoured at 3 $\sigma$) with the refined INH molecule in *brown*. *B*, the observed position of INH (*yellow*) compared with the predicted mode (*purple*) from Pierattelli *et al.* (1). The protein is shown in *green*, the heme group in *blue*, INH in *pink*, and waters are represented as *red spheres*.

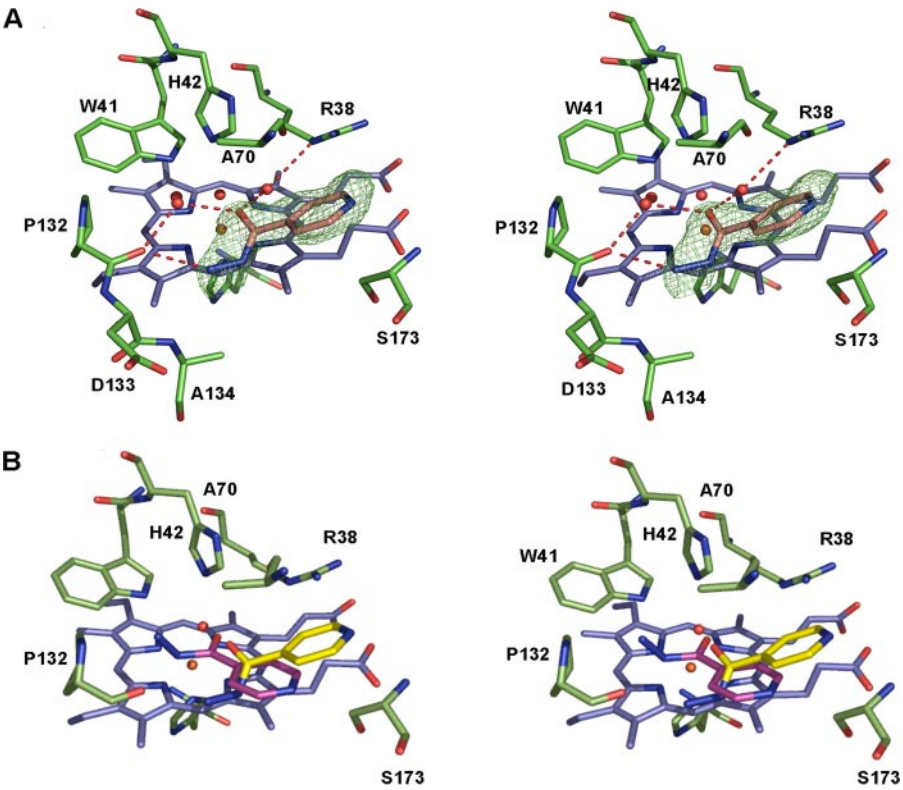


FIGURE 3. **Stereo diagrams showing INH bound in place of waters in the δ-heme edge hydrophobic binding pocket of sAPX.** *A*, observed $F_o - F_c$ difference density in *green* (contoured at 3 $\sigma$) with the refined INH molecule in *brown*. *B*, the observed position of INH (*yellow*) compared with the predicted mode (*purple*) from Pierattelli *et al.* (1). The protein is shown in *green*, the heme group in *blue*, INH in *pink*, and waters are represented as *red spheres*.

on station ID14–3 at the European Synchrotron Radiation Facility (ESRF) (Grenoble, France) using an ADSC Q4R detector. Data from sAPX·(H42A)·INH were also collected at ESRF using ID14–1 and an ADSC Q4R detector. All data were collected at 100 K. Data were indexed, integrated, and scaled using MOSFLM (15) and SCALA (16). 5% of the data were flagged for the calculation of $R_{free}$ and excluded from subsequent refinement. Data collection statistics are shown in Table 1. The C*c*P·INH structure was refined from the 1.70 Å wild-type C*c*P structure (17) (Protein Data Bank entry 2CYP). The sAPX·INH and sAPX (H42A)·INH structures were refined from models derived from the 1.45 Å sAPX·ascorbate complex (9) (Protein Data Bank entry 1OAF), and the sAPX (W41A)·INH structure was derived from the 1.35 Å sAPX·W41A structure (14) (Protein Data Bank entry 2GGN). All refinement used REFMAC5 (18) from the CCP4 suite (19). Calculation of difference Fourier maps showed clear and unambiguous electron density for bound INH molecules in all the structures. INH was incorporated into the last cycles of refinement. COOT (20) was used throughout for manual adjustment, ligand fitting, and interpretation of the water structure. The refinement statistics are shown in Table 1.

*Steady-state Kinetic Experiments*—Steady-state oxidations of guaiacol (2-methoxy phenol) in 50 mM sodium phosphate, pH 7.0, 25 °C, were carried out according to published protocols (21) both in the absence of INH and in the presence of INH (50 mM). Steady-state data were fitted either to the Michaelis-Menten or Hill equations as described previously (21).

## RESULTS AND DISCUSSION

*Identification of the Hydrophobic Binding Pockets in CcP and sAPX*—Numerous studies have shown that aromatic substrate oxidation in the class I peroxidases occurs at the δ-heme edge (6, 11, 23, 24). This site

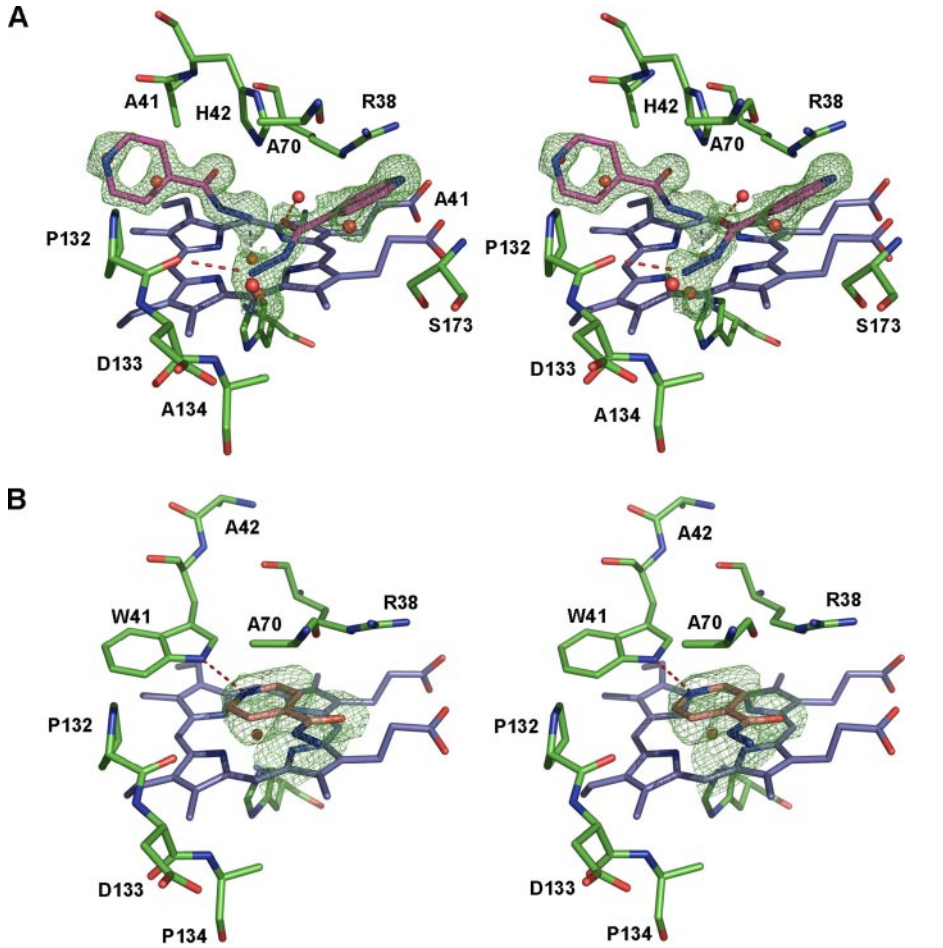


FIGURE 4. **Stereo diagrams showing INH bound in the active site mutants of sAPX W41A and H42A.** *A*, in sAPX·(W41A), two molecules of INH (*brown*) are bound in the distal cavity, one in the same position as sAPX and a second coordinated directly to the heme iron. The figure shows observed $F_o - F_c$ difference density (in *green*, contoured at 3 $\sigma$). *B*, in sAPX (H42A) the orientation of INH (*brown*) is rotated relative to the wild type and is held in position by a hydrogen bond to Trp-41. Observed $F_o - F_c$ difference density is shown in *green*. In both cases the occupancy of the INH is partial and shared with water molecules that are represented as *red spheres*.

is compared in KatG, C*c*P, and sAPX in Fig. 1. In the unliganded C*c*P structure the hydrophobic pocket itself is defined, as predicted from the crystal structure (17), by residues Pro-145, Ser-81, Ser-185, Arg-48, Trp-51, and His-52, with the "bottom" of the pocket being defined by pyrrole ring IV of the heme while one "side" is left open to solvent (Fig. 1*B*). Examination of electron density within this pocket in C*c*P reveals water molecules hydrogen-bonded within the pocket and leading out into bulk solvent. This open side forms a channel to allow the substrate to access the binding pocket.

The unliganded sAPX structure (Fig. 1*C*) shows an almost identical active site architecture with the hydrophobic pocket defined by Trp-41, His-42, Pro-132, Ser-173, and Ala-70, and again the bottom of the pocket is defined by pyrrole ring IV of the heme. Like C*c*P (17) and KatG (6), ordered water molecules occupy this pocket in sAPX with a substrate access channel leading to bulk solvent. Thus, the pockets in all three of these class 1 peroxidases are similar and available to bind hydrophobic aromatic substrates.

*The Structures of INH Bound to CcP and sAPX*—INH binds in place of four of the water molecules within the hydrophobic pocket of C*c*P (Fig. 2*A*). The structure allows hydrogen bonds between N2 of the substrate and the main chain oxygen of Pro-145, the carbonyl oxygen on the substrate and the side chain of Arg-48, and the pyridinyl nitrogen on the substrate and a water molecule leading out to bulk solvent. The guanidinium group of Arg-48 swings out to accommodate the substrate (C$\zeta$ moves by 2 Å) and displaces a further water molecule. The overall position of the INH in the crystal structure reported here is similar to the NMR-derived model (Fig. 2*B*) (1) except for the interactions of N2 and N3. Notably, the crystal structure is inconsistent with a predicted (1) hydrogen bond between the globally conserved distal tryptophan (Trp-51 in the case of C*c*P) and N3 of INH.

The structure of sAPX in complex with INH also shows INH bound in the hydrophobic pocket at the $\delta$-meso heme edge (Fig. 3*A*). However, in this case the INH is rotated through ~90° compared with the orientation in C*c*P and the predicted sAPX·INH model (Fig. 3*B*) (1). The pyridine ring of INH is positioned directly over Ser-173, and the complex is locked into position via three hydrogen bonds, two of which are to the same residues that are used to bind INH in C*c*P. The main chain carbonyl of Pro-132 hydrogen bonds to N3 of the INH, the carbonyl oxygen of INH hydrogen bonds via a water molecule to the N$\epsilon$ group of Arg-48, and the N2 of INH is hydrogen-bonded to a water molecule.

Previous mechanistic studies have proposed a KatG-catalyzed activation mechanism that involves splitting of the C–N bond of the hydrazide moiety of INH, yielding a diazene that is stabilized by Asp-137 (Scheme 1) (1, 6). In *M. tuberculosis* KatG the acid group of Asp-137 is predicted to be located directly above the carbonyl of INH and is ideally orientated to provide a stabilizing acid-base interaction with the reacting INH. However, in C*c*P and sAPX, Asp-137 is replaced with Ser-81 and Ala-70, respectively. Ser-81 could still offer some rudimentary stabilization for the activated INH, whereas this is unlikely with Ala-70. This hypothesis is supported by the relative reaction rates of INH oxidation, KatG $\gg$C*cp* $>$sAPX (1).

*The Structures of INH Bound to sAPX Mutants W41A and H42A and the Role of Point Mutations in Drug Resistance*—A major problem in treating tuberculosis is resistance to the clinically effective drugs rifampicin and INH. Various point muta-

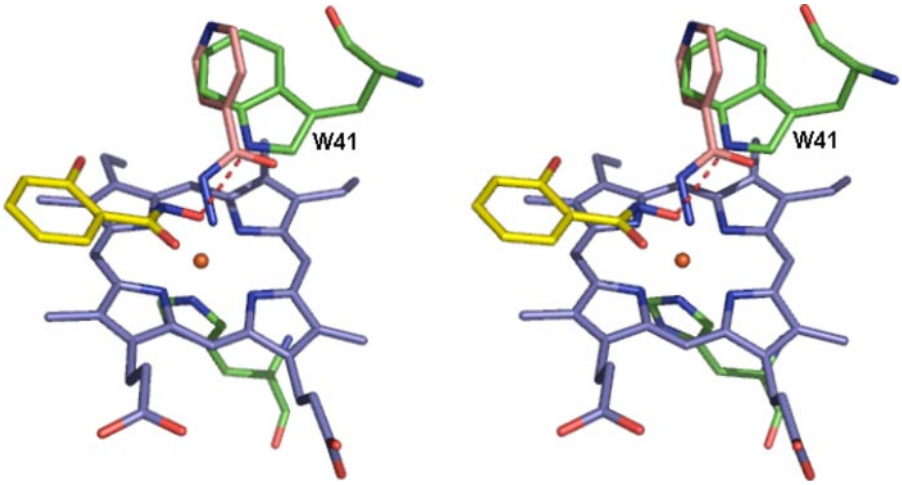


FIGURE 5. **Stereo diagram showing the superposition of INH binding as an inhibitor of sAPX·W41A (*pink*) with the previously determined SHA binding orientation (*yellow*) in sAPX (10).** The hydrogen bond between the coordinating oxygen of SHA and Trp-41 is shown as a *broken red bond*. An analogous hydrogen bond cannot form between the coordinating $NH_2$ of INH and Trp-41, so that coordination is only possible when Trp-41 is absent in sAPX (W41A).

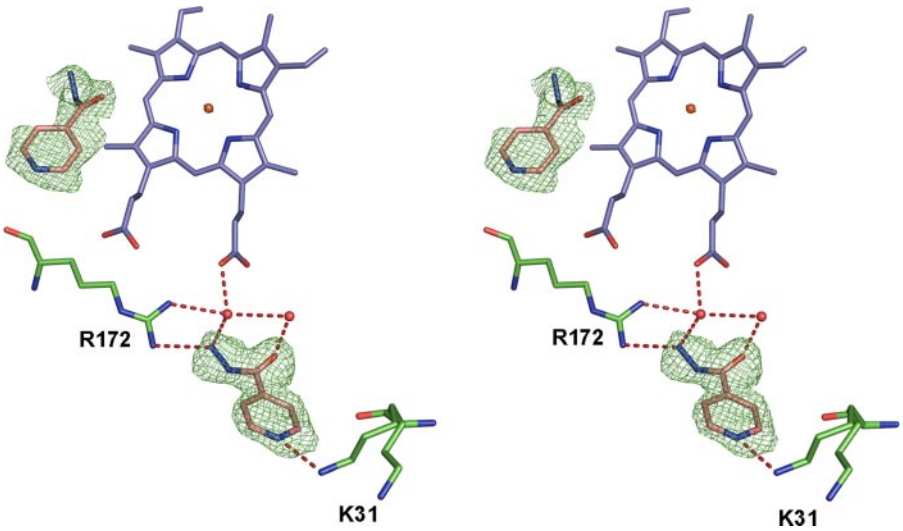


FIGURE 6. **Stereo diagram showing INH bound in the ascorbate binding pocket of sAPX.** Hydrogen bonding interactions are observed between INH and Arg-172 and Lys-31 and via a water to the propionate group of the heme. There are INH molecules bound in identical positions in the sAPX (W41A) and sAPX (H42A) structures. The first INH molecule bound in the distal cavity is also shown to aid orientation. The protein is shown in *green*, the heme group in *blue*, and INH in *pink*. Waters are represented as *red spheres*. The observed $F_o - F_c$ difference density (contoured at 3 $\sigma$) for the INH molecules is shown in *green*. Figs. 2–6 were prepared with PyMOL (22).

tions of KatG have been identified in INH-resistant strains (25), with one of the mutation hotspots being Ser-315 (mutated to asparagine, isoleucine, arginine, and glycine, but most commonly threonine) (26–28). Ser-315 is conserved in both C*c*P and sAPX (Fig. 1) as Ser-185 and Ser-173, respectively. In the C*c*P·INH structure the C$\alpha$ of Ser-185 is ~4.0 Å from the aromatic ring of INH, and in sAPX the C$\beta$ of Ser173 is ~3.8 Å away and located directly below it. All of these mutations would introduce considerably more steric bulk than serine, thereby placing the side chain of the mutated residue at position 315 closer than allowed Van der Waal's contact distances, blocking the binding of the INH molecule. These observations are consistent with predictions that these mutations produce a steric interference to INH binding (6, 29).

Active site residues His-108 and Ala-110 are also frequently mutated in KatG sequenced from isolates demonstrating resistance to INH (30–32). Mutation of active site residues of peroxidases has been shown (14) to introduce conformational mobility into the distal cavity, possibly promoting alternative inhibitive INH binding orientations. To probe this, we have determined the structures of INH bound to two active site mutations of sAPX (W41A and H42A). Removal of the distal tryptophan in the W41A mutant of sAPX opens up the distal cavity and imparts a degree of conformational mobility (14). Electron density from crystals of INH-soaked sAPX (W41A) shows a molecule of INH occupying the hydrophobic pocket in an identical position to that found in the wild-type sAPX·INH complex. A second INH molecule is also seen coordinated directly to the heme iron through the $NH_2$ of the acyl hydrazide, with the aromatic ring occupying the pocket created by removal of the indole of Trp-41 (Fig. 4*A*). This mode of binding has been seen previously (10) in APX for aromatic acids such as SHA, which is an inhibitor of APX peroxidase activity. However, coordination of INH to the iron is only possible when an additional pocket is created in the W41A mutant, whereas coordination of SHA is possible with Trp-41 *in situ* (10). This is because SHA forms a hydrogen bond between its iron coordinating $O^-$ and the NH of Trp-41 (Fig. 5). However, INH has an $NH_2$ group coordinated to the iron that is unable to hydrogen bond to the NH of Trp-41; furthermore, its bulk would also result in a steric clash. The removal of Trp-41 allows the INH to move around through 90° to coordinate to the iron without this steric conflict (Fig. 5). Kinetic studies show that INH becomes an inhibitor of sAPX (W41A) peroxidase activity, determined by competition with guaiacol ($k_{cat}$ for guaiacol oxidation is 98.3 ± 1.2 $s^{-1}$ in the absence of INH compared with 5.0 ± 0.04 $s^{-1}$ in the presence of 50 mM INH). These observations are consistent with the structure of sAPX (W41A)·INH that shows INH bound directly to the heme iron; thus, in solution the reaction of the enzyme with $H_2O_2$ is blocked by preventing the formation of the compound I intermediate (by a mechanism similar to that proposed for SHA) (10).

The structure of INH bound to the H42A mutant of sAPX reveals a third binding orientation of INH within the distal cavity (Fig. 4*B*). In this structure the INH again occupies the δ-heme edge but is rotated 90° anticlockwise compared with the orientation in sAPX. The removal of His-42 creates enough space for the aromatic ring of INH to sit directly above the iron and hydrogen bond through N1 to the NH of Trp-41. This provides further evidence that Trp-41 influences coordination to the heme iron. Although the cavity in sAPX·H42A can contain the INH molecule, the steric clash with Trp-41 (see Fig. 5) prevents coordination. Kinetic studies show no INH turnover by sAPX (H42A) (data not shown); however, it has been previously shown that peroxidase activity in this mutant (21) is severely reduced. A reduction in INH activation is consistent with the observation of INH resistance in *M. tuberculosis* strains with mutations at the distal His-108 residue of KatG (30, 31).

*Occupation of the Ascorbate Binding Site of sAPX by INH*—The electron density maps of INH-soaked sAPX (Fig. 6) and mutants (data not shown) also show density consistent with a second INH molecule bound within the ascorbate binding pocket at the γ-heme edge, which has previously been identified as the primary site of catalysis within the enzyme (9) (Fig. 6). The INH molecule binds in place of six well ordered water molecules that occupy the pocket in the absence of ascorbate. The $NH_2$ group of INH forms two hydrogen bonds, one to the side chain of Arg-172 and one via a water molecule to one of the heme propionate groups. The flexible Lys-31 also partially swings in from solvent to form a hydrogen bond to N1 of INH. Movement of Lys-31 on binding of ascorbate has also been observed (9). The role of the heme propionates has traditionally been believed to be in stabilizing the heme prosthetic group within the protein structure. However, there are now several examples where the heme propionates are involved in substrate or cofactor binding, notably in manganese peroxidase (33), ascorbate peroxidase (9), and in nitric-oxide synthase (34–36); this has led to the suggestion (37) that there might be a broader role for the proprionates than merely keeping the heme in place. The data above add to this by indicating, for the first time, that the γ-heme edge might also be capable of binding aromatic substrates.

In summary, we have provided unambiguous structural evidence for the location of INH binding in the class I peroxidases *Cc*P and sAPX. These data expand on previous predictions and provide a molecular understanding of prodrug binding and activation. Furthermore, by comparing mutations engineered into our peroxidase models with naturally occurring INH-resistant variants of *M. tuberculosis*, we have identified three separate means of drug resistance: steric hindrance of the δ-heme edge INH binding site, direct binding to the heme iron (and consequent inhibition of compound I formation), and the loss of peroxidatic activity due to the mutation of essential catalytic residues. Finally, we have expanded the framework of understanding for aromatic substrate binding and activation in the heme peroxidases. We have shown that single point mutations can dramatically alter substrate binding and oxidation, indicating that the sites may be more promiscuous than previously thought. These observations provide a fundamental platform upon which our understanding of the enzyme-catalyzed activation of this prodrug can now be developed for more effective tuberculosis therapies in the future.

*Acknowledgments—We thank staff at the European Synchrotron Radiation Facility, Grenoble for providing synchrotron time and Sandip Badyal for providing crystals of sAPX-(W41A).*

## REFERENCES


1. Pierattelli, R., Banci, L., Eady, N. A. J., Bodiguel, J., Jones, J. N., Moody, P. C. E., Raven, E. L., Jamart-Gregoire, B., and Brown, K. A. (2004) *J. Biol. Chem.* **279,** 39000–39009
2. World Health Organization (2002) Vallanjohn, M., ed *Report on Infectious Diseases*, Geneva
3. Zhang, Y., Heym, B., Allen, B., Young, D., and Cole, S. (1992) *Nature* **358,** 591–593
4. Nagy, J. M., Cass, A. E. G., and Brown, K. A. (1997) *J. Biol. Chem.* **272,** 31265–31271
5. Johnsson, K., Froland, W. A., and Schultz, P. G. (1997) *J. Biol. Chem.* **272,** 2834–2840
6. Bertrand, T., Eady, N. A. J., Jones, J. N., Nagy, J. M., Jamart-Gregoire, B., Raven, E. L., and Brown, K. A. (2004) *J. Biol. Chem.* **279,** 38991–38999
7. Welinder, K. G. (1992) *Curr. Opin. Chem. Biol.* **2,** 388–393
8. Poulos, T. L., Freer, S. T., Alden, R. A., Edwards, S. L., Skogland, U., Takio, K., Eriksson, B., Xuong, N., Yonetani, T., and Kraut, J. (1980) *J. Biol. Chem.* **255,** 575–580
9. Sharp, K. H., Mewies, M., Moody, P. C. E., and Raven, E. L. (2003) *Nat. Struct. Biol.* **10,** 303–307
10. Sharp, K. H., Moody, P. C. E., Brown, K. A., and Raven, E. L. (2004) *Biochemistry* **43,** 8644–8651
11. Henriksen, A., Schuller, D. J., Meno, K., Welinder, K. G., Smith, A. T., and Gajhede, M. (1998) *Biochemistry* **37,** 8054–8060
12. Fishel, L. A., Villafranca, J. E., Mauro, J. M., and Kraut, J. (1987) *Biochemistry* **26,** 351–360
13. Lad, L., Mewies, M., and Raven, E. L. (2002) *Biochemistry* **41,** 13774–13781
14. Badyal, S. K., Joyce, M. G., Sharp, K. H., Seward, H. E., Mewies, M., Basran, J., Macdonald, I. K., Moody, P. C. E., and Raven, E. L. (2006) *J. Biol. Chem.* **281,** 24512–24520
15. Leslie, A. G. W. (1992) *Joint CCP4 + ESF-EAMCB Newsletter on Protein Crystallography, No. 26* Daresbury Laboratory, Warrington, UK
16. Evans, P. R. (2005) *Acta Crystallogr. Sect. D Biol. Crystallogr.* **62,** 72–82
17. Finzel, B. C., Poulos, T. L., and Kraut, J. (1984) *J. Biol. Chem.* **259,** 13027–13036
18. Murshudov, G. N., Vagin, A. A., and Dodson, E. J. (1997) *Acta Crystallogr. Sect. D Biol. Crystallogr.* **53,** 240–255
19. Bailey, S. (1994) *Acta Crystallogr. Sect. D Biol. Crystallogr.* **50,** 760–763
20. Emsley, P., and Cowtan, K. (2004) *Acta Crystallogr. Sect. D Biol. Crystallogr.* **60,** 2126–2132
21. Lad, L., Mewies, M., Basran, J., Scrutton, N. S., and Raven, E. L. (2002) *Eur. J. Biochem.* **369,** 3182–3192
22. DeLano, W. L. (2002) *The PyMOL Molecular Graphics System*, DeLano Scientific, San Carlos, CA
23. Itakura, H., Oda, Y., and Fukuyama, K. (1997) *FEBS Lett.* **412,** 107–110
24. Tsukamoto, K., Itakura, H., Sato, K., Fukuyama, K., Miura, S., Takahashi, S., Ikezawa, H., and Hosoya, T. (1999) *Biochemistry* **38,** 12558–12568
25. Heym, B., Alzari, P. M., Honore, N., and Cole, S. T. (1995) *Mol. Microbiol.* **15,** 235–245
26. Cockerill, F. R., Uhl, J. R., Temesgen, Z., Zhang, Y., Stockman, L., Roberts, G. D., Williams, D. L., and Kline, B. C. (1995) *J. Infect. Dis.* **171,** 240–245
27. Haas, W. H., Schilke, K., Brand, J., Amthor, B., Weyer, K., Fourie, P. B., Bretzel, G., StichtGroh, V., and Bremer, H. J. (1997) *Antimicrob. Agents Chemother.* **41,** 1601–1603
28. Marttila, H. J., Soini, H., Eerola, E., Vyshnevskaya, E., Vyshnevskiy, B. I., Otten, T. F., Vasilyef, A. V., and Viljanen, M. K. (1998) *Antimicrob. Agents Chemother.* **42,** 2443–2445
29. Kapetanaki, S., Chouchane, S., Girotto, S., Yu, S. W., Magliozzo, R. S., and

Schelvis, J. P. M. (2003) *Biochemistry* **42,** 3835–3845
30. Rouse, D. A., Li, Z. M., Bai, G. H., and Morris, S. L. (1995) *Antimicrob. Agents Chemother.* **39,** 2472–2477
31. Rouse, D. A., and Morris, S. L. (1995) *Infect. Immun.* **63,** 1427–1433
32. Musser, J. M., Kapur, V., Williams, D. L., Kreiswirth, B. N., van Soolingen, D., and van Embden, J. D. A. (1996) *J. Infect. Dis.* **173,** 196–202
33. Sundaramoorthy, M., Kishi, K., Gold, M. H., and Poulos, T. L. (1994) *J. Biol. Chem.* **269,** 32759–32767
34. Raman, C. S., Li, H. Y., Martasek, P., Kral, V., Masters, B. S. S., and Poulos, T. L. (1998) *Cell* **95,** 939–950
35. Crane, B. R., Arvai, A. S., Ghosh, D. K., Wu, C. Q., Getzoff, E. D., Stuehr, D. J., and Tainer, J. A. (1998) *Science* **279,** 2121–2126
36. Fischmann, T. O., Hruza, A., Niu, X. D., Fossetta, J. D., Lunn, C. A., Dolphin, E., Prongay, A. J., Reichert, P., Lundell, D. J., Narula, S. K., and Weber, P. C. (1999) *Nat. Struct. Biol.* **6,** 233–242
37. Poulos, T. L. (2007) *Nat. Prod. Rep.* **24,** 504–510
38. Bodiguel, J., Nagy, J. M., Brown, K. A., and Jamart-Gregoire, B. (2001) *J. Am. Chem. Soc.* **123,** 3832–3833

BIOCHEMISTRY



Article

# Engineering the Substrate Specificity and Reactivity of a Heme Protein: Creation of an Ascorbate Binding Site in Cytochrome *c* Peroxidase

Emma J. Murphy, Clive L. Metcalfe, Jaswir Basran, Peter C. E. Moody, and Emma Lloyd Raven

*Biochemistry*, **2008**, 47 (52), 13933-13941 • DOI: 10.1021/bi801480r • Publication Date (Web): 05 December 2008



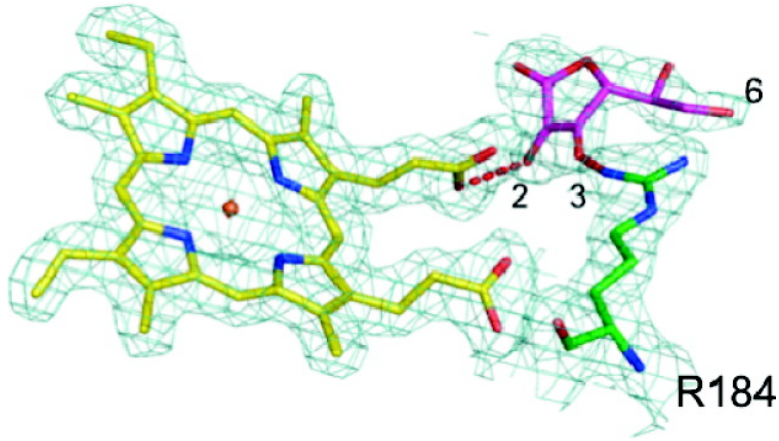


## More About This Article

Additional resources and features associated with this article are available within the HTML version:

- Supporting Information
- Access to high resolution figures
- Links to articles and content related to this article
- Copyright permission to reproduce figures and/or text from this article

View the Full Text HTML

# Engineering the Substrate Specificity and Reactivity of a Heme Protein: Creation of an Ascorbate Binding Site in Cytochrome *c* Peroxidase[†]

Emma J. Murphy,[‡] Clive L. Metcalfe,[‡] Jaswir Basran,[§] Peter C. E. Moody,[§] and Emma Lloyd Raven[‡,*]

*Department of Chemistry, Henry Wellcome Building, University of Leicester, University Road, Leicester, LE1 9HN, England U.K., and Department of Biochemistry and Henry Wellcome Laboratories for Structural Biology, Henry Wellcome Building, University of Leicester, Lancaster Road, Leicester, LE1 9HN, England U.K.*

*Received August 6, 2008; Revised Manuscript Received November 7, 2008*

ABSTRACT: The binding of substrates to heme enzymes has been widely assumed to occur at the so-called $\delta$-heme edge. Recently, however, a number of examples have appeared in which substrate binding at an alternative site, the $\gamma$-heme edge, is also possible. In previous work [Sharp et al. (2003) *Nat. Struct. Biol. 10*, 303−307], we showed that binding of ascorbate to ascorbate peroxidase occurred at the $\gamma$-heme edge. Here, we show that the closely related cytochrome *c* peroxidase enzyme can duplicate the substrate binding properties of ascorbate peroxidase through the introduction of relatively modest structural changes at Tyr36 and Asn184. Hence, crystallographic data for the Y36A/N184R/W191F triple variant of cytochrome *c* peroxidase shows ascorbate bound to the $\gamma$-heme edge, with hydrogen bonds to the heme propionate and Arg184. In parallel mechanistic studies in variants incorporating the W191F mutation, we show that a transient porphyrin $\pi$-cation radical in Compound I of cytochrome *c* peroxidase, analogous to that observed in ascorbate peroxidase, is competent for ascorbate oxidation but that under steady state conditions this intermediate decays too rapidly to sustain efficient turnover of ascorbate. The results are discussed in terms of our more general understanding of substrate oxidation across other heme proteins, and the emerging role of the heme propionates at the $\gamma$-heme edge.

Our understanding of substrate binding across various heme enzymes developed largely from crystallographic information for a number of heme peroxidase enzymes. The first structures to appear showed binding of aromatic substrates close to the so-called $\delta$-heme edge (*1*−*5*), and these structures were consistent with other observations, for example from earlier chemical modification work (*6*−*8*), in which substrate binding at the $\delta$-heme edge was also implicated. As a consequence, a consensus emerged in which substrate binding and oxidation at the so-called $\delta$-heme edge was widely assumed. With the exception of the cytochrome *c* peroxidase/cytochrome *c* complex—which was known to be anomalous in part because of its unusual substrate—the only outlier to this general "trend" was the structure for the manganese peroxidase/Mn(II) complex, which showed Mn(II) bound at a different location, close to the $\gamma$-heme edge and ligated by carboxylate groups and the heme 6-propionate (*9*). Later on, two other structures appeared, for the ascorbate peroxidase/ascorbate (*10*) and nitric oxide synthase/tetrahydrobiopterin (*11, 12*) complexes. These structures also revealed hydrogen bonding interactions between the substrate and the heme 6-propionate at the $\gamma$-heme edge. It became clear, therefore, that substrate binding at the $\delta$-heme edge was not the only means by which the enzyme and substrate might productively associate with one another. As far as the protein is concerned, this offers distinct advantages over the "one-site-fits-all" model, because it provides more than one route through which electron delivery can be channeled. Consequently, oxidation of different *types* of substrate can be accommodated within the *same* protein framework, for example in ascorbate peroxidase where (hydrophobic) aromatic substrates and (hydrophilic) ascorbate are oxidized at different sites (*1, 10*).

In previous work (*10*), we identified the ascorbate binding site in ascorbate peroxidase (APX[1]), Figure 1. The structure was helpful not only because it revealed the details of the binding interactions in APX but also because but also because it helped to rationalize differences with the closely related cytochrome *c* peroxidase enzyme. Hence, we noted that the residues required for ascorbate binding (Arg172, Lys 30, Figure 1 (inset)) are replaced by Asn184 and Asp33 in C*c*P; conversely, the residues required for binding of cytochrome *c* (Asp34, Glu35, Asp37, Glu290 (*13*)) are completely missing in APX. This comparison of the two structures also accounted for the observation that Trp179 is not essential for catalysis in APX (*14*) while the equivalent residue (Trp191) in C*c*P is (*15*), because in APX there is direct coupling of the substrate to the heme propionate, completely bypassing Trp179. In this work, we demonstrate that C*c*P can, with relatively modest changes in protein structure

[†] This work was supported by grants from the BBSRC (Project Grants BB/C00602X/1, BB/C001184/1 and IIP 0206 /009, and a studentship to E.J.M.).

* To whom correspondence should be addressed. Tel: +44 (0)116 2297047. Fax: +44 (0)116 252 2789. E-mail: emma.raven@le.ac.uk.

[‡] Department of Chemistry.

[§] Department of Biochemistry and Henry Wellcome Laboratories for Structural Biology.

[1] Abbreviations: APX, ascorbate peroxidase; C*c*P, cytochrome *c* peroxidase.

10.1021/bi801480r CCC: $40.75 
Published on Web 12/05/2008

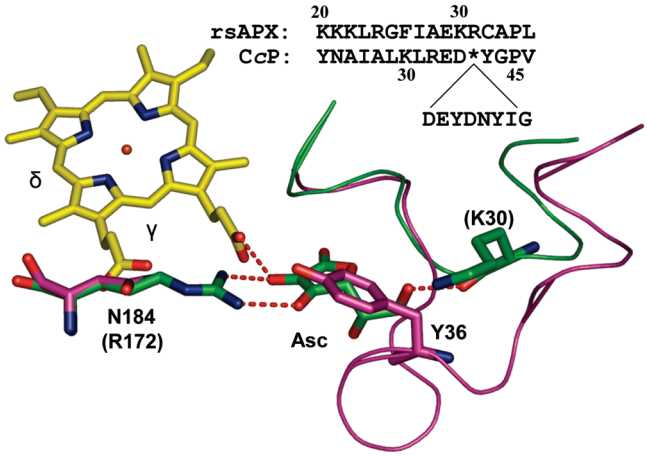


FIGURE 1: Comparison of APX with C*c*P, as described previously (*10*). The structure of the APX−ascorbate complex (PDB accession code 1OAF, in green) (*10*) overlaid with the structure of C*c*P (PDB accession code 2CYP in purple). The three main hydrogen bonding interactions between APX and ascorbate (Asc) are shown in red. C*c*P residues are indicated and those for APX given in parentheses. The $\delta$- and $\gamma$-heme edges are indicated. The loop regions (APX residues 26−36 and C*c*P residues 28−45) are shown along with the side chain of Tyr36 in C*c*P which blocks the equivalent ascorbate binding site found in APX. Residues important for ascorbate binding in APX are also shown (K30, R172) along with the residue equivalent to R172 in C*c*P (N184). Inset: Structural alignment of APX and C*c*P in the region of the ascorbate binding site. The sequence from 34 to 41 is missing in APX and is replaced with a single arginine residue at position 31. Glu 290 is also missing in APX due to a C-terminal truncation. This figure was prepared using PyMol (*43*).

around Tyr36 and Asn184 (Figure 1), be re-engineered to bind and oxidize ascorbate at the $\gamma$-heme edge.

## EXPERIMENTAL PROCEDURES

*Materials.* L-Ascorbic acid (Aldrich Chemical Co.) and buffers (Fisher) were all of the highest analytical grade (99%+ purity) and were used without further purification. Water was purified by an Elga purelab purification system and all buffers were filtered (0.2 $\mu$m) prior to use. Hydrogen peroxide solutions were freshly prepared by dilution of a 30% (v/v) solution (BDH): exact concentrations were determined using the published absorption coefficient ($\varepsilon_{240}$ = 39.4 $M^{-1}$ $cm^{-1}$) (*16*). All molecular biology kits and enzymes were used according to manufacturer's protocols.

*Mutagenesis, Protein Expression and Purification.* Site-directed mutagenesis on C*c*P was performed according to the Quikchange protocol (Stratagene Ltd., Cambridge, U.K.). Mutations were confirmed by DNA sequencing as reported previously (*17*). A number of single, double and triple variants of C*c*P were prepared involving Tyr36, Asn184 and Trp191. In total 7 variants were prepared: Y36A, N184R, W191F, Y36A/N184R, Y36A/W191F, N184R/W191F and Y36A/N184R/W191F.

Wild type C*c*P and all variants were prepared and isolated with modifications to published procedures (*18*). All variants containing the Y36A mutation failed to recrystallize against water as per the published procedure, and so further purification after gel filtration chromatography was carried out by FPLC (Superdex 75 gel filtration column), after which crystallization occurred. Absorption coefficients for all variants were determined using the pyridine-hemochromogen method (*19*) and are given in Table 1; the absorption coefficients of wild type C*c*P and W191F have been reported previously (*15, 18*).

Wavelength maxima for the ferric derivatives of all variants are given in Table 1. Wild type C*c*P and the single variants have spectra which are consistent with a predominantly high-spin heme species, either 5- or 6-coordinate with a water at the axial position. In contrast, the Y36A/W191F, Y36A/N184R and Y36A/N184R/W191F variants have similar spectra which are consistent with a predominantly low-spin heme species, as observed in the alkaline form of C*c*P (*20*). Spectra are shown in Figure S1 of the Supporting Information. For all variants, the crystal structures (below) show an oxygen ligand bound to the iron with Fe−O bond distances ranging between 2.15 and 2.87 Å. However, these distances do not correlate with the high-spin/low-spin distributions seen in the electronic spectra (i.e., expected longer bond lengths for high-spin species compared to low-spin) and we interpret these bond distances as arising from coordination of either water or hydroxide.

*Protein Crystallography.* Crystals were prepared by microdialysis with 100 $\mu$L of a 10−30 mg/mL solution of enzyme in 500 mM potassium phosphate, pH 6.0 against 10 mL of 50 mM potassium phosphate, pH 6.0 containing 30% 2-methyl-2,4-pentanediol by volume. With the exception of the triple variant, crystals were grown at 4 °C for approximately two days, yielding large red crystals. The triple variant needed up to two weeks to crystallize at 4 °C, and crystals were much smaller. For the structure of the Y36A/N184R/W191F−ascorbate complex, crystals were soaked in mother liquor containing 100 mM ascorbate for 5 min before rapid cooling to 100 K. Soaks at higher concentrations of ascorbate and for longer times caused the crystals to crack, and many variations of the soak (including variations in length of soak and ascorbate concentration) were attempted before the ascorbate bound structure was obtained. Although less than 50% of the unique data was collected, the presence of bound ascorbate was validated by difference Fourier calculations (discussed in Figure S3 of the Supporting Information).

*Data Collection and Refinement.* Diffraction data were collected for all variants in house using a Rigaku RU2HB X-ray generator with copper anode and Xenocs multilayer optics and an R-Axis IV detector. All data were collected at 100 K. Data were indexed, integrated and scaled using MOSFLM (*21*) and SCALA (*22*). Data collection statistics are shown in Table 2, and 5% of the data were flagged for the calculation of $R_{free}$ and excluded from subsequent refinement. The structures were refined from the 1.70 Å wild type C*c*P structure (*23*) (Protein data bank entry 2CYP). All refinement used REFMAC5 (*24*) from the CCP4 suite (*22*). Calculation of difference Fourier maps showed clear and unambiguous electron density for bound ascorbate in the Y36A/N184R/W191F structure. Ascorbate was incorporated into the last cycles of refinement. COOT (*25*) was used throughout for manual adjustment, ligand fitting and interpretation of the water structure.

*Steady State Kinetics.* Steady-state measurements (100 mM potassium phosphate, pH 6.0, 25.0 °C) for ascorbic acid, guaiacol (2-methoxy phenol) and cytochrome *c* (horse heart, Sigma) were carried out according to published protocols (*26*−*28*). For L-ascorbic acid initial

Table 1: Wavelength Maxima (nm) for the Ferric Derivatives of the Variants Examined in This Work[a]

| variant | wavelength maximum (nm) | | | | |
|---|---|---|---|---|---|
| | soret | CT1 | $\beta$ | α | CT2 |
| wild type C*c*P | 408 (102) | 506 | 544 (sh) | 589 (sh) | 647 |
| N184R | 408 (102) | 507 | 544 (sh) | 589 (sh) | 644 |
| Y36A | 408 (104) | 502 | 538 (sh) | 585 (sh) | 630 |
| W191F | 408 (109) | 504 | 544 (sh) | 589 (sh) | 645 |
| N184R/W191F | 412 (99) | | 536 | 563 (sh) | 645 (sh) |
| Y36A/W191F | 414 (350 sh) (98) | 485 (sh) | 533 | 566 | 632 (sh) |
| Y36A/N184R | 414 (354 sh) (96) | 489 (sh) | 534 | 568 | 620 (sh) |
| Y36A/N184R/W191F | 414 (350 sh) (100) | 489 (sh) | 536 | 567 | 620 (sh) |

[a] Absorption coefficients for the ferric derivatives ($mM^{-1}$ $cm^{-1}$) are shown in parentheses. sh = shoulder.

Table 2: Data Collection and Refinement Statistics for the Variants Examined in This Work and for the Y36A/N184R/W191F−Ascorbate Complex[a]

| protein | N184R | Y36A | W191F | N184R/ W191F | Y36A/ W191F | Y36A/ N184R | Y36A/N184R/ W191F | Y36A/N184R/ W191F−ascorbate complex |
|---|---|---|---|---|---|---|---|---|
| | | | | Data Collection | | | | |
| space group | $P2_12_12_1$ | $P2_12_12_1$ | $P2_12_12_1$ | $P2_12_12_1$ | $P2_12_12_1$ | $P2_12_12_1$ | $P2_12_12_1$ | $P2_12_12_1$ |
| unit cell (Å) | | | | | | | | |
| A | 51.0 | 51.1 | 51.1 | 51.0 | 51.0 | 51.1 | 51.0 | 51.0 |
| B | 74.5 | 75.8 | 75.3 | 74.6 | 75.0 | 75.1 | 74.5 | 74.4 |
| C | 106.3 | 107.1 | 106.3 | 106.7 | 106.4- | 107.3 | 106.5 | 106.6 |
| resolution (Å) | 61.78−1.40 (1.48−1.40) | 46.13- 2.01 (2.12−2.01) | 27.16−1.80 (1.90−1.80) | 27.17 −1.80 (1.90−1.80) | 45.93−2.10 (2.21−2.10) | 30.28−2.01 (2.11−2.01) | 39.13 - 1.86 (1.96−1.86) | 42.03- 2.01 (2.12−2.01) |
| total observations | 411140 (31869) | 58833 (8129) | 74923 (6085) | 87578 (8923) | 196453 (27085) | 38648 (4669) | 120110 (16654) | 15047 (2103) |
| unique reflections | 80702 (11309) | 26868 (3737) | 29668 (3257) | 34080 (4620) | 24405 (3514) | 18732 (2625) | 31259 (4618) | 12304 (1668) |
| $I/\sigma I$ | 15.6 (4.4) | 15.2 (6.6) | 22.9 (4.0) | 18.7 (5.3) | 9.1 (4.3) | 15.1 (3.0) | 18.0 (3.4) | 17.3 (5.2) |
| $R_{merge}$ | 0.082 (0.275) | 0.047 (0.112) | 0.039 (0.218) | 0.044 (0.125) | 0.076 (0.298) | 0.055 (0.389) | 0.063 (0.271) | 0.033 (0.104) |
| completeness (%) | 98.9 (95.9) | 95.0 (92.1) | 76.8 (59.4) | 88.8 (77.5) | 99.7 (99.5) | 65.8 (64.6) | 90.4 (92.3) | 45.9 (42.5)[b] |
| | | | | Refinement Statistics | | | | |
| $R_{work}$ | 0.172 | 0.161 | 0.174 | 0.186 | 0.168 | 0.165 | 0.169 | 0.187 |
| $R_{free}$ | 0.193 | 0.203 | 0.214 | 0.216 | 0.210 | 0.201 | 0.205 | 0.246 |
| RMSD | | | | | | | | |
| bonds (Å) | 0.007 | 0.015 | 0.012 | 0.013 | 0.015 | 0.014 | 0.013 | 0.013 |
| angles (deg) | 1.12 | 1.37 | 1.41 | 1.37 | 1.34 | 1.39 | 1.25 | 1.44 |

[a] Values in parentheses refer to the outer resolution bin. [b] Discussed in Figure S3 of the Supporting Information.

rates were calculated from time-dependent absorbance changes at 290 nm and multiplied by a factor of 2 to allow for disproportionation of the monodehydroascorbate radical (*26*). Substrate concentrations were calculated using the following absorption coefficients: L-ascorbic acid, $\varepsilon_{290} = 2.8$ $mM^{-1}$ $cm^{-1}$ (*29*); guaiacol, $\varepsilon_{470} = 22.6$ $mM^{-1}$ $cm^{-1}$ (*30*); cytochrome *c*, $\varepsilon_{550} = 27.7$ $mM^{-1}$ $cm^{-1}$. Concentration ranges were 10−750 $\mu$M for ascorbate, 2 mM to 60 mm for guaiacol, and 5−200 $\mu$M for cytochrome *c*; the concentration of peroxide was 200 $\mu$M in all assays. Data were fitted to the Michaelis−Menten equation as previously described (*26, 28*).

*Transient-State Kinetics.* Transient-state kinetics were performed using a SX.18 MV stopped-flow spectrophotometer (Applied Photophysics Ltd.) in 100 mM potassium phosphate, pH 6.0 at 10 °C. Time-dependent spectral changes occurring upon reaction of C*c*P with $H_2O_2$ were monitored using a photodiode array detector and X-SCAN software (Applied Photophysics Ltd.). In these experiments the protein (2 $\mu$M) was mixed with either a stoichiometric or 10-fold molar excess of $H_2O_2$ (reaction cell concentrations). Spectral deconvolution was performed by global analysis and numerical integration methods using PROKIN software (Applied Photophysics Ltd.).

Oxidation of L-ascorbate by the W191F and N184R/W191F variants of C*c*P was measured using the sequential mixing mode of the stopped-flow apparatus: enzyme (4 $\mu$M) was mixed with $H_2O_2$ (6 $\mu$M) and the solution allowed to age for 20 ms (enabling formation of the porphyrin $\pi$-cation radical intermediate) prior to mixing with excess ascorbate. Oxidation of ascorbate was monitored at 423 nm at a range of substrate concentrations.

## RESULTS AND DISCUSSION

*Design of Site-Directed Variants.* We noted originally (*1*) that a comparison of the C*c*P and APX structures in the region of the ascorbate binding site shows that the additional loop in C*c*P and the side chain of Tyr36 together prevent binding of ascorbate, and that Asn184 in C*c*P overlays with Arg172 in APX, Figure 1. In total 7 variants of C*c*P were therefore prepared with different combinations of the mutations Y36A, N184R and W191F. These were Y36A, N184R, W191F, N184R/W191F, Y36A/W191F, Y36A/N184R, and Y36A/N184R/W191F. The rationalization for the mutations was as follows: (i) Tyr36 directly blocks the equivalent ascorbate binding site in C*c*P and was therefore replaced with a less bulky residue; (ii) the N184R variant introduces

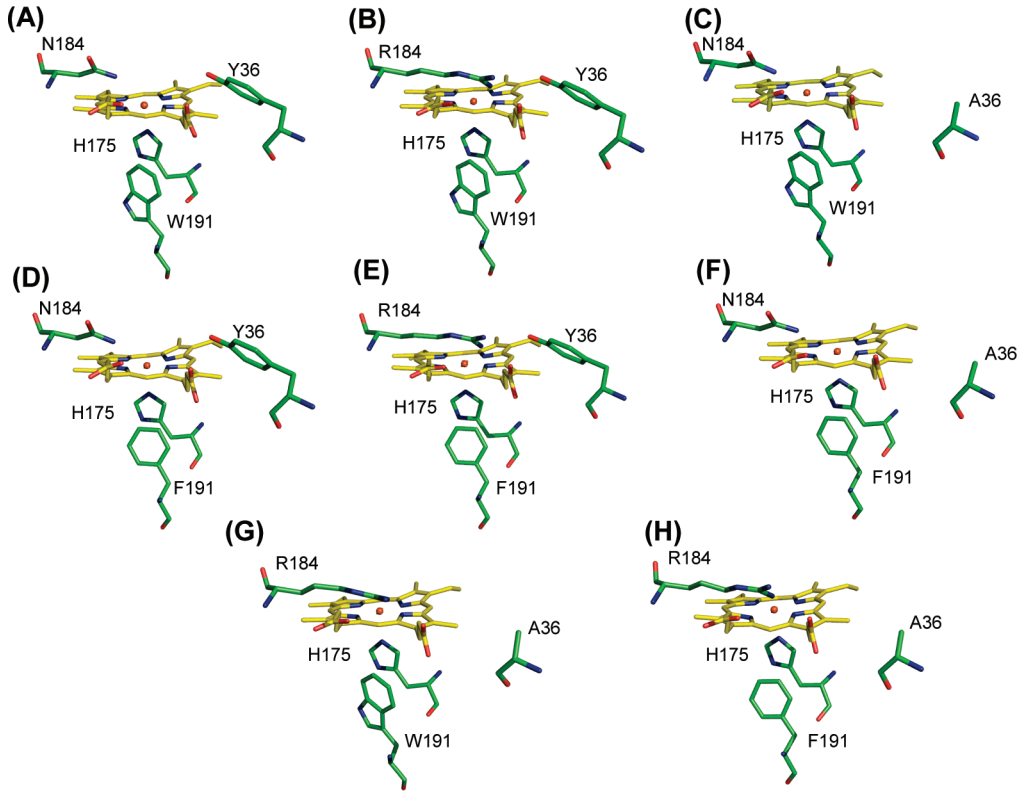


FIGURE 2: Structures of the C*c*P variants in the region of the heme. (A) Wild type C*c*P, (B) N184R, (C) Y36A, (D) W191F, (E) N184R/W191F, (F) Y36A/W191F, (G) Y36A/N184R and (H) Y36A/N184R/W191F. See also Figure S2 of the Supporting Information for electron densities. This figure was prepared using PyMol (*43*).

potential hydrogen bonding interactions for ascorbate binding; (iii) the W191F mutation was incorporated with the other mutations to assess whether C*c*P can support electron transfer directly through the heme edge, bypassing Trp191 (as in APX). Mutations that included a Lys in C*c*P were not included as part of this mutational analysis, because Lys 30, Figure 1, has been shown (*32*) to have little effect on ascorbate binding in APX.

*Crystallographic Studies.* We obtained structures for all of the variants presented in this paper, Table 2. The structures in the region of the heme are shown in Figure 2. In all cases, the structures were as expected and did not show major perturbations compared to the wild type protein (see also Figure S2 of the Supporting Information for electron densities).

Figure 3 shows the structure of the triple Y36A/N184R/W191F mutant close to the expected ascorbate binding site. The new variant, Figure 3(A), contains a cavity which was previously occupied by the side chain of Tyr36 and a single water molecule, Figure 3(C). Examination of the electron density in the new cavity, Figure 3(A), reveals two well-ordered water molecules which form hydrogen bonds to the engineered Arg184 residue and the heme 6-propionate. The first water molecule (labeled 1 in Figure 3(A)), is 2.70 Å from the O1 of the heme 6-propionate and 2.82 Å from the 1-NH group of Arg 184; the second is 2.82 Å from the 2-NH of Arg 184. Comparison of this structure with that of APX in the absence of ascorbate, Figure 3(B), shows that these water molecules in the triple C*c*P mutant are in analogous positions to two (also labeled 1 and 2 in Figure 3(B)) of the five water molecules seen in the ascorbate binding site of APX.

*Crystal Structure of the Y36A/N184R/W191F−Ascorbate Complex.* The structure of the Y36A/N184R/W191F triple mutant in complex with ascorbate is shown in Figure 3(D).[2] Comparison with the ascorbate-free structure shows that binding of ascorbate leads to no major structural rearrangements of the enzyme (data not shown). Ascorbate binds at the new cavity created at the $\gamma$-heme edge in place of the two water molecules seen in the unbound structure and in an analogous position to that observed for ascorbate bound to APX, Figure 3(A) (*10*). The refined atomic positions, Figure 3(D), show hydrogen bonds between the 2-OH (p$K_a$ 4.0 (*31*)) of the substrate and the heme 6-propionate (2.6 Å) and from the 3-OH (p$K_a$ 11.3 (*31*)) of the substrate and the 1-NH of Arg184 (2.4 Å). There are no clear hydrogen bonding interactions for the 6-OH group which is hydrogen bonded to Lys30 in APX; however, this interaction has been shown to have a minor role in stabilization of the substrate bound complex in APX (*32*). There is no evidence of ascorbate binding to any other site in the protein. By comparing the structure of the Y36A/N184R/W191F−ascorbate complex with that of the APX−ascorbate complex, Figure 3(E), it is clear that the ascorbate is orientated slightly differently in the two cases and that this affects the hydrogen bonding patterns. In the APX−ascorbate complex, Figure 3(E), the 2-OH group of the substrate makes two hydrogen bonds to the heme 6-propionate and Arg172; on the other hand, in the Y36A/N184R/W191F−ascorbate

[2] We have assigned the electron density as ascorbate since the enzyme has not been oxidized and therefore we assume that the substrate is not oxidized either. Note, however, that we are unable to distinguish between ascorbate and either of its oxidized products (monodehydroascorbate radical or dehydroascorbate).

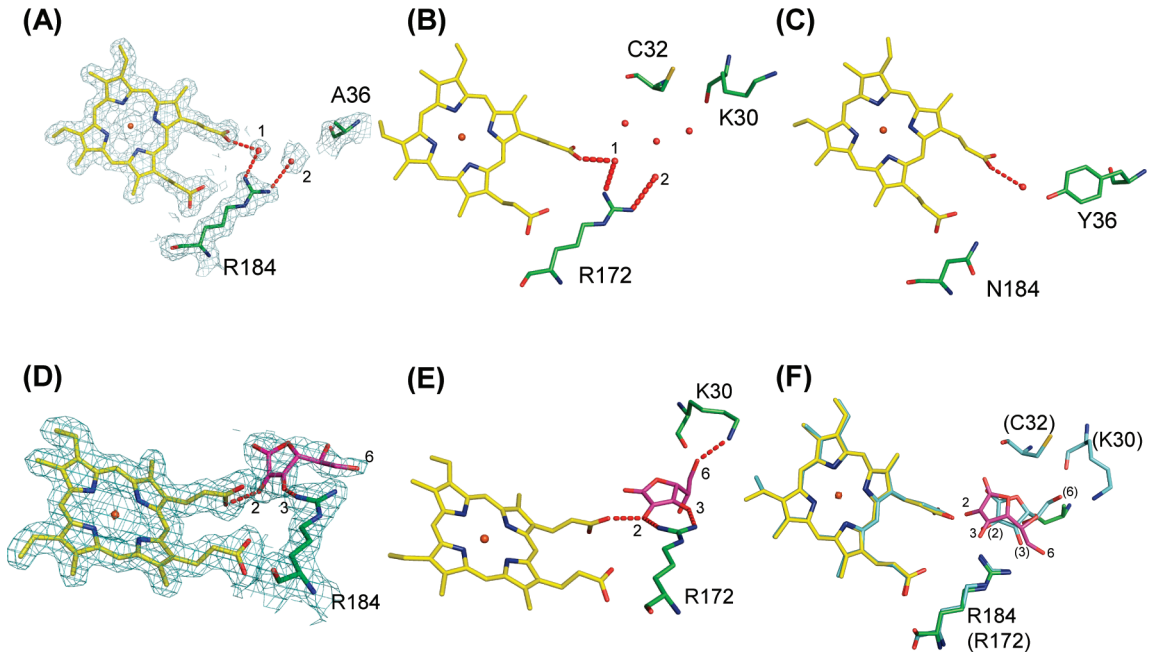


FIGURE 3: Comparison of the structures of the C*c*P variants with those of the APX−ascorbate complex. (A) The structure of Y36A/N184R/W191F. The F191 residue in the Y36A/N184R/W191F variant lies directly underneath the heme and is not shown in this orientation. In comparison to wild type C*c*P (C) two well ordered water molecules (labeled 1 and 2) occupy the new cavity created in similar positions to two of the water molecules (also labeled 1 and 2) seen in the ascorbate binding cavity of APX. (B), (C) The structures of wild type APX and C*c*P, respectively. (D) Refined electron density (aquamarine) for ascorbate (magenta) bound to the new cavity in Y36A/N184R/W191F (hydroxyl groups are labeled 2, 3 and 6). (E) The structure of the APX−ascorbate complex (*10*) (hydroxyl groups are as for (D)). (F) Comparison of the binding orientation for ascorbate in the APX−ascorbate complex (cyan) and Y36A/N184R/W191F (magenta). C*c*P residues are labeled with those for APX in parentheses and the hydroxyl groups of ascorbate are also labeled as in (E) and (F). In all figures, hydrogen bonds are indicated as red dotted lines and water molecules are shown as red spheres. This figure was prepared using PyMol (*43*).

complex, Figure 3(D), the altered binding orientation prevents the equivalent hydrogen bonding interaction between the 2-OH of the substrate and the 1-NH of Arg184. Equally, the 3-OH group of the substrate interacts with the 2-NH of Arg172 in APX, Figure 3(D), whereas this hydroxyl group interacts instead with the 1-NH group of Arg184 in the Y36A/N184R/W191F-ascorbate structure. A direct overlay of the APX-ascorbate complex and the Y36A/N184R/W191F-ascorbate complex is given in Figure 3(F).

*Nature of the Reactive Intermediates.* It was important to assess the nature of the intermediates formed during reaction of C*c*P and its variants with $H_2O_2$, so that the steady state data (*vide infra*) might be sensibly reconciled with the structural information. Reactions with $H_2O_2$ were examined by rapid scanning stopped-flow over a 500 ms time scale. For the wild type protein, addition of a stoichiometric amount of $H_2O_2$ leads to a red shift of the Soret band (from 410 to 421 nm) and the formation of two new bands at 533 and 562 nm, Figure 4(A), consistent with formation ($k_1 = 1 \times 10^7$ $M^{-1}s^{-1}$) of the expected Compound I species with a protein radical on Trp191.

The corresponding time-dependent spectroscopic changes for N184R and Y36A, under the same conditions, were similar to the wild type protein, Figures 4(B), (C) and we propose that formation ($k_1 = 1 \times 10^7$ $M^{-1}s^{-1}$ in both cases) of a normal Compound I with a radical on Trp191 occurs in these cases.

There are four variants which included the W191F mutation, and we wanted to assess whether a porphyrin $\pi$-cation radical was formed in these cases. For W191F and N184R/W191F this proved to be the case, because spectroscopic changes on reaction with $H_2O_2$ showed evidence for formation ($k_1 = 1.2 \times 10^6$ and $1.6 \times 10^6$ $M^{-1}$ $s^{-1}$, respectively) of an initial intermediate ($\lambda_{max} = 412$, 543 and 656 nm in both cases), Figures 4(D), (E), which is consistent with a transient porphyrin $\pi$-cation radical, as observed previously for W191F (*33*). This intermediate is very unstable and decays over 500 ms in a first-order process ($k_2 \sim 20$ $s^{-1}$ in both cases) to a final product ($\lambda_{max} = 423$, 535 and 565 nm) which is very similar to that of the wild type and is consistent with an oxy-ferryl species and a protein radical (*34*); since Trp191 is not available, the radical must reside on another residue, previously proposed as a tyrosine (*35*). For the Y36A/W191F variant, no significant spectroscopic changes on reaction with stoichiometric or higher amounts of $H_2O_2$, Figure 4(G), were seen. The Y36A/N184R variant, Figure 4(F), shows similar behavior, and this has been observed previously in other variants of C*c*P (*36, 37*).[3] As mentioned above, it is likely that nonspecific reactions, perhaps involving protein radical formation, occur in these cases, but this was not explored further.

In contrast to W191F and N184R/W191F, the Y36A/N184R/W191F variant shows no evidence for a porphyrin $\pi$-cation radical. In this case, reaction with peroxide is observed as for the wild type ($k_1 = 10^7$ $M^{-1}$ $s^{-1}$). Since a porphyrin $\pi$-cation radical is clearly observed for Compound I species of the other variants containing the W191F mutation (W191F and N184R/W191F, above), we conclude that the formation of this species likely also occurs for Y36A/N184R/

[3] This variant also has a higher proportion of 6-coordinate heme in the ferric form, which may moderate reactivity.

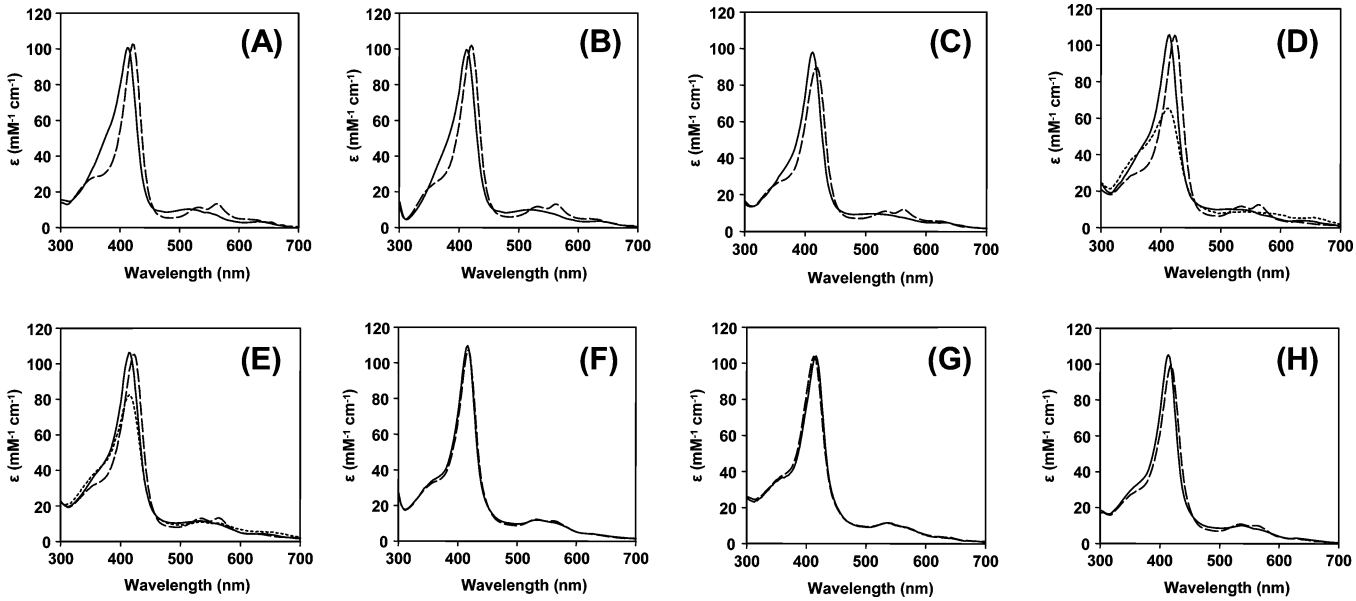


FIGURE 4: Photodiode array spectra for reaction of the C*c*P variants with $H_2O_2$. (A) Wild type C*c*P, (B) N184R, (C) Y36A, (D) W191F, (E) N184R/W191F, (F) Y36A/N184R, (G) Y36A/W191F and (H) Y36A/N184R/W191F. In each case the solid line indicates the spectrum before addition of $H_2O_2$ and the dashed line is after addition. Time-dependent changes were fitted either to an A → B model (panels (A), (B), (C), (F) and (H)) or an A → B → C model (panels (D), (E)); where intermediates were observed (panels (D), (E)), these are indicated by a dotted line. Enzyme was reacted stoichiometrically with $H_2O_2$, except for Y36A/W191F, panel (G), which was reacted with a 10-fold excess of $H_2O_2$.

Table 3: Kinetic Parameters for the Oxidation of Guaiacol Ascorbate and Cytochrome *c*[a]

| | guaiacol | | ascorbate | | cytochrome *c* | |
|---|---|---|---|---|---|---|
| variant | $k_{cat}$ ($s^{-1}$) | $K_M$ (mM) | $k_{cat}$ ($s^{-1}$) | $K_M$ (mM) | $k_{cat}$ ($s^{-1}$) | $K_M$ ($\mu$M) |
| wild type C*c*P | 4.1 ± 0.3 | 53 ± 6.0 | 0.83 ± 0.14 | 0.71 ± 0.22 | 1510 ± 259 | 93 ± 31 |
| N184R | 3.0 ± 0.1 | 27 ± 1.6 | 1.5 ± 0.10 | 1.7 ± 0.21 | 570 ± 40 | 140 ± 18 |
| Y36A | 5.4 ± 0.2 | 36 ± 3.1 | 1.3 ± 0.08 | 1.7 ± 0.19 | 580 ± 35 | 230 ± 28 |
| W191F | 14 ± 0.6 | 57 ± 4.6 | 0.25 ± 0.01 | 0.45 ± 0.004 | 1.7 ± 0.13 | 100 ± 16 |
| N184R/W191F | 4.9 ± 0.2 | 34 ± 2.2 | 0.27 ± 0.01 | 0.31 ± 0.004 | 0.08 ± 0.01 | 670 ± 110 |
| Y36A/W191F | 3.2 ± 0.2 | 45 ± 2.5 | 0.45 ± 0.06 | 0.50 ± 0.13 | 0.06 ± 0.01 | 160 ± 17 |
| Y36A/N184R | 0.9 ± 0.01 | 16 ± 0.7 | 0.66 ± 0.03 | 0.48 ± 0.06 | 600 ± 27 | 110 ± 10 |
| Y36A/N184R/W191F | 1.5 ± 0.1 | 14 ± 1.2 | 2.6 ± 0.35 | 1.3 ± 0.22 | 1.6 ± 0.13 | 300 ± 27 |

[a] All assays were carried out in 0.1 M KPi buffer at pH 6.0 and 25 °C.

W191F but that the introduction of the Y36A mutation destabilizes the porphyrin $\pi$-cation radical such that it decays on a time scale that is too rapid for the stopped-flow experiment. This is consistent with the data for Y36A/W191F (above), which also show no evidence for a porphyrin $\pi$-cation intermediate.

*Steady-State Oxidation of Substrates.* The competency of the variants to support oxidation of various substrates was assessed in parallel steady state assays. Table 3 shows data for oxidation of guaiacol, ascorbate and cytochrome *c*. We use this information to make correlations with the pre-steady data above.

As expected (*15, 33*), the W191F mutation dramatically reduced the activity toward cytochrome *c*, but in the other variants which did not contain the W191F mutation the activity toward cytochrome *c* was largely unaffected, Table 3.

Guaiacol oxidation was not significantly affected by any of the mutations, including W191F, which is consistent with the idea that aromatic substrates such as guaiacol bind at a separate location close to the $\delta$-heme edge (*1, 38*) and is clearly indicative of a different electron transfer pathway for the oxidation of these types of aromatic substrate.

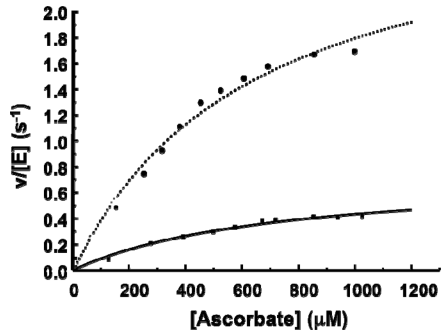


FIGURE 5: Steady-state oxidation of L-ascorbate by C*c*P. Wild type C*c*P (solid line) and Y36A/N184R/W191F (dashed line) (0.1 M potassium phosphate, pH 6.0, 25 °C). The solid lines are a fit to the Michaelis−Menten equation.

Ascorbate oxidation is measurable but slow for wild type C*c*P, with clear changes in absorbance at 290 nm which report directly on ascorbate oxidation (as in APX (*26*)). We determine $k_{cat} = 0.83 \pm 0.14\ s^{-1}$ for the wild type enzyme, Figure 5, which compares with a previous value of 3 $s^{-1}$ (*39*). We also clearly observe oxidation of ascorbate for all the variants, Table 3 and Figure 5. On the whole, however, the rates of oxidation are not markedly increased from those

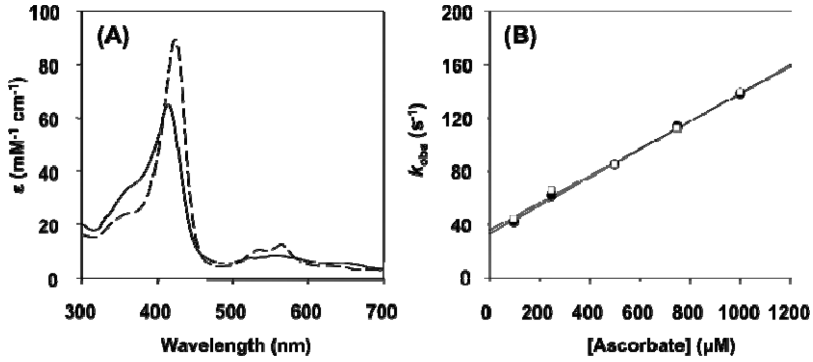


FIGURE 6: Oxidation of ascorbate by the transient porphyrin $\pi$-cation intermediate. (A) Deconvoluted spectra for the reaction of the porphyrin $\pi$-cation intermediate in W191F with ascorbate. The solid line indicates the porphyrin $\pi$-cation intermediate formed after mixing enzyme with $H_2O_2$; the dashed line is the final species after addition of ascorbate to the first intermediate. Similar spectra were observed for W191F/N184R (not shown). (B) Dependence of the observed rate constant, $k_{obs}$, for reduction of the porphyrin $\pi$-cation intermediate on ascorbate concentration for W191F (filled circles) and N184R/W191F (open squares). Conditions: [enzyme] = 4 $\mu$M, [$H_2O_2$] = 6 $\mu$M (both cell concentrations), 0.1 M potassium phosphate, pH 6.0; delay time of 20 ms before reaction with ascorbate contained in the same buffer.

of wild type C*c*P, with the highest value of $k_{cat}$ observed for the Y36A/N184R/W191F variant ($k_{cat}$ = 2.6 ± 0.35 $s^{-1}$, Figure 5).

Together, these kinetic data allow us to make useful comparisons between APX and C*c*P. Hence, although W191F and N184R/W191F (and, we assume, Y36A/N184R/W191F) clearly forms a porphyrin $\pi$-cation radical as for APX (above), the formation of this intermediate does not translate into high ascorbate activity in the steady state. We conclude that in the C*c*P variants the decay of the essential porphyrin $\pi$-cation species is much too rapid ($k_1 \approx 20$ $s^{-1}$ compared to $\approx 0.03$ $s^{-1}$ for APX) to support oxidation of the substrate ($k_{cat} \approx 1$ $s^{-1}$ compared to $\approx 80$ $s^{-1}$ for APX) in the steady state.

*Reactivity of the Porphyrin π-Cation Intermediate with Ascorbate.* The above data raise the question about the inherent reactivity of the porphyrin $\pi$-cation intermediate, and whether it may, in fact, be competent for ascorbate oxidation under different conditions where its rapid decay was not competitive with substrate oxidation (i.e., in the pre-steady state).

To assess this, we carried out double mixing experiments with W191F, Figure 6, and N184R/W191F (data not shown) in the presence of $H_2O_2$ and ascorbate. Initial formation of the transient porphyrin $\pi$-cation intermediate was observed (as above) on reaction of both ferric enzymes with $H_2O_2$. On addition of ascorbate in a second mixing event, we then observe that conversion to the final product (i.e., B → C) occurred much more rapidly than in the absence of ascorbate, Figure 6.[4] There is a linear dependence of the observed rate constants on ascorbate concentration (data not shown), from which a second order rate constant $k_{on} \sim 1.0 \times 10^5$ $M^{-1}$ $s^{-1}$ can be derived in both cases; this linear dependence also shows an intercept, $k_{off} \approx 34$ $s^{-1}$, which most likely reflects decay of the intermediate (with $k_{off}$ approximately the same as that measured above (≈20 $s^{-1}$)).[5] A direct comparison with wild type C*c*P is not possible, see footnote 6, but it is possible to compare the second order rate constant measured above with that for reduction of Compound I by ascorbate in horseradish peroxidase (HRP). For HRP, a rate constant of $1.8 \times 10^5$ $M^{-1}$ $s^{-1}$ is reported (*44*), which compares well with our value above.

These data highlight two important points. First, they show that in cases where a porphyrin $\pi$-cation intermediate forms it is indeed capable of ascorbate oxidation, but that its decay under steady state conditions occurs much too rapidly for efficient turnover. This presumably means that the porphyrin $\pi$-cation intermediate is competent for electron transfer, in the sense that it can be reduced by substrate in a step that requires only electron transfer (and not proton transfer, see below). Second, since the on rate constants in the presteady state experiments ($k_{on,obs} \approx 40-120$ $s^{-1}$) are much faster than our measured values for $k_{cat}$ in the steady state, substrate binding is not likely to be limiting in the steady state, and we conclude that some other process (e.g., proton transfer during reduction of Compound II) controls turnover. This would explain why the $k_{cat}$ values are broadly similar in all variants.[6]

*Implications for Substrate Binding in Other Heme Enzymes.* Our appreciation of the substrate binding specificities across a range of heme proteins has changed as we have learned that different heme enzymes can bind and oxidize different substrates at different sites. Although C*c*P has an anomalous substrate, we have recently shown (*38*) that C*c*P binds the aromatic substrate isoniazid at the $\delta$-heme edge. In this sense, C*c*P is behaving more conventionally insofar

[4] In contrast, in experiments with Y36A/N184R/W191F and wild type protein, neither of which forms a porphyrin $\pi$-cation radical, there were no changes to the transients in the presence of ascorbate (compared to those in the absence of ascorbate, Figure 4).

[5] The corresponding reaction of C*c*P with ascorbate was also examined in control reactions. (This does not provide a direct comparison, however, because the structure of the Compound I intermediate for the wild type protein (Trp radical) is different from that in W191F and N184R/W191F.) In this experiment, stoichiometric addition of $H_2O_2$ led to formation of the expected Compound I, but on addition of ascorbate very small changes in spectra were observed over 1 s that most likely represent reduction to Compound II (i.e., reduction of the protein radical occurs). Over longer time scales (60 s), reduction back to ferric heme is observed, which is consistent with the steady state data.

[6] We cannot rule out a further possibility that the ascorbate site seen in our structure is not the site of oxidation, and that a second ascorbate site exists. We consider this unlikely because our other structural work on both APX and C*c*P (in the presence of high concentrations of ascorbate) has never revealed a second binding site. We note, however, that in lignin peroxidase two binding sites for substrate have been proposed (Choinowski, T., Blodig, W., and Winterhalter, K. (1999) *J. Mol. Biol. 286*, 809−827; Blodig, W., Smith, A. T., Doyle, W., Piontek, K. (2001) *J. Mol. Biol. 305*, 851−861).

as it is binding a substrate and oxidizing it at the $\delta$-heme edge as observed for other peroxidase enzymes. This must mean that a separate conduit for electron transfer, independent of that used for oxidation of cytochrome *c*, must be available, and our steady state data for oxidation of guaiacol support this.

But it is now clear that the $\delta$-heme edge does not have a monopoly on substrate oxidation, and that the $\gamma$-heme edge is also important. There are three examples: the manganese peroxidase/Mn(II) complex (*9*), the nitric oxide synthase/tetrahydrobiopterin complex (*12*) and the APX/ascorbate complex (*10*). In all three cases, the heme propionate is involved in a hydrogen-bonding interaction with the bound substrate (although it is not the same propionate in all cases) and the role of these propionate groups as direct participants in the catalytic process has recently attracted attention (*40*−*42*). The data presented here now show that this same binding interaction can also be engineered in C*c*P. Hence, we have shown that relatively minor alterations in structure at Tyr36 and Asn184 are enough to allow ascorbate to bind to C*c*P at the $\gamma$-heme edge in the same site and with essentially the same hydrogen bonding pattern as that observed for APX. Although we only have a structure for the triple variant, we suggest that binding, albeit weakly, most likely occurs at this same site in the other variants and possibly even in the wild type protein.

Our data also show that C*c*P is functionally competent for oxidation of the ascorbate in the engineered variants, but there is little real enhancement of activity over the latent activity of the wild type enzyme in this or any of the other variants studied in the steady state. In this sense, the steady state turnover certainly does not approach that observed in APX ($k_{cat} \approx 80\ s^{-1}$) even in the Y36A/N184R/W191F variant. The pre-steady state data for W191F and N184R/W191F demonstrate an intrinsic competency of the porphyrin $\pi$-cation radical in Compound I for ascorbate oxidation, as a simple electron transfer process. This is not, however, enough to support steady state turnover because the decay of the transient porphyrin $\pi$-cation radical outruns ascorbate oxidation. This is in contrast to the situation in APX, where decay of Compound I is much slower and not competitive with steady state turnover. In fact, even if the decay of the porphyrin $\pi$-cation intermediate were not so rapid, it is likely that proton transfer during reduction of Compound II by ascorbate would be rate limiting during turnover (as is the case for APX) so that the straightforward introduction of a substrate binding site would need also to be coupled to proton delivery.

It appears, therefore, that the combination of efficient substrate binding, together with the formation of a suitably stable porphyrin $\pi$-cation radical, seems to be the key to rapid substrate oxidation at the $\gamma$-heme edge (and, indeed, the $\delta$-heme edge) and that hydrogen bonding plays a crucial role. The wider role of the heme propionates should also not be underestimated: it may well be the case that, in addition to providing glue for substrate binding, these charged groups have other, as yet unidentified, biological roles.

## ACKNOWLEDGMENT

We thank Grant Mauk for the gift of the C*c*P expression vector and Dr Igor Efimov for helpful discussions. We are also grateful to an anonymous reviewer for insightful comments on the kinetic data.

## NOTE ADDED DURING REVIEW

While this paper was under review, another paper appeared (Meharenna et al. (2008) *Biochemistry 47,* 10324−10332), based on the APX-ascorbate structure (*10*), in which C*c*P was also engineered to encourage ascorbate binding. In this paper, the LREDDEYDNYIGY loop, Figure 1, was replaced with the corresponding APX sequence (IAEKKC) and coupled with the N184R and W191F mutations. Crystal structures are presented but none have ascorbate bound to the enzyme. Molecular dynamics calculations indicate that Asn80 allows movement of the ascorbate and thus prevents ascorbate binding. These calculations are not consistent with our crystallographic data for the ascorbate-bound complex of Y36A/N184R/W191F, Figure 3(D), since the same Asn (Asn87) is present and cannot, therefore, prevent binding of ascorbate. In addition, the Meharenna et al. paper reports an enhancement of ascorbate activity ($k_{cat} = 12\ min^{-1}$) for the best mutant, but this is based on a complete absence of ascorbate activity for wild type C*c*P, whereas we and others ($\approx 1\ s^{-1}$, Table 1, and $\approx 3\ s^{-1}$ (*39*), respectively) observe clear activity for wild type C*c*P at greater than $12\ min^{-1}$.

## SUPPORTING INFORMATION AVAILABLE

Electronic spectra and structures for the variants, plus electron density for the ascorbate site. This material is available free of charge via the Internet at http://pubs.acs.org.

## REFERENCES

1. Sharp, K. H., Moody, P. C. E., Brown, K. A., and Raven, E. L. (2004) Crystal structure of the ascorbate peroxidase-salicylhydroxamic acid complex. *Biochemistry 43*, 8644–8651.
2. Henriksen, A., Schuller, D. J., Meno, K., Welinder, K. G., Smith, A. T., and Gajhede, M. (1998) Structural interactions between horseradish peroxidase C and the substrate benzhydroxamic acid determined by x-ray crystallography. *Biochemistry 37*, 8054–8060.
3. Itakura, H., Oda, Y., and Fukuyama, K. (1997) Binding mode of benzhydroxamic acid to arthromyces ramosus peroxidase shown by X-ray crystallographic analysis of the complex at 1.6 angstrom resolution. *FEBS Lett. 412*, 107–110.
4. Tsukamoto, K., Itakura, H., Sato, K., Fukuyama, K., Miura, S., Takahashi, S., Ikezawa, H., and Hosoya, T. (1999) Binding of salicylhydroxamic acid and several aromatic donor molecules to *Arthromyces ramosus* peroxidase, investigated by X-ray crystallography, optical difference spectroscopy, NMR relaxation, molecular dynamics, and kinetics. *Biochemistry 38*, 12558–12568.
5. Henriksen, A., Smith, A. T., and Gajhede, M. (1999) The structures of the horseradish peroxidase C-ferulic acid complex and the ternary complex with cyanide suggest how peroxidases oxidize small phenolic substrates. *J. Biol. Chem. 274*, 35005–35011.
6. DePillis, G. D., Sishta, B. P., Mauk, A. G., and de Montellano, P. R. O. (1991) Small substrates and cytochrome-*c* are oxidized at different sites of cytochrome-*c* peroxidase. *J. Biol. Chem. 266*, 19334–19341.
7. Ator, M. A., David, S. K., and de Montellano, P. R. O. (1987) Structure and catalytic mechanism of horseradish-peroxidase - regiospecific meso-alkylation of the prosthetic heme group by alkylhydrazines. *J. Biol. Chem. 262*, 14954–14960.
8. Ator, M. A., and de Montellano, P. R. O. (1987) Structure and catalytic mechanism of horseradish peroxidase. *J. Biol. Chem. 262*, 1542–1551.
9. Sundaramoorthy, M., Kishi, K., Gold, M. H., and Poulos, T. L. (1994) The crystal structure of manganase peroxidase from *Phanerochaete crysosporium* at 2.06 Å resolution. *J. Biol. Chem. 269*, 32759–32767.

10. Sharp, K. H., Mewies, M., Moody, P. C. E., and Raven, E. L. (2003) Crystal structure of the ascorbate peroxidase−ascorbate complex. *Nat. Struct. Biol. 10*, 303–307.
11. Wei, C. C., Crane, B. R., and Stuehr, D. J. (2003) Tetrahydrobiopterin radical enzymology. *Chem. Rev. 103*, 2365–2383.
12. Poulos, T. L., Li, H. Y., Raman, C. S., and Schuller, D. J. (2001) Structures of gas-generating heme enzymes: nitric oxide synthase and heme oxygenase. *Adv. Inorg. Chem. 51*, 243–293.
13. Pelletier, H., and Kraut, J. (1992) Crystal-structure of a complex between electron-transfer partners, cytochrome-*c* peroxidase and cytochrome-*c*. *Science 258*, 1748–1755.
14. Bonagura, C. A., Sundaramoorthy, M., Pappa, H. S., Patterson, W. R., and Poulos, T. L. (1996) An engineered cation site in cytochrome *c* peroxidase alters the reactivity of the redox active tryptophan. *Biochemistry 35*, 6107–6115.
15. Mauro, J. M., Fishel, L. A., Hazzard, J. T., Meyer, T. E., Tollin, G., Cusanovich, M. A., and Kraut, J. (1988) Tryptophan-191-phenylalanine, a proximal-side mutation in yeast cytochrome-*c* peroxidase that strongly affects the kinetics of ferrocytochrome-*c* oxidation. *Biochemistry 27*, 6243–6256.
16. Nelson, D. P., and Kiesow, L. A. (1972) Enthalpy of decomposition of hydrogen peroxide by catalase at 25 degrees C (with molar extinction coefficients of $H_2O_2$ solutions in the UV). *Anal. Biochem. 49*, 474–478.
17. Metcalfe, C. L., Ott, M., Patel, N., Singh, K., Mistry, S. C., Goff, H. M., and Raven, E. L. (2004) Autocatalytic formation of green heme: Evidence for $H_2O_2$-dependent formation of a covalent methionine-heme linkage in ascorbate peroxidase. *J. Am. Chem. Soc. 126*, 16242–16248.
18. Fishel, L. A., Villafranca, J. E., Mauro, J. M., and Kraut, J. (1987) Yeast cytochrome-*c* peroxidase - mutagenesis and expression in escherichia-coli show tryptophan-51 is not the radical site in compound-I. *Biochemistry 26*, 351–360.
19. Antonini, M., and Brunori, E. (1971) *Hemoglobin and myoglobin and their reactions with ligands*, North Holland Publishers, Amsterdam, p 10.
20. Pond, A. E., Sono, M., Elenkova, E. A., Goodin, D. B., English, A. M., and Dawson, J. H. (1999) Influence of protein environment on magnetic circular dichroism spectral properties of ferric and ferrous ligand complexes of yeast cytochrome *c* peroxidase. *Biospectroscopy 5*, S42−S52.
21. Leslie, A. G. W. (1992) Joint CCP4 + ESF-EAMCB newsletter on protein crystallography. No. *26*.
22. Bailey, S. (1994) The CCP4 suite - programs for protein crystallography. *Acta Crystallogr., Sect D: Biol. Crystallogr. 50*, 760–763.
23. Finzel, B. C., Poulos, T. L., and Kraut, J. (1984) Crystal-structure of yeast cytochrome-*c* peroxidase refined at 1.7 A resolution. *J. Biol. Chem. 259*, 3027–3036.
24. Murshudov, G. N., Vagin, A. A., and Dodson, E. J. (1997) Refinement of macromolecular structures by the maximum-likelihood method. *Acta Crystallogr., Sect. D: Biol. Crystallogr. 53*, 240–255.
25. Emsley, P., and Cowtan, K. (2004) Coot: Model-building tools for molecular graphics. *Acta Crystallogr., Sect. D: Biol. Crystallogr. 60*, 2126–2132.
26. Lad, L., Mewies, M., and Raven, E. L. (2002) Substrate binding and catalytic mechanism in ascorbate peroxidase: Evidence for two ascorbate binding sites. *Biochemistry 41*, 13774–13781.
27. Kang, D. S., and Erman, J. E. (1982) The cytochrome-*c* peroxidase-catalyzed oxidation of ferrocytochrome-*c* by hydrogen-peroxide - steady-state kinetic mechanism. *J. Biol. Chem. 257*, 2775–2779.
28. Lad, L., Mewies, M., Basran, J., Scrutton, N. S., and Raven, E. L. (2002) Role of histidine 42 in ascorbate peroxidase - kinetic analysis of the H42A and H42E variants. *Eur. J. Biochem. 269*, 3182–3192.
29. Asada, K. (1984) Chloroplasts - formation of active oxygen and its scavenging. *Methods Enzymol. 105*, 422–427.
30. Santimone, M. (1975) Titration study of guaiacol oxidation by horseradish-peroxidase. *Can. J. Biochem. 53*, 649–657.
31. Bryan, D. M., Pell, S. D., Kumar, R., Clarke, M. J., Rodriguez, V., Sherban, M., and Charkoudian, J. (1988) Stable pentaamminеruthenium(III) complexes of reductic acids - synthesis, linkage isomers, and autoxidation kinetics. *J. Am. Chem. Soc. 110*, 1498–1506.
32. Macdonald, I. K., Badyal, S. K., Ghamsari, L., Moody, P. C. E., and Raven, E. L. (2006) Interaction of ascorbate peroxidase with substrates: A mechanistic and structural analysis. *Biochemistry 45*, 7808–7817.
33. Miller, M. A., Vitello, L., and Erman, J. E. (1995) Regulation of interprotein electron-transfer by Trp-191 of cytochrome-*c* peroxidase. *Biochemistry 34*, 12048–12058.
34. Hoffman, B. M., Roberts, J. E., Kang, C. H., and Margoliash, E. (1981) Electron-paramagnetic and electron nuclear double-resonance of the hydrogen-peroxide compound of cytochrome-*c* peroxidase. *J. Biol. Chem. 256*, 6556–6564.
35. Scholes, C. P., Liu, Y. J., Fishel, L. A., Farnum, M. F., Mauro, J. M., and Kraut, J. (1989) Recent endor and pulsed electron-paramagnetic resonance studies of cytochrome-*c* peroxidase - compound-I and its site-directed mutants. *Isr. J. Chem. 29*, 85–92.
36. Pearl, N. M., Jacobson, T., Arisa, M., Vitello, L. B., and Erman, J. E. (2007) Effect of single-site charge-reversal mutations on the catalytic properties of yeast cytochrome *c* peroxidase: Mutations near the high-affinity cytochrome c binding site. *Biochemistry 46*, 8263–8272.
37. Vitello, L. B., Erman, J. E., Miller, M. A., Mauro, J. M., and Kraut, J. (1992) Effect of Asp235Asn substitution on the absorption-spectrum and hydrogen-peroxide reactivity of cytochrome-*c* peroxidase. *Biochemistry 31*, 11524–11535.
38. Metcalfe, C., Macdonald, I. K., Murphy, E. J., Brown, K. A., Raven, E. L., and Moody, P. C. E. (2008) The tuberculosis prodrug isoniazid bound to activating peroxidases. *J. Biol. Chem. 283*, 6193–6200.
39. Yonetani, T., and Ray, G. S. (1965) Studies on cytochrome *c* peroxidase: Purification and some properties. *J. Biol. Chem. 240*, 4503–4514.
40. Poulos, T. L. (2007) The Janus nature of heme. *Nat. Prod. Rep. 24*, 504–510.
41. Schoneboom, J. C., Cohen, S., Lin, H., Shaik, S., and Thiel, W. (2004) Quantum mechanical/molecular mechanical investigation of the mechanism of C-H hydroxylation of camphor by cytochrome P450(cam): Theory supports a two-state rebound mechanism. *J. Am. Chem. Soc. 126*, 4017–4034.
42. Guallar, V., Baik, M. H., Lippard, S. J., and Friesner, R. A. (2003) Peripheral heme substituents control the hydrogen-atom abstraction chemistry in cytochromes P450. *Proc. Natl. Acad. Sci. U.S.A. 100*, 6998–7002.
43. DeLano, W. L. (2002) DeLano Scientific, San Carlos, CA.
44. Lambier, A.-M., Dunford, H. B., and Pickard, M. A. (1987) Kinetics of the oxidation of ascorbic acid, ferrocyanide and p-phenolsulfonic acid by chloroperoxidase Compounds I and II. *Eur. J. Biochem. 163*, 123–127.

BI801480R